

Effective and Efficient Non-Destructive Testing of Large and
Complex Shaped Aircraft Structures

BY
JOHN P.SMITH

Thesis submitted to the University of Central Lancashire in
partial fulfilment of the requirements for the degree of

DOCTOR OF PHILOSOPHY

08/11/2004

The work presented in this thesis was carried out in the applied digital signal and image processing research centre (ADSIP) at the University of Central Lancashire and the Materials engineering and test department at BAE SYSTEMS, Warton and a number of production inspection sections at BAE SYSTEMS Samlesbury

DECLARATION

I declare that whilst registered with the University of Central Lancashire for the degree of Doctor of Philosophy I have not been a registered candidate or enrolled student for any other award of the University of Central Lancashire or any other academic institution. No portion of the work referred to in this thesis has been submitted in support of an application for any other degree or qualification of any other university or institute of learning.

John P.Smith

ABSTRACT

The main aim of the research described within this thesis is to develop methodologies that enhance the defect detection capabilities of non-destructive testing (NDT) for the aircraft industry.

Modern aircraft non-destructive testing requires the detection of small defects in large complex shaped components. Research has therefore focused on the limitations of ultrasonic, radiosopic and shearographic methods and the complimentary aspects associated with each method.

The work has identified many parameters that have significant effect on successful defect detection and has developed methods for assessing NDT systems capabilities by noise analysis, excitation performance and error contributions attributed to the positioning of sensors.

The work has resulted in

1. The demonstration that positional accuracy when ultrasonic testing has a significant effect on defect detection and a method to measure positional accuracy by evaluating the compensation required in a ten axis scanning system has revealed limits to the achievable defect detection when using complex geometry scanning systems.
2. A method to reliably detect 15 micron voids in a diffusion bonded joint at ultrasonic frequencies of 20 MHz and above by optimising transducer excitation, focussing and normalisation
3. A method of determining the minimum detectable ultrasonic attenuation variation by plotting the measuring error when calibrating the alignment of a ten axis scanning system
4. A new formula for the calculation of the optimum magnification for digital radiography. The formula is applicable for focal spot sizes less than 0.1 mm.
5. A practical method of measuring the detection capabilities of a digital radiographic system by calculating the modulation transfer function and the noise power spectrum from a reference image.
6. The practical application of digital radiography to the inspection of super plastically formed diffusion bonded titanium (SPFDB) and carbon fibre composite structure has been demonstrated but

has also been supported by quantitative measurement of the imaging systems capabilities.

7. A method of integrating all the modules of the shearography system that provides significant improvement in the minimum defect detection capability for which a patent has been granted.
8. The matching of the applied stress to the data capture and processing during a shearographic inspection which again contributes significantly to the defect detection capability.
9. The testing and validation of the Parker and Salter [1999] temporal unwrapping and laser illumination work has led to the realisation that producing a pressure drop that would result in a linear change in surface deformation over time is difficult to achieve.
10. The defect detection capabilities achievable by thermal stressing during a shearographic inspection have been discovered by applying the pressure drop algorithms to a thermally stressed part.
11. The minimum surface displacement measurable by a shearography system and therefore the defect detection capabilities can be determined by analysing the signal to noise ratio of a transition from a black (poor reflecting surface) to white (good reflecting surface). The quantisation range for the signal to noise ratio is then used in the Hung [1982] formula to calculate the minimum displacement.

Many of the research aspects contained within this thesis are currently being implemented within the production inspection process at BAE Samlesbury.

Acknowledgements

It is probably true that all research is never performed solely by one individual. In the case of this thesis there were many people who played a part in the final outcome and I wish to thank them all.

Professor Lik-kwan Shark has never faltered in his support and supervision, and has gone to great lengths to ensure that the work came to a satisfactory conclusion. Thank you Lik-kwan for all you have done. Dr Bogdan Matuszewski my second supervisor and Dr Martin Varley have also helped and encouraged me through the difficult times and I wish to take this opportunity to thank them.

I would also like to extend my gratitude to all the researchers within the ADSIP group at the University of Central Lancashire who have either helped me with particular problems, or offered friendly advice and encouragement.

Tuition fees and research time has been sponsored by BAE SYSTEMS and I would like to take this opportunity to thank Mr Alan Mason and Mrs Lesley Allger for supporting this work and constantly encouraging me towards its completion.

Finally I must mention my wife Val and my two sons James and Oliver who have been patient and supportive for such a long time. Thank you for being there when needed and giving me your support throughout.

Contents

Declaration	ii
Abstract	ii
Acknowledgements	v
Abbreviations	x
1. Introduction to the research	1
1.1 Introduction	1
1.2 Current Non-destructive Testing Requirements	2
1.3 Project Aims	4
1.4 Organisation of the thesis	6
1.5 Summary	7
2. Manufacturing, Materials and Associated Defects	9
2.1. Introduction	9
2.2. Diffusion bonding	9
2.2.1. Diffusion bonding of titanium	10
2.2.2. Solid state diffusion bonding	10
2.2.2.1. Temperature	11
2.2.2.2. Pressure	12
2.2.2.3. Time	12
2.2.3. Material requirements	12
2.3. Super plastic forming	13
2.3.1. Introduction	13
2.3.2. Material properties	14
2.3.3. Super plastic forming of titanium	15
2.3.4. Cellular structure	16
2.3.5. Typical defects found in SPFDB structure	18
2.3.6. Geometrical deviations	18
2.4. Inspection requirements	20
2.5. Carbon fibre composites	21
2.5.1. Introduction	21
2.5.2. Properties of carbon fibre composite	21
2.5.3. Honeycomb sandwich structures	24
2.5.4. Component geometries	25
2.5.5. Typical lay-up configuration	26
2.5.6. Typical component configuration	27
2.5.7. Typical defects found in composite structure	28
2.5.7.1. Material inclusions	28
2.5.7.2. Porosity and voiding	30
2.5.7.3. Porosity in the matrix	31
2.5.7.4. Porosity at the carbon matrix interface	31
2.6. Inspection requirements	32
2.7. Reference specimens and test samples	32
2.7.1. Composite material test samples	33
2.7.2. Titanium diffusion bonded super plastically formed test samples	36
2.8. Summary	37
3. Ultrasound	41
3.1. Transducer analysis	42
3.1.1. Piezoelectric materials	42
3.1.1.1. Piezo Material properties	43

3.1.2. Ceramic	44
3.1.3. Polyvinylidene Difluoride	45
3.2. Transducer parameters	47
3.3. Ultrasonic beam geometrical parameters	49
3.4. Description of the near field	50
3.5. Focussed transducers	52
3.5.1. Lateral Resolution	52
3.5.2. Beam width	58
3.5.3. Depth of Field	58
3.6. Phased array transducers	59
3.6.1. Reception	62
3.6.2. Limitations of Phased array technology	63
3.7. Acoustic Impedance	63
3.8. Interface characteristics	66
3.9. Ultrasound generation and reception	70
3.10. Modelling of the ultrasonic beam profile	76
3.11. Low voltage excitation	81
3.12. Practical and Simulation Results	82
3.13. Essential parameters for robust defect detection	85
3.14. Current state of the art ultrasonic systems	89
3.14.1. Through transmission squirter system	89
3.14.2. Multi axes manipulators	89
3.14.3. Ten axis complex geometry scanning system	99
3.14.3.1. Analysis of compensation method	100
3.14.3.2. Computer Aided Three Dimensional Interactive Application (CATIA) interface	104
3.14.4. Pulse echo immersion system	105
3.15. Ultrasonic data acquisition modules	107
3.15.1. Pulser receiver	107
3.15.2. Analogue to digital converter	109
3.15.3. Multiplexer	110
3.15.4. Digital Signal processor	111
3.16. Results	112
3.16.1. Effects of pulse length	112
3.16.2. Ultrasonic defect detection capabilities composite and diffusion bonding	114
3.17. Summary	119
4. Radiography	121
4.1. X-ray Generation	121
4.1.1. Cathode	122
4.1.2. Focusing cup	124
4.1.3. Focal spot	125
4.1.4. Heel effect	126
4.2. Geometric principles	126
4.3. Radiation spectra	129
4.3.1. Characteristic radiation	129
4.3.2. Bremsstrahlung or white radiation	130
4.3.3. Effect of increasing potential difference and filament current	132
4.4. Micro focus generation sources	133
4.5. Image Parameters	135
4.6. Image quality	135
4.6.1. Contrast	136

4.6.2. Noise.....	137
4.6.3. Scattered Radiation.....	138
4.6.4. Unsharpness.....	141
4.6.5. Blur.....	150
4.6.5.1. Motion Blur.....	150
4.6.6. Total Unsharpness or blur.....	151
4.6.6.1. Distortion.....	153
4.7. Image Formation systems.....	154
4.7.1. Film.....	154
4.7.2. Image intensifiers.....	156
4.7.3. Flat Panel X-ray image receptors.....	157
4.7.3.1. Amorphous silicon.....	158
4.7.3.2. Amorphous selenium.....	158
4.8. Characteristic curves.....	159
4.9. Assessment of Image quality.....	161
4.9.1. Limiting Resolution.....	163
4.9.2. Point spread function.....	164
4.9.3. Modulation transfer function.....	165
4.9.4. Detective quantum Efficiency.....	166
4.9.5. Noise Power Spectrum.....	167
4.9.6. Estimation of the modulated transfer function.....	169
4.10. Defect Detection capabilities.....	174
4.11. Radiographic inspection of SPFDB.....	177
4.12. Radiographic inspection of Composite.....	178
4.13. Application of real time radiography.....	179
4.13.1. Results using an Amorphous silicon detector.....	180
4.14. Summary.....	183
5. Shearography.....	185
5.1. Principles of shearography.....	185
5.1.1. Laser speckle.....	186
5.1.2. Speckle Size.....	187
5.1.3. Fringe Patterns.....	189
5.1.4. Phase stepping.....	191
5.1.5. Image Un-wrapping.....	191
5.1.5.1. Spatial unwrapping.....	192
5.1.5.2. Temporal Unwrapping.....	193
5.1.5.2.1. Data cancellation.....	193
5.1.5.2.2. Noise.....	195
5.1.6. Stressing methods.....	195
5.1.7. Application of thermal stressing methods.....	199
5.1.8. Laser illumination.....	201
5.2. System Implementation.....	203
5.2.1. Illumination stage.....	204
5.2.2. Shearing optics.....	205
5.2.3. Optical Detection system.....	207
5.2.4. Graphical User Interface.....	207
5.2.5. Vacuum Pump.....	208
5.2.6. Manipulation stage.....	209
5.3. Application to composite aerospace components.....	210
5.3.1. Impact damage detection.....	211
5.4. Application to metallic honeycomb structures bonded to thin metallic skins... 219	
5.5. Defect detection capabilities.....	222

5.6. Summary	225
6. Calibration and Data processing	227
6.1. Introduction	227
6.2. Calibration	228
6.2.1. Calibration procedures	229
6.2.1.1. Ultrasonic calibration.....	229
6.2.1.2. Radiographic calibration	231
6.2.1.2.1. Bad Pixels.....	232
6.2.1.2.2. Gain correction.....	232
6.2.1.3. Shearographic calibration	233
6.2.1.4. Motion Control.....	234
6.3. Data visualisation and analysis.....	235
6.4. Data Processing	237
6.4.1. Mosaic Construction.....	237
6.4.2. Data Registration.....	242
6.4.2.1. Computer assisted data registration	242
6.4.2.2. Automatic data registration.....	244
6.4.3. Defect Visualisation	247
6.4.3.1. Visualisation by structure decomposition.....	247
6.4.3.2. Visualisation by 3D surface construction	250
6.4.3.3. Visualisation by data fusion	250
6.4.4. Defect Detection.....	252
6.4.4.1. Automatic extraction of defects	252
6.4.4.2. Automatic detection of geometrical deviations	253
6.5. Summary	255
7. Conclusions and recommendations for further work	256
7.1. Summary and conclusions.....	256
7.1.1. Introduction	256
7.1.2. Ultrasound	256
7.1.3. Radiography	258
7.1.4. Shearography.....	259
7.1.5. Calibration and data processing	260
7.2. Recommendations for further work	262
References	263
Appendix A Patent	272
Appendix B Awards	282
Appendix C Publications	286

Abbreviations

A to D	Analogue to digital.
ASNT	American society for non-destructive testing.
ASTM	American society for testing of materials.
BS	British standard.
BVID	Barely visible impact damage.
CAD	Computer aided drawing.
CATIA	Computer Aided Three Dimensional Interactive Application.
CCD	Charge coupled device
CFC	Carbon fibre composite.
DAC	Digital to analogue converter.
DC	Direct current.
DIAPS	Data integration and processing system.
DOF	Depth of field.
DQe	Detective quantum efficiency.
DSP	Digital signal processor.
EN	European normative.
EPSRC	Engineering and physical sciences research council.
IEEE	Institute of electrical and electronic engineers.
IQI	Image quality indicator.
Matlab	Matrix Laboratory (software environment)
MFGPROG	Manufacturing program.
MOSFETS	Metal oxide field effect transistors.
MTF	Modulation transfer function.
NDT	Non Destructive Testing.
PC	Personal computer.
PRF	Pulse repetition frequency.
PSD	Power spectral density.
PTFE	Poly-TetraFluoroEthylene
PVDF	Polyvinylidene difluoride
PZT	Lead titanate zirconate
SPF	Super plastic forming
SPFDB	Super plastic forming and diffusion bonding

USL	Ultrasonic Sciences Ltd
2D	Two dimensional
3D	Three dimensional

Chapter 1

1. Introduction to the research

1.1 Introduction

Non-destructive testing (NDT) is an engineering discipline whose remit is to discover internal and external material flaws by processes that do not interfere with the parts' integrity. NDT is used extensively throughout industry and the methods adopted from one industry to another differ in the way they are implemented, but all are based on the same physical principles.

Non-destructive testing adopts measurement and instrumentation methods to measure the physical state of an object. The choice of method or methods is governed by the objects' physical size, material, location and expected flaw that would be detrimental to the object's function.

Earliest forms of NDT consisted of visual inspection, penetrant testing, radiographic and sonic methods. Early methods were generally performed manually and the inspector would use tools such as a magnifying glass as a visual aid, oil and chalk to aid penetrant testing or a hammer for sonic testing. An early example of NDT was the testing of railway engine wheels which were tested for cracks by tap testing method. In this case the sonic response was in the audible range and the person tapping the wheel could detect defects by the frequency of oscillation. Magnetism was also used for the detection of surface defects in ferrous metals. A crack in a ferrous material will deform a magnetic field, so by dispersing magnetic particles on the surface of a component and applying a magnet a crack can be highlighted by the distortion of the magnetic flux lines indicated by the particles.

In general the engineering discipline of NDT has evolved by the application of the laws of physics and the interaction of electromagnetic waves with materials to detect imperfections in material structures. Today's engineers use the same philosophy as early pioneers in the NDT discipline of applying sound, magnetics and light to the problem of defect detection however, in today's environment there are many

technological advances both in electronics and computing that can aid NDT engineers in their quest for improved defect detection.

NDT today makes use of advances in electronics and computing to such an extent that the vast majority of methods have some form of automation attached. However, the philosophy of the NDT engineer having a number of tools to aid the inspection is still as true as it was in the early formative days of this engineering discipline.

In the aerospace industry NDT is used as a tool for determining the quality of materials as they are manufactured into components and also NDT is applied to components that are in-service. Numerous design and manufacture techniques are used in the production of a modern airframe and it is these design and manufacturing methods that determine the appropriate NDT method. Each design has associated manufacturing problems and coupled with the human intervention factor there is always a possibility that the process may fail. Once a process fails the component may be defective. Knowledge of the likely modes of failure and the component design are therefore key to selecting the appropriate NDT method.

The drive in the aerospace industry is to reduce costs both in terms of manufacturing and aircraft operation. Both these areas have an impact on NDT as it means that NDT not only has to be performed more cost effectively but also must provide supportive data to qualify the use of new and lighter materials.

Automation is heavily relied upon to provide cost effective production NDT support, and the use of mechanical manipulation and electronic data acquisition systems are the tools that provide this capability. Software data processing is also used to enhance the sensitivity of NDT methods and permit cost effective implementations.

Penetrants, magnetics, ultrasound and radiography are all used for aircraft production inspection. These complimentary methods are further supplemented by the eddy current method for in-service inspection. Other less used methods for aircraft inspection are thermography and shearography. However, due to the drive for more cost effective inspections these methods are being more widely adopted.

1.2 Current non-destructive testing requirements

Aircraft design and manufacturing methods are continuously being driven by the requirement from commercial and military operators to increase aircraft performance and reduce operational costs. In general, increasing performance whilst reducing operational cost is contradictory and can therefore only be achieved by introducing innovative ideas at all stages of the aircraft lifecycle. In terms of airframe design and manufacture this drive is to reduce costs both in terms of manufacturing and aircraft operation.

There are numerous designs and hence manufacturing methods used in production of an aircraft structure and it is therefore impossible in this thesis to identify them all. However, in order to understand the philosophy behind the determination of a suitable NDT method it is pertinent to describe a few of the more modern techniques.

Modern aircraft components are usually categorised as either composite or metallic parts and from this initial categorisation there are further subdivisions into types of metals or different composite materials and the processing that has been applied to the material in question. Processing metallic materials can include forming, machining, welding, casting and forging with casting and forging processes being performed by specialist companies and welding, forming and machining processes being performed at the aircraft manufacturers.

Non destructive test methods are employed both at the material suppliers and the manufacturers to ensure that the material and the final component are fit for purpose. Aerospace NDT for metallic components is therefore focussed on identifying flaws caused by material processing rather than inherent material flaws, as the material supplier would certify that the material was fit for purpose prior to delivery. Manufacture of aircraft components from composite materials however, encompasses both the inherent material and the process induced flaw detection as the material supplied has to be formed by placing layer upon layer of fibres onto a mould and cured in ovens. Following the curing of the composite into the required shape machining has to be performed to finish the part. Therefore the NDT requirement is to identify both manufacturing flaws and flaws caused by the curing process.

Aerospace components are notably light but strong. This is achieved by adopting special design techniques. A great number of aerospace components are manufactured by bonding thin skins to honeycomb sub-structure. Both metallic and composite materials are used in this process: however more recent airframe structures tend to adopt the composite designs in preference to metallic. Solid composites are also widely used for primary aircraft structure such as wing skins, spars, and ribs.

Titanium structures are also becoming more common as the process of diffusion bonding and subsequent super plastically forming parts with complex sub-structures becomes cost effective.

There are numerous potential flaws that can occur when manufacturing using the above methods. In the case of metallic honeycomb structure the potential flaws are usually in the form of disbonds, crushed core and foreign objects in the structure. Similarly in composite honeycomb structures the above defects can occur, however as the composite skin is manufactured from raw materials flaws such as porosity and/or inclusions are possible during the laying up and curing process.

Today's aircraft makes extensive use of composite materials because of their strength to weight properties and typically large sections of aircraft structure are now manufactured from composite materials. The challenges facing non-destructive testing therefore involve developing a capability to rapidly inspect large areas of carbon fibre composite and titanium super plastically formed diffusion bonded primary structure in order to establish structural integrity without significant cost penalty.

1.3 Project aims

The current challenge for non-destructive testing is to increase its defect detection capability in order to meet the requirements of modern aircraft structure but at a reduced cost. Increased defect detection however has to be performed on very large and complex parts which makes the initial requirement far more taxing. Whilst increased defect detection may be demonstrated under laboratory conditions implementing such methods in a production inspection environment can be difficult.

The aims of this project are therefore to improve the defect detection capabilities in terms of ultrasonic, radiographic and shearographic inspection methods and demonstrate that the methods produced are capable of being implemented on very large complex structures in a production environment. The improved methods are to be applied to new aircraft structure designs which are manufactured from carbon fibre composite and super plastically formed diffusion bonded titanium. In both of these applications current minimum defect detection requirements are in the order of millimetres. Diffusion bonded titanium requires a minimum defect detection of 1 mm and current composite requirements are around 4 mm. Therefore in order to improve the minimum defect detection capabilities the detailed project aims are:-

1. The evaluation of excitation/stimulation processes and development of optimum excitation for ultrasound and radiography and shearography.
2. Evaluation and development of experimental methods for the assessment of optimum motion control for multi axis complex geometry ultrasonic scanning systems which will reveal the limits to the achievable accuracy and therefore can be related to the limit of defect detection.
3. Evaluation and development of analysis and data presentation methods which aid operator interpretation.
4. Introduction of calibration techniques pertinent to the implementation of enhanced defect detection methods that ensure inspection parameters are within tolerance so that defect detection can be maintained.
5. The implementation of new and novel methods that enhance defect detection on aircraft structures on production inspection systems.
6. Demonstrate the 15 μm pores in a diffusion bond are detectable by ultrasonic means and develop the methodology required to implement this on a complex shaped component. Also identify the limitations of current radiographic, ultrasonic and shearographic systems and detail the detection limits observed.

The work in this thesis is based on the qualification and improvement of new NDT technologies. The emphasis of the work presented here is that the techniques adopted for generation of the stimulating energy greatly affect the overall sensitivity to defect detection. Therefore significant improvements can be achieved by carefully matching the stimulation to the specific energy generation method.

1.4 Organisation of the thesis

It can be seen that the non-destructive inspection of aircraft components is a broad subject consisting of many applications and techniques. This thesis is therefore structured such that the reader is first briefly informed in chapter 2 of the material and processing methods used in the aerospace industry and some of the material parameters that affect component strength and serviceability.

Chapter 3 starts by introducing the ultrasonic method and goes on to describe the research performed in the field of ultrasound by explanations of the effects of pulse generation and detection with some computer simulation to substantiate the conclusions. Low voltage excitation is then discussed as a method of evaluating optimum pulse parameters. Also within this chapter there is a detailed evaluation of focused transducers and the criticalities of focussing when applied to diffusion bonding inspection. Angle of inclination is evaluated and there is a section describing state of the art ultrasonic techniques and associated equipment and how they are applied to typical aerospace super plastically formed diffusion bonded (SPFDB) and composite components. The calibration and evaluation of motion control when applied to complex geometry scanning is presented and the results of optimising each parameter are documented in the form of ultrasonic scans.

Chapter 4 opens with a description of radiographic principles followed by a detailed evaluation of a state of the art real time radiographic system. The work draws attention to the magnification achievable by micro-focus systems and develops a solution to the optimum geometric magnification by analysing the unsharpness in the image for various geometric magnification factors. Key parameters that affect sensitivity are detailed which therefore highlight the importance of calibration and

quality control. The conclusions of this chapter will show the relevance of this method to the inspection of composite components and superplastically formed structures.

A third NDT method, shearography, is explained in detail in chapter 5 which after some introductory information relates the importance of applying the correct stimulation and image processing techniques in order to maximise defect detection. This chapter details how different stimulation methods will reveal different defect types and discusses the implementation problems associated with optimised stimulation. A patent has been granted based on the novel implementation of shearography described in this chapter. As with the other chapters this chapter concludes with a detailed look at how this method can be successfully applied to typical aerospace composite components but also details an occurrence of a large defect that is grossly underestimated by more conventional NDT methods.

The next chapter (chapter 6) details the importance of calibration and data processing and highlights the importance of correct application of calibration particularly when enhanced defect detection is required. Data processing work builds on the complementary detection capabilities of the three methods and demonstrates how design data can be used for the evaluation of NDT data.

Following a summary of results, conclusions will be drawn with an expansion of the results to deal with the inspection of large area and complex shapes and recommendations for implementation and further work will be made.

1.5 Summary

Due to the nature of the manufacturing process described above the non-destructive testing requirement formulates into the detection of disbonds and the evaluation of the geometrical correctness of the internal structure. Ultrasound is therefore employed for the detection of disbonds as this method is best suited to the detection of planar type defects that are normal to the surface. The ultrasonic method is readily automated by integrating the ultrasonic equipment with mechanical scanning systems and electronic signal data capture and digital processing modules.

Radiography however is used for evaluation of the geometrical features in the internal structure. This method complements the ultrasonic flaw detection in that it is highly sensitive to discontinuities that are on the axis of the radiation beam; therefore cracks and tears in the substructure wall that would go unnoticed by ultrasonic examination are readily identified by radiography. Shearography can be used to compliment both ultrasound and radiography particularly in the detection of disbonds in honeycomb structures. This thesis demonstrates how the identification, evaluation and optimisation of key parameters can significantly enhance the defect detection capabilities of ultrasound, radiography and shearography. It also highlights the importance of accurate motion control and develops a method of analysing the positional errors so that the optimum parameters can be determined.

Chapter 2

2. Manufacturing, Materials and Associated Defects

2.1. Introduction

Design and manufacturing methods for aircraft structures are continuously being driven by the customer requirement to increase performance and reduce operational costs. In general meeting this requirement in terms of structural airframe, results in the use of advanced materials and processes such as super plastic forming and diffusion bonding of titanium (SPFDB) and manufacture using carbon fibre composites. These processes allow both the structural and design engineers to create complex shaped components with high strength to weight ratios thus producing lighter airframes with enhanced static and fatigue strength properties. Improved structural performance can then be utilised to enhance aircraft performance or reduce operational costs such as fuel due to the reduction in overall weight. Commercial aircraft manufacturers are likely to take advantage of the achievable fuel savings whereas military operators may wish to expand the operational role of the aircraft without impairing the operational cost.

2.2. Diffusion bonding

The ability to join two or more sheets of material and maintain the mechanical properties of the base material are the main reasons why the diffusion bonding process has become popular in the aerospace industry. When compared with other metallic joining methods in terms of shear strength the advantages of diffusion bonding are clearly seen [Stephen 1986] for instance a riveted joint would typically have a shear strength of 10 MPa compared to a diffusion bonded joint which at parent metal shear strength would be 575 MPa.

Diffusion, can be described as the flow of energy or matter from a higher concentration to a lower concentration, resulting in an even

distribution. For instance if one end of a rod is heated or electrically charged, the heat or electricity will travel or diffuse from the hot or charged portion of the rod to the cool or uncharged portion. Similarly two metals can diffuse together if they are placed in intimate contact with each other and subjected to changes in temperature and pressure. It is this process that forms the basis of diffusion bonding of titanium aircraft structures.

Whether diffusion is in the form of heat, electricity or metallic bonding the process obeys the same physical laws. These are that the rate of diffusion is proportional to the cross sectional area, temperature and in the case of metallic diffusion bonding the material diffusion coefficient. Also the amount of material that diffuses in a certain time is proportional to the square root of time [Microsoft Encarta 2002]. In the aerospace industry titanium is regularly diffusion bonded to form complex shaped components with high strength to weight ratios that are able to operate in highly loaded areas or extreme environmental conditions on the aircraft

2.2.1. Diffusion bonding of titanium

There are two methods of diffusion bonding applicable to titanium these are solid state and liquid phase bonding methods. In short solid diffusion bonding consists of joining the materials by means of applying heat and pressure but without melting the material. Liquid phase diffusion bonding requires the applied heat to be such that it produces a liquid at the bond interface. This is normally achieved by the use of an interlayer material at the bond interface. For large aerospace structures solid diffusion bonding is the preferred method.

2.2.2. Solid state diffusion bonding

There are various stages that the material to be bonded has to go through before a good diffusion bond can be achieved. First and foremost the material has to be in intimate contact before the diffusion process can start. Therefore the material condition in terms of surface roughness and flatness are important at the initial bonding stages. The material will deform under the applied load and therefore certain areas of the surface

will come into intimate contact leaving voids where the surface roughness is such that the hollows in the surface do not come into contact. These initial voids are elliptical in shape [Partridge 1986] but also maintain the surface roughness effect around the inside of the elliptical void. After some time the void closes and the surface roughness inside the void then comes into contact creating smaller voids. Eventually all the voids close and the diffusion process can finally take effect over the complete surface area.

The closing of the larger voids and subsequent smaller micro voids is dependant on the materials creep rate which can be described by the formula below:-

$$\varepsilon = A\sigma_0^n \exp(-q_c / RT) \quad (2-1)$$

where ε = creep rate, σ = stress, q_c = activation energy for diffusion, R = gas constant, T = temperature in Kelvin and A and n are constants. n being related to the materials grain size.

Whilst plastic deformation and pressure play a role in removing the large voids it is the diffusion process itself that removes the micro voids i.e. less than 20 μm by diffusion of the two adjoining materials at the intimate contact surfaces. The main contributing factors to the surface diffusion process are time and temperature with applied pressure contributing to the closing of all the micro voids.

2.2.2.1. Temperature

Metallic diffusion is a molecular process that is dependant on the random motion of individual molecules. Therefore the rate at which diffusion takes place is directly proportional to the average velocity of the molecular activity. When titanium is raised in temperature the molecular activity increases thus increasing the average velocity. The diffusion rate therefore increases accordingly. In practice titanium is generally heated in a press in which the atmosphere has been subjected to a vacuum and subsequently purged with an

inert gas such as argon. The component is subjected to constant pressure from the press whilst at a temperature between 790 and 940 °C.

At high temperatures titanium becomes highly reactive and will absorb oxide from the surrounding atmosphere. This is why diffusion bonding is performed in an inert atmosphere such as argon. Care has to be taken to ensure that the argon used is of the highest quality with little or no oxygen content. The property of titanium being highly reactive at high temperature can be used to reduce the oxygen content of the argon gas being pumped into the press. Hot titanium wires are placed in the gas feed lines and when the gas flows over the titanium it absorbs any remaining oxygen present.

2.2.2.2. Pressure

As stated previously for diffusion bonding to occur the materials in question must be in intimate contact. Pressure is applied to ensure that the materials are initially brought together and as the diffusion process takes place the pressure also ensures that the voids formed by surface roughness effects are closed thus producing a total intimate contact surface. When this has been achieved the diffusion process can take place fully and the bond properties can be achieved.

2.2.2.3. Time

The amount by which two materials will diffuse together is proportional to the square of root of time. For instance if it takes 1 hour for titanium to diffuse through 10 µm of material then it will take 4 hours to diffuse through 20 µm. In practice good base material properties can be achieved on thin sheet materials after 1 to 1.5 hours but the diffusion process is usually performed for longer periods to take into account the surface effects and to guarantee good static and fatigue strength properties.

2.2.3. Material requirements

The essential material requirements for good diffusion bonding are flatness, surface finish and cleanliness. The effects of material flatness

and surface finish have been discussed in 2.2.2. Cleanliness however is a very important factor as the existence of any inorganic or organic films at the joint interface may cause surface reactions at high temperatures and therefore prevent bonding [Partridge 1986]. Insoluble materials at the interface will generally either form voids if it is an insoluble gas or a joint of intimate contact material with low bond strength properties i.e. an oxide layer.

Whilst it is undesirable to prevent bonding by joint contamination the inclusion of yttrium or barium substances at planned locations within the component (figure 2-1) can have the advantage of bonding the material in a pattern which can subsequently be formed using the super plastic forming process.

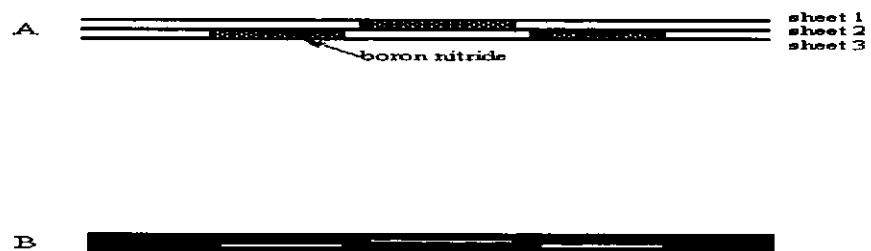


Figure 2-1 Typical three sheet diffusion bonded structure

2.3. Super plastic forming

2.3.1. Introduction

Super plasticity is the ability of a poly crystalline material to undergo extensive tensile deformation without severe thinning or failure usually associated with this amount of elongation. Conventional forming techniques i.e. bending, rolling, hammer forming etc inherently produce parts of low accuracy and repeatability, have poor surface finish and

generally require heat treatment before and after the forming process. Super plastic forming however can produce high tolerance parts in a repeatable manner without the use of pre / post heat treatment. There is however certain governing factors that require consideration before the super plastic forming process can be applied.

2.3.2. Material properties

For a material to be super plastic it must be a two phase alloy and have a fine grain constitution. Super plasticity is achieved by a sliding effect at the material grain boundaries. In order to maintain this sliding effect as the primary forming control a material with high strain rate sensitivity is required. Strain rate sensitivity is directly related to grain size with the smaller the grain size the higher the strain rate sensitivity and the more efficient the grain boundary sliding effect. In single phase materials high temperatures normally associated with super plastic forming result in rapid grain growth which decrease the strain rate exponentially. Therefore in order to maintain small grain size at high temperatures a two phase alloy has to be used. Generally the second phase restricts grain growth at high temperatures but also aids grain boundary sliding as the size of the second phase is relatively small and is evenly distributed at the grain boundaries. A materials strain rate sensitivity is often referred to as its m value and is defined by :-

$$\sigma = k\varepsilon^m$$

therefore

$$m = (\log \sigma - \log k) / \log \varepsilon$$

(2-2)

where σ = stress, ε = strain. k represents the gradient and m represents the value at the intersect with the y axis when log stress is plotted against log strain for the material.

The presence of a neck or localised thinning in a material that is subjected to tensile straining will lead to a localised high strain rate which for materials with high m values causes a sharp increase in the

flow stress at that region. The neck feature then undergoes strain rate hardening which inhibits further elongation. Therefore for super plastic forming to be successful the material must have a high strain rate sensitivity which infers that the material has a high resistance to neck development.

2.3.3. Super plastic forming of titanium

The most common titanium material used in the aerospace industry is Ti-6AL-4V. This material is usually super plastically formed between 790 to 940°C has a m value between 0.6 and 0.8 and 1400% elongation can be achieved. The stress range for this material is 5 to 30 MPa and the strain rate per second is in the range of 0.0001 to 0.001 which makes this material an ideal candidate for the manufacture of highly loaded large complex shaped aircraft structures.

Complex shaped aircraft components are readily formed using the elongation characteristics obtained by the super plastic forming process. Deep drawn shapes can be obtained by placing the material over a sealed cavity and applying gas pressure to force the material into the cavity shape. Complex surfaces are regularly formed this way however by diffusion bonding a number of sheets of titanium together with a pattern of un-bonded material (figure2-2C) between each sheet and then super plastically forming by inflating the pack. Complex shaped components with internal structure can be readily manufactured.

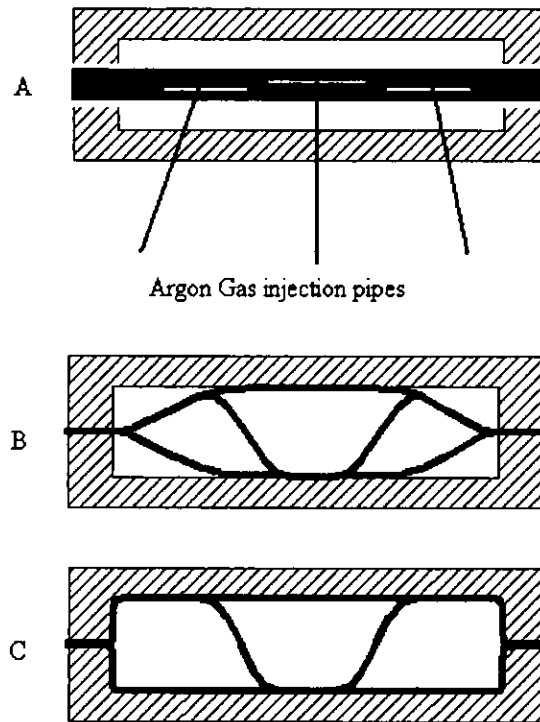


Figure 2-2 Super plastic forming process performed on a previously diffusion bonded pack

2.3.4. Cellular structure

The cellular structure implementation of the super plastic forming diffusion bonding (SPFDB) process is significantly different from the method described previously. Cellular structure is usually formed from four sheets of titanium with the two outer sheets being pressurised and formed to the profile of the encapsulating tool (figure 2-3B). Once this has been achieved gas pressure is then applied to the cavity between the two inner sheets and these are then formed to meet the outer sheets (figure 2-3C). The two inner sheets are diffusion bonded in thin strips prior to the assembly of the four sheet pack (figure 2-3A) and when they are subsequently pressurised the sheets form a structural web configuration (figure 2-3D). The difference with this technique is that the diffusion bond takes place after the super plastic deformation and the requirements for cleanliness, surface roughness and small grained material are stricter. As can be seen from figure 2-3C parts of the inner structure will be in intimate contact while other parts are still forming,

this has the effect of creating varying strain rates for different parts of the component. The degree of cavitation and therefore surface roughness are related to the strain rate [Partridge 1987] which means that the surfaces to be bonded will have varying levels of intimate contact and therefore the possibility of micro voiding is increased. Also during the forming of the outer two sheets argon gas is pumped into the cavity to form the two outer skins. When the inner section is formed this argon gas has to be slowly released. If the inner structure does not form uniformly then argon gas may be trapped at the bondline resulting in large voiding and a weaker joint.

Baker and Partridge [Baker 1984] revealed that pores at the bondline gave rise to a reduction in fatigue strength when the percentage porosity was high. But also conclude that porosity in a diffusion bond has a greater influence on the impact strength than any other material parameter with some instances of high void levels reducing the impact value to 12% of the parent material.

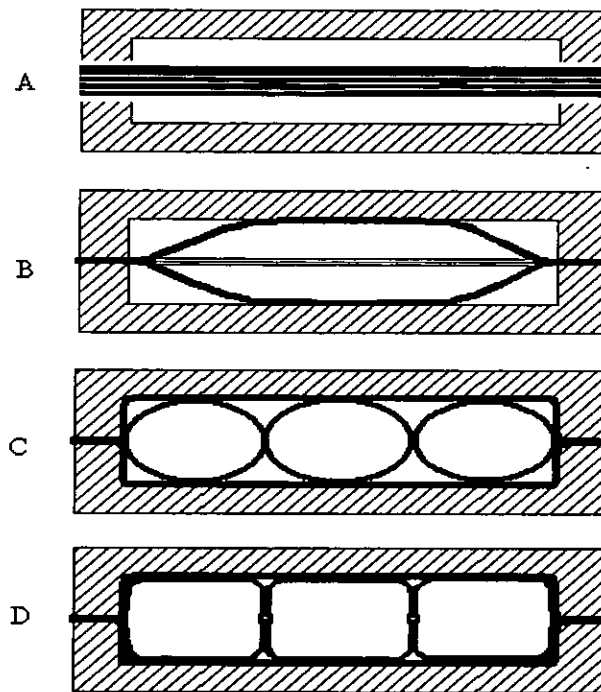


Figure 2-3 Stages of the cellular SPFDB process

2.3.5. Typical defects found in SPFDB structure

From the description of the diffusion bonding and super plastic forming processes it can be clearly seen that there are a number of ways in which the process can fail. Failure of the process will result in a defective bondline and or component shape. Typical defects therefore fall into two categories i.e. geometrical deviations and bondline discontinuities.

Bondline discontinuities can be further subdivided into three categories

1. Large voids, usually caused by a complete breakdown in the process or gross contamination at the bondline where the contamination turns to a non soluble gas which is entrapped at the joint.
2. Micro voids, usually attributed to incorrect bond parameters. Incorrect pressure or time will have the effect of closing the larger voids but being insufficient to close the smaller voids that are caused by the imperfections in the contact surfaces. Microvoiding is usually $< 40 \mu\text{m}$ but can be smaller still (around material grain size i.e. $10 \mu\text{m}$).
3. Intimate contact disbonds can be caused by two effects one is incorrect bond parameters where the time, pressure, and temperature have been adequate to bring the two materials into intimate contact but are short in terms of allowing the diffusion process to complete. The other cause is bondline contamination where the contaminant does not form a gas but melts and forms a layer of intimate contact foreign material at the bondline.

2.3.6. Geometrical deviations

This category is usually associated with the super plastic forming (SPF) process. Typical geometric deviations are shown in figure 2-5 below. The bond in the centre section of this type of structure is not accessible via ultrasonic means and therefore bond integrity cannot be determined in the usual way. However this bond is made prior to SPF which is useful, as the subsequent forming process tests the bond

integrity and radiographic inspection can therefore be used to look for deformations at this bondline which are a result of incomplete or insufficient bond.

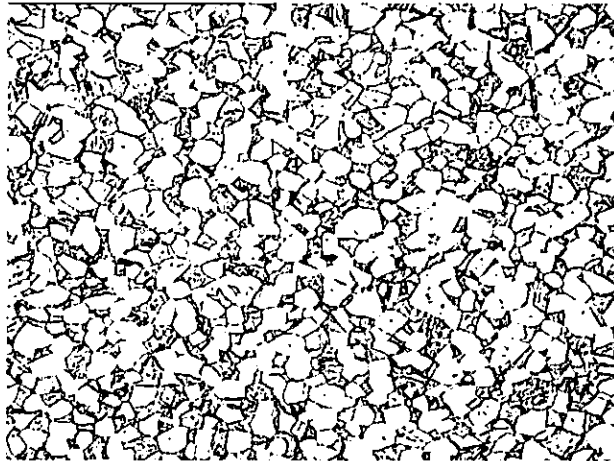


Figure 2-4 Micro section of a diffusion bond with 80% bonding and voids around 15 μm

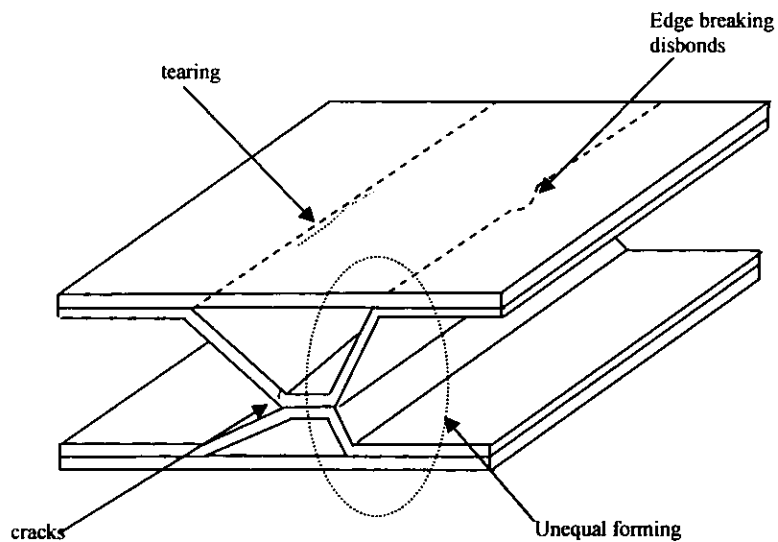


Figure 2-5 Cross section of a SPFDB X-core structure showing typical defects

2.4. Inspection requirements.

The inspection requirements for super plastically formed diffusion bonded structures are therefore quite complex. For structures that are diffusion bonded prior to the SPF process, experience and confidence in the process control has led to an NDT requirement of detecting and rejecting the part if a disbond exceeds 20 mm². These structures can range in size from 1600 mm² to 2 m² with bonds being inspected from each side of the aerofoil surface. In general the process control for these structures is such that micro voiding and intimate contact defects are eliminated. There is however a requirement to inspect the inner geometry as this does give an indication of the diffusion bond quality and the inner structure plays a significant role in the overall structural strength. Ultrasonic inspection is performed to search for the disbonds between the outer skin and the outer surface of the inner skin and radiographic techniques are used for geometric evaluation of the inner structure.

Large cellular structures where a one shot process is used to SPF the part and diffusion bond the inner structure to the outer skin however presents a new set of requirements to the NDT community. Small defects < 30 µm in diameter can be expected to be present to some degree and intimate contact bonds with little or no strength are possible. These defects not only have to be detected but also have to be classified in terms of their contribution to effective bond surface area. Here groups of micro voids have to be assessed as a percentage disbond with the acceptance criteria for large primary aircraft structure being bonds areas in excess of 80%. As with the two stage process the internal geometric shape is important but in this instance deviations in geometric shape are not necessarily connected to the bond quality. Again cellular structure components are very large and complex. Typical components are 4m² in surface area which makes searching for voids that are less than 30 µm in diameter very difficult. Ultrasonic technology is again used for this inspection with radiography for the geometric inspection. However the importance of the ultrasonic inspection is greater with a similar reduction in the requirement for radiographic inspection.

2.5. Carbon fibre composites

2.5.1. Introduction

Composites consist of two distinct materials namely a reinforcement and a binder. Each of these materials has its own mechanical properties which when combined to form a composite, produce new material properties which are dependant on the amounts of the two materials used. Carbon fibre composites are manufactured from carbon fibres and an epoxy. The material is usually supplied to a component manufacturer in reels where the fibre is impregnated with the epoxy resin and is in the form of a thin sheet. This is known as the pre-preg. The pre-preg sheets are then stacked on a tool to form the shape with enough layers to give the correct component thickness. The tool and pre-preg stack are covered and vacuum sealed and then placed in an autoclave for curing.

The raw fibre is manufactured from a continuous acrylic fibre known as the precursor. Bundles of fibres (typically 3000 to 12000) are heated in a furnace and undergo oxidation, carbonisation and graphitisation by subjecting the fibres to different gas mixes at temperatures up to 2000 °C. Following the heat treatment the fibres are then mixed with the resin to form a matrix. The proportion of fibres to matrix epoxy is varied according to the properties required but a typical fibre to resin ratio would be around 60% fibre to 40% epoxy. This ratio is known as the fibre volume fraction.

2.5.2. Properties of carbon fibre composite

Material properties can be determined by considering the force and direction of the force when applied to the material and how the resulting strain is dissipated through the material.

If the composite is to withstand a force and remain in equilibrium then the applied force must be balanced by an equal and opposite force. The applied force F must therefore have opposing forces in the matrix (F_m) and the reinforcement (F_r) i.e.

$$F = F_m + F_r$$

(2-3)

The applied stress σ is force per unit area therefore:-

$$\sigma A = \sigma_m(1-f)A + \sigma_r fA$$

$$\sigma = \sigma_m(1-f) + \sigma_r f$$

(2-4)

Where f is the cross sectional area of the fibre reinforcement of the composite, A is the total area, σ_m is the stress in the matrix and σ_r is the stress seen by the reinforcement.

By applying Hooke's law which states that the stress experienced by a material is proportional to the strain we can then determine how the applied force is dissipated through the material. Of course this only applies as long as the material in question is elastic and the force does not exceed the materials elastic limit. From Hooke's law:-

$$\sigma = E \epsilon$$

(2-5)

Where E is the elastic modulus and ϵ is the strain.

ϵ must be the same in both the matrix and the reinforcement otherwise holes would appear in the composite as it was stretched. Therefore since the matrix and reinforcement have quite different elastic moduli the stress must be different in each of the materials. In fact the stress must be higher in the material with the higher elastic modulus as again if this were not the case the two materials would expand unequal amounts and holes would appear at the ends on the material.

The analysis above is true for applied forces along the axis of the reinforcement where:

$$E \epsilon A = E_m \epsilon_m A_m + E_r \epsilon_r A_r$$

(2-6)

Taking into account that the strain must be the same in both materials and that the area ratios are simply the volume fractions the above formula can be re-written to express the modulus of elasticity for a continuous and aligned fibrous composite in the direction of alignment [Callister 1999] as:-

$$E = v_m E_m + v_r E_r$$

(2-7)

Considering the applied load P we can say that

$$\frac{P_m}{P_r} = \frac{E_m v_m}{E_r v_r} \quad (2-8)$$

where P_m and P_r represent the load in the matrix and the reinforcement respectively, E_m and E_r represent the Young's modulus and v_m represents the volume fraction of the matrix which means that the percentage load carried by the reinforcement is proportional to the percentage volume fraction. For instance a composite made from polyester and 70% E-glass would result in the following:-

$$E_{\text{polyester}} = 6.9 \times 10^3 \text{ MPa}$$

$$E_{\text{E-glass}} = 72.4 \times 10^3 \text{ MPa}$$

Therefore

$$E = (0.3)(6.9 \times 10^3) + (0.7)(72.4 \times 10^3)$$

$$E = 52.75 \text{ MPa}$$

But the E-glass contribution is 96% i.e. nearly the entire load is carried by 70% of the material.

In the case when the loading is applied perpendicular to the reinforcement a different analysis has to be applied. In this case the strain in both materials is the same and the elongation and therefore stress is different. The elastic modulus for a composite loaded perpendicular to the reinforcing fibres is calculated using [Callister 1999]:

$$E = \frac{E_m E_r}{v_m E_r + v_r E_m} \quad (2-9)$$

where E = Young's modulus and subscripts m and r represent the matrix and the reinforcement respectively. v = the volume fraction.

Inserting the same material parameters as before results in an elastic modulus of 18.81 MPa

From the evaluation above it can be clearly seen that carbon fibre composites are highly anisotropic and it is for this reason that carbon fibre components are normally manufactured using lay up configurations

that orientate the fibres through 0 ,45, 90, 135 and 180 degrees as each layer is applied.

However the resulting properties for each pre-preg layer and the component achieved by the volume fraction and the lay up technique are both dependant on the correct interface properties at the boundary between the carbon fibres and the matrix. It is this interface that transfers the load from the fibres to the matrix and vice versa. Therefore in order to achieve maximum tensile strength of the carbon fibres with the ductility of the matrix the interface must be a chemical interphase of the two materials. If this is not achieved then the fibres are likely to slip out of the matrix resulting in the composite exhibiting the undesirable properties of each component.

2.5.3. Honeycomb sandwich structures

A typical carbon composite honeycomb structure consists of two relatively thin carbon fibre skins separated by a lightweight core. The reason for using this design technique is that by separating the skins by a low density core, the overall structure benefits from an increase in the moment of inertia with very little weight penalty. The mechanical properties of such a structure are dependant on the core and face material properties as well as the thickness of the core and skins.

A very general analysis where it is assumed that the total beam thickness comprises mainly of the core material i.e. skins that are substantially thinner than the core the equivalent flexural rigidity $(EI)_{eq}$ can be calculated as follows:-

$$(EI)_{eq} = \frac{E_f b t c^2}{2} \tag{2-10}$$

where E_f = the longitudinal stiffness of the face material , b = the width of the beam, t is the skin thickness and c represents the core thickness.

The equivalent shear rigidity $(AG)_{eq}$ can be expressed as:-

$$(AG)_{eq} \approx bcG^*c \tag{2-11}$$

where $G^*c = C_2E_s\left(\frac{\rho^*c}{\rho_s}\right)^2$ (2-12)

ρ^*c is the overall density of the foam and ρ_s is the density of the actual foam material alone, E_s is the elastic modulus and C_2 is a constant with a value of approximately 0.4. From these two formulas it can be seen that the mechanical properties of the structure are dependant on both the geometrical parameters of the component and the longitudinal stiffness of the face material for flexure rigidity and to a lesser extent the stiffness of the core material for shear rigidity. As stated above both these parameters are calculated assuming that the interface between the composite components are in phase and therefore an average of the component properties can be achieved.

2.5.4. Component geometries

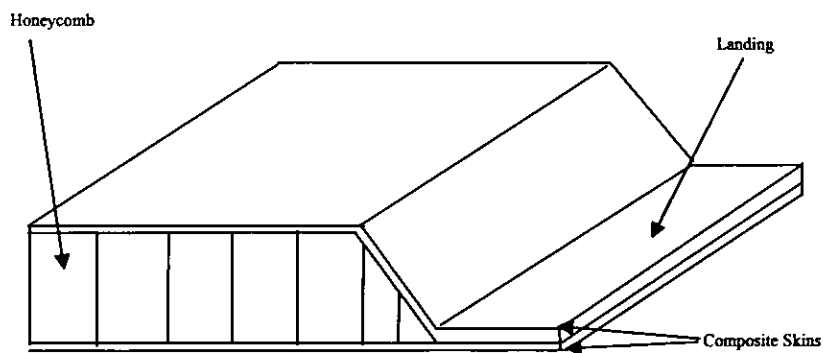


Figure 2-6 Cross section of honeycomb panel with composite skins that taper to form a solid landing

Figure 2-6 above is a schematic representation of typical honeycomb structures. Two thin carbon fibre skins are bonded onto a honeycomb sandwich and formed to create a thick structure that tapers to a solid

laminate. The solid laminate section is usually drilled and is used to mate up to the airframe substructure where it is mechanically fastened.

2.5.5. Typical lay-up configuration

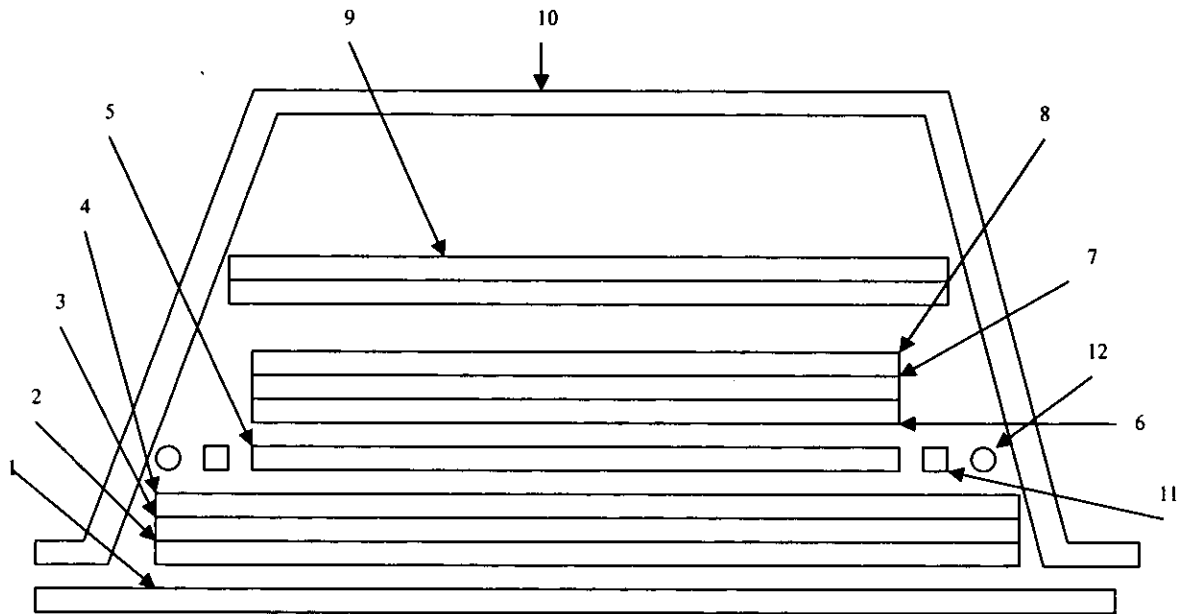


Figure 2-7 A typical lay-up configuration showing most of the common ancillary materials used in the process.

key

- | | | |
|------------------------|----------------------------|-------------------------|
| 1. Moulding plate | 2. Non-porous release film | 3. Resin Bleed. |
| 4. Porous release film | 5. CFC laminate. | 6. Porous release film. |
| 7. Resin bleed. | 8. Intensifier. | 9. Air Breather. |
| 10. Vacuum membrane. | 11. Edge dam. | 12. Sisal string. |

The moulding plate in figure 2-7 is in this example a simple plate used for manufacturing flat composite plates. It can however be shaped so that laminates with curves and /or angles can be made. The moulding plate supports the material whilst under pressure during the curing cycle. It must therefore be rigid at the curing temperature.

The non-porous release film is placed on the moulding plate and acts to prevent the resin from the composite running and adhering to the mould

plate. At the end of the cure cycle the component can be readily removed from the tool without damage to the composite material or the tool. The resin bleed material is porous and therefore allows the surplus resin and gases to escape from the stack. The porous release film allows the escape of gases but remains in place to aid separation of the composite component from the tool after cure. The ancillary materials on top of the composite act the same way as those below except that in this case there is no need for a non-porous release film as the intensifier above is either discarded or cleaned. The intensifier is usually made from aluminium plate and covers the surface of the composite. Pressure applied to the intensifier is then evenly distributed and the composite is therefore evenly consolidated. The edge dam and sisal are used to prevent excessive resin flowing from the edges of the composite and the membrane is completely sealed, and a vacuum drawn by suction through a valve attachment.

2.5.6. Typical component configuration

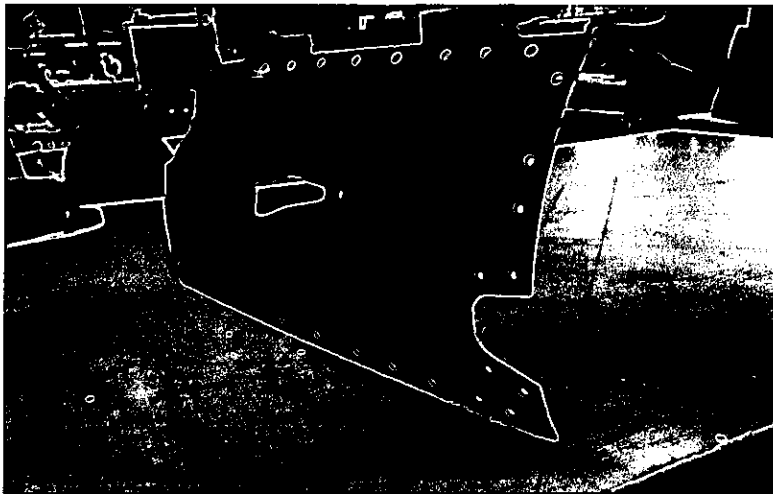


Figure 2-8 Images showing a typical slightly curved honeycomb structure.

The component shown in figure 2-8 is a typical aircraft honeycomb component where the centre section is constructed from honeycomb with thin composite skins and the outer edge is made from monolithic carbon

fibre composite. In this case the component has a slight curvature in the vertical plane.

2.5.7. Typical defects found in composite structure.

A comprehensive list of defects that may occur when manufacturing and processing carbon fibre composite is detailed in the BAE SYSTEMS specification [BAE SYSTEMS 2004]. The important thing to note when discussing defects is that the majority can be grouped into the classification of either pores/voids, disbonds or foreign material inclusions.

The types and locations of all the defects that can occur in a carbon fibre composite material is very complex and therefore impossible to simulate. In

general reference specimens are manufactured to aid the calibration of NDT equipment. A typical reference specimen is sketched in figure 2.13 on page 34.

The diagram shows a typical step wedge reference specimen that is manufactured from the same materials as the component to be tested and has stepped thickness' to match the thickness variation of the component. To simulate the defect, folded polytetrafluoroethylene (PTFE) patches are inserted into the lay-up at various depths. The folded PTFE has air entrapped in the fold which provides an interface of vastly different acoustic impedances. The aim here is to provide a composite panel that on the whole is well consolidated and therefore free from porosity, voiding or defects of any nature other than the simulated PTFE defects. A comparison of the attenuation of the known good reference specimen at the thickness of interest can be performed with respect to the component under test.

2.5.7.1. Material inclusions

One of the problems associated with carbon fibre composite manufacture is the great number of ancillary materials required during the lay-up and curing process as these materials can be accidentally entrapped in the composite structure. If this occurs then the material

properties change as there is now a third component to account for in the elastic modulus calculation. i.e.

$$E = v_m E_m + v_r E_r + v_i E_i \quad (2-13)$$

where v_i and E_i are the volume fraction and elastic modulus of the inclusion material.

There are two further effects that need to be considered when assessing the effect of an inclusion in a composite material. First the inclusion is likely to be localised which means that although the volume fraction will be small when taken as a percentage of the whole material, its localised nature will significantly affect the area of composite in that proximity. Significant localised changes in a materials property lead to crack or failure initiation points as stress concentrations become more intense at these locations.

Secondly some ancillary materials are volatile and tend to burn causing gas bubbles (porosity or voids) in the matrix and possibly at the reinforcement / matrix interface therefore increasing the potential for phase separation.

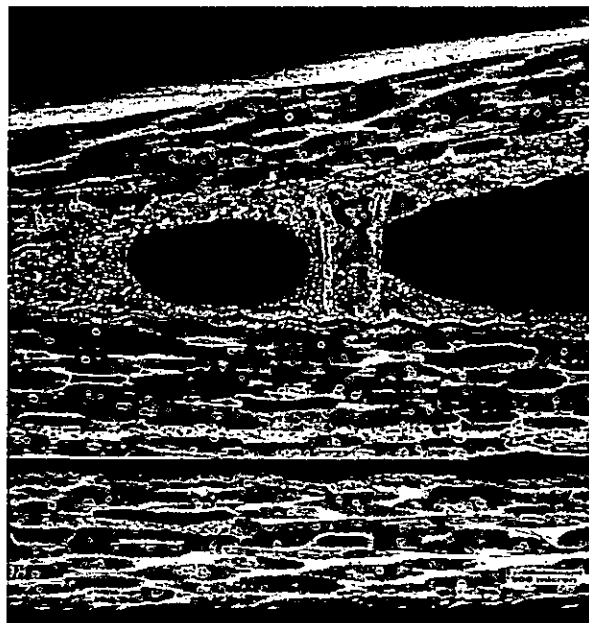


Figure 2-9 Micro-section of a paper backing foreign material included in a carbon honeycomb structure. (note voiding in composite also)

2.5.7.2. Porosity and voiding

Porosity and voiding can occur when the consolidation pressure is not correctly applied. The small gas bubbles that are present when the matrix is molten are not extruded from the composite due to the lack of pressure. The effect of porosity in the material is dependant on its location in the structure relative to the fibres and the amount in terms of percentage volume fraction.

Voiding is a general term used to describe larger pores. Voiding can be caused by complete loss of vacuum and hence pressure, and/or the presence of volatile ancillary materials during the curing process. A vacuum loss will occur if the membrane becomes damaged and splits during the cycle. When this happens air enters the stack and becomes entrapped with the molten polymer matrix. Some of the ancillary materials are close to their combustion point at the curing temperature. If the lay up is suddenly subjected to a rush of air then these materials are likely to burn off releasing more gases into the stack. Large volumes of gas result in large voids in the composite material.

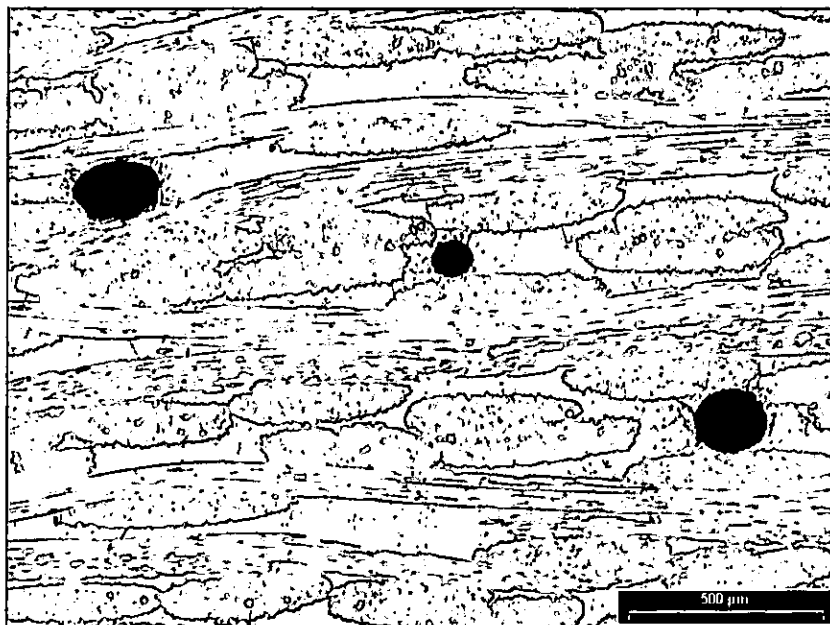


Figure 2-10 Micro-section of porosity in a carbon fibre composite material

2.5.7.3. Porosity in the matrix

The most important parameter of a carbon fibre material is the proportions and properties of the matrix and the reinforcement of the composite. The proportions can be described either by the weight fraction or more commonly by the volume fraction. The weight is obviously related to the density of the material and therefore the presence of porosity changes the density of the matrix. A less dense matrix leads to a change in overall volume fraction which results in changes in the materials overall strength properties.

2.5.7.4. Porosity at the carbon matrix interface.

The high tensile strength of carbon fibre composites is achieved by the efficient transfer of the load from the matrix to the fibres. Transfer of the load is dependant on the interface being a well balanced mixture of the two materials, good cohesion between the matrix and the fibre and the surface area of the adhered materials. Porosity at the matrix fibre interface therefore interferes with the balance of the mixture and reduces the surface area of the adhered materials thus reducing efficient transfer of the load.

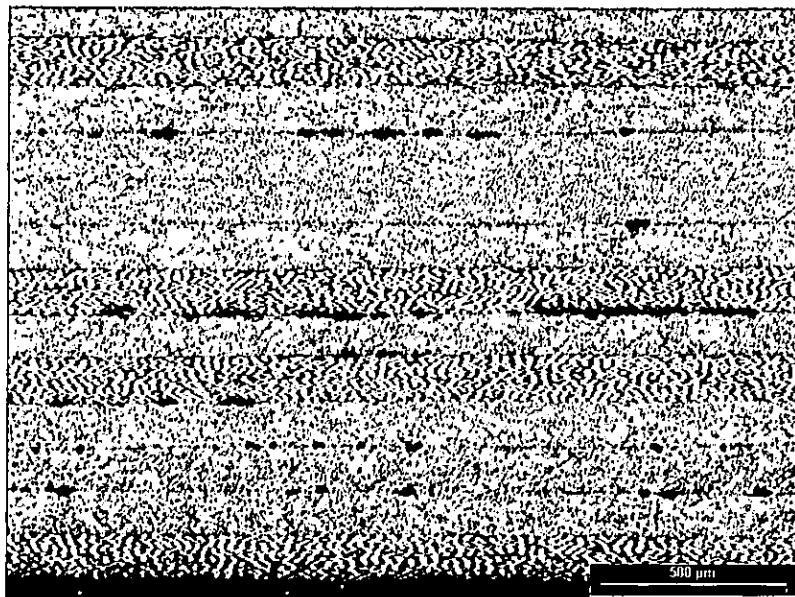


Figure 2-11 Micro-section of porosity at the carbon matrix interface

2.6. Inspection requirements

To ensure the structural integrity of composite aircraft structures it is important that both material inclusions and significant porosity levels are readily detected and reported. In the case of sandwich structures core defects and disbonds between the skin and core are also significant. As with the SPFDB process the inspection methods primarily used are ultrasound and radiography. However the voids / porosity pertaining to composite manufacture can in certain instances be detected by both ultrasound and radiography. Typical defect detection requirements state that inclusion and delamination type defects in excess of 36 mm² should be detected and reported and porosity levels around 4% are structurally important. Ultrasonic detection of porosity below 4% can in certain circumstances be detected and evaluated but it is difficult to achieve a robust method when inspecting large complex shapes.

With composite material technology developing rapidly it is anticipated that in the not to near future the detection and assessment of porosity below 4% will become an NDT requirement. For this to be achieved improvements in all aspects of ultrasonic inspection need to be sought as reliable defect detection is achieved by a combination of data capture, manipulation and data evaluation.

2.7. Reference specimens and test samples

The use of reference specimens to establish the parameters required for a particular inspection is a common practice within non-destructive testing. Reference specimens are generally either manufactured with simulated defects or taken from a defective part that has undergone macro or micro graphic examination. The problem with simulated defect reference specimens is that the defect response is usually ideal i.e. the defect is conveniently located and manufactured from a material that has a good indicative response. Real defects taken from defective components overcome the problems associated with simulated defects but only represent one set of defect conditions in terms of location and

material. Also real defect reference specimens cannot truly be examined microscopically as this would destroy the specimen. In reality an area close to the defect is examined and the results are assumed to match the remaining area that is to be used for reference. Care has to be taken therefore when defining the significant defect standard for a part. Designers, Structural and NDT engineers need to confer on their interpretation of the structural requirements to ensure that there is no ambiguity, and on establishing the inspection method ensure that the process is controlled via a suitable reference standard. All parties should be aware of the limitations of the process control reference standard and build in safety factors that are tolerant to the inaccuracies that occur when using such specimens. The samples described below consist mainly of simulated defect types, there are however a few that contain real defects such as impact damage in composite material and an example of a real disbond in a titanium diffusion bonded structure. They have been included to establish a link between the parameters required for the correct detection of simulated defects in comparison to the detection of real defects.

2.7.1. Composite material test samples

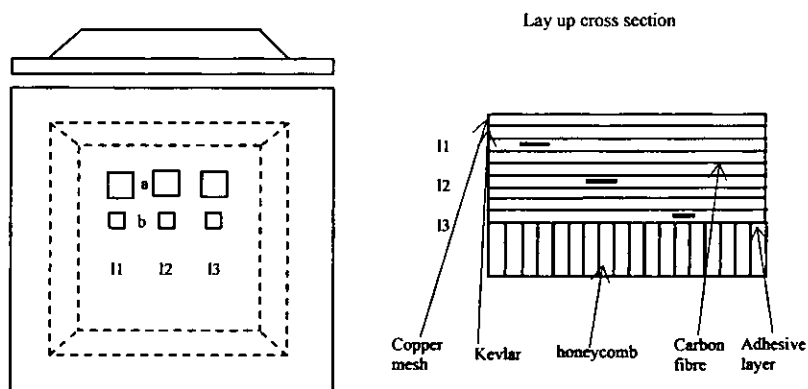


Figure 2-12 Typical reference specimen used for calibration when inspecting structures containing honeycomb and solid CFC

In figure 2-12 above, folded PTFE Teflon patches have been used to simulate defects in the adhesive of the skin to core bond, at mid depth in the skin and near the surface of the skin in this panel. The size of the patches varies from 6 x 6 mm to 12 x 12 mm. This is a typical configuration for calibrating both ultrasonic and mechanical impedance NDT equipment. The sample has a copper mesh layer on the surface and a Kevlar layer immediately below it. This is frequently used on aircraft structures. The copper mesh is used for lightning strike protection and the Kevlar is used to prevent delamination damage when drilling fastener holes.

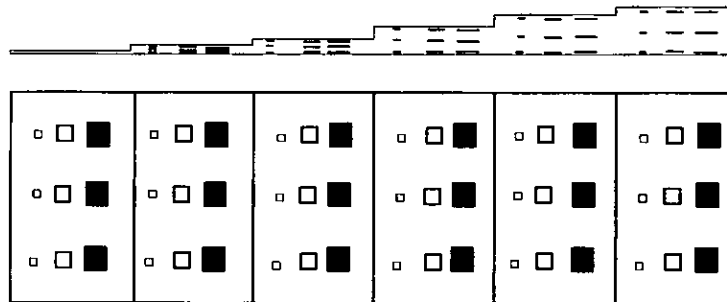


Figure 2-13 Typical configuration of a step wedge reference specimen.

Figure 2-13 shows a standard reference specimen used by most aerospace manufacturers when inspecting CFC using conventional ultrasonic techniques. The step wedge contains in each step, folded PTFE square inclusions situated 2 plies down from each surface and at mid-depth of each step. Folded PTFE is used in an attempt to entrap a small amount of air in the fold. Defect sizes are usually sized in accordance with the defect acceptance criteria defined in the relevant process specification. In the case above the middle sized defect would correspond to the limit in which a defect becomes unacceptable. The smaller defect represents a minimum detectable defect requirement and the largest is usually used for defect sizing purposes.

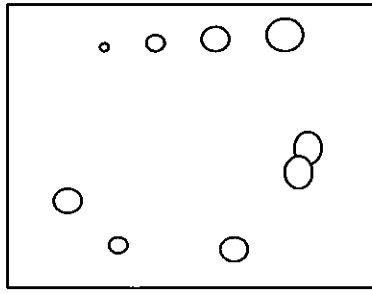


Figure 2-14 A schematic showing the position and relative sizes of impact damage sites in a solid composite panel.

This specimen is manufactured from a solid CFC laminate and has been subjected to various levels of impact causing eight damaged sites ranging from 19 x 16 mm to 67 x 24 mm in size. The panel size is 450 mm².

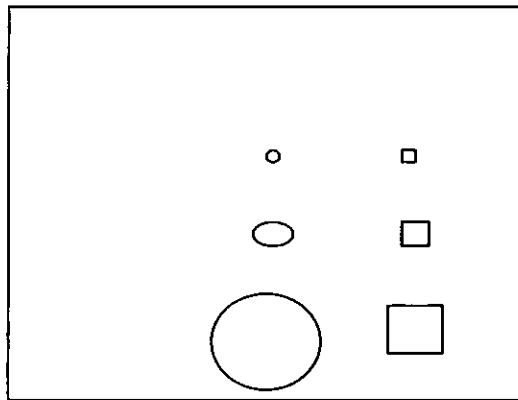


Figure 2-15 A schematic of a solid carbon fibre composite panel containing ancillary material inclusions.

This panel is 300 mm² and 4 mm thick solid CFC and contains six inclusions ranging from 6 mm² to 25 mm² and oval inclusions 20 x 27 mm to 50 x 30 mm all at depths of 2mm

2.7.2. Titanium diffusion bonded super plastically formed test samples

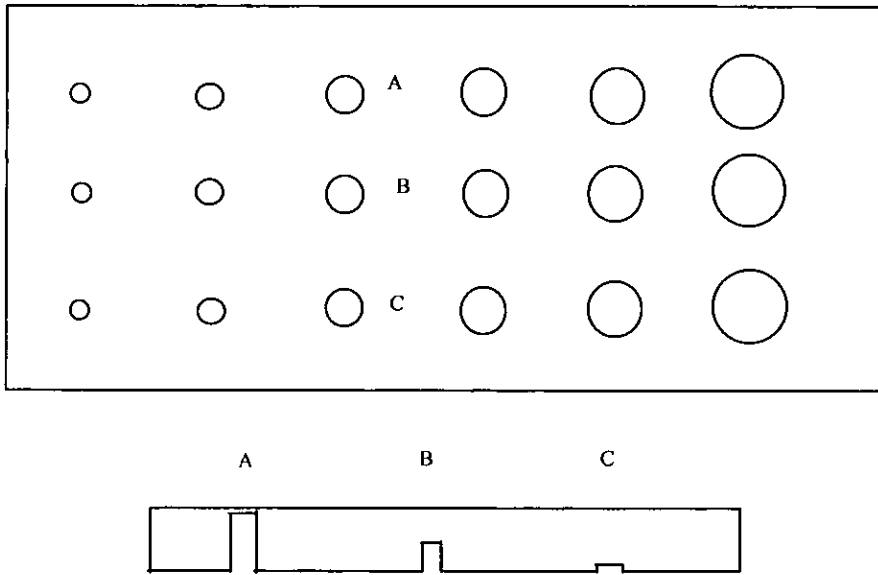


Figure 2-16 Typical diffusion bonding flat bottom holed reference specimen.

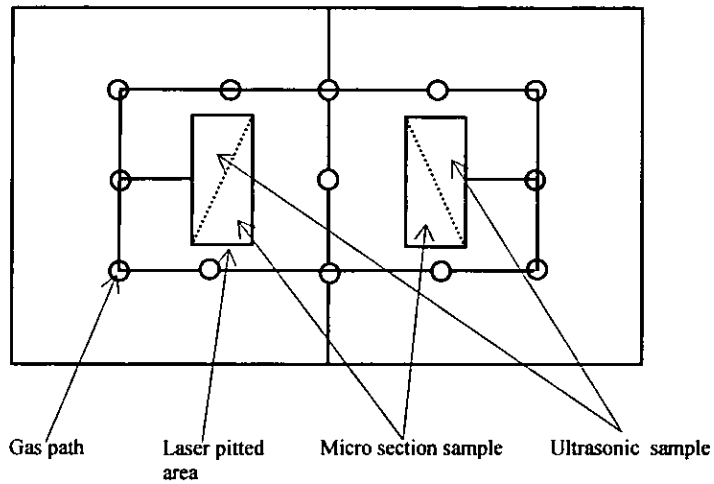


Figure 2-17 Sketch showing the area of laser pits and the gas paths used for manufacture.

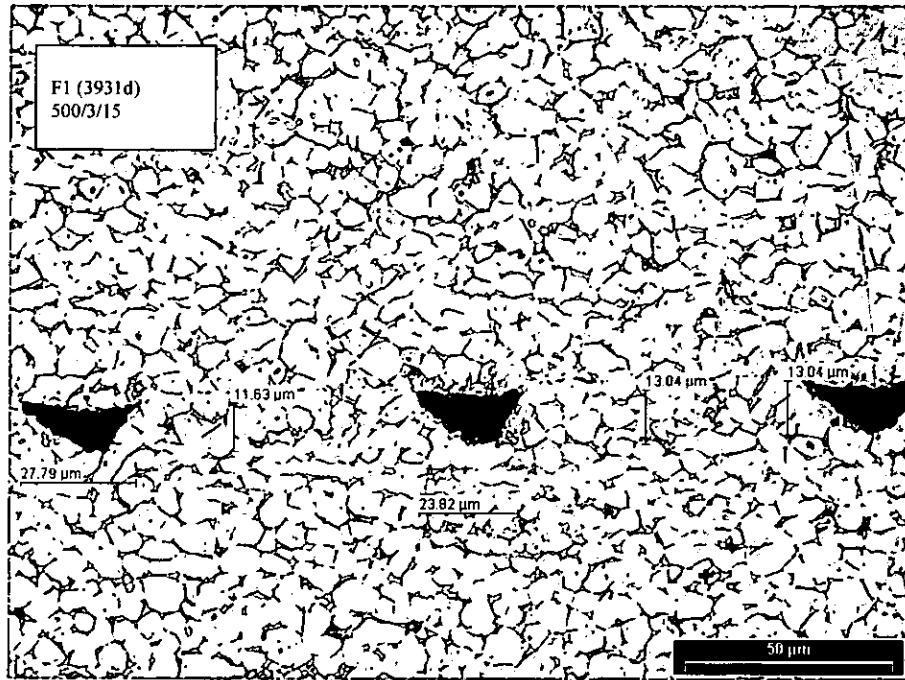


Figure 2-18 Micro section of a laser pitted reference sample.

2.8. Summary

Typical mechanical properties for different component materials and forming methods are given below [Stephen 1986, Curtis 1985]:-

Method/material	Shear Strength (MPa)
SPFDB	575
Riveted joint	10
Unidirectional Carbon fibre Composite	1000 approximately

From the above table it can be clearly seen that the use of composite and titanium super plastic forming/diffusion bonding methods results in components that are significantly stronger and potentially lighter than the conventional riveted aircraft structure. However, to achieve these design strengths the manufacturing process has to be strictly controlled to avoid the introduction of harmful defects. Porosity in composites is detrimental to most of the mechanical properties but primarily reduces the fracture toughness and shear strength. Micro voids in diffusion bonds will degrade the fatigue performance of the component without significantly affecting the static strength. [Baker Partridge ,1984]. Whilst every care is

taken by process control to eliminate these defects it falls on the NDT engineers to thoroughly search for the presence of any artefact that could contribute to a components failure.

The drive to reduce weight and increase strength results in designers making the best possible use of new materials and using these materials to manufacture very large aircraft structures. The job of the NDT engineer is therefore exasperated as the significant defect size reduces and the components become larger and more complex.

The potential for defects to occur during manufacture of modern aircraft structures has expanded with the introduction of new materials and techniques. Previously aircraft structures were machined or fabricated and the quality of material was controlled at supply. Typical defects after manufacture were therefore process induced. Manufacturing components from composites however has added further quality control because the structural effects of both material and process induced defects are now only apparent after component manufacture. Quality control of material at the supply stage is still a requirement but poor lay up and curing of composites will result in material that is not fit for purpose.

For robust and accurate defect detection it is important for NDT engineers to understand the product in terms of manufacturing detail, component geometry and process parameters. This knowledge should then be applied to predict where defects may occur and how they should be reliably detected. Engineers with years of experience in NDT of composite and titanium diffusion bonding methods still came across completely new instances of process failure which makes accurate prediction and hence successful detection of defects very difficult.

Categorising potential defects does however help in the estimation of likely failure and in terms of composite manufacture, defects can be labelled as process failure, material failure, and /or human error induced. Process failure and its associated defects can be readily detected by monitoring. Data in terms of pressure, temperature and time for a process curing cycle can be used to identify potential faults with the component. NDT can then be tailored to the expected fault. Material failure can again

be monitored by using the data from the manufacturer and also monitoring the material storage history. The relationship between material data and potential defects is not as apparent as the process data but experienced engineers are able to make sound judgements based on this information. Defects caused by human error usually fall into the class of inclusions and whilst not all ancillary materials are easily detected the use of complimentary NDT methods does reduce the potential risk of this type of defect being missed at the inspection stage.

In terms of part integrity and hence aircraft safety every effort has to be made to ensure all possible defects are detected at the earliest stage. There is therefore no single NDT method that can reliably detect and characterise every combination of defect or imperfection. Ultrasound, Radiography and Shearography are complimentary NDT techniques that offer a vast range of defect detection capabilities. Good ultrasonic defect detection is reliant on the imperfection being normal to the transmitted wave. The transmission angle is therefore adapted to the expected orientation of potential flaws. For composite and diffusion bonding inspection the ideal transmission and reception angle is normal to the surface as composite layers and titanium bondlines are generally normal to the surface. Imperfections at these interfaces can be detected by generating longitudinal waves. Radiography is highly sensitive to changes in material density and therefore flaws that have their major axis (i.e. most significant density change) parallel to the radiation beam are easier to detect. This is the opposite to the ultrasonic case and therefore demonstrates why radiography and ultrasound are often used as complimentary methods. Shearography is a relatively new NDT method and is particularly useful for detection of disbonds in composite honeycomb and thin skin components. Like radiography shearography supplements the ultrasonic method by being able to fully characterise disbonds.

A potential disbond detected by the ultrasonic method would be indicated by an area of higher attenuation. Ultrasonic attenuation can be attributed to a number of anomalies within a component of which not all

are considered unacceptable. It is these cases where shearography can be quite definitive on the question of disbond.

The application of ultrasound, radiography and shearography to aircraft structures is therefore complex in terms of product knowledge and expertise of the adopted inspection methods. The use of composite and titanium diffusion bonding is now common practice and NDT methods for inspection of these materials are well established. There are however many research and development programmes aimed at further developing the technology in order to produce more efficient manufacturing processes and / or lighter and stronger components. The implications to NDT are that the current methods have to be developed in line with material and processing developments.

In conclusion therefore it is imperative to the development and implementation of new materials and manufacturing methods that non-destructive testing is able to reliably detect flaws that may occur. New methods invariably result in a whole new set of inspection parameters that cannot be dealt with using standard methods. However whilst developing novel inspection methods it is important to understand the effect each inspection parameter has on the overall result. The work in the following chapters therefore analyses the performance of current technology and use the results of experiments and output from mathematical models to deliver enhanced techniques in shearography, ultrasound and radiography.

Chapter 3

3. Ultrasound

Ultrasonic defect detection is performed by, transmitting a beam of sound energy through a homogeneous material and detecting the amplitude and temporal location of the reflected beam. Materials containing discontinuities will be distinguished by the temporal displacement and/or the energy attenuation of the reflected beam with respect to the expected values for the material under test.

Ultrasonic waves are generated in a material via a piezoelectric transducer which when excited causes particles within the material to vibrate. Inertial and elastic forces within the material caused by the ultrasonic wave are analogues to the vibration of a spring and each particle can therefore be treated as a tiny spring which follows the theory of Hooks Law i.e. "within the elastic limit of any body the ratio of the stress to the strain produced is constant."

The generated ultrasound travels through the material until it is either absorbed by the material or is reflected at an interface. The amount of absorption is governed by the size of specula reflectors the material contains and the frequency of the ultrasonic wave, i.e. course grained material such as cast iron absorbs ultrasound quite readily whereas fine grained material such as titanium absorbs less. The amount of ultrasonic scattering is also frequency dependent because specula reflectors that are less than a quarter of the ultrasonic wavelength in size are generally considered to be transparent to the ultrasonic wave.

When inspecting airframe structure manufactured from either composite or super plastically formed and diffusion bonded titanium the defect types will in general be normal to the surface therefore longitudinal waves are employed as the reflection and hence detection of these waves is greater than any other types of ultrasonic wave. Modelling work for the diffusion bonded inspection carried out by Lowe [Lowe 1992] concluded that the use of Lamb waves offered no advantage over normal incidence ultrasonic testing for this application. Longitudinal waves are the most common form of ultrasonic wave that is used in production inspection of composites and

super-plastically formed diffusion bonded titanium therefore further discussion will be centred on longitudinal waves only.

Carbon fibre composites readily absorb ultrasound. This is due to the manufacturing method adopted where fibres are contained in a polymer matrix and orientated in the material such that they are normal to the ultrasonic beam. The differences in acoustic impedance between the fibre and the matrix act as reflection interfaces and the slightly uneven distribution of the fibre/resin cause high frequency ultrasonic waves to be reflected at resin rich areas. Because of this, relatively low frequency ultrasound (5 MHz) is used to inspect this material. Titanium however is a dense material with a fine grain structure and as such causes little attenuation to the ultrasonic wave when compared to composite. The potential discontinuities in titanium processed by diffusion bonding and super plastically forming are much smaller than that expected or critical to the performance of composite structures and therefore the ultrasonic inspection has to be tailored to finding sub millimetre reflectors. This results in high frequency transducers, pulser receivers and data acquisition systems having to be employed.

The author therefore presents two different applications that both require ultrasonic inspection albeit with different parameters. The production inspection technique however can be analysed using the same tools with emphasis placed on the parameters pertinent to the application.

3.1. Transducer analysis

3.1.1. Piezoelectric materials

Piezoelectricity is the ability of a material to vibrate when stimulated by an electrical charge and inversely to produce a charge when stimulated by an external pressure. Various materials exist that contain or can be made to contain this property. The most common material used for ultrasonic inspection is ceramic namely the various types of lead titanate zirconate (PZT). However polyvinylidene difluoride (PVDF), a relatively new material, is now being used in certain applications. The properties along

with the advantages and disadvantages of each material will now be discussed.

3.1.1.1. Piezo Material properties

Acoustic impedance (ρc)

A materials acoustic impedance is calculated by multiplying the materials density by the speed of sound in the material in question. In ultrasound the ratio between transmitted and reflected ultrasound is determined by the differences in acoustic impedance at the interface of the two materials and is determined using equation 3-23 on page 63.

Coupling factor (k'_{33})

The coupling factor is an expression of the amount of electrical energy that will be converted to a mechanical vibration for a particular transducer and can therefore be used to determine the electrical stimulation pulse energy requirements. Typical values for PVDF and PZT are 0.2 and 0.49 respectively which indicates that there is a significant reduction in sensitivity in the PVDF case. The clamped coupling factor k'_{33} is realised from 3 material piezoelectric properties by the formula

$$k'_{33} = \epsilon_{33} / (c_{33} e_{33}) \tag{3-1}$$

where ϵ_{33} denotes the dielectric constant

c_{33} denotes the elastic compliance and e_{33} is the piezoelectric stress constant

Piezoelectric stress constant (e_{33})

The piezoelectric stress constant and the dielectric constant are important factors in determining materials sensitivity and hence defect detection capability. For instance when comparing PZT ($e_{33} = 15.8$) with PVDF ($e_{33} = 0.16$) the difference results in an electrical load impedance 2000 times higher for polyvinylidene difluoride (PVDF) in comparison to lead titanate zirconate (PZT). This is equated by using the relationship between acoustical load impedance and electrical load impedance, which can be calculated by:-

$$Z_r = Z_e / 4\alpha^2 \tag{3-2}$$

with $\alpha = e_{33}a/t$

$$\tag{3-3}$$

For maximum power transfer from the electronic pulser circuit to the transducer, the pulsers output impedance should match the transducer impedance. When comparing PVDF and PZT transducers of the same area (a) and thickness (t), the piezoelectric stress constant has a direct influence on the electrical load impedance and as such determines the requirements for the electronic pulser circuitry. A pulser circuit that has a output impedance matched for maximum power transfer for PZT therefore is far from optimum for the excitation of a geometrically similar PVDF transducer.

Relative dielectric constant (ϵ_r)

This transducer parameter is dependant on the degree of restraint applied to the material in question and is a ratio between the clamped dielectric constant ϵ_{33}^s and the dielectric constant of a free transducer ϵ_0 . This constant is used to determine a transducers capacitance by the relationship

$$C_0 = A\epsilon_r / d \tag{3-4}$$

3.1.2. Ceramic

Ceramics posses good electromechanical properties but have high acoustic impedance (Table 3-1). The high coupling factor results in approximately 50% of the electrical excitation energy being converted to ultrasonic energy, but, due the materials high acoustic impedance only 15% of the acoustic energy is actually transmitted into the coupling medium. Also ceramics are highly resonant materials with high electrical and even higher mechanical Q factors which if not damped produce narrow band signals. Another disadvantage of ceramics becomes apparent when constructing ultrasonic arrays as this material has a high degree of lateral

cross talk (i.e interference between elements of the array). Cross talk occurs when sound waves reverberate laterally in the transducer material which induce electrical signals as they stress and strain the material. Cross talk adversely influences the radiation pattern and therefore degrades the imaging properties of the transducer. Array transducers manufactured from ceramic material are usually fabricated by setting the ceramic in a polymer base and machining each element by cutting a slot across the face of the material. The aim is to cut each individual slot as deep as possible without completely slicing through the material. This technique is called dicing.

Acoustic velocity (c) (m/s)	Acoustic impedance (Z) (kg m ⁻² s ⁻¹)	Electro-mechanical coupling K _t	Dielectric constant ε _r	Electrical quality factor	Mechanical quality factor	Dielectric loss tangent (radians)
4350	340	0.5	600	50	250	0.02

Table 3-1 Typical ceramic parameters taken from Berlincourt et al 1964

3.1.3. Polyvinylidene Diflouride

From Table 3-2 it can be seen that polyvinylidene diflouride (PVDF) has a low electromechanical coupling factor, has a high dielectric loss tangent and a low dielectric constant which make this material a poor transmitter of ultrasonic energy. However being a polymer this material can be readily formed into a flexible array, its acoustic impedance is closer matched to the coupling medium and therefore the converted energy be it less than that of ceramics, is readily transmitted into the medium and also does not suffer from lateral cross talk making array fabrication a lot simpler.

Acoustic velocity (c) (m/s)	Acoustic impedance (Z) (kg m ⁻² s ⁻¹)	Electro-mechanical Coupling K _t	Dielectric Constant ε _r	Electrical quality factor	Mechanical quality factor	Dielectric loss tangent (radians)
2260	42	0.2	6.2	4	10	0.25

Table 3-2 Typical PVDF parameters taken from AMP data sheets

Work by Silk [Silk 1984] has shown that the overall transmit/receive efficiencies are quite comparable between the two materials, however

when designing the transmit/receive circuitry for PVDF high input impedance amplifiers are required due the materials low dielectric constant and cable lengths have to be kept to minimum so that this effect is not exaggerated. Formulae derived by Silk [Silk 1984] for transmit (Yt) and receive(Yr) efficiencies are given below:-

$$Y_t = \left(\frac{k_t}{1 - k_t^2} \right) \cdot \sqrt{\left(\frac{\epsilon_{33}}{c_{33}} \right)} \quad (3-5)$$

and

$$Y_r = \frac{k_t t}{\sqrt{(c_{33} \cdot \epsilon_{33})}} \quad (3-6)$$

Where k_t = electromechanical coupling coefficient, ϵ_{33} = piezoelectric stress constant , c_{33} = elastic compliance and t = thickness of piezoelectric material.

From these formulae it can be seen that the permittivity ϵ_{33} which is related to the dielectric constant should be high for transmission and low for reception therefore the PVDF's low dielectric constant whilst poor for transmission becomes advantageous when used as a receiver. The net effect of this situation is that overall PVDF has a transmit receive efficiency (Yt times Yr) of approximately 9.30 whilst PZT comes out at 14.6 which considering the order of magnitude difference in the dielectric constant is a rather surprising result.

3.2. Transducer parameters

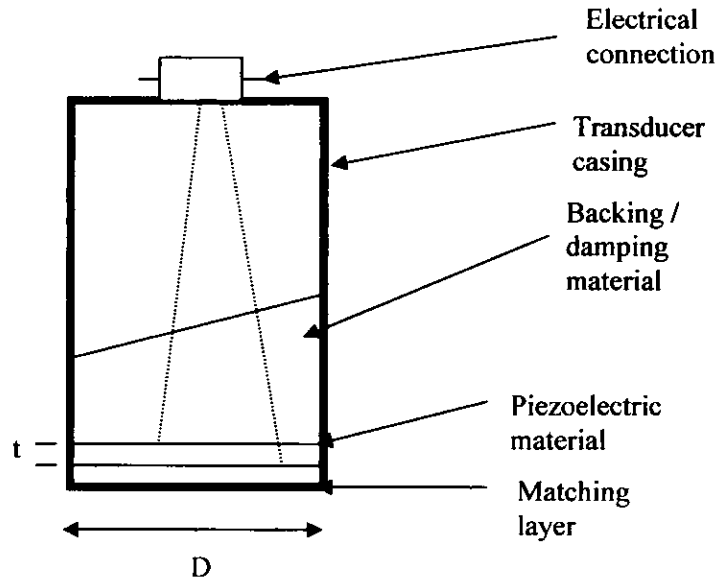


Figure 3-1 Cross section of an ultrasonic transducer

The characteristic frequency of an ultrasonic transducer is directly proportional to the thickness of the piezo material.i.e.

$$f_o = \frac{c}{2t} \text{ or } t = \frac{\lambda}{2} \tag{3-7}$$

where c is the velocity of sound in the materials and t is the thickness. The oscillation resulting from the pulsed excitation of a piezo-electric material does not remain constant but decays over time.

This decay is caused by internal losses due to friction inside the material but more importantly by energy transmission into the neighbouring materials. This energy loss has therefore a damping effect on the natural oscillation of the material and is known as the damping coefficient. Whilst damping reduces the amplitude and hence sensitivity of the ultrasonic signal it does increase the bandwidth of the signal which in turn enhances the axial resolution. Pulsed operation and manipulation of the damping parameters by bonding materials to the back face of the transducer can be

made to produce wide band ultrasonic pulses which in turn can be used for high resolution material investigations.

The resonant frequency of a transducer therefore is dependant on the characteristic frequency described above and the damping coefficient δ which can be calculated from by [Krautkramer1977]:-

$$\delta = \left(\frac{(z_0 + z_1)(z_0 + z_2)}{(z_0 - z_1)(z_0 - z_2)} \right) \quad (3-8)$$

when both the face materials have a greater or lower acoustic impedance. In the case where one face material has a lower acoustic impedance value and the other is greater then the transducer will oscillate at $\lambda/4$ resonance and the characteristic frequency will be halved in this case the damping coefficient is given by [Krautkramer1977] :-

$$\delta = \frac{(z_0 + z_1)^2 (z_0 + z_2)^2}{(z_0 - z_1)^2 (z_0 - z_2)^2} \quad (3-9)$$

Which means that the plate will only oscillate at a quarter wavelength and the magnitude of the oscillation and hence the transmitted energy will be significantly reduced.

To further explain the effects of damping an analogy with a series resonance circuit can be made. It is well known that for series resonance to occur the phases of the inductive and the capacitive reactance must be in opposition and therefore cancel. When this occurs the frequency can be determined by:-

$$f = \frac{1}{2\pi\sqrt{LC}} \quad (3-10)$$

At this frequency the impedance z is equal to the resistance.

The Q factor for series resonance can be determined by:-

$$Q = \frac{1}{r} \sqrt{\frac{L}{C}} \quad (3-11)$$

By making an analogy to the mechanical parameters of an ultrasonic transducer it can be shown that the capacitance represents the compliance, the inductance represents the mechanical stiffness or mass of the material, and the resistance represents the dissipative mechanisms within the crystal.

For an un-backed ultrasonic transducer the value of r is relatively low when compared to the capacitance and inductance. However when a backing material is applied the resistive element is increased and therefore the Q factor for the transducer is reduced.

The addition of backing materials to ultrasonic transducers also affects the centre frequency but to a lesser extent. The backing material adds to the overall mass and hence the mechanical stiffness which would effectively change the inductance value in the series circuit and hence change the resonant frequency.

The wavelength is determined by velocity of sound in the material and the frequency:-

$$\lambda = c / f \quad (3-12)$$

3.3. Ultrasonic beam geometrical parameters

When a circular piezoelectric crystal is stimulated by an electrical pulse it creates an ultrasonic wave in the medium that it is in contact with. This wave has the geometrical features as shown below:

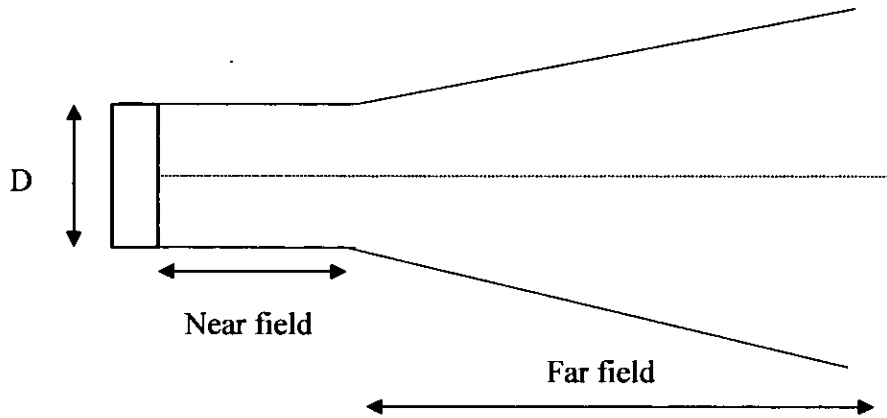


Figure 3-2 Schematic showing the beam spread, near a far fields of an ultrasonic beam.

Initially the ultrasonic beam is cylindrical and perpendicular to the crystal centre. However after some time the beam begins to diverge. The initial cylindrical beam is called the near field or Fresnel zone and the divergent part is called the far field or Fraunhofer zone.

3.4. Description of the near field

Within the near field region of an ultrasonic beam there are a series of pressure maxima and nulls along the axis. The number of maxima and nulls depends on the frequency of the transducer. The variation in amplitude between a null and maxima is dependant on the transducer diameter. The reason for nulls and maxima can be explained by applying the Huygens principle and simulating the wave fronts from the transducer as a wave passing through a circular orifice. See below:-

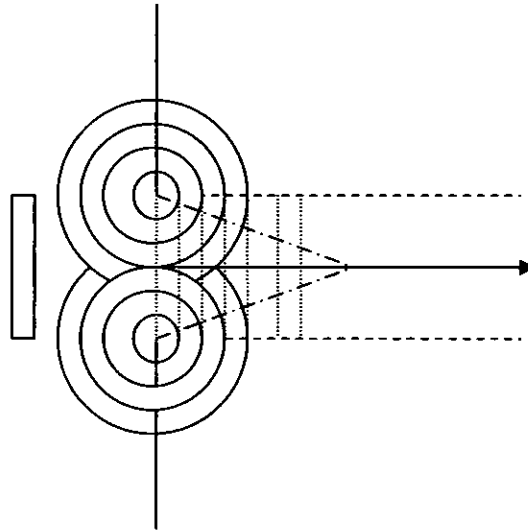


Figure 3-3 Interference structure according to Huygens principle.

According to geometric principles the plane wave passing through the orifice should have a sharply defined cylinder with a surrounding shadow. However due to diffraction from the edges of the orifice this is not the case. Huygens principle states that plane waves will pass through the centre of the orifice whilst at the edges annular waves are produced. The superposition of these two waves produces a field of maxima and nulls. If arcs were drawn that connected each intersection of the circles with the vertical lines in the above figure a cross section of the possible beam would result. Also if each intersection was considered to be a null point then a pictorial representation of the near field could be established.

The diagram above is a pictorial representation of how maxima and minima occur. The effects of these interferences gradually decrease with time and the ultrasonic beam starts to diverge. At this point the near field ends and the far field begins. The length of the near field is proportional to the diameter (D) of the transducer and the wavelength (λ) and is calculated by the formula [Krautkramer ,1977.]:-

$$N = \frac{D^2 - \lambda^2}{4\lambda} \quad (3-13)$$

It should also be noted that there is a slight focusing effect in the near field. [Krautkramer ,1977.]

3.5. Focussed transducers

In many ultrasonic applications there is a need to increase the ultrasonic pressure amplitude in order to reliably detect small reflectors. The inspection of diffusion bonded titanium is one such application. Focussing the ultrasonic beam is achieved by either machining a spherical radius on the ceramic faces or by the addition of an acoustic lens. The performance and beam profile of a spherically focused acoustic transducer can be assessed in terms of the gain in ultrasonic response which is directly linked to the degree of focusing and an improvement in lateral resolution.

3.5.1. Lateral Resolution

The effective lateral resolution of ultrasound imaging systems is related to the off axis amplitude of the beam. For systems using flat transducers, beam spread in the far field and transducer diameter in the near field have to be considered when assessing lateral resolution. Systems using focused, (spherical radiator) transducers however need to be assessed for lateral resolution by evaluating the effective beam diameter at the focal point. Diffraction at the boundaries of the transducer coupled to the fact that generally the dimensions of the radiator are not sufficiently large when compared to the wavelength mean that focusing to a point is not possible [Krautkramer, 1977]. As can be seen in figure 3-4 at the point of focus i.e. where the pressure is maximum, the beam still has some width. The lateral resolution is therefore dependant on the beam width achieved. Beam width, focal length and the focal point are all dependant on the radius of curvature and the wavelength of the transmitted ultrasonic wave which in turn determines the gain in pressure of the ultrasonic wave.

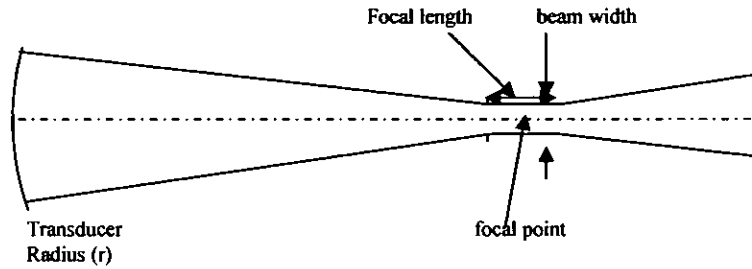


Figure 3-4 Schematic showing the focusing effect from a curved transducer.

The focal point for a spherical radiator is determined by calculating the point along the axis where the maximum pressure occurs. O'Neil [1949] concludes that the pressure along the axis of a focused radiator can be determined by the formula below:-

$$|p| = |P| \rho c u_0 \quad (3-14)$$

where

$$P = E \sin k\delta / 2 \quad \text{and} \quad E = 2 / (1 - a/r) \quad \delta = B - a$$

$$k = 2\pi / \lambda$$

ρ = density

c = velocity of propagation

u_0 = A normalised velocity of uniform amplitude and phase

$\rho c u_0$ represents the reference pressure

r = radius of curvature of the transducer

B = distance from point on the axis where the pressure amplitude is being calculated to the outer edge of the transducer.

a = distance from the centre of the transducer to the point where the pressure is being calculated.

Krautkramer [1977] expand the formula above to give :-

$$p = p_0 \left| \frac{2}{1-a/r} \right| \left| \sin \left[\frac{\pi}{\lambda} \left(\sqrt{(a-h)^2 + D^2/4} - a \right) \right] \right| \quad (3-15)$$

with

$$h = r - \sqrt{r^2 - d^2/4} \quad (3-16)$$

Where r is the radius of curvature, D is the diameter of the transducer

The structure of the relationship above does not allow a simple formula to calculate the focal point to be derived and therefore an iterative approach has to be taken where the pressure is calculated for many values of a and the maximum value extracted. This formula however will always give the maximum pressure at the geometric focal point due to E or $2/(1-a/r)$ going to infinity when $a = r$.

In order to use an iterative approach the formula has to be manipulated and the case where E or $2/(1-a/r)$ goes to infinity has to be catered for. The pressure (P) at the centre of curvature is equal to kh [O'Neill,1949] therefore this value can be calculated and used as a special case in the iteration when $a = r$ and all pressures are calculated by the following formula:

$$p = E \sin \frac{\pi NF}{2Ea} \quad (3-17)$$

where $E = kh$ when $a =$ radius of curvature (r)

and

$E = r/(r-a)$ for all other points. NF= near field

Plots for a 37 mm radius 10 mm diameter transducer generating ultrasound in water (velocity 1480 m/s) at different frequencies are shown below.

This graph confirms the O'Neil conclusions that the degree of focusing is dependant on the wavelength of the ultrasonic wave with the higher the frequency the higher degree of focus achievable and the geometry of the transducer. As the frequency increases the maximum pressure at the focal point increases which increases sensitivity. In this example a 20 MHz flat faced transducer is used for comparison against the value of the maximum pressure for a 20 MHz 37 mm radius transducer. The maximum pressure for the focused transducer is 0.25255 Pa whereas the peak pressure for a flat transducer is calculated to be 0.017482 Pa. Therefore a gain of approximately 23dB is achieved by focusing a 10 mm diameter transducer with a 37 mm radius of curvature.

Krautkramer and other authors define the degree of focusing as

$$K = F / NF = 4F\lambda / D^2$$

(3-18)

which is equivalent to the beam diameter reduction at the focus compared with the beam diameter at the same point in the near field. The smaller the value of K the sharper the focusing effect.

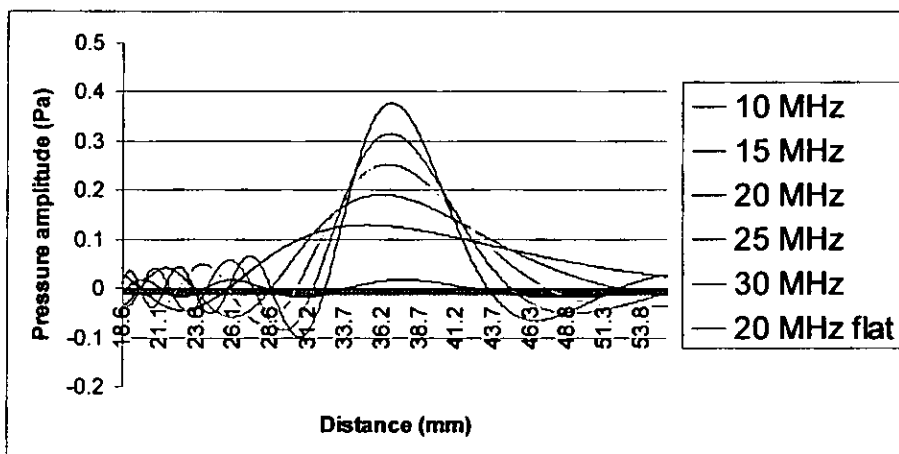


Figure 3-5 Pressure amplitude versus distance for 10 mm diameter transducers of various frequencies.

Typical commercial high frequency (>20 MHz) focused transducers are supplied as 6 mm diameter. The effect of reducing the transducer diameter from 10 mm to 6 mm can be determined by comparing the graph above with the plot below. From this data it can be seen that this reduction in transducer diameter significantly reduces the near field and therefore reduces the focusing gain. It should also be noted however that the focal point has moved closer to the transducer face, i.e. from 36.48 mm to 33.59 mm and that the curves for the 6mm transducer are now more spread out which indicates that the depth of focus has increased. The gain in pressure amplitude for this case when compared with a flat faced transducer is 14.5 dB which is approximately 8.5 dB less than the 10 mm focused transducer.

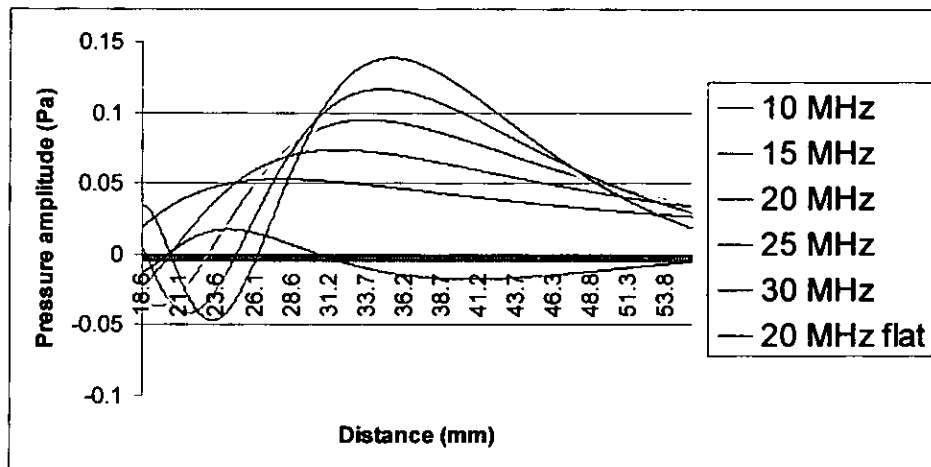


Figure 3-6 Pressure amplitude versus distance for 6 mm diameter transducers of various frequencies.

Increasing the radius of curvature of the transducer increases the value of h and therefore increases the gain in pressure. The graph below is calculated for a 37 mm radius transducer generating into water but with a 20 mm diameter element size. Comparing the results of the flat and spherical transducers responses at 20 MHz the maximum pressure has risen from 0.25255 Pa for the 10 mm diameter transducer to 1.00297 Pa for the 20 mm transducer. The gain is therefore 35 dB when compared to a flat transducer.

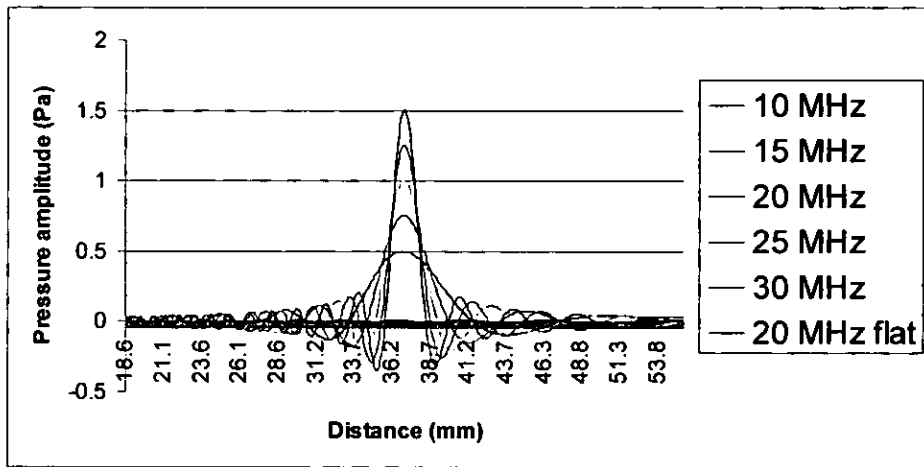


Figure 3-7 Pressure amplitude versus distance for 20 mm diameter transducers of various frequencies.

The effects of radius of curvature on the overall gain are not as great as that achieved by an increase in transducer diameter. The graph below plots the result for a number of frequencies for a 10 mm diameter transducer but with a 25 mm radius. Here the peak amplitude for the 20 MHz case is 0.37232 Pa which when compared to the equivalent flat faced transducer produces a gain of 26 dB i.e. 3dB increase over the equivalent 37 mm radius of curvature transducer.

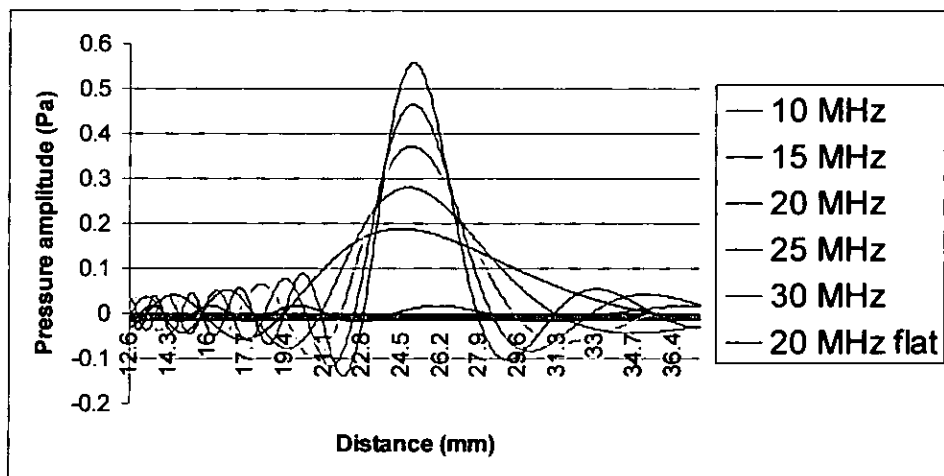


Figure 3-8 Pressure amplitude versus distance for 10 mm diameter transducers of various frequencies with a 25 mm radius of curvature.

It should also be noted that the distance of the focal point in relation to the centre of curvature decreases with an increase in frequency but

decreases with a reduction in transducer diameter. At 20 MHz the focal point is 36.48 mm from a 10 mm diameter transducer with a radius of 37 mm.

3.5.2. Beam width

The beam width of a focused transducer can be determined by using methods developed by Kossoff [Kossoff 1963] and further explained by Hunt et al. [Hunt 1983] where the Full Width of the beam at Half Maximum is used to calculate the beam diameter.

$$FWHM = 1.41\lambda(f_{number}) \quad (3-19)$$

where f_{number} = focal distance/transducer diameter or f/D

In the example used above diameter = 10 mm, focal length = 36.48 mm and the wavelength at 20 MHz in water (1480 m/s)= 0.074 mm.

Therefore

$$f_{number} = 36.48/10 = 3.648$$

$$FWHM = 1.41 \times 0.074(3.648) = 0.38 \text{ mm}$$

It can be clearly seen by this formula that wavelength, focal length which is determined by the radius of curvature and diameter all contribute to the beam width.

3.5.3. Depth of Field

A similar relationship to the beam diameter has been determined for strongly focused transducers by Hunt et al [Hunt 1983] where again f_{number} is used in connection with constant K and the wavelength:-

$$DOF = K\lambda(f_{number})^2 \quad (3-20)$$

where $K \approx 7.1$ when defined at the half maximum intensity (-3 dB) and $K \approx 9.7$ when using the half maximum amplitude (-6 dB) . When applied to the

10 mm diameter 37 mm radius 20 MHz example above the DOF results in:-

$$\text{DOF}(-3 \text{ dB}) = 7.1 \times 0.074(3.648)^2 = 6.99 \text{ mm}$$

$$\text{DOF}(-6 \text{ dB}) = 9.7 \times 0.074(3.648)^2 = 9.55 \text{ mm}$$

3.6. Phased array transducers

In contrast to using spherical radii transducer elements for focusing, a method exists whereby an array of rectangular elements is formed into a linear or annular array and is excited in a sequence. The excitation sequence is calculated for each element in the transducer and delays are incorporated to effectively steer the beam at an angle and/or to form the beam to a focal point. As the applications studied here only require longitudinal transmission normal to the surface phased array techniques will only be evaluated for their focusing capabilities.

The advantage of phased array systems is the ability to dynamically focus through a wide range of focal lengths and dynamically steer the beam. To perform these operations correctly careful consideration has to be taken in the array design. When electronically focusing an array small grating lobes will appear at each side of the main lobe. For good defect detection only reflections from targets in the main lobe should be received.

The grating lobes therefore have to be significantly reduced or eliminated. Steinberg [Steinberg 1976] states that grating lobes will occur at λ/d and will have a width of λ/l where λ is the wavelength d is the element spacing and l is the length of the array. Therefore to reduce the grating amplitude use of the Nyquist sampling criterion can be implemented by arranging the array so that the element spacing is less than $\lambda/2$. Von Ramm et al [Von Ramm 1983] also concludes that short excitation pulses reduce the relative amplitude of grating lobes.

At high frequencies i.e. 20 MHz the ultrasonic wavelength in water is 0.074 mm. Therefore to obey the Nyquist sampling theorem the element pitch would have to be < 0.037 mm. For a 64 element transducer with this element pitch the overall length would be 2.5 mm giving a near field of 21 mm. The maximum focal depth would therefore be limited to 21 mm. The gain in signal response is related to the shortening of the near

field by the focus but as the near field is so short the gain in sensitivity from focusing is greatly reduced i.e. a weakly focused transducer.

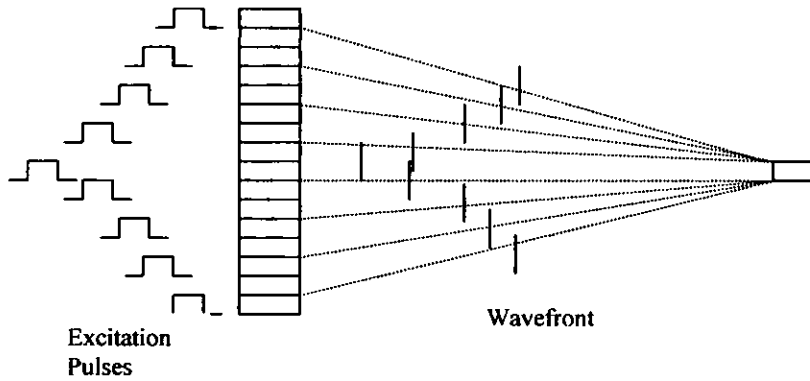


Figure 3-9 Diagram showing the focusing effect from multiple transducers with delayed excitation

The diagram above shows how a delayed excitation of individual elements would produce a focused ultrasonic beam. Focusing occurs by the in-phase summation of the wave fronts from each element at the focal point.

For this to happen each element has to be excited such that the wave travelling from each element reaches the focal point at the same instant as all the other waves from the rest of the elements. A parabola excitation is therefore necessary which for a given focal point the time delays can be expressed as [Yerima 1991]

$$\tau_n = \frac{\sqrt{f^2 + (nd)^2} - f}{c} \quad (3-21)$$

Where f = the required focal length

d = the element spacing

c = the velocity of ultrasound in the medium

n = the element number.

The table 3-3 shows the required excitation timing sequence to focus a 20 MHz transducer at 37 mm in water

element spacing	focal length	velocity				
0.074 (mm)	37 (mm)	1480000 (mm/s)				
n	firing delays (μ s)	firing timing interval (ns)	reception delay (ns)	reception interval (ns)		
10	24.664917	0.962925	-4.999500	-0.949828		
9	24.663954	0.861596	-4.049672	-0.849877		
8	24.663092	0.760257	-3.199795	-0.749915		
7	24.662332	0.658908	-2.449880	-0.649945		
6	24.661673	0.557552	-1.799935	-0.549966		
5	24.661115	0.456188	-1.249969	-0.449982		
4	24.660659	0.354819	-0.799987	-0.349991		
3	24.660304	0.253445	-0.449996	-0.249997		
2	24.660051	0.152068	-0.199999	-0.149999		
1	24.659899	0.050690	-0.050000	-0.050000		
0	24.659848	-0.050690	0.000000			
1	24.659899	-0.152068	-0.050000	-0.050000		
2	24.660051	-0.253445	-0.199999	-0.149999		
3	24.660304	-0.354819	-0.449996	-0.249997		
4	24.660659	-0.456188	-0.799987	-0.349991		
5	24.661115	-0.557552	-1.249969	-0.449982		
6	24.661673	-0.658908	-1.799935	-0.549966		
7	24.662332	-0.760257	-2.449880	-0.649945		
8	24.663092	-0.861596	-3.199795	-0.749915		
9	24.663954	-0.962925	-4.049672	-0.849877		
10	24.664917	-1.064242	-4.999500	-0.949828		

Table 3-3 Timing delays required to focus a 20 MHz phased array at 37 mm in water

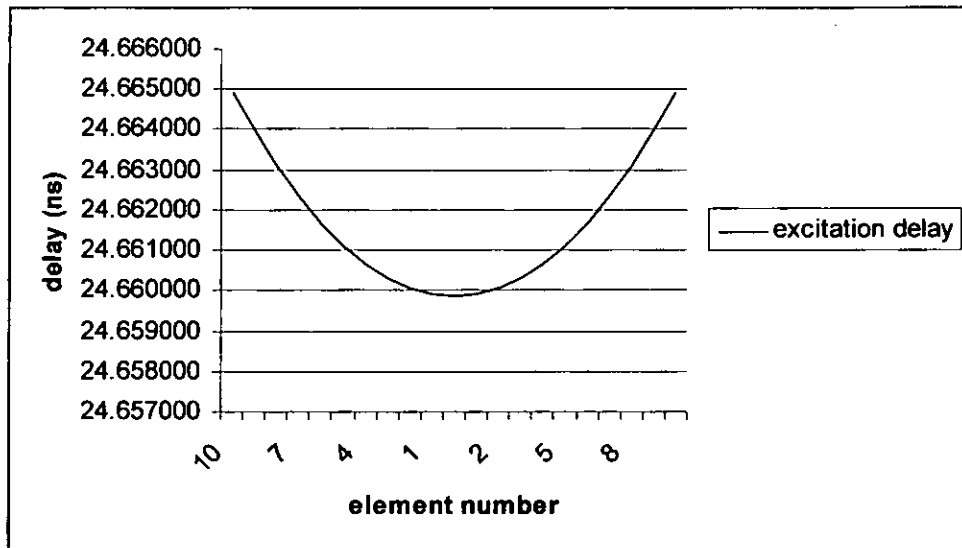


Figure 3-10 Plot of the excitation delays required to focus a 20 MHz transducer at 37 mm with an element spacing of 0.074 mm

Examining the data in the table above it is evident that the timing delay for a 37 mm focus transducer in water requires around 24 μs delays. However when the interval between each delay is considered it can be seen that fractions of a nanosecond intervals are required. This puts a severe restriction on the permissible error of the delay timing circuit which if not maintained will result in weaker focusing than expected and the introduction of grating lobes of significant amplitude.

3.6.1. Reception

The detection of returned signals from a focused array can also be improved by only making each element active at a point in time when the contribution from the focal point is expected to arrive back at the element face. This is the inverse of the time delay used for excitation and can be calculated from the expression given by Von Ramm and Smith[1983]:-

$$T(n, \phi) = \frac{F}{c} \left[1 - \left(1 + \left(\frac{nd}{F} \right)^2 - 2 \left(\frac{nd}{F} \right) \sin \phi \right)^{1/2} \right] + t_0(n)$$

(3-22)

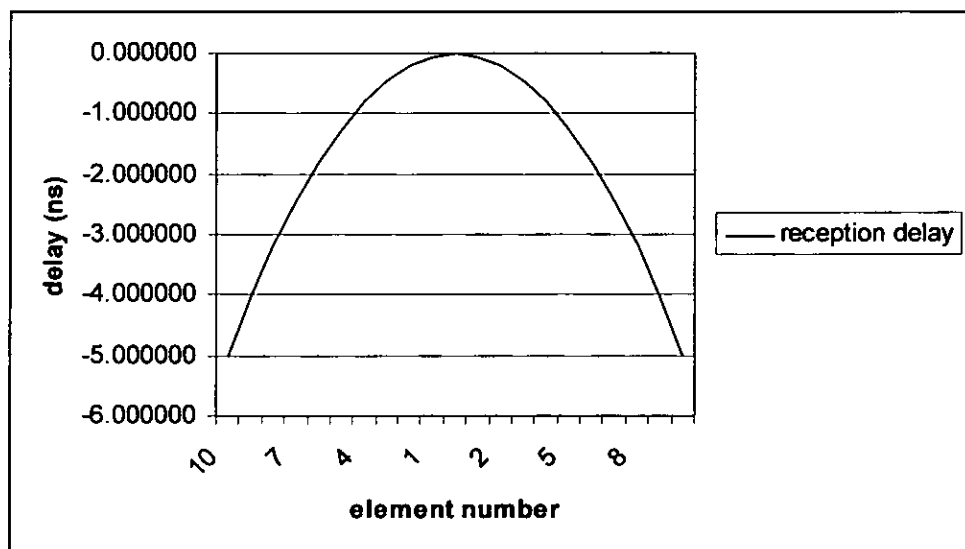


Figure 3-11 Plot of the reception delays required to receive a 20 MHz beam focused at 37 mm with an element spacing of 0.074 mm

The graph above plots the time intervals required for successful focusing at reception. Here the delay times are of the order of a few nanoseconds but as with the transmission delays the interval between each element time delay is fractions of a nanosecond and the penalty of late switching has to be considered.

3.6.2. Limitations of Phased array technology

From the data presented above it can be clearly seen that high frequency ultrasonic inspection using phased array technology is problematic. Reducing grating lobe affects results in very small element spacing and timing intervals. This problem is further compounded when dynamically steering the beam. An array transducer that upholds the element spacing rule but is large enough to produce a strong focus i.e. 37 mm focus 10 mm width would have over 200 elements which is beyond the capabilities of multi channel technology to-date. The requirements for high fidelity inspection when applied to Titanium diffusion bonding therefore cannot be fully achieved with this technology.

Carbon composite inspection however is usually performed at a frequency of 5 MHz and therefore does not ordinarily require the employment of strong focusing techniques. Array technologies are currently being applied to composite aircraft structures with the array being used purely to facilitate large area scanning.

3.7. Acoustic Impedance

An ultrasonic wave is reflected when it meets a boundary between two media of different acoustic impedances. The acoustic intensity reflected is given by [Wells 1977]

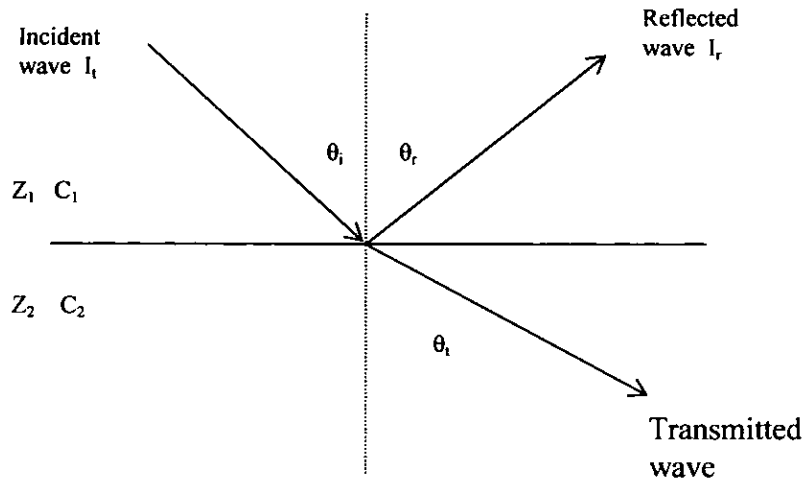


Figure 3-12 Diagram showing reflected and refracted waves due to differences in acoustic impedance at an interface.

$$I_r = \left[\frac{Z_2 \cos \theta_i - Z_1 \cos \theta_t}{Z_2 \cos \theta_i + Z_1 \cos \theta_t} \right]^2 \tag{3-23}$$

and the intensity transmitted is

$$I_t = \frac{4Z_1 Z_2 \cos \theta_i \cos \theta_t}{(Z_2 \cos \theta_i + Z_1 \cos \theta_t)^2} \tag{3-24}$$

where Z_1 is the acoustic impedance of the transmitting medium and Z_2 is the acoustic impedance of the receiving medium.

Material	Acoustic Impedance
Carbon Fibre Composite	$4.70 \times 10^6 \text{ kg.m}^{-2}.\text{s}^{-1}$
Titanium	$27.32 \times 10^6 \text{ kg.m}^{-2}.\text{s}^{-1}$
Water	$1.48 \times 10^6 \text{ kg.m}^{-2}.\text{s}^{-1}$
PZT	$34 \times 10^6 \text{ kg.m}^{-2}.\text{s}^{-1}$ [Berlincourt]
Air	$427 \text{ kg.m}^{-2}.\text{s}^{-1}$

Table 3-4 Acoustic impedances taken from [ASNT handbook vol 7 ultrasonic testing]

From the formula above it can be determined that at a water to titanium interface total reflection of longitudinal waves occurs at around 14 degrees and at a water to carbon fibre composite interface total reflection occurs at approximately 29 degrees. From the graph below it can be seen that when ultrasonically inspecting titanium the amount transmitted between water and titanium is highly dependant on angle, with small changes in angle producing large amounts of refraction. An angular change of 7 degrees results in a 2% reduction in amount transmitted. For water to composite interfaces the angular conditions are not so extreme a 2% change occurs at 9 degrees but the amount reflected at incident angles is around 25% compared to approximately 80% for titanium.

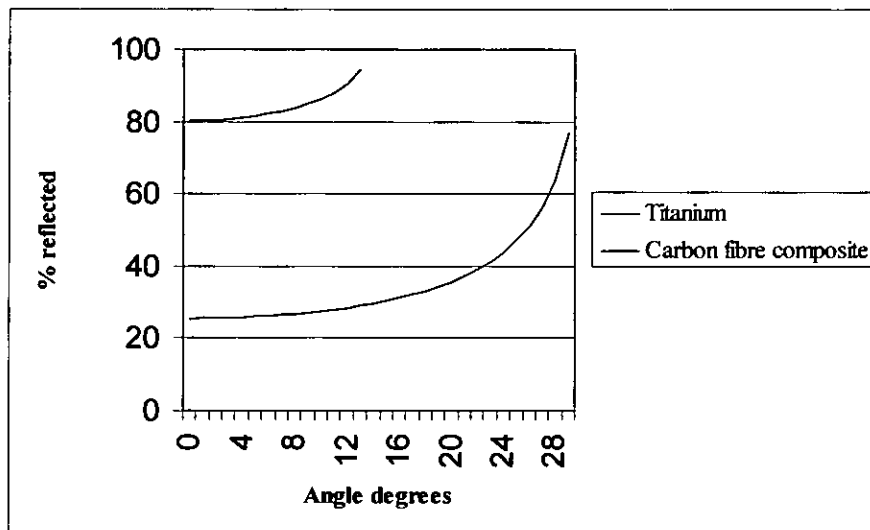


Figure 3-13 Plot showing percentage of ultrasound reflected at an interface for varying angles of incidence.

The angle of reflection equals the angle of incidence which is useful when inspecting both carbon fibre composite and diffusion bonded titanium as the majority of flaws are planar and therefore longitudinal ultrasonic waves that travel normal to the component surface. Discontinuities can be detected by measuring the reflected ultrasonic wave travelling back along the same plane as it was transmitted with the same transducer (pulse echo method). Production methods employed for carbon fibre composite inspection generally utilise two transducers, one each side of the component and are configured in a pitch catch arrangement i.e. one

transmits ultrasound whilst the other receives the signal that has passed through the component. Defect detection is achieved by detecting a change in signal position and reduction in amplitude of the signal from the far surface in the pulse echo method or a reduction in signal amplitude when the through transmission method is used. Independent of the method employed a change in signal amplitude and/or a reflection from an interface is caused by an acoustic impedance boundary see table 4.

The low acoustic impedance of air has two effects on the ultrasonic inspection

- a) discontinuities within a material usually contain gases such as air, therefore the ultrasonic reflection is large providing the defect size is comparable to the ultrasonic wavelength.
- b) transmitting sound from a solid piezoelectric material into the material under test usually requires elimination of the air interface that exists between the two materials. This is accomplished using liquid couplants or grease. However the efficiency of the transmitted and received energy is poor because of the mismatch in impedances in the various mediums.

3.8. Interface characteristics

When performing automated ultrasonic inspection, it is imperative that transducer normality is maintained over the entire inspection area as failure to do this would result in significant reduction in defect detection sensitivity. Wells reports that for planar transducers a loss of signal equivalent to 20 dB is experienced when the incident angle is moved just three degrees from normal incidence. Wells also states that focused transducers do not exhibit the same losses as planar transducers.

Experimental work has confirmed this to some extent (table 3-5), but the range of transducers available limits the results and hence the conclusion. The loss of signal due to inclination of the probe was evaluated by selecting a range of transducers listed in table 3-5 and connecting each in turn to the scanning system describe in paragraph 3.14.4. Having optimised the pulser receiver settings the probe was then normalised on a glass plate by manipulating the vertical and tip axes, figure 3-14. Once normalised the amplifier gain was adjusted so that the ultrasonic signal

response was at 80% full screen height. The gain figure was noted and one tip axes was rotated by ± 3 degrees, figure 3-15. The gain was then increased to bring the signal back to the 80% screen height. The increase in gain required to maintain the full screen height signal accounts for the signal loss in table 3-5. Reasonable conclusions can be drawn from the data in table 3-5 if the Technisonic transducer results are ignored and the result identified by the * is removed from the conclusion. Removing these results is reasonable as the Technisonic transducer response is completely different to the equivalent Harisonic.

This is primarily due to the focal spot and depth of the Technisonic transducers being less pronounced and in the case of the 6 mm, 25 mm radius, 25 MHz transducer the radius of curvature was uneven. This explains the differences in loss of signal from the ± 3 degrees rotation.

From the remainder of the results however it is clear that planar transducers do in fact suffer losses when they are inclined from the surface.

Furthermore as the radius of curvature increases i.e. the degree of focus is increased, the loss due to inclination decreases. The 24.5 dB loss from the 12 mm diameter planar transducer is the same as the 100 mm focus transducer. This can be explained as the 100 mm radius gives rise to a very weak focus and can therefore be considered planar for these purposes. An interesting observation is the 5 dB difference between the loss of the 6 mm 37 mm radius and the 6 mm 25 mm radius transducers and the 2 dB difference between the corresponding 9.5 mm radius transducers. This would suggest that the stronger the focus and the larger the transducer diameter the less susceptible to losses due to inclination from normal.

Whilst such a small set of results cannot be conclusive the explanation given by Wells [Wells 1977] that a qualitative explanation can be derived by describing the portion of the cylindrical beam that reflects back to the transducer will be crescent shaped as it is still part of the near field and therefore increasing the angle decreases the area of the crescent that will receive the reflected signal. Wells does go on further to suggest that focussed transducers do not suffer from inclination losses. The results below however show that there are losses even with the strongest focal parameters. A loss of between 6 to 11 dB for a 6 mm diameter transducer

would be very significant when inspecting for voiding in diffusion bonded titanium, therefore the conclusion drawn has to be that in order to maximise defect detection the largest possible transducer with the strongest focus should be used.

Transducer diameter	Radius of curvature	Frequency (MHz)	Gain (dB) 0 degrees	Gain (dB) -3 degrees	Loss of signal (dB)	Manufacturer
12 mm	Planar	5	28	52.5	24.5	Harisonic
12 mm	100 mm	5	18	42.5	24.5	Harisonic
12 mm	50 mm	5	-2.5*	3.5*	6*	Harisonic P
6 mm	25 mm	20	-3.5	2.5	6	Harisonic
6 mm	37 mm	20	6.5	17.5	11	Harisonic
6 mm	50mm	25	10	30	20	Technisonic
6 mm	25 mm	25	17	22	5	Harisonic
6 mm	25 mm	25	37.5	47.5 +41	10 and 3.5	Technisonic
9.5 mm	37 mm	25	22.5	27.5	5	Harisonic
9.5 mm	25 mm	15	4.5	7.5	3	Harisonic

Table 3-5 Results obtained from transducer inclination experiment.

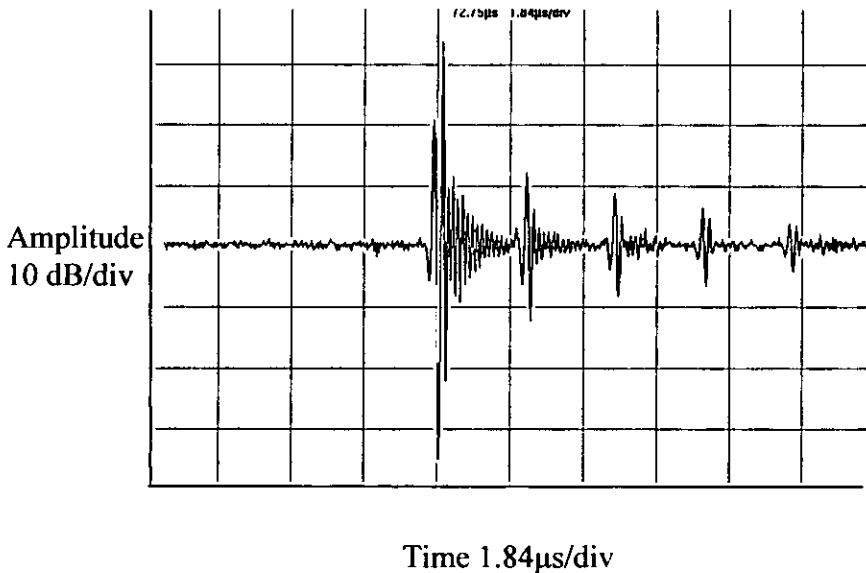


Figure 3-14 Signal response from a 12 mm diameter 5 MHz planar transducer, operating in pulse echo when normalised on a flat glass plate.

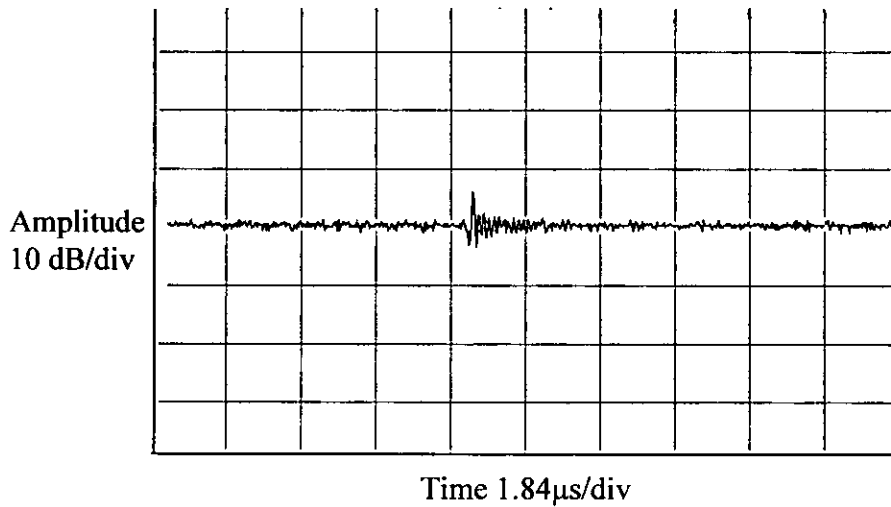


Figure 3-15 Signal response when the same transducer in figure3-14 is rotated 3 degrees

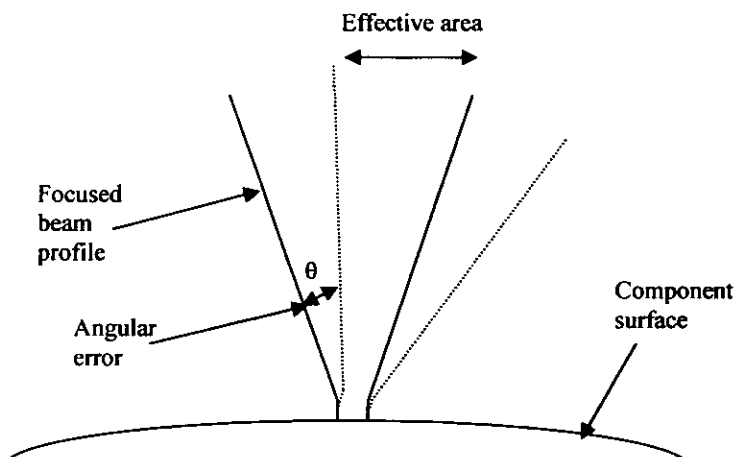


Figure 3-16 Schematic showing effect of angular displacement of a focused transducer

In general factors that contribute to the loss of transmission and reception due to non-normality are

1. The angle of refraction increases which at large acoustic impedance differences results in total reflection at relatively small angles.
2. The area of the transducer that contributes to the focal point and receives the returned pressure wave is reduced.

3. Nikoonahad and Iravani [Nikoonahad 1989] state that under broadband excitation pulses that emit from a focused transducer do not arrive at the focus at the same time but providing the difference in arrival time is less than the pulse period this effect can be neglected. However when the arrival difference is greater than the pulse period the contribution from the edges of the transducer can be insignificant and therefore the effective focus is reduced. This can be extended to the effect of probe inclination in that when a focused transducer is inclined by a few degrees from normal the path length from the extremities of the transducer will change. Figure 3-16 shows a focused ultrasonic beam which has some width will create a path length difference when angulated off normal. Applying the assumptions of Nikoonahad [Nikoonahad 1989] if the modified path length is greater than the pulse period then the sound intensity at the focus will be reduced.

3.9. Ultrasound generation and reception

Generally ultrasonic energy is generated by exciting a piezo electric material via an excitation pulse of several hundred volts. This is accomplished by applying the high voltage to the drain of a metal oxide field effect transistor (MOSFET), connecting the source to 0 volts and operating the device as a switch [Yerima 1991.] Figure 3-17 is a typical circuit that was built to gain experience of this method of ultrasonic excitation. A 555 timer configured to output a pulse every millisecond is connected to the input of the MOSFET driver integrated circuit which in turn drives the gate of the MOSFET. As the gate is turned on the high voltage is short circuited to 0 volts producing a sharp fall in voltage at the output.

When switched off the output returns to the high voltage level. Therefore the overall effect is a several hundred volt spike. Rise times are dependent on the ability of the MOSFET driver to charge the capacitance between gate and source. Once the applied gate voltage reaches the gate threshold the device begins to conduct and the voltage between drain and source is decreased whilst the input capacitance is increased due to the

feedback effect of the gate to drain capacitance i.e. Miller effect. The fall time is largely dependent on the load resistance but decreasing this also decreases the amplitude of the pulse and increases the pulse rise time which produces poor pulse characteristics.

The ideal pulse for the excitation would be one that coincides with the transducer centre frequency therefore maximising the energy transferred to the transducer. The frequency required for this application is 5 MHz which has a period of 200 ns therefore a single polarity pulse would have to have a duration of half the period i.e. 100 ns which means that the rise and fall times would have to be no greater than 50 ns. Using this pulser circuitry, matching the pulser period with the transducer centre frequency is difficult to achieve as altering load resistance to shorten the fall time affects the pulse rise time and amplitude.

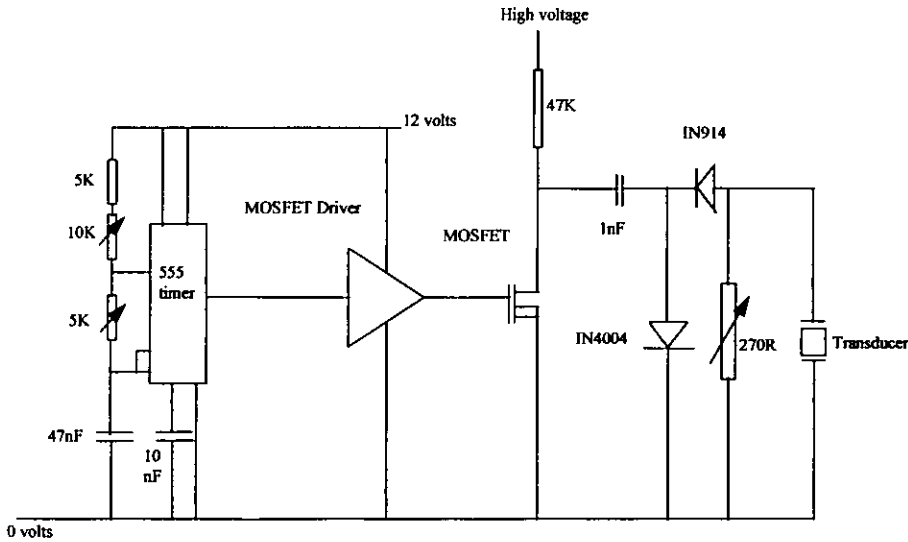


Figure 3-17 Typical Pulser Circuit

Reflected ultrasonic signals are very weak and require amplification before they can be measured. The amplification stage of the circuit consisted of a RS560C integrated circuit configured to operate as a low noise amplifier with a fixed gain of 10. Although not designed and constructed for these experiments a peak detector circuit and an analogue to digital converter are used to measure the amplitude of the ultrasonic signal which after digital processing is combined with positional data and used to generate two dimensional plots (c-scans) of the component under test.

Experiments using high voltage were conducted using the purpose built pulser / receiver circuit described previously. The objective of this exercise was to analyse the loading effects on the performance of ceramic transducers. Some experiments were conducted using PVDF as the transducer however there were problems making good electrical connection to this material and therefore the high voltage experiments were inconclusive.

Pspice, a software package for circuit simulation studies has been used to simulate the excitation of ultrasonic transducers. Figure 3-18 shows the simulation model consisting of two transducer sub-circuits connected together via a transmission line. In Figure 3-18, V_{pulse} represents the excitation voltage and V_{out} represents the received signal voltage, C_{in} and R_{in} represent the output impedance of the transducer driving circuit, and R_{back} represents the resistance of the transducer backing material.

The transducer sub-circuit shown in Figure 3-19 was modelled using an electronic equivalent circuit developed by Morris and Hutchens [Morris 1986]. The four transducer sub-circuit ports shown in Figures 3-18 and 3-19 are numbered 1, 2, 3, and 4 in both figures. As shown in Figure 3-19, the transducer sub-circuit consists of an input resistor/capacitor network, a negative capacitance, an ideal transformer, and a transmission line.

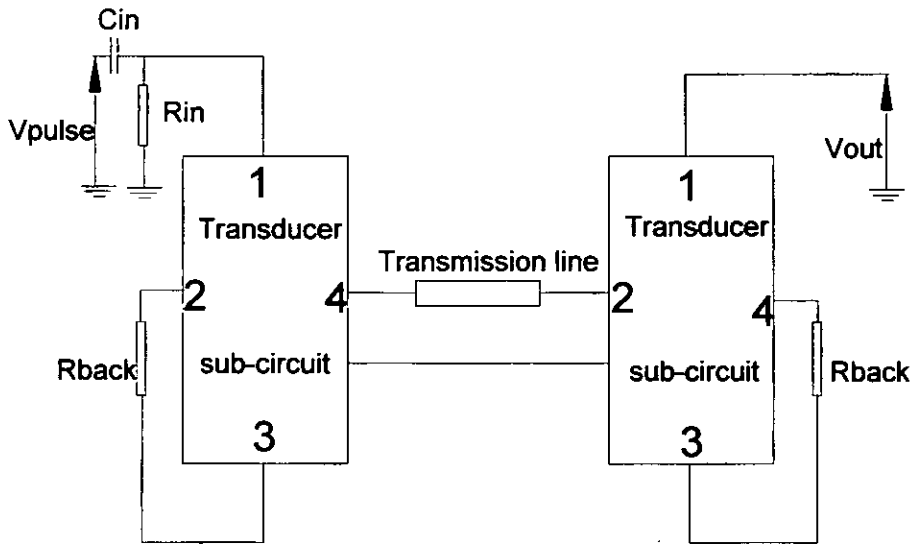


Figure 3-18 Transducer simulation model

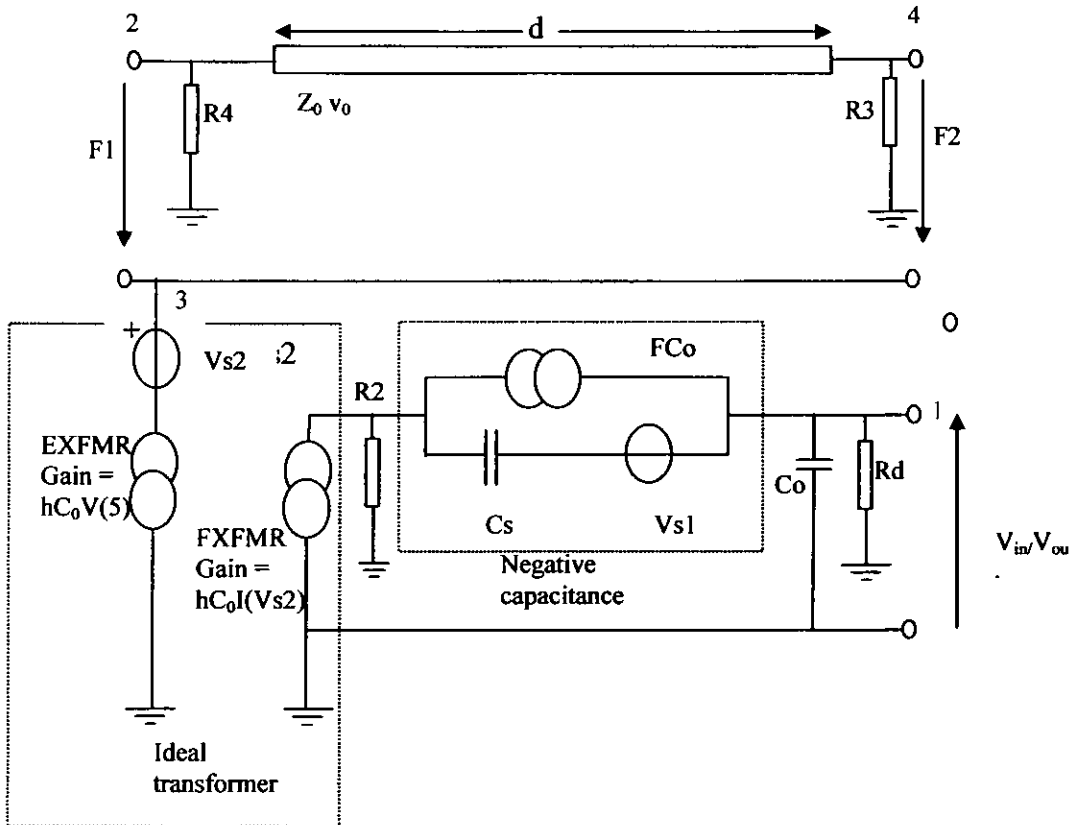


Figure 3-19 Equivalent transducer sub-circuit.

The input resistor/capacitance (R_d and C_0) represents the dielectric losses and the static capacitance, respectively. For ceramic transducers the dielectric loss is negligible and is usually ignored, however, using PVDF this dielectric loss is significant and therefore has to be taken into consideration. The negative capacitance [Mason, 1942] is simulated by a capacitor, C_s , in series with an independent voltage source, V_{s1} , which are both in parallel with a current controlled current source, F_{Co} (Figure 3-19). Positive current flows from the positive node of the F_{Co} through V_{s1} to the negative node of F_{Co} . The effect of this is to produce a charging current on the positive side of capacitor C_s , and hence produces an approximation of a negative capacitance. The ideal transformer simulates the electromechanical coupling of the transducer and utilizes a voltage controlled voltage source, $EXFMR$, and a current controlled current source, $FXFMR$, coupled to an independent voltage source V_{s2} . The conversion ratio of electrical energy to mechanical energy within a piezoelectric material is then calculated by equations (3-25) and (3-26).

$$C_0 = \frac{\epsilon_s A}{\tau v_0} \tag{3-25}$$

$$hC_0 = \frac{e_{33} C_0}{\epsilon^s_{33}} \tag{3-26}$$

where A is the transducer area, τ is the acoustic transit time, v_0 is the velocity of sound, e_{33} is the dielectric constant of the material at constant strain, and ϵ^s_{33} is related to the relative dielectric constant ϵ_r by equation (3-27)

$$\epsilon_r = \frac{\epsilon^s_{33}}{\epsilon_0} \tag{3-27}$$

The output of the ideal transformer is connected to the transmission line which contains inductance in both conductors. The transmission line stage represents the reverberations of ultrasound that occur in a piezoelectric material. The transmission line parameters are calculated using equations 3-28 and 3-29.

$$Z_0 = \rho v_0 A \tag{3-28}$$

$$\tau = \frac{d}{v_0} \tag{3-29}$$

where Z_0 is the transmission line characteristic impedance, ρ is the material density and d is the material thickness

The amount transmitted into backing materials and the material under test is then dependent on the different values of acoustic impedance of each material.

The transducer parameters used in the simulation study were (a) those derived by Berlincourt *et al*, [Berlincourt 1964]. in the case of PZT-5A material and (b) those obtained from AMP data sheets in the case of PVDF. The material parameter values are given in Table 1 and 2 (page 45).

Modelling with the PVDF parameters showed that the desired performance was achieved when the transducer input capacitance was set to 500 pF, and a 50 % bandwidth was achieved when the value of the back load matched the impedance of the transmission line used in the transducer model i.e. corresponding to an exact match between the transducer impedance and the back load impedance, hence giving loss less transmission. By experimenting with the excitation pulse shape and duration, it was found that the best transducer response was achieved when the pulse rise and fall times were approximately 10 ns or less, namely the timing of the pulse edges correspond to the natural expansion and contraction actions of the transducer material.

3.10. Modelling of the ultrasonic beam profile

In an attempt to derive the effects of reducing the amplitude of the excitation voltage, a mathematical model developed by Hutchins *et al* [Hutchins 1987] and Lockwood, Willette [Lockwood 1973] was implemented using the MATLAB software environment. Using the coordinate system described in Figure 3-20 the impulse response of a circular piston is calculated by:

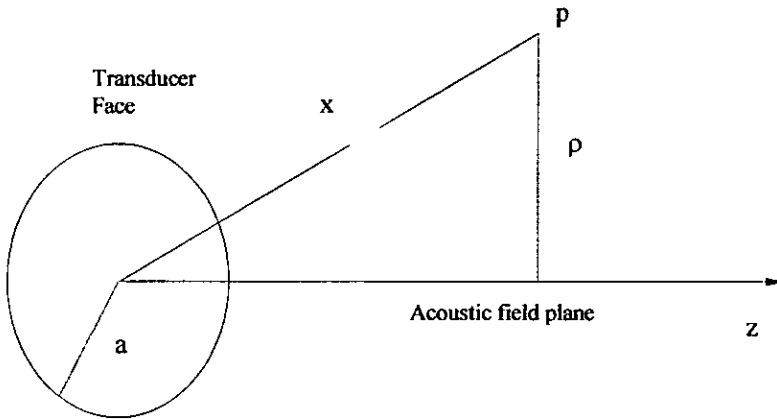


Figure 3-20 Diagram showing coordinates for modelling of radiation field

if $\rho < a$

$$h(x,t) = \frac{cUa}{\pi} \begin{cases} 0 & \dots\dots\dots t \leq t_1 \text{ and } t > t_3 \\ \lambda & \dots\dots\dots t_1 < t < t_2 \\ \cos^{-1} \frac{c^2 t^2 - z^2 + \rho^2 - a^2}{2\rho\sqrt{c^2 t^2 - z^2}} & \dots\dots\dots t_2 < t \leq t_3 \end{cases}$$

(3-30)

whereas if $\rho > a$

$$h(x,t) = \frac{cUa}{\pi} \begin{cases} 0 & \dots\dots\dots t \leq t_1 \text{ and } t > t_3 \\ \cos^{-1} \frac{c^2 t^2 - z^2 + \rho^2 - a^2}{2\rho\sqrt{c^2 t^2 - z^2}} & \dots\dots\dots t_2 < t \leq t_3 \end{cases} \quad (3-31)$$

where $t_1 = z/c$ $t_2 = [z^2 + (\rho^2 - a^2)]^{1/2}/c$ $t_3 = [z^2 + (\rho^2 + a^2)]^{1/2}/c$

The result $h(x,t)$ is in the form of a scalar velocity potential ϕ which has been plotted in figure 3-21. The acoustic pressure P is therefore found by differentiating the velocity potential with respect to time:-

$$p = -\rho_0 \frac{\delta\phi}{\delta t} \quad (3-32)$$

where ρ_0 is the density of the medium.

For the actual pressure to be calculated the excitation function must be convolved with the acoustic pressure therefore the final pressure at a given point within the acoustic field is given by :-

$$P(x,t) = -\rho_0 \frac{\delta[h(x,t)]}{\delta t} * f(t) \quad (3-33)$$

The impulse response has been calculated and some results are presented in Figure 3-21. Parameters for this example were $z = 0.25$, $a = 5$, $\rho = [0, 0.5, 1, 1.5, 2, 2.5, 3, 3.5, 4, 4.5, 5, 5.5, 6, 6.5, 7, 7.5, 8, 8.5, 9, 10]$ and time increments of 10 ns.

The impulse response reaches a maximum when making calculations that are inside the transducer diameter but quickly decay with the rate of decay increasing as the outer edge of the transducer is approached. At the boundary edge of the transducer and beyond the impulse amplitude is less than 50% and becomes broader as the distance ρ increases. On the transducer centre line the impulse response is a square step function and

although not shown here the step gets shorter as the distance from the transducer face is increased.

These results and the differentiation of these results match those detailed by Robinson et al [Robinson 1974] Using the convolution formula above the actual acoustic pressure for a given excitation function can be derived for each position in the acoustic field and by plotting the peaks of the resulting pressures a beam profile can be displayed.

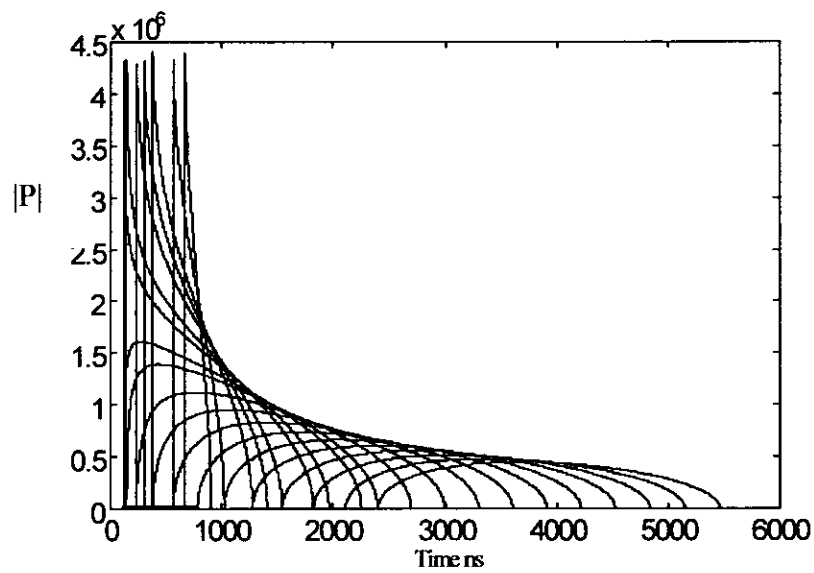
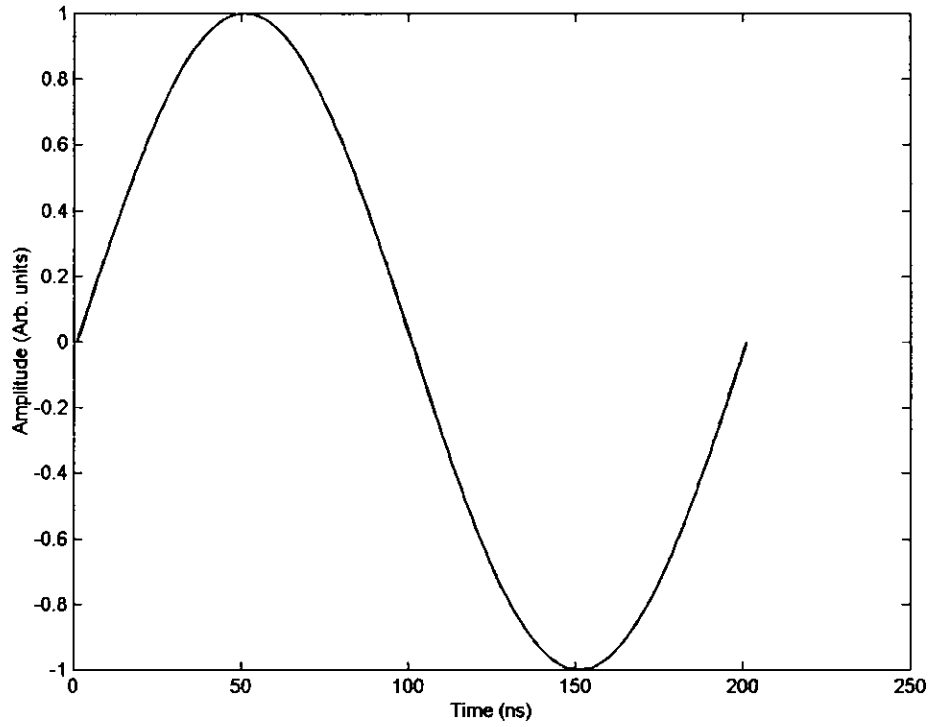
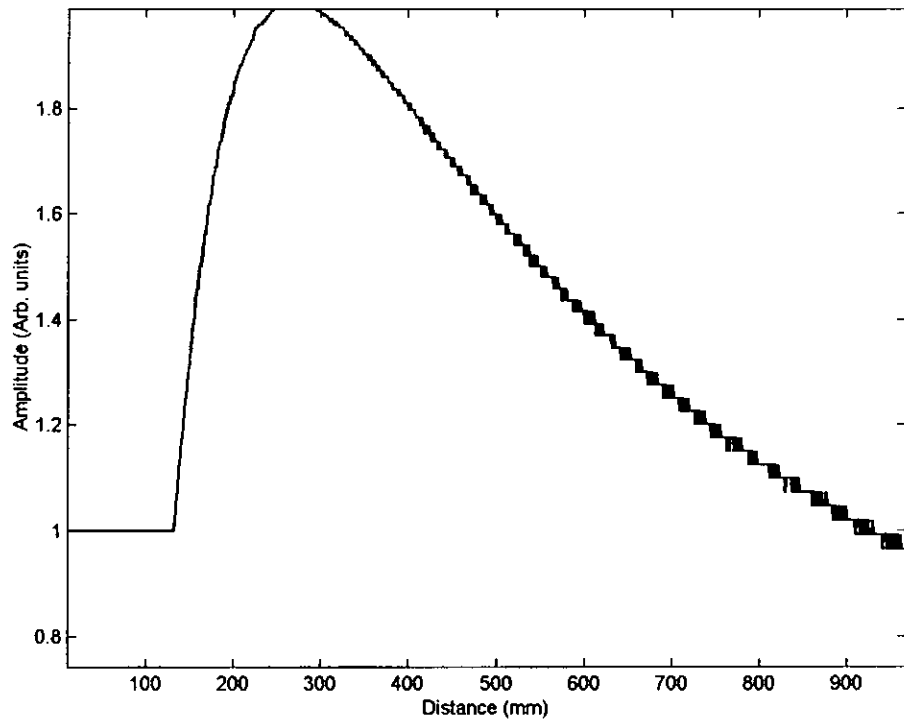


Figure 3-21 Calculated impulse response

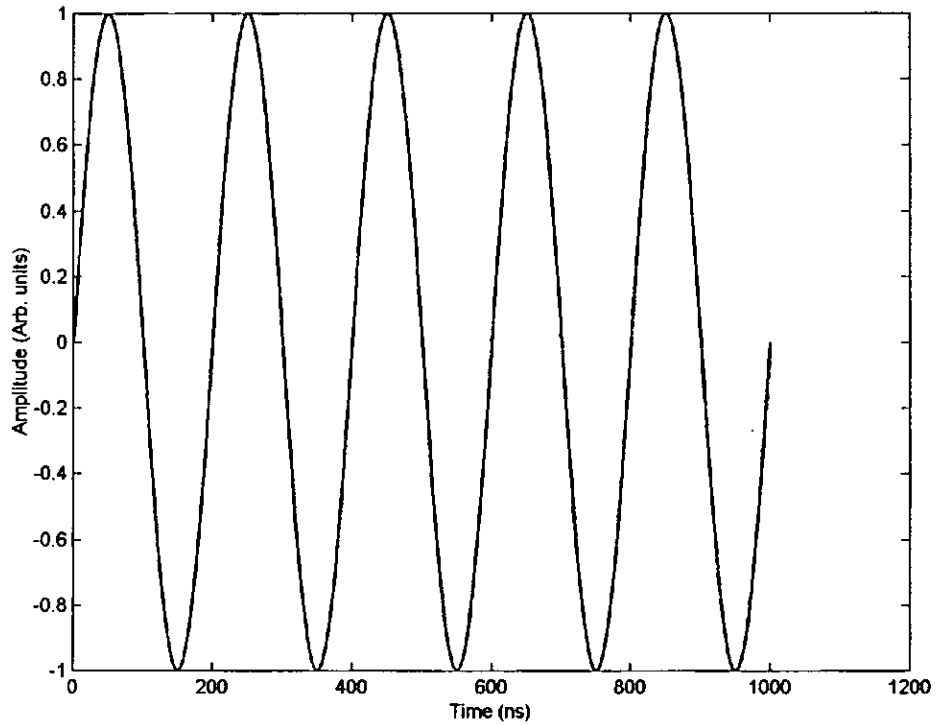


(a)

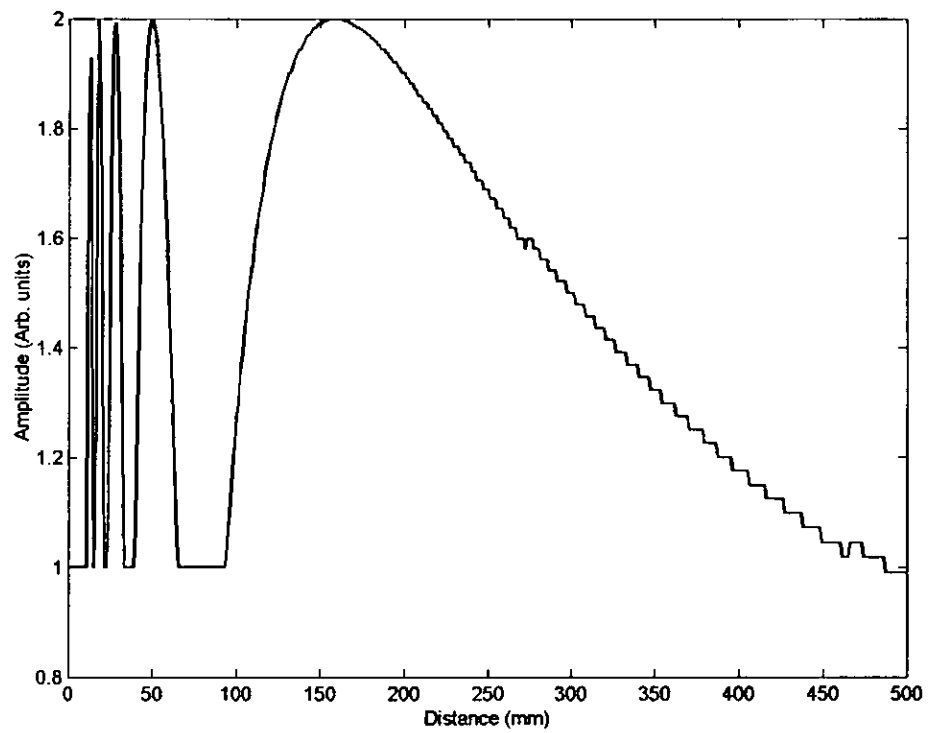


(b)

Figure 3-22 Results from the Matlab simulation of the Robinson et al calculation (a) single cycle transducer excitation pulse (b) pressure field for a 5 MHz single cycle excitation pulse.



(a)



(b)

Figure 3-23 Results from the Matlab simulation of the Robinson et al calculation (a) five cycle excitation (b) pressure field for a 5 MHz 5 cycle excitation pulse.

Figure 3-22(b) shows the pressure field for a single cycle excitation ultrasonic pulse and the boundary between the near and far fields is clearly shown by the sharp rise in amplitude. Comparing figure 3-22(b) with 3-23(b) it is evident that when the initial ultrasonic pulse contains more cycles the disturbance in the near field becomes more complex. It can also be shown that deviations from a sine wave pulse create very complex near fields [Hutchins 1987]. The conclusion drawn from this is that when the timing of the electrical excitation pulse is not coincident with the transducer centre frequency it affects the ultrasonic near field within the material. Hence as most of the inspection cases described previously are performed in the near field and that ultrasonic focusing can only be achieved in the near field it follows that optimum pulse characteristics are important for robust focusing and therefore defect detection.

3.11. Low voltage excitation.

By reducing the excitation voltage from the normal hundreds of volts to tens of volts the problems of producing fast rise time and controllable pulse shapes are greatly reduced and also allows smaller electronic components to be used. The disadvantage of reducing the excitation pulse is that there is a corresponding reduction in ultrasonic pulse energy, coupled to this the use of PVDF as the transmitter and receiver which for practical transducer construction purposes would be beneficial, results in a further reduction in pulse energy. However experimental results [Smith 1996] have shown that for the application described in the introduction it may be possible to produce ultrasonic signals of sufficient strength under these conditions.

One method of reducing the effects caused by low voltage excitation is to use a tone burst excitation voltage. Tone burst excitation causes the transducer to resonate at its natural resonant frequency and providing the tone burst timing matches the period of the transducers resonant frequency then on each subsequent excitation burst, energy will be added in phase to the reverberation of the transducer material thus increasing the amplitude of the reverberation and subsequently increasing transmitted ultrasonic energy. However the prolonged duration of the tone burst the ultrasonic

signals bandwidth reduces. Narrow band ultrasonic signals result in poor resolution particularly when inspecting thin materials or close to a surface, therefore over use of tone burst excitation would be detrimental. Low voltage experiments were carried out by connecting a Hewlett Packard function generator with tone burst capabilities directly to the transducer and observing the received signal on an oscilloscope. In the case of the PVDF experiments, some amplification was required therefore a commercial pulser / receiver system with variable pulse capabilities was used. When using the function generator for transducer excitation the pulse width could be set to match the transducers resonant frequency and tone burst generation could be used.

This experimental work was necessary to observe the natural response of a single element ceramic transducer when excited by a single spike and compare this response with various forms of tone burst excitation. Results showed that a three cycle tone burst had little effect on signal bandwidth but significantly increased signal amplitude. However in the case of PVDF material which inherently has a low Q factor and therefore broad bandwidth, tone burst excitation would reduce the bandwidth as the excitation time would exceed the natural reverberation of this material.

However as long as the bandwidth is not significantly reduced beyond the response observed for ceramic materials then tone burst excitation could be used.

3.12. Practical and Simulation Results

The effect of the excitation pulse on the resulting ultrasonic signal has been evaluated by modelling and practical experimentation. As stated previously the conversion of electrical energy to mechanical energy is at its maximum when the timing of the excitation pulse matches the period corresponding to the centre frequency of the transducer. Also the resulting signal amplitude is directly related to the amplitude of the excitation pulse. Fast rise time pulses create wide bandwidth ultrasonic pulses which is usually preferable in NDT. The limits to this are that in practice the conductive plating used to make electrical contact with the piezoelectric material will be destroyed if the voltage applied is too great and the

piezoelectric material can in some cases be damaged by high voltages. Fast rise time pulses that are not affected by the applied load are difficult to achieve using standard electronic components as high voltage MOSFETS generally have slow switching times which is influenced by the applied load.

In order to confirm the feasibility of reducing the excitation voltage amplitude for ultrasonic inspection of carbon fibre composite material, experiments were carried out using a commercially available ultrasonic system, a standard 5 MHz PZT transducer and a PVDF, sheet 110 μm thick. An ultrasonic excitation pulse of $\pm 15\text{V}$, and an amplification factor of 5 dB were used, for the experiment.

As previously calculated by Silk [Silk 1984] the received signals from the commercially available PZT transducer were significantly larger in amplitude than the PVDF signals when transmitted through the same thickness of material. This is due to PVDF having a relatively low electromechanical coupling factor, which resulted in a transmit / receive efficiency five times less than that of PZT-5A. Another factor to consider is that the pulser / receiver was designed for high voltage ceramic transducer excitation / amplification which, when used with PVDF material, reduces sensitivity. The signals displayed in Figure 3-24 show the backwall echoes from 5 and 10 mm of carbon fibre composite material, and the signal amplitude is approximately 200 and 100 mV respectively. Figure 3-25 shows the corresponding signals obtained from PVDF material. The signal amplitude is significantly reduced in comparison with the PZT result, with the backwall amplitude being approximately 40 mV and 20 mV respectively for the 5 and 10mm material thickness. In comparison with the computer simulation results, the actual signal amplitude is significantly less, and is due to the attenuation of ultrasound in carbon fibre composite, which had not been included in the computer simulation model. Nevertheless, it can be clearly seen from the computer simulation results (Figures 3-26 and 3-27) and the experimental results, that the amplitude response using PZT is approximately five times greater than that obtained using PVDF.



Figure 3-24 Experimental results using PZT material with ± 15 volts excitation: (a) 5 mm and (b) 10 mm of Carbon Fibre Composite

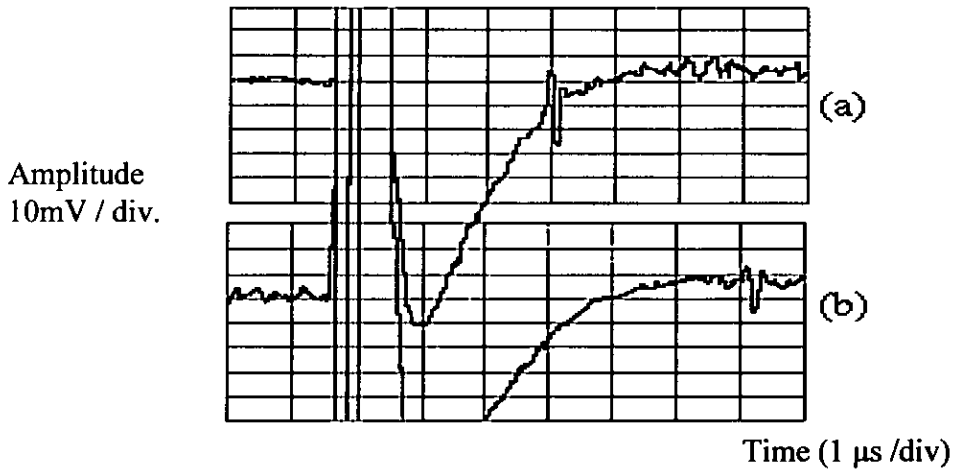


Figure 3-25 Experimental results using PVDF material with ± 15 volts excitation: (a) 5 mm and (b) 10 mm of Carbon Fibre Composite.

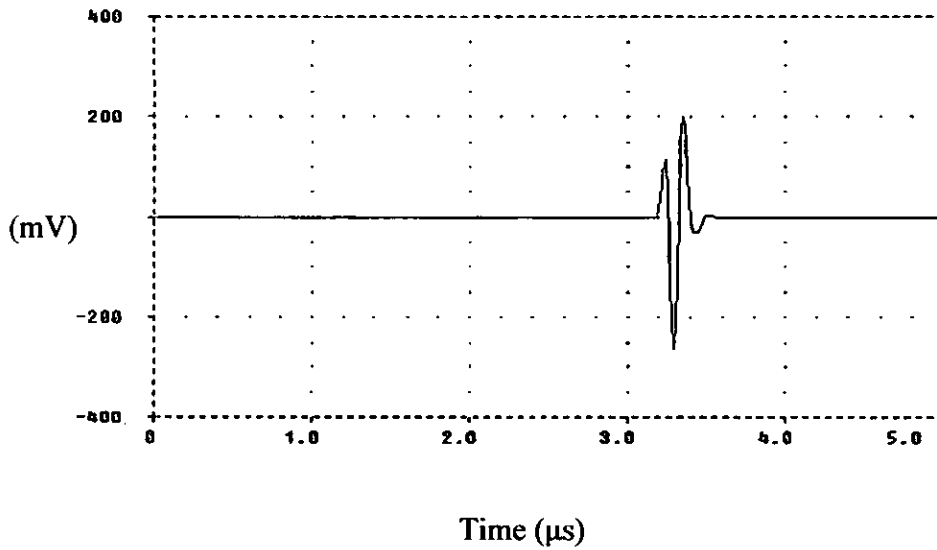


Figure 3-26 Pspice simulation result for PVDF model, 30 Volt excitation,

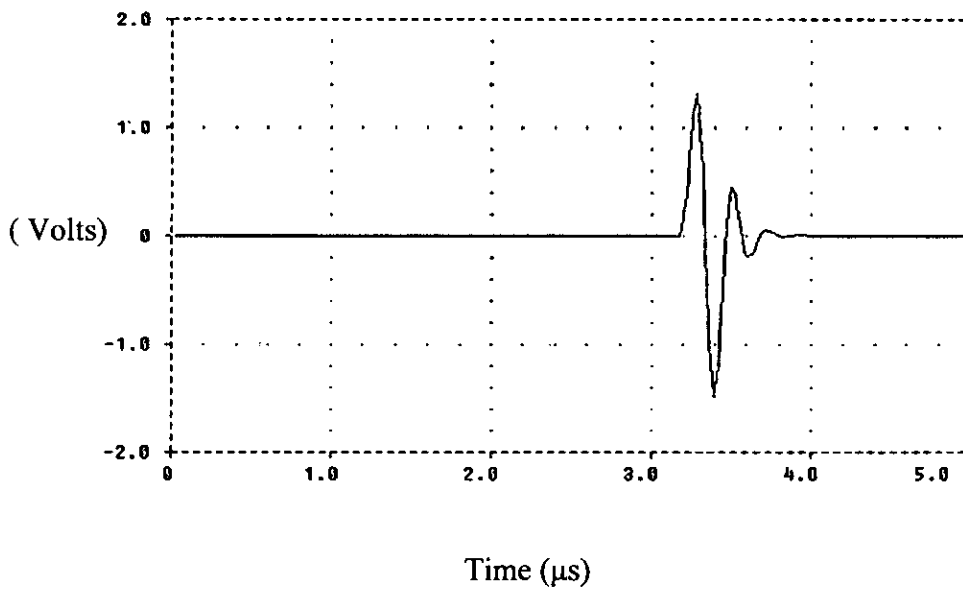


Figure 3-27 Pspice simulation result for PZT-5A, 30 Volt excitation

3.13. Essential parameters for robust defect detection

From the experimental results it can be deduced that a compromise has to be sought between high sensitivity and good near surface resolution. In the case titanium diffusion bonding inspection the bondline is 1 mm from the surface and the defects are in the order of 10 to 15 μm in diameter a

compromise is hard to find. Tober et al [Tober 1986] concluded that high frequency ultrasound >35 MHz would be the only practical way to detect large voiding at the bondline and that micro voids could only be assessed by micrographic sectioning. Tober [Tober 1986] also reported that scanning acoustic microscopy may reduce the minimum detectable defect. The practical implementation of very high frequency over very large and complex shapes is hindered by the increased absorption of high frequency ultrasound in water and the achievable resolution and accuracy of a large area complex geometry scanning system. The results presented here however demonstrate that acceptable defect detection can be achieved at lower frequencies (25 MHz) providing the correct approach is undertaken. The mathematical and experimental evaluations have clearly shown that the only way to achieve both good resolution and high sensitivity is to optimise the transducer geometry in terms of focus gain by increasing transducer diameter which then permits a slight increase in the damping factor to achieve high resolution. The modelling also indicates that matching the excitation pulse to the resonant frequency of a wide band transducer slightly increases sensitivity without impairing resolution. Long pulse lengths will however impair the near surface resolution and pulses that are too short will reduce sensitivity. For titanium diffusion bonding inspection therefore a high resolution, large aperture, strongly focused transducer with matching pulser parameters is essential for adequate defect detection. The loss in sensitivity by high damping cannot be overcome by optimised pulser parameters. Strong focus is the only way to overcome this problem, however as demonstrated previously strongly focused transducers are highly dependant on surface normality and care must be taken to ensure that normality is maintained throughout the inspection.

In the case of Carbon fibre composite inspection the requirements and therefore the interpretation of the analysis differs. Carbon composites are inhomogeneous and anisotropic and therefore create different ultrasonic responses than homogeneous isotropic materials such as titanium. Typical composite lay up patterns result in a material that can be considered quasi isotropic. However from an ultrasonic point of view a single ply unidirectional laminate could be considered homogenous and orthotropic

only if the ultrasonic wavelength is considerably larger than the individual permissible features inherent in a composite material lay up [Barrowcliff 1988]. If the material contains large voids or the ultrasonic wavelength is larger than the inherent features then the material should be considered heterogeneous. Work by Davey, Curtis [Davey 1997] and Stone [Stone 1976] concluded that a frequency of 5 MHz would be sufficient for successful defect detection without disturbance from the natural inherent features.

Modern composite manufacturing methods however place an extra burden on the ultrasonic inspection as new ancillary materials that aid the curing process have acoustic impedances close to that of the base material and the significance of porosity becomes more of a concern as structures are optimised for strength to weight ratios. In this case the requirement is to differentiate from the natural responses of the fibres and the resin matrix and defects that have similar ultrasonic responses. Attenuation values caused by surface roughness have the same ultrasonic attenuation effect as low volume porosity (<3%) [ASNT 1991]. Increasing the frequency in this case would result in both the inherent permissible features and porosity being detected simultaneously with the operator unable to differentiate between the two.

Current automated production inspection practices utilise narrow band transducers and excitation for detection of all types of composite defects. Porosity is detected as an attenuation of the received signal and is usually identified by comparison with a reference specimen and the general attenuation of the panel. Individual pores are not resolved. Inclusions with matching impedances to the base material are detected using the same ultrasonic methodology but are identified by the out gassing effect at the edge of the inclusion which results in a line of higher attenuation around the edge of the defect. From the work performed here it can be demonstrated that the reliable detection of these more difficult defect situations could be enhanced by the correct use of transducer and ultrasonic parameters. Narrow band ultrasound does have the advantage of being highly responsive to a particular defect but the problems associated with ensuring that the correct frequency is chosen for each defect type and that

such frequencies generated correctly, significantly reduces the applicability of this approach. Wide band ultrasound will tend to indicate all features in the material and therefore would over inspect the component and produce false indications. The solution obtained from this analysis is that the introduction of PVDF transducers would enable wide band inspection but would significantly reduce sensitivity. Therefore, coupled to the use of PVDF slight focusing should be adopted. This would overcome the loss in sensitivity and would also increase resolution thus aiding the detection and interpretation of discreet defects. The use of PVDF must be carefully controlled however as this material has a high static capacitance that requires the driving source to supply extra current [ASNT 1991]. Long cable lengths introduce a further capacitance that adds to the already high static capacitance of the transducer material and therefore requires extra current from the pulser. Many pulsers are not capable of supplying high currents and therefore unsuitable to this application. Defect detection in carbon fibre composites would be significantly enhanced by the introduction of wide band inspection. This would however create an extra burden at the interpretation stage and therefore wide band methods must include techniques for isolating the detrimental indications from those inherent in the material. Modern data acquisition systems cater for multiple measurements from one pulse and also provide many pulses per scan point. There is therefore the possibility to tailor measurements to specific defects and use digital image processing methods to extract the features of interest.

Enhancing the ultrasonic inspection for carbon fibre composite as described above cannot be reliably introduced without careful control. Image processing techniques are highly reliant on repeatable data and again careful control of the signal transmission and detection is necessary.

3.14. Current state of the art ultrasonic systems

3.14.1. Through transmission squirter system

In the aerospace industry, large area composite components that require ultrasonic inspection during the production cycle are generally scanned by a mechanical manipulation of two ultrasonic transducers and automated electronic data capture under computer control.

Two water jets are aligned to face each other and ultrasound is transmitted down the column of one water jet, which is then transferred to the facing water jet where it is received by a similar receiving transducer. The component is then placed centrally between the two jets which results in the ultrasound being transmitted through the volume of the component and received at the opposite side. Ultrasonic attenuation measurements are then made electronically which determine the components acceptability for use. The transducers are manoeuvred by a stepper motor manipulator which as a minimum would consist of x and y axis. An attenuation map is constructed by “thresholding” the received ultrasonic signal amplitude and plotting the result in either grey scale or colour for each scan position on the component. The lateral resolution of the scan is governed by the minimum allowable defect size and it is usual to ensure that the scan resolution is at least half the minimum detectable defect size, thus ensuring that at least two pixels in the image contain the defect indication. The preferred C-scan implementation is a raster scan where the majority of the motion is along the major axis of the component and the indexing is at 90 degrees to this is.

3.14.2. Multi axes manipulators

During ultrasonic inspection the transducers have to be kept normal to the surface so that good transmission of ultrasonic longitudinal waves is achieved. On relatively flat components this is readily achieved by x,y axis manipulation that can be driven by stepper motors which may or may not have feedback encoding. However, for complex shape components, further axes have to be added to the manipulator so that transducer normality can

be maintained. With the addition of multiple axes comes the added complication of ensuring that each axis can be accelerated and decelerated at the correct rates in order to maintain transducer normality. Motors without positional feedback are not capable of maintaining normality when multiple degrees of freedom are used because the calculation and prediction of each axis position at any one point in the scan cannot cater for mechanical error and potential error in motor position. The result of attempting complex geometry scanning without precise encoding of the motor position would be gross misalignment of the two transducers hence attenuation of the ultrasonic signal resulting in severely impaired defect detection.

The systems used for the experimental work were designed and manufactured by Ultrasonic Sciences Ltd. The motion controller in these systems is the PMAC manufactured by Delta Tau. The PMAC is a high speed motion controller with built in hardware look-ahead and inverse kinematic algorithms. Look-ahead optimises the motion path by automatically adjusting the profile acceleration and velocity whilst the inverse kinematics solves the joint position calculation as the scan is being performed. This function therefore allows the software programmer to work in Cartesian coordinates and maintains the tool tip velocity along each scan path [Delta Tau applications notes].

Whilst look-ahead and inverse kinematics reduce the programming burden, motor parameters still have to be determined and set correctly in order to ensure probe normality. Reliance on the manipulator to maintain normality is paramount to good defect detection especially in the case of titanium diffusion bonding inspection where high gains are used and signals from the front and back surface are saturated. In these cases the amplitude of signals reflected from bondline imperfections can be 32 dB smaller than the transmission signal, therefore, ensuring adequate transmission by monitoring the returned signal strength is not possible due to the limited dynamic range of the measuring system.

Using dc servo motors for accurate positioning involves calculating the number of encoder lines the motor must rotate through in order to get to its commanded position. The motor controller will apply power to the motor

and the motor will rotate. It will accelerate at a predetermined rate until maximum speed has been reached or it has achieved its position. As the motor gets close to its command position the controller will decelerate the motor. The actual position that the motor comes to rest at will not be the command position but will include some error depending on motor parameters and the mass the motor is moving. In positional mode the controller will then reverse the motor and try to compensate for positional error. The resulting trajectory will be as depicted below.

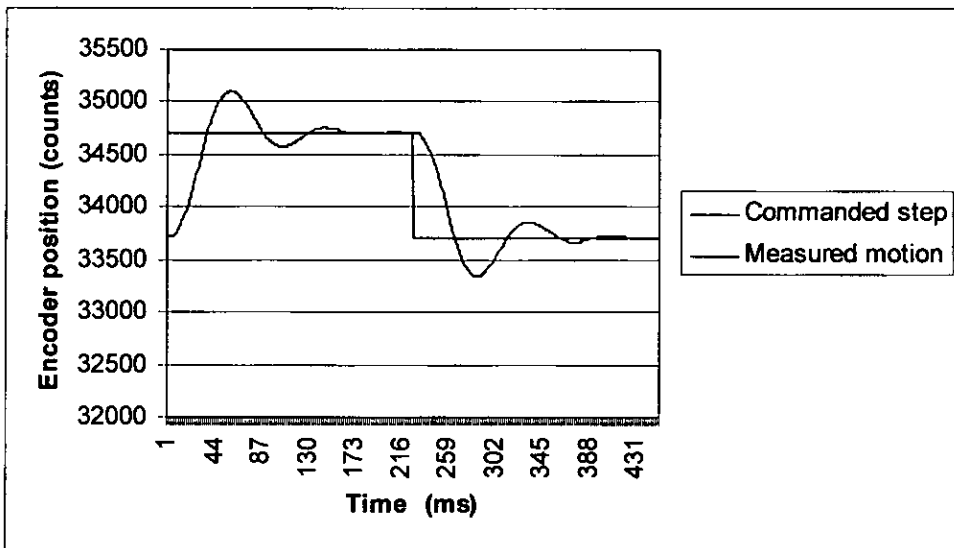


Figure 3-28 Plot describing overshoot of an undamped servo motor scanning system to a step command.

If the above motion occurred at every point in an ultrasonic scan an erratic scan pattern would result and data capture would be repeated for several points. Whilst software algorithms could be designed to sort the data into logical order the inspection process would be very time consuming. Ultrasonic scanning is therefore performed by moving the transducer across the surface of the component with a continuous motion.

The motion controller therefore has to accelerate all motors at the start of each scan line and maintain a smooth transition along the scan path. Look-ahead algorithms are implemented on the motion control board which calculate the real position required by each motor for the current and subsequent time periods. These positions are then used to individually alter the speeds so that the required position is achieved. When look-ahead is

applied the actual motion will initially head for a command point but as it approaches the motion will then change to the next command point and therefore the actual trajectory takes a course similar to the command trajectory but with each corner rounded off.

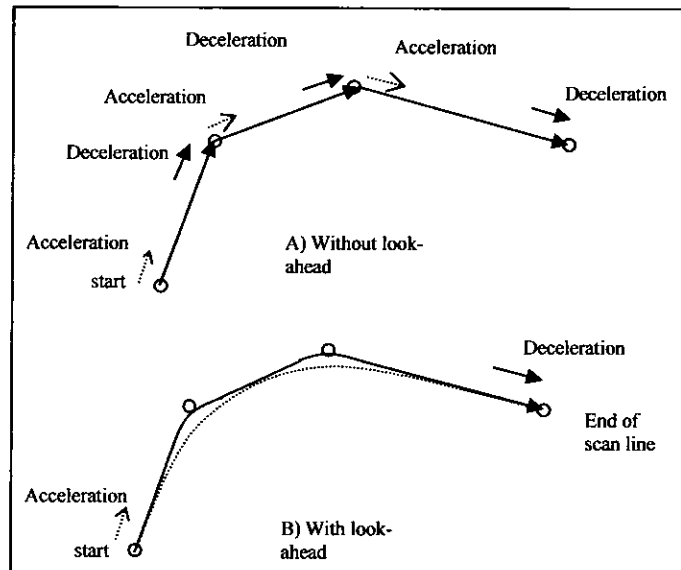


Figure 3-29 Typical motion paths for A) command path without look-ahead and B) with look-ahead

With look-ahead disabled the trajectory will take the path shown in A) above. Here each trajectory position will be achieved within the set error limit. The controller will accelerate away from and decelerate as it approaches each command position. With look-ahead enabled the trajectory will be similar to B) where the path deviates from the command positions but the motion is continuous. In this case the amount of deviation from command position is dependant on the permissible positional error parameter and the values used in the proportional integral derivative filter (PID loop). Accelerations of individual axis are governed by the trajectory. With this type of operation the permissible positional error governs the maximum speed and there is a trade between scan speed and positional accuracy.

Allowable position errors are determined from the normality requirement and the degree of curvature found on the component under

inspection. The motor filter parameters (PID loop) need to be tuned to ensure system stability when each axis is accelerated at its maximum velocity. A servomotor system will become unstable if there is a delayed reaction to a move to position command when there is high gain fed to the motors. This occurs because the controller will apply a current to the motor and expect a change in position. If there is lag and the controller detects little or no change in position i.e. the error between expected position and actual position is large it will increase the current in an attempt to correct the error. If this occurs in a system with high gain the increase in current will be large and therefore a rapid change in position and an overshoot error will result. The controller will sense the positional error due to the rapid current change and immediately reduce the current to compensate. A negative effect i.e. rapid deceleration will occur which will in turn be detected and compensated for by a rapid increase in current and so on. It is therefore necessary to apply the correct amount of current at the correct time within the motion cycle. For instance high current would be required during the initial acceleration as friction and the mass of the axis has to be overcome but less current is required as the motor reaches its maximum velocity. It can be seen then that the controlling algorithm for motion control is complex as rapid changes in the drive current required when the current applied to the motor is not sufficiently long to cause an effect on the velocity and therefore the velocity change is not sufficient to make a change in position, result in an unstable movement and possible oscillation.

To overcome this effect most motion controllers have a digital proportional integration and damping filter (PID loop). This filter is fed three constant values namely the proportional gain (K_p), proportional damping (K_d) and the integrator (K_i). All three parameters are combined to produce an output to the motor amplifier which feeds the motor. The accuracy and smoothness of the motion will depend on how the K_p , K_i and K_d parameters are tuned. In modern motion control systems software tools are provided that automatically tune the digital filter parameters and interfaces are available to plot the errors and effects of altering each value. A complete system analysis is possible mathematically but as these tools are available and when used properly provide good tuning results such a

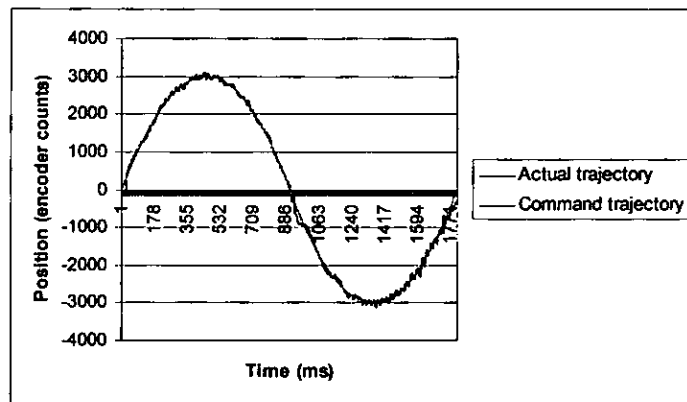
derivation is not necessary for this work. However a simple explanation of the underlying principles is given in order to establish the effects motion stability can have on defect detection. The PID loop in an ideal closed loop system takes the error i.e. in this case the required position minus the actual position and calculates a new value according to the following:-

$$u = K_p e + K_i \int e dt + K_d \frac{de}{dt} \quad (3-34)$$

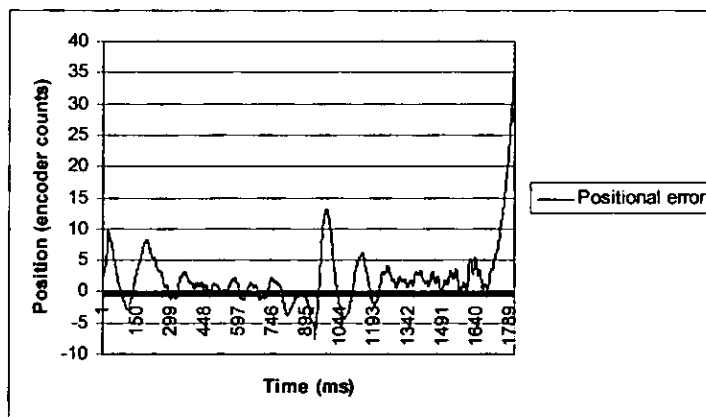
From the above equation it can be seen that the new signal output is now equal to the proportional gain times the magnitude of the error, plus the integral gain times the integral of the error, plus the derivative gain times the derivative of the error. This new signal will therefore be used to correct the positional error and a new error value will be produced and the process will be repeated. The proportional gain (K_p) will have the effect of reducing the response time i.e. the lag between a signal being generated and the motion being performed and will contribute to the position accuracy. The integral gain (K_i) will further improve accuracy and in a steady state actually eliminate error but will make the transient response worse. The derivative gain (K_d) has the effect of reducing overshoot, improving the transient response and increasing the stability of the system.

Figure 3-30a is a plot of a parabolic move commanded on one of the x-axis and figure 3-30b is a plot of the positional error experienced when this move was performed. From 3-30b it can be seen that the most significant error occurs when the axis has to change direction and that once the axis has accelerated there is little positional error. The opposite X-axis however does exhibit some significant positional error for the same parabolic move (figure 3-31b) when the axis is driven in the negative direction. This error is due to a mechanical problem but it does result in significant loss of ultrasonic signal and can be seen in the scan of the inclusion panel shown later in this chapter where alternate lines in the scan vary in attenuation. In figure 3-32 the proportional gain has been changed from 700000 to 100000

and integral gain, velocity, and acceleration feed forward parameters have been optimised to produce a smooth parabolic move with small positional error. The maximum error on this axis when optimum parameters are used is + 1.75, -2 encoder counts. The resolution of this particular encoder is 0.012 mm therefore the positional error is +/- 0.024 mm. In comparison the positional error shown in figure 3-30b is +13, -7 counts i.e. an overall error of 20 counts which equates to +/- 0.24 mm. The excessive error shown in figure 3-31b is 260 encoder counts which equates to 3.12 mm which if left would result in an unacceptable attenuation of the ultrasonic signal. The plot of the trajectory when performing a scan (figure 3-33) shows the positional error of the y axis to be approximately +/-1 mm with the error only occurring when there is a sharp change in direction when the PID loop is tuned correctly.

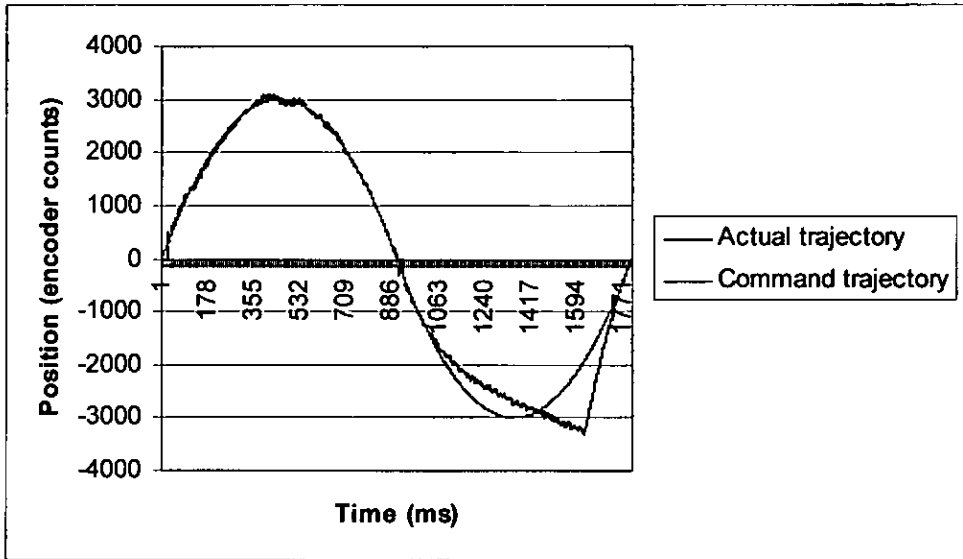


(a)

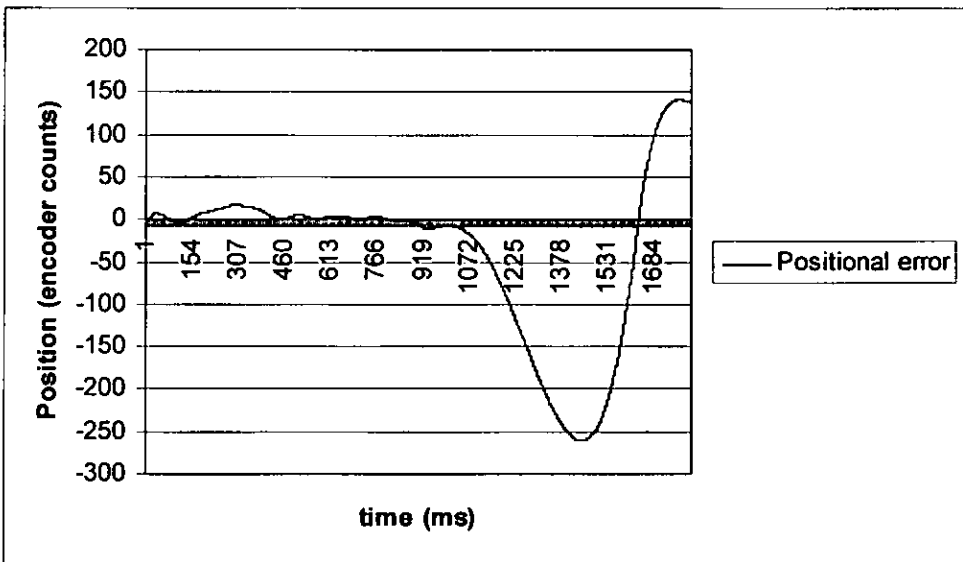


(b)

Figure 3-30 a) PID loop command trajectory and actual trajectory plotted against time and b) the positional error for the trajectory in (a)

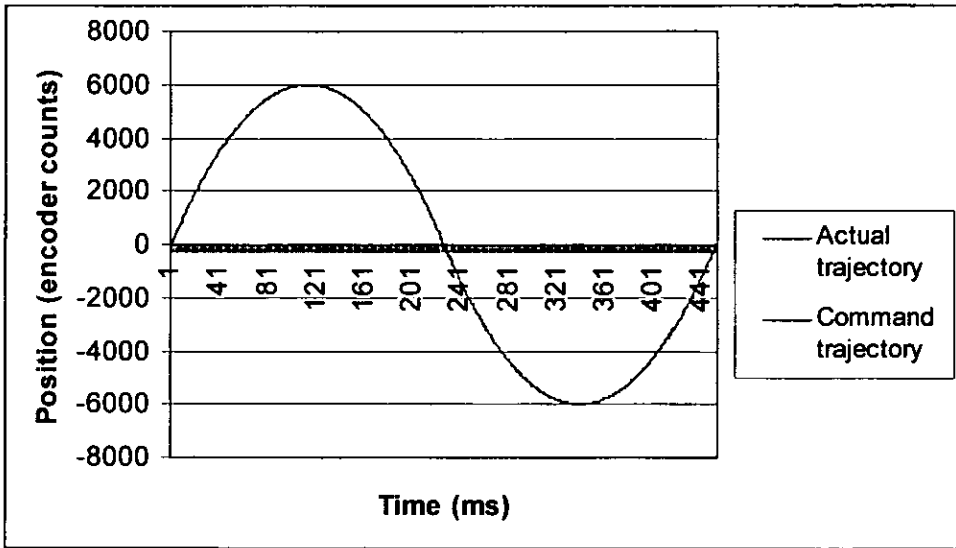


(a)

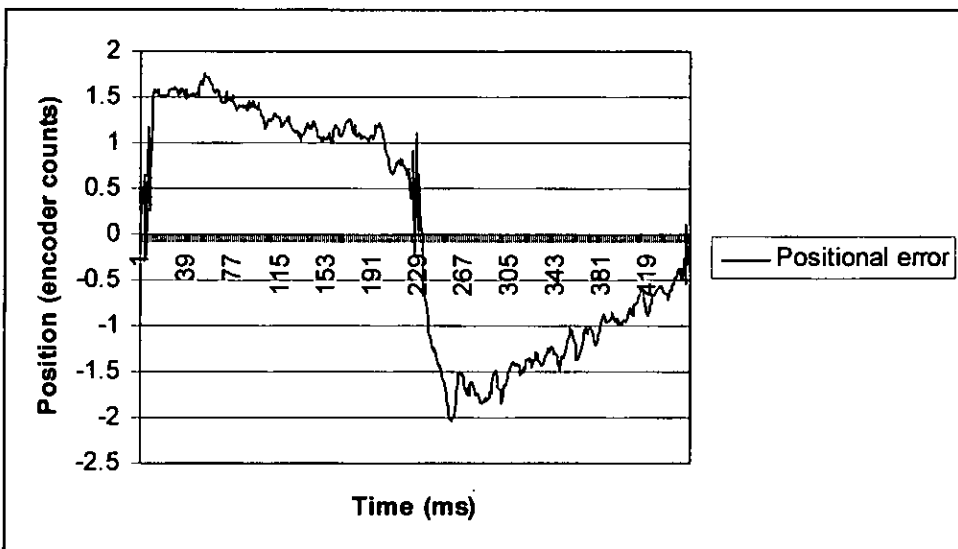


(b)

Figure 3-31 A poorly tuned PID loop with a) plot of actual and command position during a parabolic move b) positional error

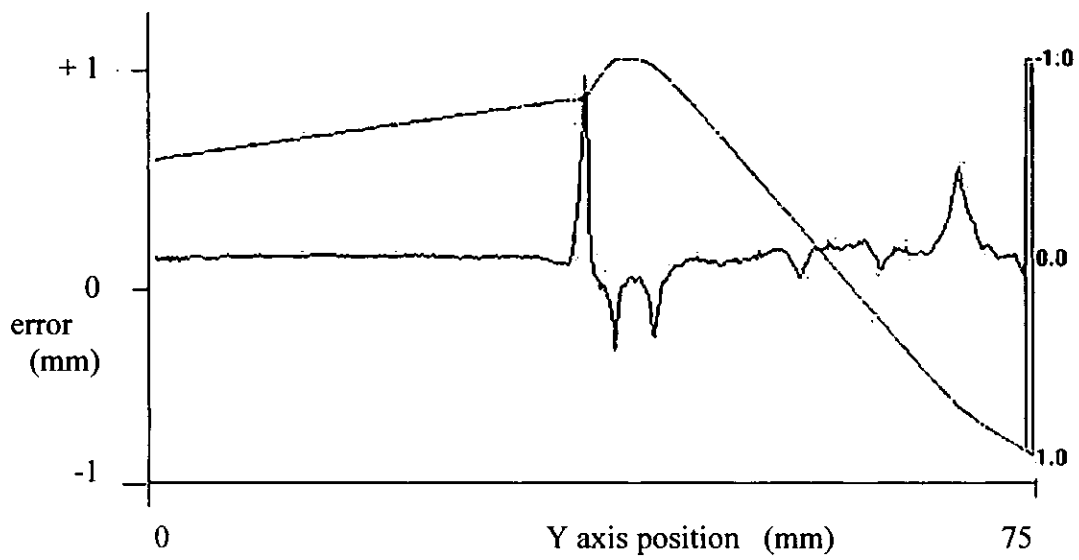


(a)

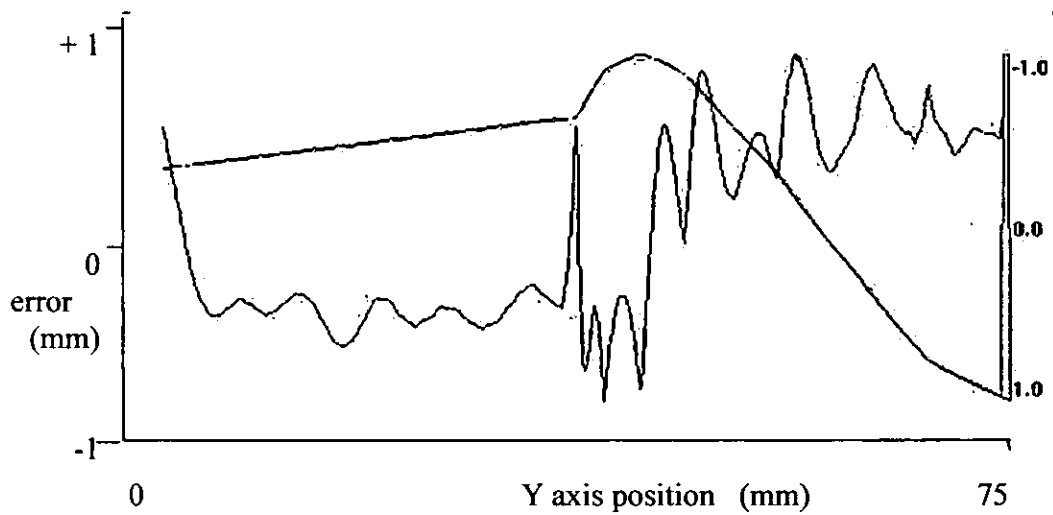


(b)

Figure 3-32 Plots of (a) the command trajectory and actual trajectory (b) the positional error, for a correctly tuned PID loop.



(a)



(b)

Figure 3-33 Scan trajectory and positional error for Y right axis (a) optimum PID loop (b) poor PID loop

3.14.3. Ten axis complex geometry scanning system

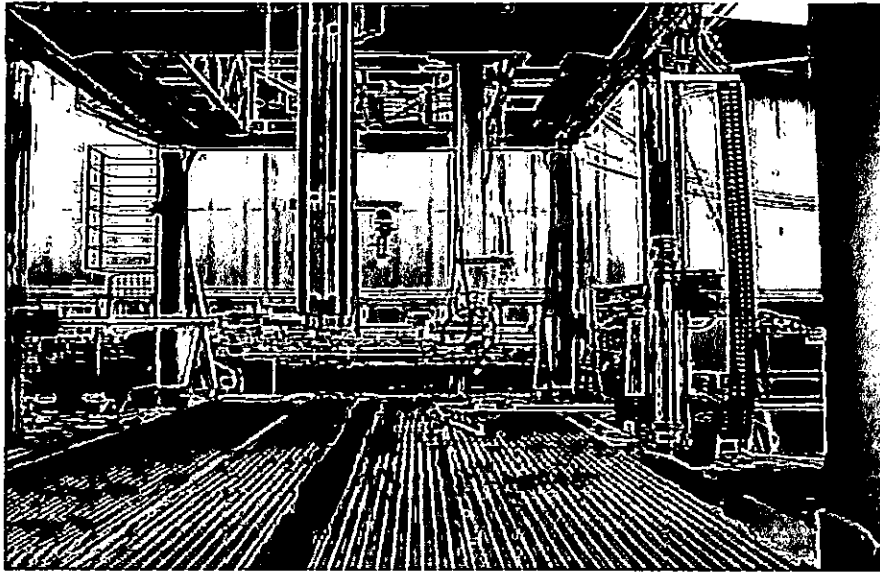


Figure 3-34 Picture of the 10 scanning axis and 5 axis part location system installed at BAE SYSTEMS

Figure 3-34 above shows a ten axis complex geometry scanner designed and manufactured by Ultrasonic Sciences Ltd (USL) and installed at BAE SYSTEMS. It is designed to give the optimum flexibility in terms of complex contour following and as such can manoeuvre through angles of ± 60 degrees in a volume of 5 x 3 x 2 metres. The scanning system has been primarily designed for through transmission scanning but the data acquisition modules and software do cater for simultaneous pulse echo operation. A five axis part holding fixture has also been incorporated. This consists of two stepper motor driven axis which allow movement in the vertical Z direction and the horizontal Y direction which are fixed at one end of the scanning envelope and a further three stepper motor axis that provide Z, Y and X movement. This configuration is capable of locating all components by making use of two tooling holes that are in each component. Constant water flow is maintained as large angular changes are approached by the use of a water flow monitor which feeds back to a dc servo motor that drives the pumping system. A reduction in water flow due to a positive angle will therefore be indicated to the motor which in turn will increase its speed to compensate.

The angular tip movement is physically restricted by the position of the x tip axis motors and the water supply pipes which collide at angles larger than 60 degrees. Large tip angle displacements would not be achievable if the two X axis gantries were not independent. Many modern complex geometry scanner designs use two bridge movements in the X axis and offset all other axis so that +/- angular displacements can be achieved. This arrangement restricts the angular displacement but does help maintain rigidity and hence positional accuracy. The USL system has independent X axis for each transducer and therefore can accommodate large angles but does suffer from probe misalignment caused by differences in the mechanical tolerances of each side of the scanner. To overcome this a compensation table for the complete rhomboid has been developed and the positional error of each axis has been measured and recorded at 100 mm intervals throughout the entire scanning volume. The error values are then software interpolated and the result used as an offset to the command position during scanning in order to maintain probe alignment. Tip axis compensation is also performed and interpolated in the same way. The result of this compensation process is a scanning system that is very flexible and accurate.

3.14.3.1. Analysis of compensation method

Reliable defect detection can only be achieved if scanning systems are accurate and repeatable both positionally and ultrasonically. The results obtained from the compensation method incorporated into the complex scanning system can be used to determine the maximum error and the accuracy of the measurement technique. The following analysis determines the measurement error and the effect the compensation error will have on the ultrasonic transmission and reception.

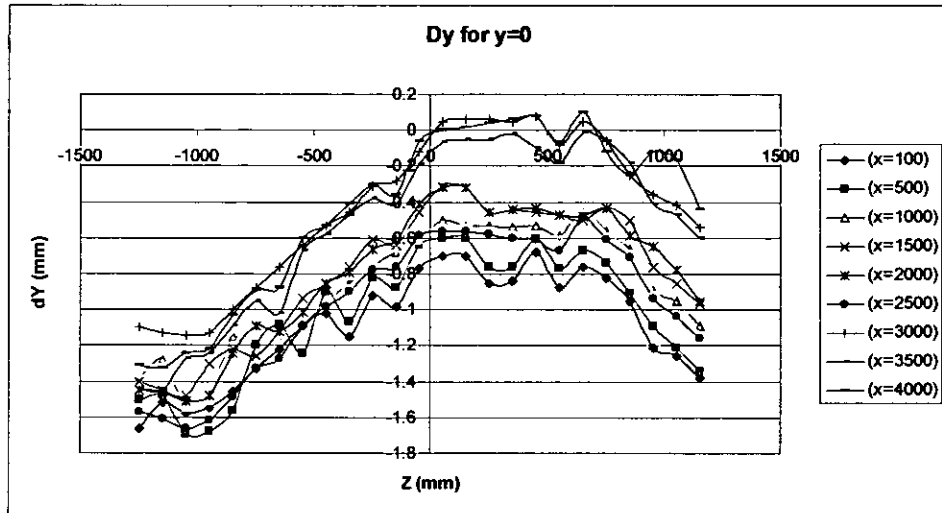


Figure 3-35 Compensation values dY along the vertical Z axis. Separate plots for positions along the X axis.

The plot above shows the amount of compensation required in the y axis position at $Y = 0$ as the Z position is increased. Each line plot represents a change in the X axis position. From the results it can be seen that the maximum error is around 1.8 mm which reduces as the z zero position is reached. Also the error plot is relatively the same throughout the whole X axis plane. A maximum error of 1.8 mm is considered very good and is relatively easy to compensate for.

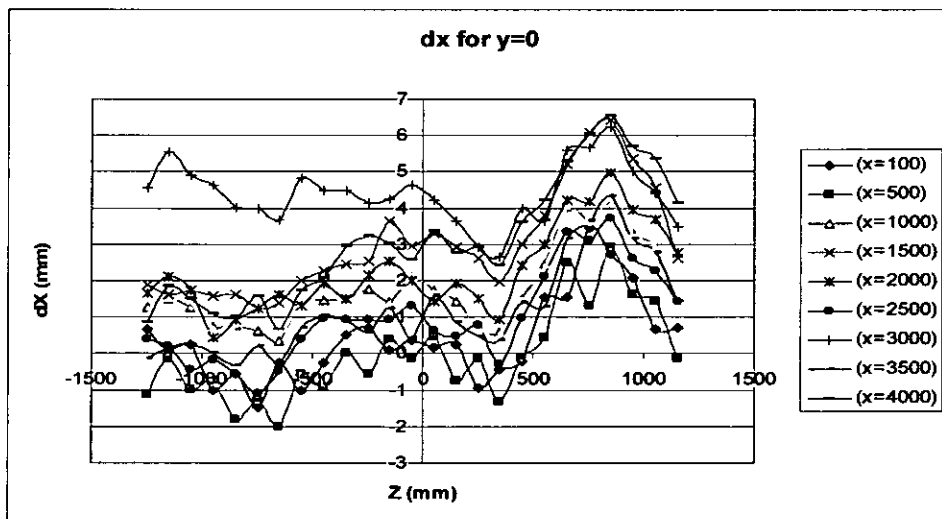


Figure 3-36 Compensation values dX along the vertical Z axis. Separate plots for positions along the X axis.

The plot of the X axis error above highlights a large error when the scanning arms are at 3000 mm along the X axis and also a significant increase the amount of compensation is required when the arms are lifted to 850 mm in the z direction for all values of X. Investigation of these features has identified a fault with the rack and pinion on the X axis at 3000 mm and insufficient shimming on the z-axis around 850 mm.

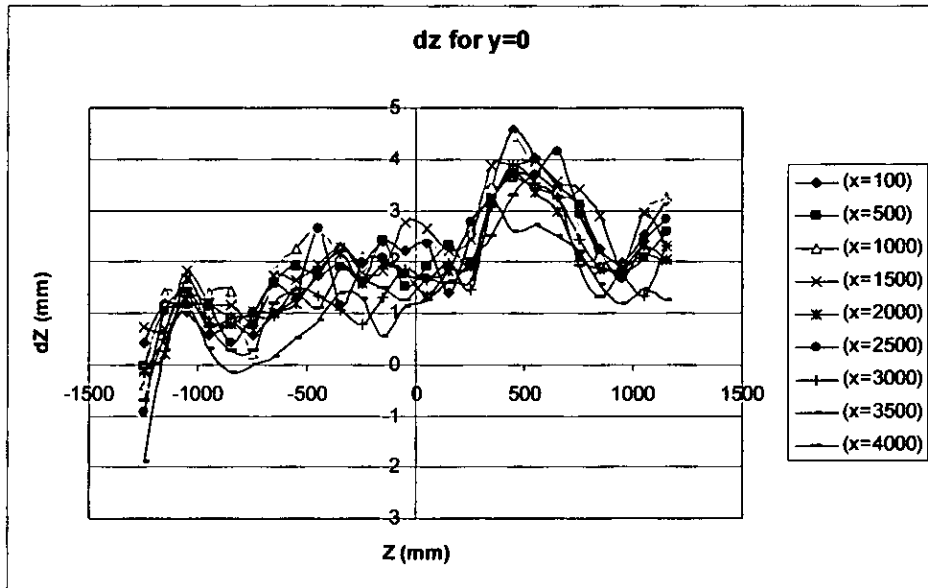


Figure 3-37 Compensation values dZ along the vertical Z axis. Separate plots for positions along the X axis.

The Z axis compensation shown above is similar to the plot for the X axis where until 500 mm the compensation is around 1 to 2 mm. Beyond 500 mm however the amount of compensation required along the z axis increases and finally reduces as the axis near the z axis limit. The increase in error here is less than that found on the X axis above but does suggest that there is a small amount of twist on the vertical Z axis that is causing significant amounts of compensation in both X and Z.

Control software has been developed to provide an automated means of acquiring the compensation data. The two transducers are driven to each position in the compensation table and then one transducer is swept in X, Y, and Z across the facing transducer while the ultrasonic amplitude response is recorded. The position where the maximum amplitude occurs is

considered to be where the transducers are best aligned. The difference in X, Y, and Z between the command position and the position where the maximum amplitude occurs is used for the 'deltas' in the compensation table. The accuracy of this compensation measurement method can be determined by analysing the oscillation between measurements in a relatively good area of the scanner. The plot below shows the error in the X axis when the Y arms are positioned at 600 mm. In the negative Z portion of the plot there is a general oscillation between each measurement which suggests that the measurement technique is not totally reliable. The portion of the line highlighted in blue is the maximum oscillation experienced within the whole scan envelope and represents an error of 2.16 mm. However, at this point in the compensation there is a trend towards a positive increase in the compensation and therefore the 2.16 mm cannot be treated as all measurement error as it includes a compensation contribution. An average of the amount of oscillation between Z = -950 mm to Z = -250 mm yields a value of 1.4 mm. The measurement accuracy for X axis compensation is therefore regarded to be 1.4 mm in the worst case.

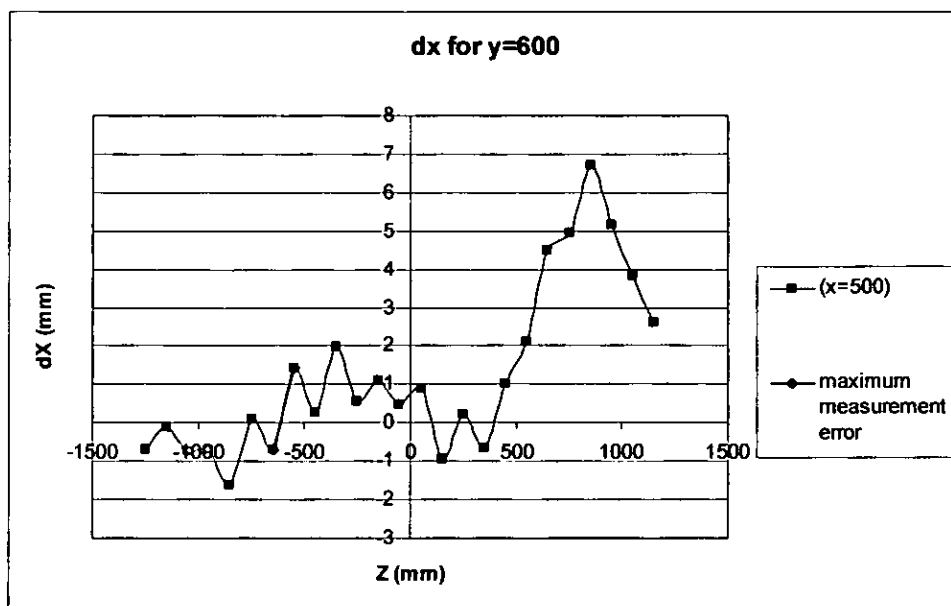


Figure 3-38 Plot of dX compensation at X=500 mm. Shown to highlight the oscillation and therefore the potential limit to the measurement method.

Having determined the error in the compensation measurement technique a simple analysis of the attenuation of the ultrasonic signal due to misalignment can be performed. The water jets used to couple the transmitted ultrasound to the reception transducer were 6 mm diameter. Misalignment of the water jets would reduce the contact area where the two water jets meet. Assuming that the amount of ultrasound transmitted is proportional to the contact area of the water jets the graph below would represent the amount of ultrasonic attenuation that would occur from inaccuracies in the alignment process. Given a compensation error of 1.4 mm and a 6 mm diameter water jet the calculated deviation in ultrasonic transmission would be around 6 dB.

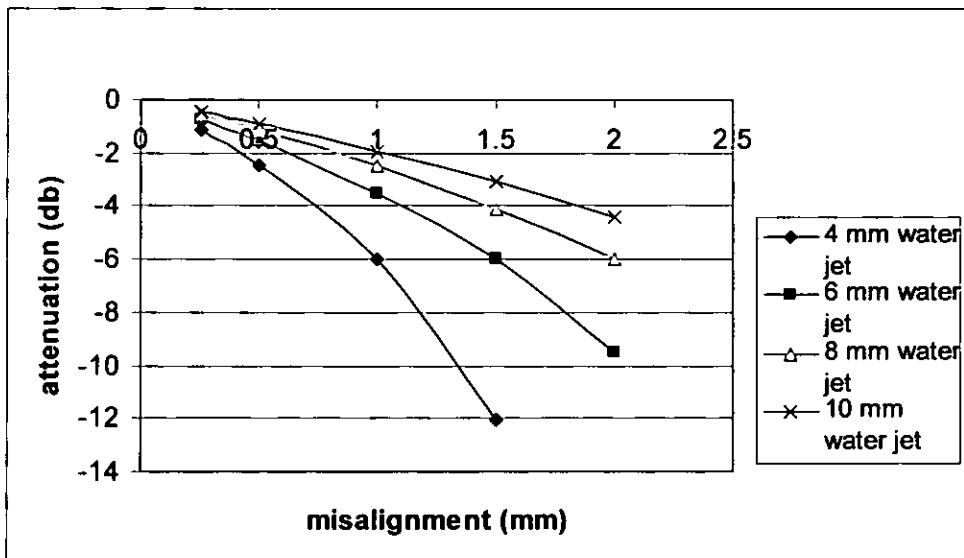


Figure 3-39 Graph showing calculated loss of signal due misalignment errors

3.14.3.2. Computer Aided Three Dimensional Interactive Application (CATIA) interface.

It is difficult to establish an accurate trajectory for large complex shaped composite panels using a teach learn method. This is mainly because composite panels do not have any readily identifiable surface features and as such the operator struggles to create a scan path that contains taught points at the most significant places on the surface. To overcome this, an interface has been developed that takes surface normal information generated from a tool within the computer aided drawing (CAD)

environment (CATIA) and uses this data to generate the scan path. Whilst this overcomes problems associated with manual teach learn a method of translating the CAD co-ordinates to match the real world situation and a method of extracting the normals without significant error has to be ensured. Manufacturing Programming (MFGPROG) is the tool within CATIA that is used to generate the surface normals and there are three parameters that control the accuracy of the calculation. These are maximum angular and linear discretization values and a tool tolerance. Ideally the discretization values should be set to generate a point for every increment that ultrasonic data is required. However, on large components there is a time penalty for this computation and also the CATIA environment is not configured for such large files. The trade off is therefore to relax the linear discretization value whilst maintaining the angular value. This, therefore, generates more points around highly curved surfaces with fewer points being generated on relatively flat areas. The tool tolerance should be such that it is significantly lower than the positional tolerance on the scanning machine and therefore does not contribute to any positional inaccuracies.

Translating the surface normals obtained from CATIA to match the actual part location within the scanning system is performed by manually teaching the position of the two location holes plus a third point that is identified on the part by a small conical raised area on the surface and using these co-ordinates and the same positions on the CAD drawing to calculate the translation.

3.14.4. Pulse echo immersion system

The picture below shows a five axis (X,Y,Z,Xtip,Ytip) ultrasonic immersion system again designed and manufactured by Ultrasonic Sciences Ltd. The motion control is the same as the ten axis system and uses the PMAC control card manufactured by Delta Tau. This system was designed to inspect super plastically formed, diffusion bonded titanium structures which are submersed in water. The transducer both transmits and receives reflected ultrasonic signals (pulse echo method) which is scanned across the surface of the component. Immersing the component provides a

more uniform coupling and therefore aids ultrasonic inspection. Clusters of pores which individually can measure around 15 μm can significantly affect joint strength. Therefore high frequency ultrasound (20 to 25 MHz) is adopted for the inspection diffusion bonded titanium as the shorter wavelength has a greater response to small imperfections in the material. Many diffusion bonded joints are made from thin sheets of titanium which means that small clusters of defects can be close to the surface. Therefore in order to improve spatial and axial resolution the high frequency transducers are spherically focused which constrains the ultrasonic beam and increases sensitivity. The motion control and ultrasonic data acquisition is the same as the ten axis system. The pulser receiver used for this inspection is a specially designed short pulse duration pulser and an amplification stage that is broadband with a centre frequency of 15 MHz.

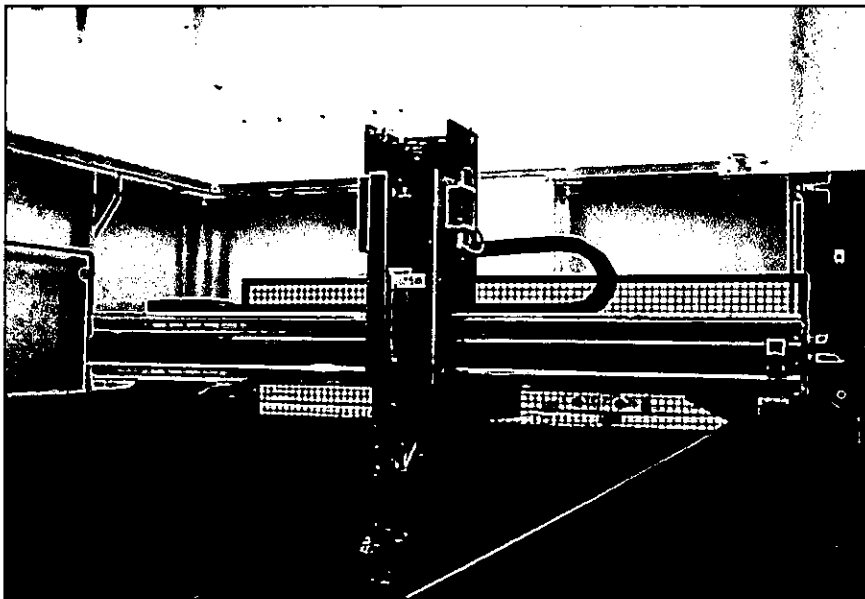


Figure 3-40 Five axis ultrasonic scanning system used for SPFDB inspection.

3.15. Ultrasonic data acquisition modules

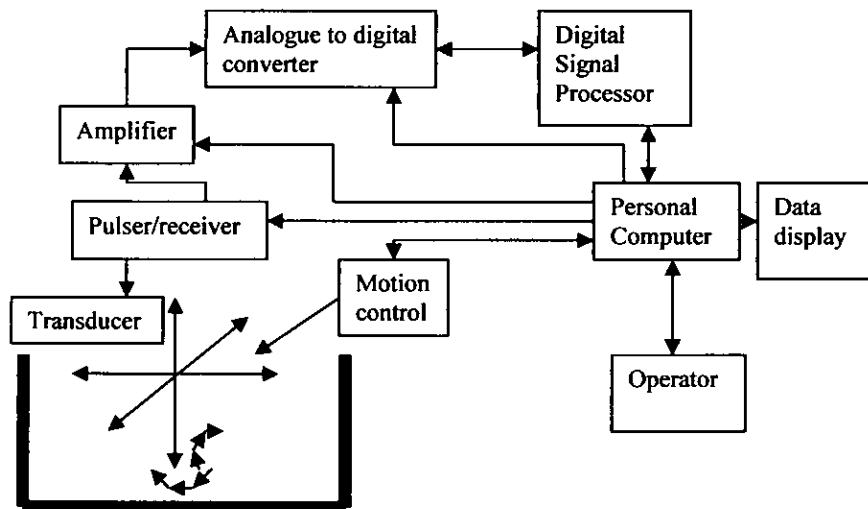


Figure 3-41 Block diagram of the key modules required for an ultrasonic scanning system

The block diagram above illustrates the key modules required for a modern ultrasonic data acquisition system. The mechanical and electronic motion control have been describe elsewhere but it is pertinent to briefly discuss the key features of the ultrasonic generation and reception modules in order to highlight the key parameters used for enhancing the defect detection for diffusion bonding and composite inspection. Data display and manipulation are discussed in chapter 6.

3.15.1. Pulser receiver

Key parameters at pulse stage are the pulse width and pulse voltage. As demonstrated in the experimental work the amplitude of the transmitted signal is directly proportional to the applied voltage. At high frequencies however excess voltages produce no increase in signal strength and do serve to reduce transducer life. The commercial pulser used in both the ten axis water jet and five axis immersion systems can output a 600 volt peak. It was found however that there was no increase in signal amplitude over 200 volts particularly when using 20 to 25 MHz transducers. The disadvantage of such a high voltage pulser for high frequency applications is that the MOSFETS used to switch 600 volts have typical turn on and

turn off delay times that are significantly longer than the centre frequency of the transducer resulting in a less than optimal pulse shape and a loss of sensitivity. Electronic damping was selectable in preset values of 33, 50, 100 and 200 Ω which went some way to matching the load impedance to that of the amplifier. Pulse repetition was variable in 1 Hz steps from 0 to 3 kHz which is ample for the scan speeds adopted for this inspection.

The bandwidth of the amplifier, the useful dynamic range and the excitation pulse shape are major contributors to successful defect detection. Two types of pulser and receiver were used for the experimental work. For the high frequency ultrasound applied to super plastic formed diffusion bonding (SPFDB) a linear amplifier operating at a centre frequency of 15 MHz was used. For the detection of small laser pits embedded in a diffusion bond a modified pulser with a fast rise time was implemented. The ultrasonic pulser receiver used for inspecting composite materials consisted of a 600 volt pulser and a combination of 15 MHz amplifier and a logarithmic detector.

Typical composite components have specific areas that are highly attenuative and other areas where the attenuation is small. Logarithmic detectors are used in these instances as they extend the dynamic range in comparison to linear amplifiers and are able to detect large and small responses without alteration to the gain. Due to the envelope detection characteristics of a logarithmic detector its ability to resolve signals occurring at short intervals does suffer. This type of detector therefore is normally only used for through transmission inspection where the amplitude of the received signal is of interest. When resolution is required i.e. the majority of pulse echo inspection tasks, a linear amplifier is employed. As the resolution requirement increases the frequency of the ultrasonic transducer is increased, hence the use of 20 to 25 MHz transducers for diffusion bonding inspection.

In conclusion therefore, when choosing a pulser receiver for a particular inspection a balance between resolution and sensitivity has to be found. The application will drive the choice in a particular direction but with today's electronic devices and advances in amplifier design and manufacture pulser receivers with tuneable pulse and bandwidth

parameters enable the compromises to be achieved from a single electronic module. Sensitivity can be increased by matching the excitation pulse rise and fall time to coincide with the natural expansion and contraction of the transducer (maximum power transfer theorem) without any significant impact on resolution. Whilst for many applications this may not be necessary, when attempting to improve of the defect detection capabilities whilst maintaining a robust inspection process matching the pulse parameters to the frequency of the transducer is a reliable implementation method.

3.15.2. Analogue to digital converter

All the ultrasonic experiments performed and reported in this chapter were conducted using modules designed and manufactured by Ultrasonic Sciences Ltd (USL). USL have a wide product range from acoustic microscopes to relatively low frequency axel scanning systems. The majority of the experimental work has focused on optimising parameters that affect the inspection whilst maintaining a process that can be routinely implemented in a production environment. This has driven the work towards maintaining sensitivity at the cost of optimal frequency.

Specialised very high frequency pulser receivers have not been used as they are difficult to implement in the production environment and sensitivity in terms of signal to noise is often reduced. Whilst the choice of pulser receiver can be justified from a practical viewpoint compromises in terms of analogue to digital conversion cannot. Nyquist sampling theorem states that the sampling frequency must be at least twice the frequency of the highest frequency signal expected in the conversion. Accurate signal peak detection using the digital result from an A to D conversion cannot be relied on if the incoming signal is close to the Nyquist limit. Fortunately the USL A to D converter was an 8 bit 100 megasamples /second conversion unit which provided ample samples for peak detection at 25 MHz. The record length of the USL A to D is 2048 samples which is variable along a 300000 ns range. This proved ample to convert the timeslots of interest at frequencies up to 25 MHz.

3.15.3. Multiplexer

Defect detection using ultrasonic scanning systems often requires more than one ultrasonic set up. When thickness measuring using the time signals take to travel from one interface to another it is not always possible to accommodate the complete thickness range. Gain settings that amplify signals far into the material also create large saturated signals from the surface making near surface measurements difficult. Also as stated previously aircraft components invariably have thin solid composite layers (termed landings) and thick honeycomb sections in the same panel. Therefore when performing inspections on this type of panel the amount of signal amplification required for the honeycomb sections means that the signal received through the thin landing is saturated. Defect detection is severely impaired in this case as a potential defect has to significantly reduce the signal amplitude such that it is no longer saturated before the attenuation can be measured. Logarithmic amplifiers and distance amplitude correction circuits are frequently used to overcome dynamic range problems but there are times when the poor resolution of a logarithmic detector or the achievable dynamic range using DAC is not sufficient for inspecting a component in one scan. There are also a number of inspection cases where inclusion type defects cannot be detected using through transmission methods i.e. a transmitter at one side of the component and a receiver at the other. In these cases the system must be capable of switching from through transmission to pulse echo operation i.e. transmits and receives from one side only. To do this multiple pulser receivers are incorporated into the system which are individually set to operate in a particular mode and are capable of operating with different parameters i.e. filters, gain, pulse voltage and width etc. The multiple pulser receivers are then rapidly switched and data is transferred to the control computer at rates significantly faster than the scan speed. On the USL 10 axis complex geometry system the multiplexing capability can be expanded to 8 channels and can operate at a switching frequency of 20 kHz. The switching frequency of the multiplexer is synchronised with the pulse repetition frequency of the pulsers but as there is no

synchronisation between the pulser and the motion it is important to ensure that there are at least two pulses for each channel at each position of the scan. The pulse repetition (PRF) rate should therefore be:-

$$PRF = \text{scan-speed} * \text{scan-increment} * \text{No-of-channels} * 2$$

Therefore a scan performed at 500mm/s at a 1mm increment using all 8 channels would require a minimum PRF of 8 kHz.

3.15.4. Digital Signal processor

Signals coming from the amplification stages pass through the analogue to digital converter and are processed by a digital signal processor (DSP). The DSP is capable of processing the data in a number of ways. It can return up to 8 measurements per channel and has enough processing power to deliver the results at PRF intervals. A digital oscilloscope display of the gating a measurement facility provided by the DSP is shown in figure 3-39 below.

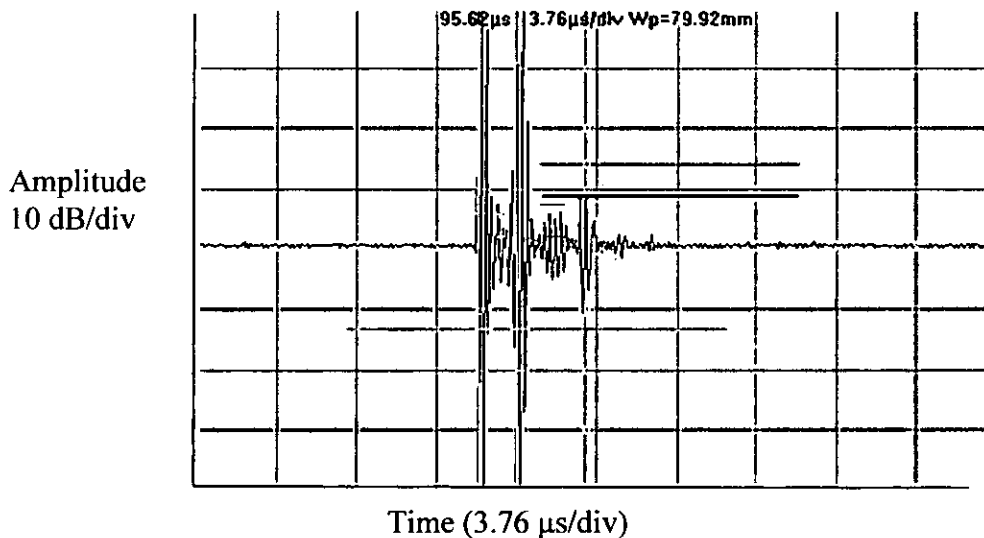


Figure 3-42 Digital oscilloscope display showing a six gate measuring technique.

There are six gates being used in figure 3-42 and to understand the purpose of these gates the ultrasonic response must be interpreted. The signal displayed above is a pulse echo response from a bonded carbon laminate and the first signal on the left is the reflection from the surface of the composite. This signal resonates for a short period and then a second

signal of equal amplitude appears. This second signal is a reflection from the bondline where the bonding material is of different acoustic impedance to the carbon fibre composite and therefore a large reflection occurs. The third broad but smaller amplitude signal to the right of the bondline signal is the response from a defect and the last one is the reflection from the far surface of the component (backwall). Although a defect indication has been shown in the second layer of the component i.e. after the bondline it is also possible in this application to experience defects prior to the bondline and in deed on the bondline itself. The gating system therefore has to be capable of detecting all possible combinations of defect response. To this end the yellow gate is used as an interface trigger. Once a signal breaks through the threshold i.e. the yellow line on the negative side of the oscilloscope display all other gate measurement will be triggered to start.

Similarly the red gate is used to trigger the time interval measurement system but will also produce an amplitude reading for the maximum signal that appears within its time limit. The time interval measurement gating system is shown as two vertical yellow lines. In this set up the time interval measurement will begin its measurement as the transmission pulse occurs but only measure events after the bondline because of the start position of the red gate. Defects prior to this measurement are therefore captured by the three other gates i.e. the small yellow, green and brown lines. This set up utilises the measurement facilities provided by one channel. When scanning this particular specimen a further channel was used for through transmission defect detection. The results of the scan are shown below (figures 3-46, 3-47, 3-38 pages 117 and 118).

3.16. Results

3.16.1. Effects of pulse length.

The pspice modelling described previously (page 84) concluded that optimum transducer response was achieved when the excitation voltage matched the transducers natural frequency. Experiments conducted at low excitation voltages verified this result. Commercial ultrasonic scanning systems however are fitted with very high voltage pulsers as they are often

required to inspect materials with large attenuation differences. An experiment was therefore conducted to verify that at high excitation voltages optimum ultrasonic response still occurred when (all other factors being equal) the excitation voltage matched the transducer frequency. Figure 3-40 shows the ultrasonic response from a 5 MHz 50 mm spherically focused transducer excited with an optimum pulse. Figures 3-41 and 3-42 show the responses of using pulse length that are too long (3-41) and out of phase with the transducers natural response (3-42). A 5 MHz transducer was chosen as it is a common frequency used in the inspection of carbon fibre composites and although the transducer was highly damped as are most transducers used in the aerospace industry it was relatively simple to vary the pulse length around the centre frequency. From the results below it is clear that long excitation pulses reduce the bandwidth and therefore near surface resolution, whilst inappropriate excitation pulses that are out of phase with the transducer create responses that are both narrow band and severely distorted.

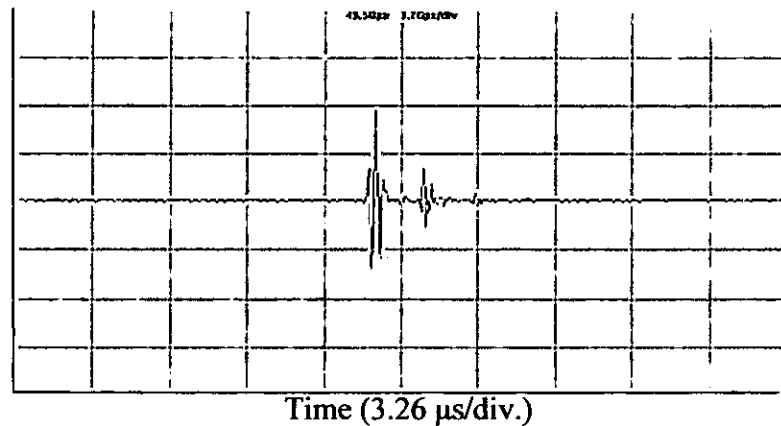


Figure 3-43 Glass plate reflected signal for a 5 MHz transducer focused with a 50 mm spherical radius. Excitation pulse optimised for best response.

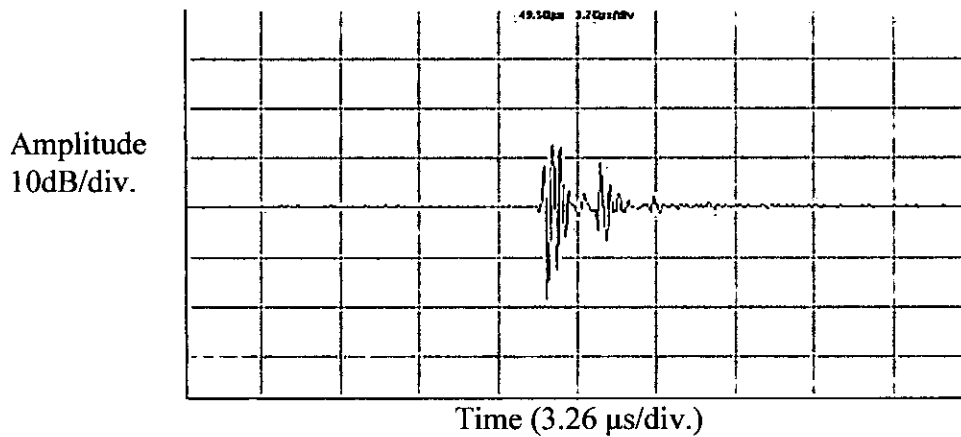


Figure 3-44 Glass plate reflected signal for a 5 MHz transducer focused with a 50 mm spherical radius. Long transducer excitation pulse.

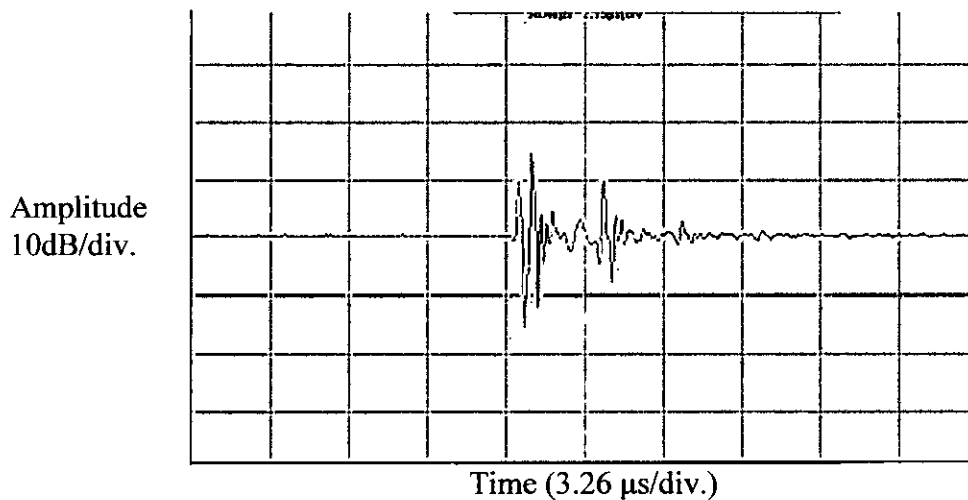


Figure 3-45 Glass plate reflected signal for a 5 MHz transducer focused with a 50 mm spherical radius. Long and out of phase excitation pulse.

3.16.2. Ultrasonic defect detection capabilities composite and diffusion bonding

To verify the general detection capabilities of ultrasonic scanning systems an inclusion panel was chosen as some of the included materials are very similar in acoustic impedance to the parent material and are therefore very difficult to detect. The specimen was located vertically in the ten axis complex geometry scanning system and a scan trajectory was taught. The gating system was set up as described previously and the resulting scans are given in figures 3-46, 3-47, 3-48. Figure 3-46 is the

result of measuring the through transmission signal. It is clear that the second column of defects from the left of the scan are completely missing as are the fourth and fifth columns. Clearly the attenuation caused by these inclusion materials is less than the minimum quantization level of the data acquisition system and therefore the defects are undetectable. The scan shown in Figure 3-47 was produced by measuring the backwall echo and from this data three possibly four more defects are visible in each of columns four and five. The last scan figure 3-48 was produced from data measured between the bondline signal and the backwall and this scan highlights 2 further defects in each of columns two four and five.

From these results it is clear that successful defect detection in modern carbon fibre structures has to employ a series of measuring techniques. However operating in pulse echo on complex surfaces does impose the restrictions of normality to the surface and it is therefore imperative that inclination to the surface is controlled. As described previously errors in motion control culminate from inappropriate PID loop tuning, incorrect axes compensation and errors associated with trajectory translation and rotation which when combined will produce significant positional error which in turn reduces defect detection.

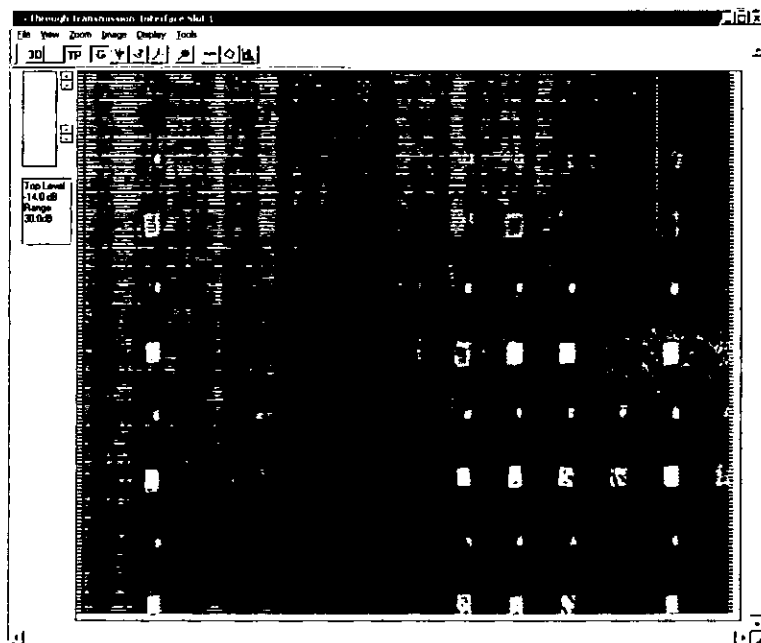


Figure 3-46 Through transmission ultrasonic scan of an inclusion reference specimen.

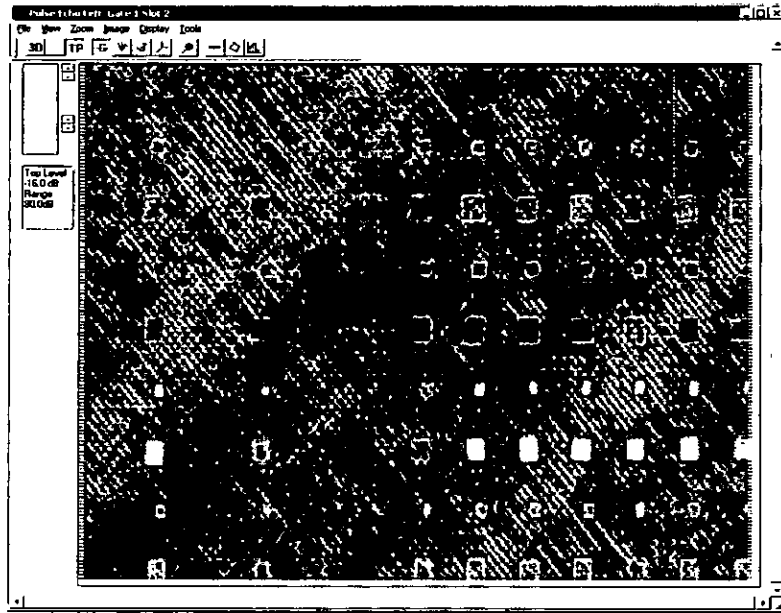


Figure 3-47 C-scan obtained from the data captured by gate 1 (the red gate in figure 3-42)

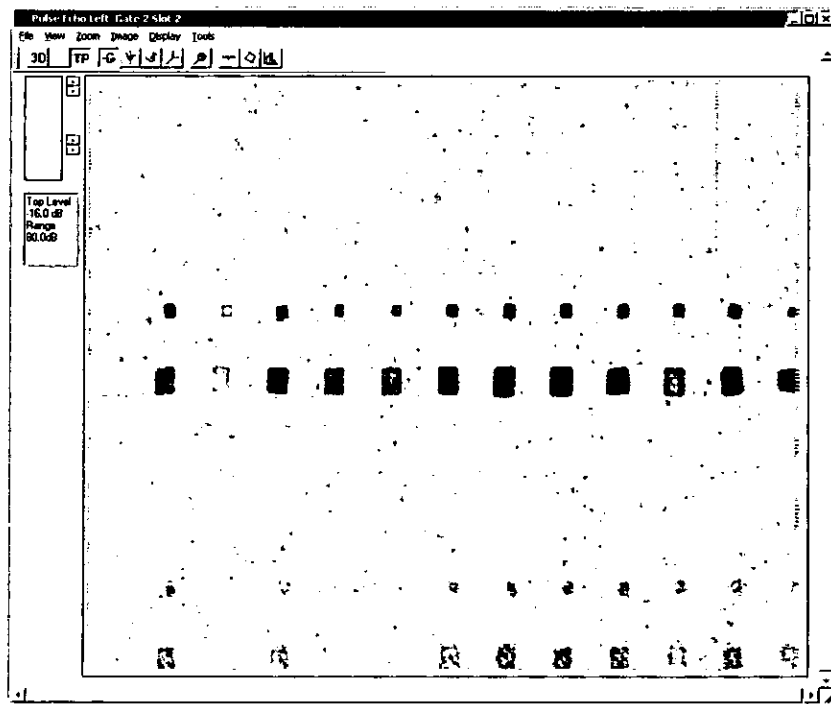


Figure 3-48 C-scan obtained from the data captured by gate 2 (the brown gate in figure 3-42)

The inspection of diffusion bonds to detect 15 μm pores at a depth of 1 mm poses a similar set of challenges to that of composite inspection in that pulse optimisation and control of inclination are very important. Because of the 15 μm defect size a 6 mm diameter 20 MHz ultrasonic transducer was employed with a 37 mm radius of curvature. This choice was a compromise between resolution achievable with a high frequency transducer and sensitivity. The results given in table 3-5 (page 68) show that a better alternative would have been the 9,5 mm diameter 25 MHz 37 mm radius transducer as this is less susceptible to inclination angle with a 5 dB loss of signal for 3 degree inclination in contrast to a 11 dB loss for the 20 MHz transducer. However the pulser receiver available for these experiments had a 15 MHz centre frequency amplifier with an adjustable pulser to match. Connecting a 25 MHz transducer to this pulser receiver arrangement gave no benefit which was almost certainly due to the minimum pulse length being out of phase with the transducer centre frequency. Therefore the best defect detection was achieved by optimising the pulse length for the 20 MHz transducer and operating the amplifier with broadband filters applied. The scan below (figure 3-49) is a plot of the signal amplitude measurement measured at the position on the timebase where the bondline signal would occur. The leftmost and centre specimens clearly show the area of laser pitting whereas the rightmost specimen only shows a small portion of the laser pitted area. This result does correspond to the metallurgical evaluation where the rightmost specimen showed individual laser pit dimensions of 28 μm and some smaller sized disbonds in-between the pits averaging 20% of the inter-pit surface area. The centre specimen had laser pit dimensions of 23 μm with even smaller disbonds in-between the laser pits that averaged some 10% of the inter-pit surface area and the rightmost specimen had laser pit dimensions of 17 μm with around 3% disbond in-between the pits. Whilst the indications from the pitted areas on the two worst cases is clear and a small area of the best specimen can be identified there are areas where significant signal indications have been captured comparable to the amplitude of the laser pit indications that are designated as areas of either 100% bond or in the case of the leftmost

specimen around 7% disbond with pores around material grain size i.e. 10 μm . The area outside the pit in all three specimens should progressively get better from left to right. This is not clear from the result below which would suggest that the ultrasonic sensitivity is such that it is not possible to differentiate small disbonds from the material structural noise. If this is the case then the limit of detection has been reached.

Whilst the result below does indicate that the limit of detection can be approached using a 20 MHz transducer which is in contrast to many researchers findings and that a more defined result is achievable by increasing the transducer frequency, the degree of focus and the transducer diameter to 25 MHz 9.5 mm diameter 25 mm focus, it should be taken into account that this experiment was conducted on flat specimens whereas components are typical aerofoil shape and can possess significant amounts of curvature. In these instances probe inclination is a significant factor on successful defect detection and if not rigorously controlled any gain in defect detection capability achieved by increased frequency and optimised excitation and amplification would be lost.

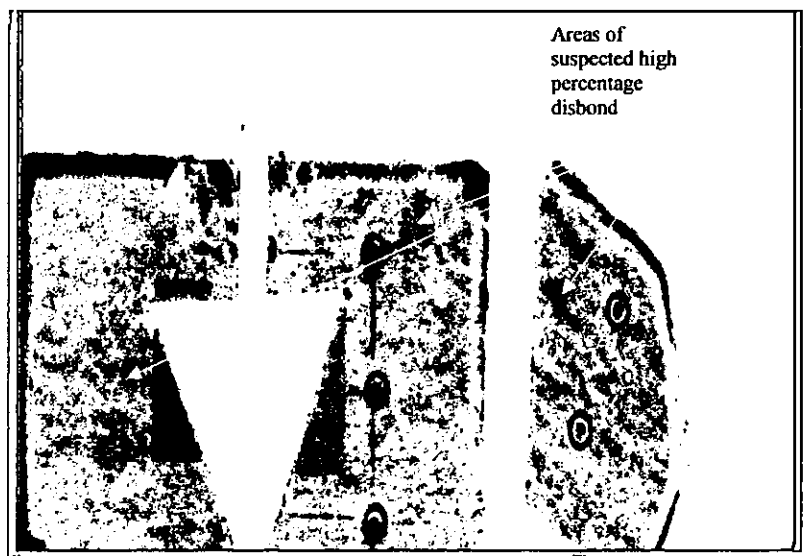


Figure 3-49 Ultrasonic C-scan showing disbonds created by laser pitting

Time interval measurements were also captured simultaneously with the amplitude data shown above however the signal responses from the small

laser pits and inter-pit disbonds are so small that they do not trigger the time measurement gates and as such the disbonds go undetected. Whilst time interval measurements are a preferred method of disbond detection for a number of diffusion bonded structures when the significant defect size is reduced to levels not much greater than grain size time interval measurement methods are no longer appropriate.

3.17. Summary

This chapter has described in detail the ultrasonic parameters that govern successful defect detection. Typical ultrasonic parameters such as probe frequency amplification gain etc, that are manipulated in day to day inspections by practicing NDT engineers and technicians are considered the major influential factors on successful defect detection. However, as the inspection requirement becomes more stringent either in terms of significant defect size or component complexity the classical parameters, whilst still important, are not the main contributors to the defect detection standard. It has been shown that defect detection is significantly impaired on complex shaped parts when errors in the positional accuracy are not removed or catered for. Likewise when inspecting diffusion bonded joints for grain size defects, maintaining normality and optimising transducer sensitivity at relatively high frequencies are the major contributors to successful defect detection. Correct motion control and PID loop tuning are now very significant factors in providing and maintaining reliable and robust inspection methods and as such have to be evaluated in terms of error and significance of that error on the inspection standard. The evaluation method used in this chapter is a practical way to assess the limits of detection of complex scanning systems and provides data that can be directly related to types of defect and the detection capabilities. In doing this it removes some of the uncertainty that can be apparent when using test samples to evaluate the defect detection capabilities as this method does not identify the key parameters but provides a list of parameters used. Test specimen evaluation also relies heavily on defect simulation which again raises an issue of how representative are the simulated defects. The conclusion drawn from this work is therefore that performing system

analysis and evaluating the error concerned with motion control are as important as the more classical evaluation measurements usually performed by the NDT engineer. Furthermore automation of the data processing steps within an ultrasonic inspection cannot be reliably performed if the data acquisition is not understood and strictly controlled.

Assessing the ultrasonic attenuation due to positional error and the performance of a transducer in respect to excitation provides data that can be used for calibration purposes so that the inspection standard is well established and maintained.

Chapter 4

4. Radiography

Radiography is used extensively in both industrial non destructive testing and the medical field. Its wide application has resulted in many system configurations with developments in both X-ray generators and image recording systems. In the aerospace industry however conventional film radiography is still used extensively and improvements in the method have focused on better quality film, faster processing and high intensity sources.

Aerospace radiography is used to inspect weldments, castings, fabrications, carbon fibre composite structures and complete structures when debris is of concern. The most recent developments in aerospace radiography however has been in the application of real time radiography to weldments and super plastically formed titanium. The successful introduction of real time radiography has been possible due to developments in image processing techniques and advances in generation and detector technology. The following chapter describes the basic principles of radiography in terms of X-ray generation and detection and then moves on to describe how these principles can be applied to developments in real time radiography.

4.1. X-ray Generation.

X rays are a form of electromagnetic radiation having wavelengths in the region of 10^{-13} to 10^{-9} metres [Bueche 1986]. It is the short wavelength that gives X-rays the ability to penetrate materials that would absorb or reflect light, and it is this capability that allows the NDT engineer to inspect the internal structure of components for potential flaws. The shorter the wavelength of the X-ray, the greater is its energy and its penetrating power.

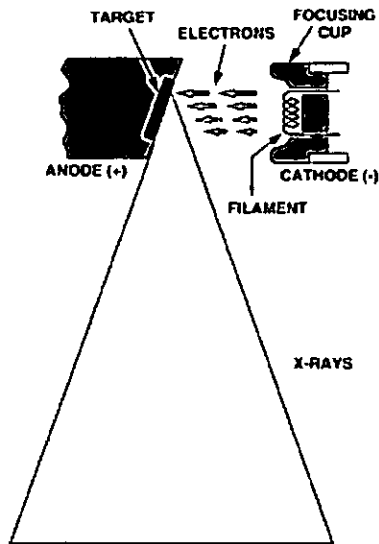


Figure 4-1 Schematic of a typical X-ray generation tube

To generate X-rays the filament is heated by passing a current through a small diameter tungsten wire (reference figure 4-1). As the temperature of the wire increases a greater number of electrons are released from the filament material. These free electrons form a cloud around the filament. A very high potential difference is then applied between the cathode and anode and the free electrons are rapidly accelerated towards the anode. As the electrons bombard the anode target most of the energy is transformed into heat with a small portion creating X-rays. The transformation of energy to heat means that a target material with a high melting point is required. Also the efficiency of the target material in the production of X-rays is proportional to the materials atomic number. Tungsten has both a high atomic number and melting point and is therefore the choice for most X-ray tubes.

4.1.1. Cathode

The cathode or filament is usually constructed from tungsten wire around 0.2 mm in diameter. The amount of electrons emitted from the tungsten wire when the temperature of the wire is raised is given by the Richardson equation:-

$$J_e = A_0 T^2 e^{-\frac{W}{kT}} \quad (4-1)$$

where

W is the work function, for tungsten $W = 4.5 \text{ keV}$

k = Boltzmann constant

T = Temperature

A_0 = Material constant, for tungsten value is approximately $60 \text{ A/cm}^2 \text{ K}^2$

The anode current used in industrial radiography varies between 0.5 and 10 mA. To achieve this, the filament has to be heated to above 2000 K. At this temperature there is little degradation of the filament due to evaporation and the lifetime of the filament exceeds 10000 hrs. However increasing the filament current and therefore raising the filament temperature can lead to metal vaporisation and hence reduced filament life. With no potential difference between the anode and cathode the electrons emerge from the cathode with little or no velocity and form a cloud. At low potential differences this cloud partially screens the generated electric field and only a portion of the electrons are accelerated towards the anode. For low voltages the space charge law applies :-

$$I_a = \frac{4}{9} \epsilon_0 \sqrt{2 \frac{e}{m}} \cdot \frac{V_a^{3/2}}{d^2} \quad (4-2)$$

where

I_a = Anode current

ϵ_0 = permittivity of a vacuum

e = electron charge

m = electron mass

V_a = Anode potential

d = Distance between cathode and anode

For high potential differences between cathode and anode all the electrons are accelerated towards the anode and the saturation current can be calculated by:-

$$I_s = J_e \cdot A_e \tag{4-3}$$

where

J_e = emission current density calculated from (4-1)

A_e = emitter surface

I_s = saturation current

At these potentials and for a constant emitter surface the anode current is directly related to the emission current density (J_e) which can be calculated from equation 4-1. Therefore it can be seen that cathode temperature (T) is the major influence on current density in a high potential x-ray generator. Cathode temperature is controlled by the amount of current flowing through the filament and therefore filament current determines the quantity of electrons that will be accelerated towards the anode.

4.1.2. Focusing cup

Electrons that are accelerated towards the anode by the high potential difference hit the anode over a relatively large area. This results in a widely smeared out distribution and therefore generates a wide X-ray beam or focal spot (see fig 4-2 below). Large focal spots lead to blurring in the resultant image. Figure 4-2 shows the cathode distorting the equipotential lines towards the anode. In this case the electrons will naturally disperse depending on how distorted the lines of equipotential are. To overcome this effect a focussing cup is implemented at the cathode which distorts the equipotential lines towards the cathode. The electrons are therefore collimated as they travel towards the anode. By applying a slightly negative potential to the focusing cup the electrons can be strongly focussed however if this voltage is excessive then it will have a blocking effect and electrons will not travel towards the anode at all.

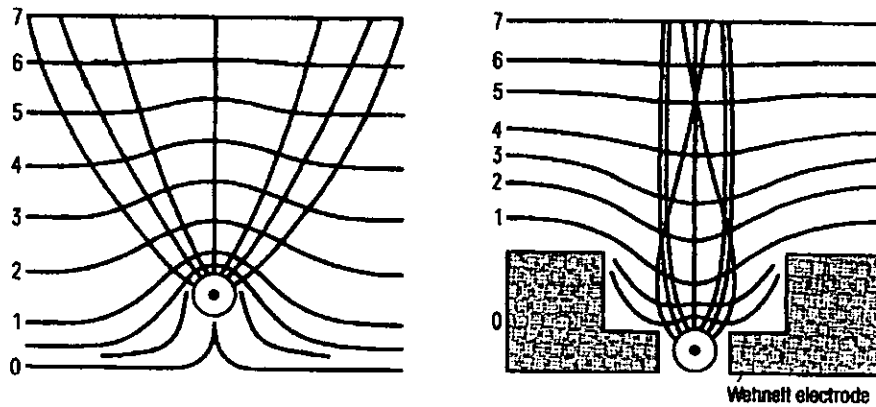


Figure 4-2 Electron spread with and without a focusing cup

4.1.3. Focal spot

The area of the anode in which electrons will strike approximates to the filament shape. The focussing cup restricts the electron path but is unable to apply sufficient force to provide a small focal point on the target. The focal spot however makes a major contribution to image sharpness and small focal spots are required. To achieve this, the anode (target) is usually displaced at a small angle from the cathode and hence the focal spot size is reduced. The figure below shows the projection of the focal spot which is termed the electronic focus and the actual focal spot due to the inclination of the anode, termed the effective focal spot.

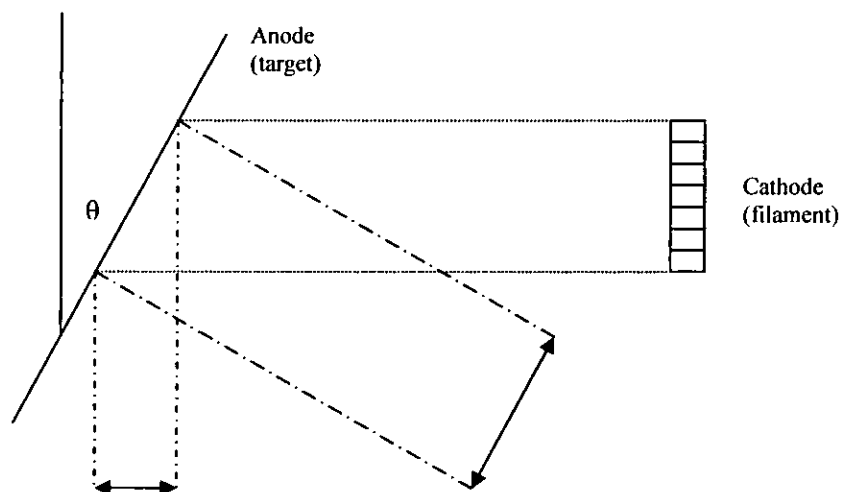


Figure 4-3 Geometrical arrangement of the focal spot

4.1.4. Heel effect

The down side to inclining the anode is that electrons that penetrate the tungsten anode have varying path lengths depending on the part of the anode that they collide with. The X-ray photons emitted from the part of the anode closer to the cathode have a shorter exit path within the tungsten whereas electrons that collide with the anode furthest away from the cathode result in photons that have longer paths within the tungsten material. The overall effect is therefore an X-ray beam that is not uniform in terms of energy and spectral distribution. The X-ray spectrum at the anode side of the beam has a higher spectral response and less energy. Figure 4-4 below shows the anode arrangement and the resulting heel effect.

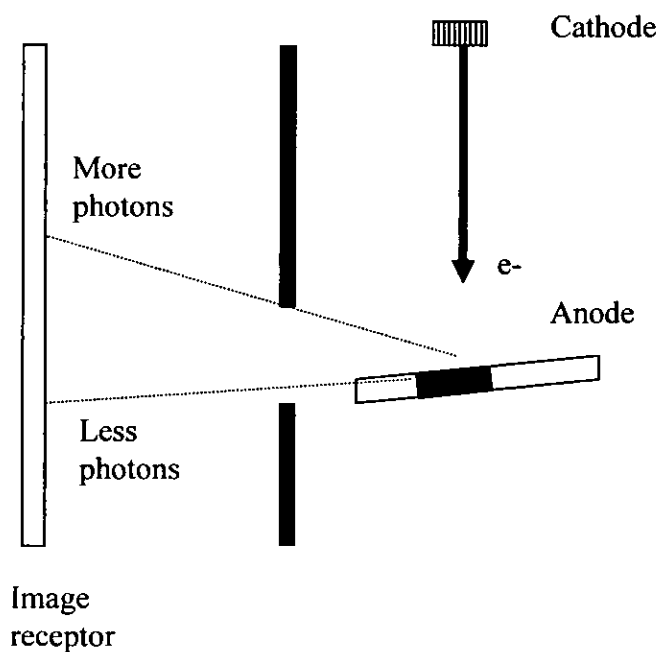


Figure 4-4 Typical Anode arrangement and heel effect

4.2. Geometric principles

Over relatively short distances X-rays can be considered to travel in straight lines and therefore are able to cast shadows of objects in the same

way as visible light behaves. Of course X-rays are able to penetrate dense materials and therefore do not behave in the same manner as light but for the purpose of explaining the geometric principles appertaining to X-ray inspection the assumption that the same geometric principles that apply to light also apply here is made.

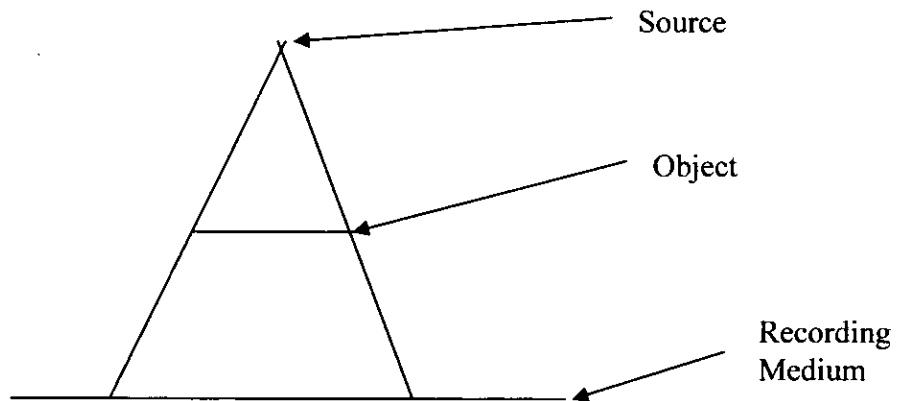


Figure 4-5 The shadow effect a geometric enlargement from a radiographic point source.

In figure 4-5 above it can be seen that for a point source the shadow caused by an object is enlarged. The degree of enlargement can be described by the following:-

$$S_0 = S_1 \frac{D_0}{D_1}$$

(4-4)

where

S_0 is the size of the object

S_1 is the size of the shadow

D_0 is the distance from the source to the object

And D_1 is the distance from the source to the recording medium

Therefore the degree of enlargement is dependant on the ratio between source to object and source to recording medium distance.

In radiography however the source is rarely considered to be a point but has significant dimensions. The geometry of the focal spot therefore contributes to the unsharpness of the image. The unsharpness of an image due to the source size can be better understood by figure 4-6 below. Here each point of the source creates its own shadow in the resulting image and each shadow is slightly displaced and overlaid on another. The result is that the edge of an object has many displaced shadows contributing to its formation which result in blurred edges. The maximum unsharpness can be calculated by considering the extremes of the focal spot or source. As drawn in the diagram each edge of the source contributes the maximum displacement of the shadow and therefore from the laws of similar triangles it can be seen that :-

$$U_g = f_s \left(\frac{t}{D_0} \right)$$

(4-5)

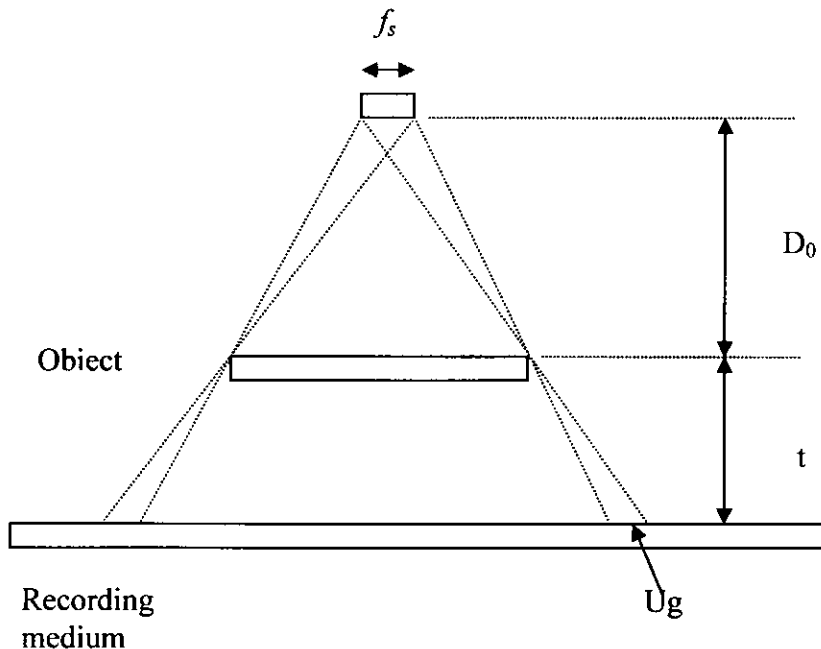


Figure 4-6 Geometric representation of image unsharpness

In conclusion therefore it can be seen that when performing an X-ray inspection there are many geometrical factors to consider and the

generation of x-rays is a compromise between optimum source geometry and an even distribution of photons in the beam. Focussing the beam of electrons into a small focal spot with the use of a focussing cup may restrict the electron flow if an excessive negative potential is applied, and attempts to alleviate image unsharpness due to the finite target size can result in an uneven distribution within the X-ray beam due to the heel effect. One other disadvantage of the focussing cup is that it raises the minimum potential difference that has to be applied before electrons will be accelerated towards the anode and therefore reduces the working range of the generator.

4.3. Radiation spectra

There are primarily two types of interaction between the electrons and the tungsten target in an X-ray generator. The majority (99%) of electrons are attenuated by the material and lose their energy in the form of heat with little or no radiation generated. The remaining electrons however do produce X-rays but by two different mechanisms.

4.3.1. Characteristic radiation

As the high energy electrons strike the target, electrons within the material are knocked from the orbit levels of the atom that they occupy during steady state to a lower orbit level. The distance an electron is to the nucleus determines its binding energy and is generally referenced by the letters K, L, M etc with K electrons having the greater binding energy. As lower level electrons are dislodged it leaves a vacancy that is filled by an electron from a higher level. For this to occur, energy has to be released. The energy released as photons is equal to the difference between the two levels that the electron passes when filling the vacancy. The X-rays emitted by this process are therefore referred to as the characteristic X-rays as they have distinct energy levels that are characteristic of the target material. Characteristic radiation only occurs when the energy of the bombarding electrons is above the binding threshold of the electrons orbiting the nucleus. For tungsten the binding energy of electrons in the K-orbit is approximately 75 keV.

4.3.2. Bremsstrahlung or white radiation

Another type of x ray emitted from the target when it is bombarded by electrons is referred to as bremsstrahlung or braking radiation. This occurs when the bombarding electrons from the anode are suddenly stopped by the nucleus. In this case the nucleus is undisturbed due to its mass and energy is therefore transformed into an X-ray photon. The majority of collisions that produce white radiation do not completely dissipate all their kinetic energy as their path is not directly in the path of the nucleus. In this case part of the energy is released and the electron carries on through the material colliding or partially colliding with other nucleus.

It is therefore rather unpredictable as to what energy the bombarding electrons will have by the time they collide with a nucleus as they may have undergone a number of electron collisions previously therefore the amount of energy released as photons and the wavelength cannot be accurately calculated. It can however be assumed that some of the electrons will fully collide with the nucleus immediately and therefore release all their energy. In this case the minimum wavelength can be calculated but the complete spectrum can only be reliably determined by empirical measurement [Boone & Seibert 1997]. The minimum wavelength is determined from the following:-

$$\lambda_{\min} = \frac{h_c}{eV} \tag{4-6}$$

where

h_c = plank's constant

e = charge of and electron and

V = applied voltage

The figure below (4-7) is a plot of data taken from Boone and Seibert results where the empirically measured data has been extrapolated for various excitation voltages. It can be seen that at 75 kV there are no K lines and therefore all the radiation emitted is considered to be generated from the Bremsstrahlung process.

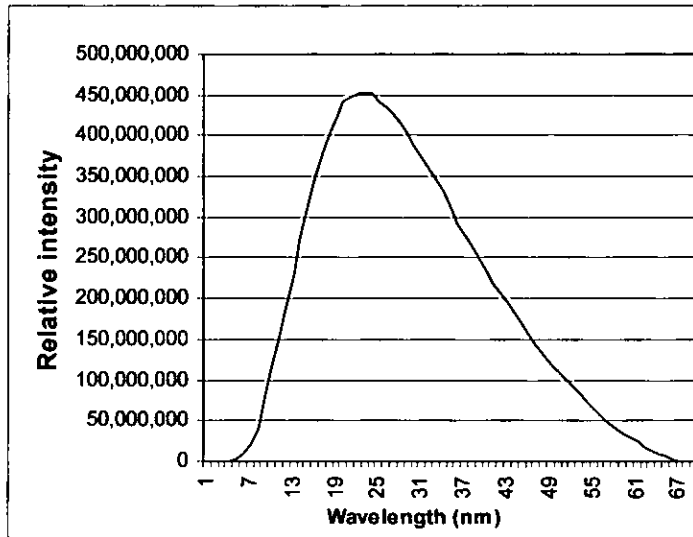


Figure 4-7 Graph of the calculated X-ray spectra at 75 kV, no K-lines are visible.

The data for figure 4-8 below was calculated using the Boone and Seibert data and it demonstrates that at 100 kV the K lines are just visible but the Bremsstrahlung radiation is more dominant. At 140 kV however (figure 4-9) the characteristic radiation is more dominant than the Bremsstrahlung and the dominant radiation is therefore narrower in bandwidth.

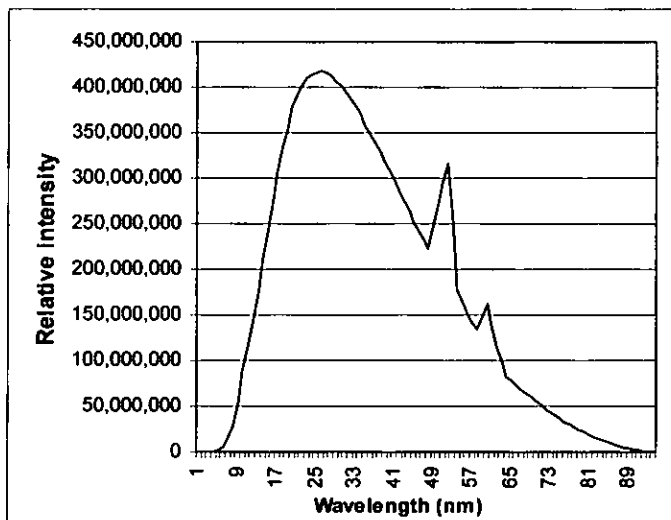


Figure 4-8 Graph of the calculated X-ray spectra at 100 kV, note the K-lines are visible but not the dominating energy.

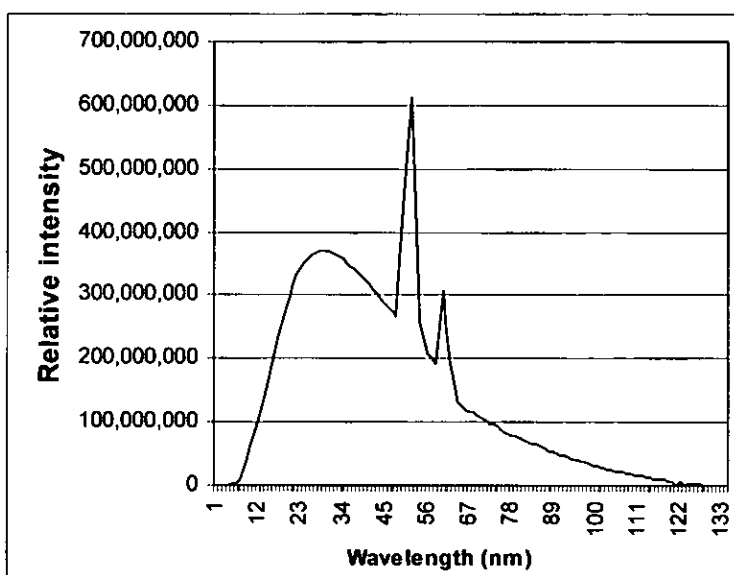


Figure 4-9 Graph of the calculated X-ray spectra at 140 kV, note the K-lines are now the dominating energy.

4.3.3. Effect of increasing potential difference and filament current

Figure 4-10 below illustrates the effect of increasing the applied potential difference between the cathode and anode. It can be seen that an increase in kV results in an increase in intensity but also decreases the minimum wavelength. A decrease in minimum wavelength permits a higher penetrating beam. It should be noted that although increasing the kV increases intensity an increase in target current also increases intensity without any alteration to the wavelength. The increase in target current is directly proportional to the increase in intensity.

Exposure is therefore controlled by adjusting the potential so that there are sufficient wavelengths to penetrate the test object and adjusting the target current and or time of exposure to allow enough photons to reach the recording medium.

As mentioned previously X-rays conform to the laws of light and as such diverge when they are emitted. The distance between the anode and the recording medium is therefore important when developing and exposure. If an area of 40 mm^2 is exposed at a distance of 300 mm then at $d = 600 \text{ mm}$ an area of 1600 mm^2 will be exposed. For $d = 600 \text{ mm}$ four times the amount of radiation is required to achieve the same radiographic density as at $d = 300 \text{ mm}$. Therefore a doubling of the anode to recording

medium distance requires four times as much radiation intensity. The inverse square law can be expressed as follows:-

$$\frac{I_1}{I_2} = \frac{D_2^2}{D_1^2}$$

(4-7)

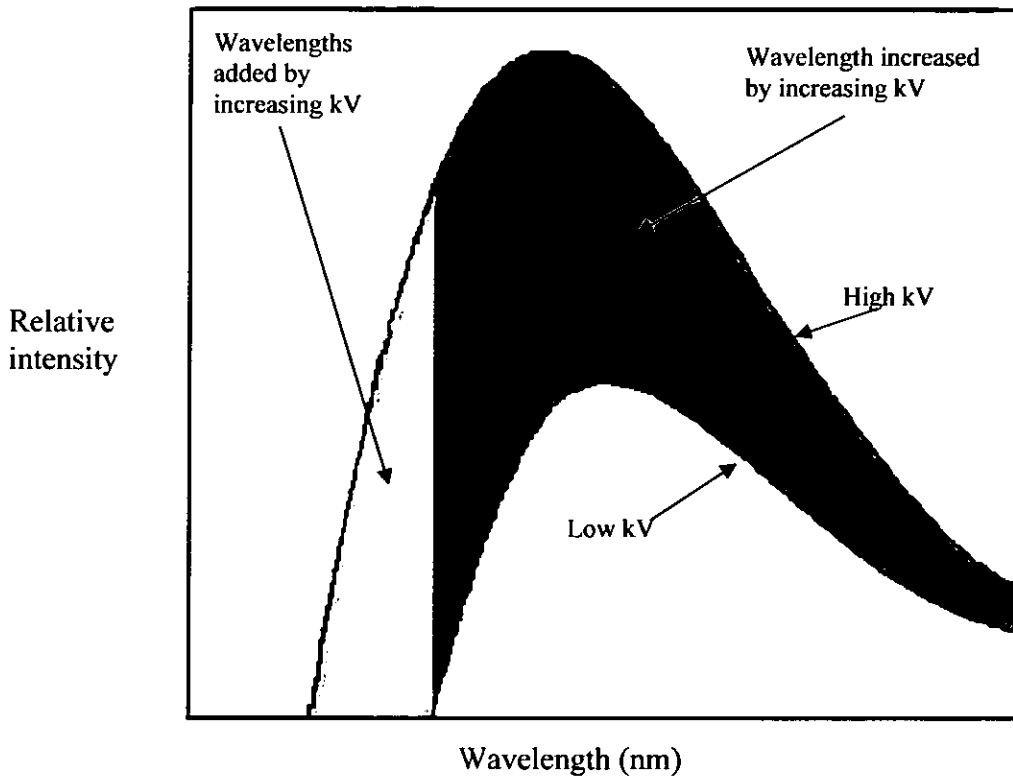


Figure 4-10 A plot taken from the Kodak radiography in modern industry text showing the effect of increasing kilovoltage.

4.4. Micro focus generation sources

Micro-focus X-ray generation systems can deliver X-rays from a focal spot as small as 5 μm . This allows for very sharp images and also permits substantial geometric magnification. The very fine focus is achieved by using a single wire for the filament in preference to a coil and using coils around the beam of electrons to focus them prior to bombarding the anode. Whilst micro-focus system have the advantage of producing a very fine focal point there are disadvantages. The problems associated with micro focus generation are:

- The filament life time is shorter than a conventional tube as the electrons have to be generated from a smaller cross section. The filament has to pass more current in order to free the same amount of electrons as a conventional X-ray source.
- The anode can only withstand around 80 watts in such a tight focal spot before it is damaged which means that either the X-ray intensity is reduced or the maximum potential difference is limited.
- Micro-focus sources are expensive; approximately two to three times the price of a conventional source.
- Sealed micro-focus sources have to be treated with care as damage cannot be rectified.

Recent developments however have alleviated some of the problems associated with micro-focus X-ray generators. Open gun technology (probably derived from electron microscope manufacturing techniques) allows the X-ray source to be opened for maintenance and re-assembled within a few minutes. The filament which is the weakest point of the X-ray source can therefore be easily renewed. Filament currents which in sealed sources have to be carefully controlled can now be increased knowing that the shortened life that results can be readily rectified.

The diagram below shows a typical layout of a micro-focus system. The manufacturer has to carefully design the focussing cup to obtain maximum control of the electrons without impairing the acceleration towards the anode. The two focussing coils surround the electron beam as they approach the anode and the magnetic field produced by the coils forces the electrons into a narrower path. Air is constantly evacuated from the gun via a turbo pump.

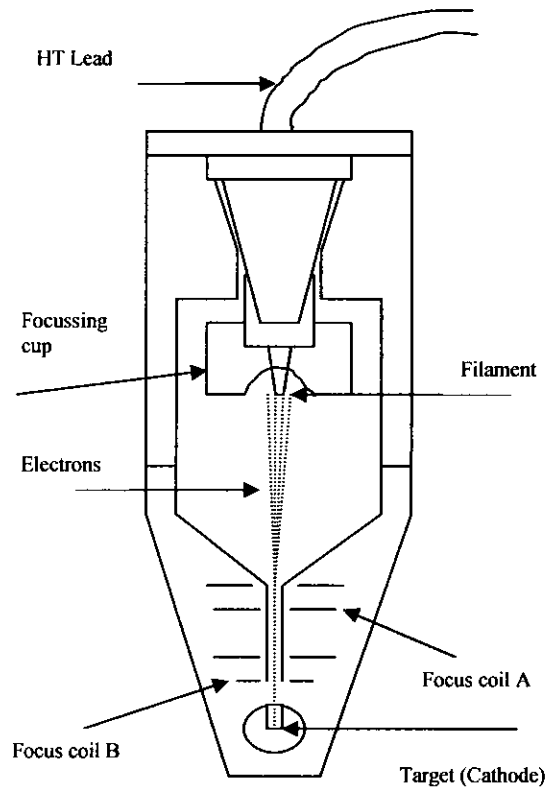


Figure 4-11 Schematic showing a cross section of a typical micro-focus x-ray generation tube.

4.5. Image Parameters

The ability of the industrial radiographer to reliably detect defects is dependant on three major imaging factors. These are

- Image quality.
- Viewing conditions.
- Experience of the interpreter.

4.6. Image quality

The re-construction of an object in a radiographic image is never perfect. Geometric distortion and unsharpness will effectively deteriorate the final image. Sprawls [Sprawls 1995] identified five components that contribute to the image quality namely contrast, noise, blur, artefacts and distortion. Each one of these components will, if not optimised for the

application, result in defect detection being impaired to a point where significant indications cannot be interpreted.

Contrast and spatial resolution have been reported by Halmshaw [Halmshaw 1971] as being two of the most important parameters for radiographic imaging.

4.6.1. Contrast

Image contrast can be divided into two sectors i.e. that of subject contrast and contrast sensitivity of the imaging system.

Subject contrast is the difference in transmitted X-rays through one part of the object when compared to another. The ideal situation here would be that no radiation penetrates the defect and therefore the maximum subject contrast is achieved i.e. 100%. Because of the nature of defects found in materials described in chapter 2 there is rarely sufficient difference in the defects atomic number, density or thickness to fully attenuate the incoming radiation and therefore the maximum possible contrast is reduced. In the inspection of composites the subject contrast is very low as carbon fibre composites have a low atomic number, the density is low and typical defects are thin laminar air pockets or low density material inclusions. Defects therefore exhibit very small changes in radiographic attenuation compared with the parent material. Super plastically formed titanium structures however do exhibit greater subject contrast as titanium is relatively dense material and the sections in the region of interest do have substantial changes in thickness. A split in the X-core structure can be difficult to image however, as the defect usually occurs in a region where significant thinning of the material has occurred and can be masked by overlapping structure. Defect contrast in this case is therefore quite low. Subject contrast can be defined by:-

$$C = \ln I_1 - \ln I_2 \tag{4-8}$$

Where I_1 and I_2 are the transmitted radiation intensities through two different thickness of material.

Sprawls et al [Sprawls 1995] have demonstrated that defect contrast can be defined by the linear attenuation coefficients of the material and the defect in question and the thickness of the defect i.e.

$$C = (\mu_m - \mu_d)t_d \quad (4-9)$$

where μ_m and μ_d are the linear attenuation coefficient of the material and the defect respectively, t_d is the thickness of the defect. From this it can be clearly seen that contrast is directly proportional to the thickness of the defect with a constant of proportionality equal to the difference in the attenuation coefficients.

4.6.2. Noise

The ultimate response of an imaging system would be one where only the subject details are present in the image. In this case parts of the subject that were constant in terms of radiographic attenuation would be represented in the image by a constant density. Practically this is never the case as it is difficult to predict the X-ray interactions with matter because of the dependency on a materials atomic number and the incident photon energy which results in different radiation patterns occurring over areas where the radiation has passed through the same thickness of material. Coupled to this each electronic module of the image conversion system will contribute noise in some way due to the inherent thermal properties of the electronic devices being used. This results in the actual image formed not truly representing the object under inspection. During the interaction of the incoming photons with the material under investigation two possible scattering effects can occur.

These interactions are photoelectric and Compton scattering. Photoelectric interactions are dependant on the energy of the incoming photon and its relationship to the binding energy of the electron. The probability of the photoelectric effect occurring is most dominant when the photon energy is the same or slightly higher than that of the electron. In this case the energy from the photon will be used to remove the electron from the atom and the remainder will be transferred to the electron in the

form of kinetic energy. As the electron is removed from its shell an outer electron must move down a level to fill the vacancy, in doing this the drop in energy produces a characteristic X-ray photon. The significance of this effect is that a defect that is detectable because of a difference in the atomic number of the defect and parent material is very dependant on the photon energy or kV(p). Low atomic numbered materials however will be restricted to low kV(p) values whereas contrast produced from defects with high atomic material numbers do have a wider range of kV(p) values in which the photoelectric effect will be significant.

Materials and flaws that depend on a change in density for good contrast separation rely on Compton scattering as the main attenuator of the photon energy. In this case photons entering the material are deflected by the electron and the photon changes its direction of travel. When this happens some of the energy from the photon is absorbed by the electron and the photon changes wavelength. Whilst Compton interactions attenuate the photon there is a problem that photons that are not totally attenuated by recursions of this process within the material that exit in a forward direction will interfere with the image in the form of noise.

Scattered radiation and electronic noise are two key factors that affect image contrast and therefore the ultimate defect detection capabilities.

4.6.3. Scattered Radiation

One major influence on the detectability of a radiographic imaging system is the presence of scattered radiation. Maher (Digital Radiography notes web page) uses the Floyd et al [Floyd 1997] formula below to demonstrate that small amount of scatter in relation to the primary beam can have a large effect on the defect detection.

$$C = \ln \left(\frac{1 + SPR}{\exp^{-(\mu_m - \mu_d)td} + SPR} \right) \quad (4-10)$$

Where SPR is the ratio of scattered radiation intensity to primary radiation.

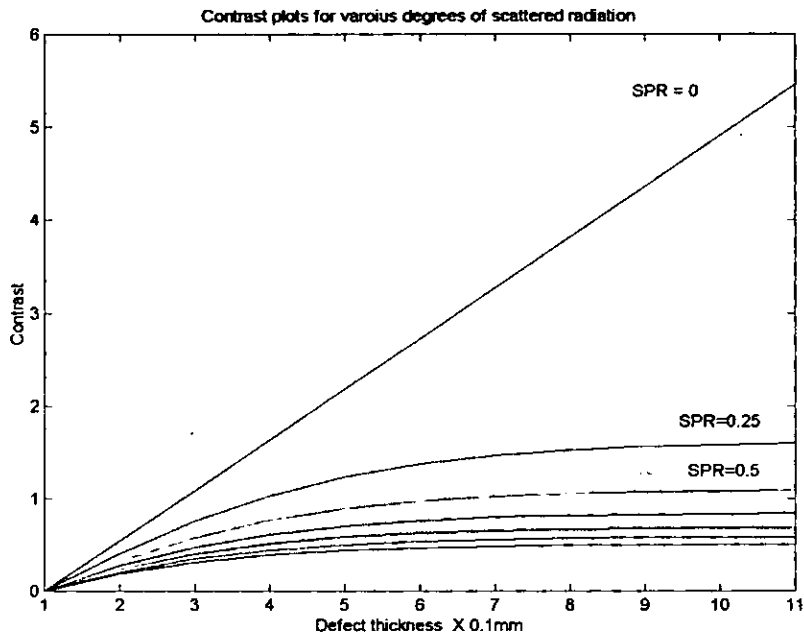


Figure 4-12 graph depicting the effect scattered radiation has on defect detection.

The graph above demonstrates that an increase in scattered radiation significantly decreases the contrast between the material and the defect.

When the ratio of scattered radiation to primary radiation (SPR) is zero then the contrast is purely a function of the difference in linear attenuation coefficients multiplied by the thickness of the defect. However the introduction of scattered radiation significantly reduces contrast. A value of 0.25 reduces contrast to less than 50%.

Halmshaw [Halmshaw 1971] manipulates this formula and introduces the characteristic gradient of the detection system to give:

$$C = \frac{2.3\Delta D}{\mu_x G_D} \left(1 + \frac{I_s}{I_D} \right) \quad (4-11)$$

Where

ΔD is a value representing the minimum discernable change in radiographic density. Typical values range from 0.008 to 0.01.

μ_x = the difference in linear absorption coefficient.

G_D represents the gradient of the recording medium.

I_s and I_D are the scattered and direct radiation respectively.

It can be seen that film gradient and change in density also play a role in successfully detecting defects.

Both equations 4-10 and 4-11 emphasise the importance of the ratio of scatter to primary radiation, Mascovski [Mascovski 1983] uses a broad beam model to analyse the factors affecting scattered radiation and proposes the following mathematical formula:-

$$SPR = 2\mu_{sr}bL\left(L + R - \sqrt{L^2 + R^2}\right)\left[1 - \frac{s}{\sqrt{R^2 + s^2}}\right] \quad (4-12)$$

Where μ_{sr} is the scattering attenuation coefficient.

b is the fraction of scattered photons that scatter in a forward direction as opposed to being reflected and the remainder are geometrical components described in figure 4-13 below.

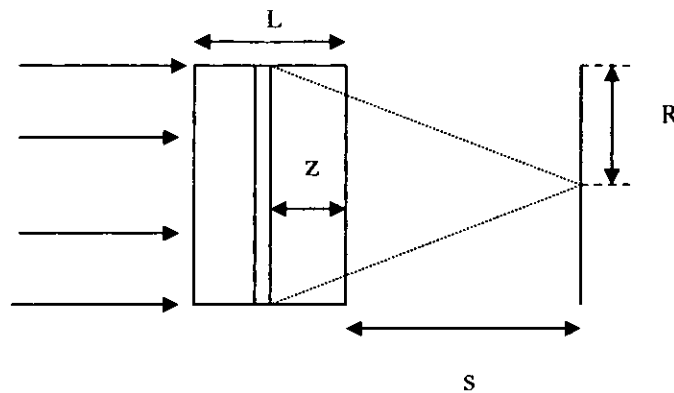


Figure 4-13 Geometrical set up for the Mascovski model

From the description above it is clear that the distance from the object to the image receiver (s) reduces the scattering effects as the distance increases. For the inspection cases described previously scattered radiation has more of an effect for film radiography than micro-focus digital radiography. When using film in these instances the cassette is usually placed directly behind the object i.e. $s = 0$ whereas for digital radiography the image receptor can be some distance from the object $s \gg 0$ therefore reducing the effect of scattered radiation.

4.6.4. Unsharpness

A radiographic image that clearly shows all the boundary detail is often described as being sharp. Geometry effects, blurring, and scattered radiation reduce the sharpness of the image. Blurring usually occurs at the edge of changes in cross sectional area and is due to the radiation over penetrating the edge and scattering effects being more pronounced from the edge geometry. This is usually overcome by blanking the edges with dense material or ensuring that the object covers the image receptor. Geometrical unsharpness caused by the focal spot and object position has been described previously however absorption, motion and reception unsharpness all contribute to the total unsharpness of an image. In film radiography motion unsharpness should be zero and the unsharpness caused by the film grain should be negligible. In digital radiography however motion, geometric and receptor unsharpness are all intrinsically linked as it is common to attempt to overcome receptor unsharpness by geometric magnification. By doing this any movement of the object during acquisition or focal spot effects will have a detrimental effect. It is therefore very important when implementing digital radiography to ensure that the source to object distance and object to recording device distance is compatible with the focal spot size.

Halmshaw et al [Halmshaw 1971] have derived a formula based on Klasens theory [Klasens 1946] for the optimum magnification. The ASTM standard [ASTM 2003] also uses the same formula:-

$$M_{opt} = 1 + \left(\frac{U_f}{\phi} \right)^{\frac{3}{2}} \quad (4-13)$$

where U_f is the unsharpness of the receptor

ϕ is the focal spot width.

And M_{opt} is the optimum magnification.

The derivation of this formula is taken from Klasens [Klasens 1946] and the simple relationship between geometric unsharpness, focal spot size and image magnification.

From equation 4-5 and taking the maximum required value of geometric unsharpness (U_g) to be equal to the detector unsharpness the maximum magnification becomes

$$m_{\max} = \frac{U_f}{\phi} + 1 \quad (4-14)$$

and from Klasens total unsharpness U_t can be calculated by:-

$$U_t = (U_g^3 + U_f^3)^{1/3} \quad (4-15)$$

Halmshaw et al then go on to further derive the optimum unsharpness by correcting for the magnification of the image i.e.

$$U_t = \frac{1}{M} [U_f^3 + (M-1)^3 f_s^3]^{1/3} \quad (4-16)$$

and by differentiation with respect to M

$$\frac{\delta U_t}{\delta M} = -\frac{1}{M^2} [U_f^3 + (M-1)^3 f_s^3]^{1/3} + \frac{1}{3M} [U_f^3 + (M-1)^3 f_s^3]^{-2/3} \times 3(M-1)^2 f_s^3 = 0$$

Multiply by M^2 and re-arrange:-

$$[U_f^3 + (M-1)^3 f_s^3]^{1/3} = \frac{M}{3} [U_f^3 + (M-1)^3 f_s^3]^{-2/3} \times 3(M-1)^2 f_s^3$$

Multiply both sides by $[U_f^3 + (M-1)^3 f_s^3]^{2/3}$ gives:-

$$U_f^3 + (M-1)^3 f_s^3 = M(M-1)^2 \text{ and dividing both sides by } f_s^3 \text{ gives:-}$$

$$\left(\frac{U_f}{f_s}\right)^3 + (M-1)^3 = M(M-1)^2 \text{ and since}$$

$$(M - 1)^3 = M^3 - 3M^2 + 3M - 1 \text{ and } (M - 1)^2 = M^2 - 2M + 1$$

$$M(M^2 - 2M + 1) - (M^3 - 3M^2 + 3M - 1) = \left(\frac{U_f}{f_s}\right)^3$$

therefore:-

$$M^2 - 2M + 1 = \left(\frac{U_f}{f_s}\right)^3 \quad M - 1 = \pm \left(\frac{U_f}{f_s}\right)^{3/2}$$

finally

$$M_{opt} = 1 \pm \left(\frac{U_f}{f_s}\right)^{3/2}$$

(4-17)

Halmshaw [Halmshaw 1971] does go on to explain that the optimum value of M for varying specimen thickness is not constant as the formula above would suggest and proposes that screen brightness, object contrast and the ability of the human eye to resolve fine detail play an important part in finding the optimum magnification.

One problem with this work is that it is based around focal spot sizes of around 0.3 mm. Modern radiation generators have the ability to focus the electrons to micron focal spot sizes and this is therefore beyond the limits of the work described previously. Sprawls and many other authors have agreed that a more robust method for determining the overall unsharpness U_t is to use either Klasens [Klasens 1946] or the formula below but calculate the detector unsharpness taking into account the magnification factor. For instance a detection system that has an inherent unsharpness of 0.25 mm will effectively display an unsharpness value of 0.125 at a 2:1 magnification factor. The result is therefore that as the object is magnified the effect of inherent detector unsharpness is reduced but the geometric unsharpness increases. Sprawls [Sprawls 1995] et al suggest the use of Nomograms to evaluate the overall unsharpness, where U_g , U_t and motion unsharpness are plotted along with the total unsharpness calculated using the following:

$$U_r = \sqrt{U_f^2 + U_g^2 + U_m^2} \tag{4-18}$$

Using the square root of the sum of the squares deviates from the Klasens proposal but in practice has little effect on the overall result. Here U_f is calculated from the following:-

$$U_f = U_{inherent} / Magnification \tag{4-19}$$

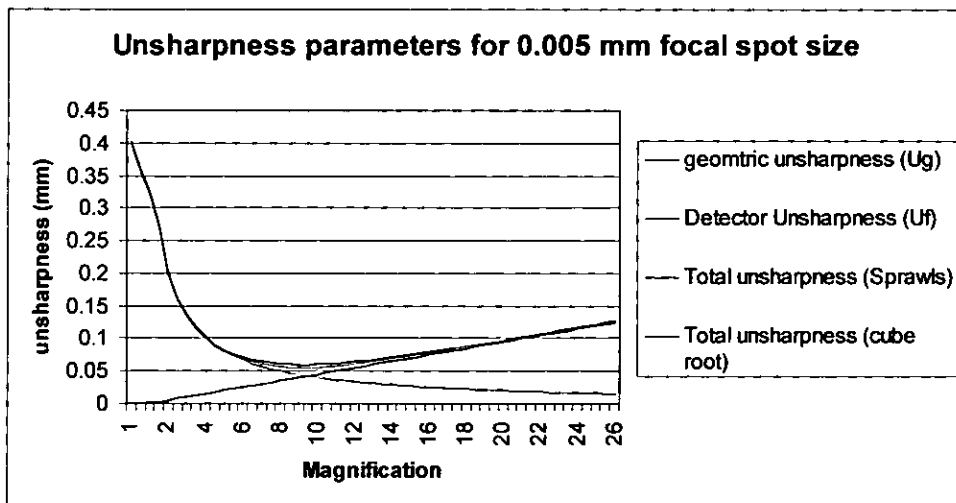


Figure 4-14 Graph plotting the Sprawls unsharpness and the cube root calculation

From the nomogram above it can be clearly seen that the optimum unsharpness occurs at a magnification value of 9.5 and that the difference in total unsharpness varies only slightly by using the square or cube root method for the calculation. From the above it can be seen that the detector unsharpness can be overcome by magnification up to a point where geometric unsharpness becomes the major unsharpness contribution. From the nomogram above the optimum magnification seems to occur at the point where the total unsharpness is at a minimum. However, if a plot is taken of the ratio of a detail in the object compared to the total unsharpness it can be shown that the optimum magnification occurs at a different magnification point to that of the optimum unsharpness.

Below are a series of graphs that have been calculated using the Klasens unsharpness calculation in (4-15) but using the equation in (4-19) to determine the detector unsharpness prior to calculating the total. The inherent detector unsharpness was 0.25 mm in all cases.

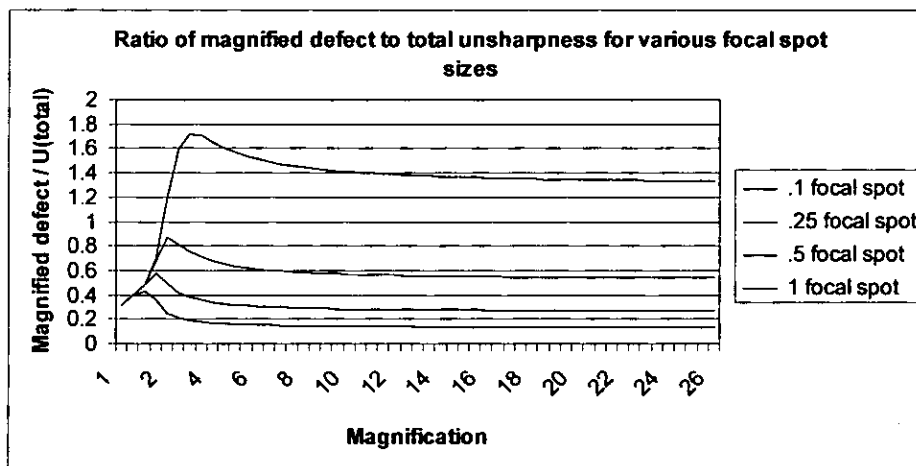
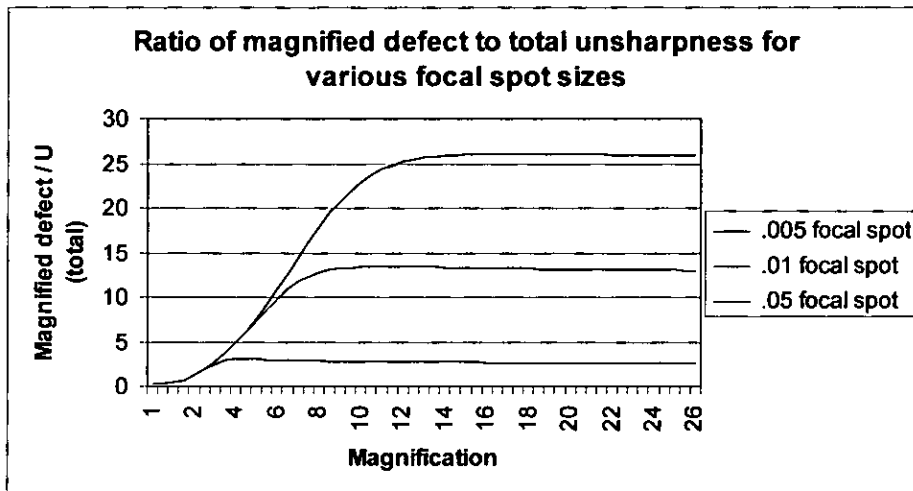


Figure 4-15 two graphs showing the magnified defect to unsharpness ratio as a function of magnification.

A series of observations can be made from the graphs above:-

1. The inherent unsharpness can only be overcome when the focal spot size is smaller than the inherent unsharpness
2. An improvement by geometric magnification is only achieved when the ratio of inherent detector unsharpness to focal spot size is less than ten. Otherwise an image at zero magnification produces the optimum result.

3. For detector unsharpness to spot size ratio greater than 5 there is little image degradation beyond the optimum magnification.
4. Even for small focal spot sizes i.e. 5 μm the optimum magnification is only 13.5. In these cases the use of higher magnification factors will not geometrically improve matters but may be used for spatial measurement improvements.

The derivation from Klassens should therefore include the magnification in the contribution from detector unsharpness. Equation 4-16 would therefore become:

$$U_t = \frac{1}{M} \left[\frac{U_f^3}{M} + (M-1)^3 f_s^3 \right]^{1/3} \quad (4-20)$$

Differentiating gives:-

$$\frac{\delta U_t}{\delta M} = -\frac{1}{M^2} \left[\left(\frac{U_f}{M} \right)^3 + (M-1)^3 f_s^3 \right]^{1/3} + \frac{1}{3M} \left[\left(\frac{U_f}{M} \right)^3 + (M-1)^3 f_s^3 \right]^{-2/3} \cdot \left[-\frac{3U_f^3}{M^4} + 3(M-1)^2 f_s^3 \right] = 0$$

then multiply both sides by $\left[\left(\frac{U_f}{M} \right)^3 + (M-1)^3 f_s^3 \right]^{1/3}$ and re-arrange :-

$$\frac{1}{M^2} \left[\left(\frac{U_f}{M} \right)^3 + (M-1)^3 f_s^3 \right] = \frac{1}{M} \left[-\frac{U_f^3}{M^4} - (M-1)^2 f_s^3 \right]$$

then

$$\left(\frac{U_f}{M} \right)^3 + (M-1)^3 f_s^3 = -\frac{U_f^3}{M^3} + M(M-1)^2 f_s^3$$

therefore:-

$$\left(\frac{2U_f^3}{M^3} \right) = (M^3 - 2M^2 + M - M^3 + 3M^2 - 3M + 1) f_s^3$$

Finally

$$(M - 1)^2 = \frac{2U_f^3}{M^3 f_s^3}$$

$$M_{opt} = 1 \pm \sqrt{\frac{2U_f^3}{M^3_{opt} f_s^3}}$$

(4-21)

for which there is no solution and has to be solved by iteration.

The minimum value for the function can be found by implementing the following formula in MATLAB and using the Fminsearch routine.

$$Min = \left(M_{opt} - 1 \pm \sqrt{\frac{2U_f^3}{M^3_{opt} f_s^3}} \right)^2$$

(4-22)

Results obtained from this calculation are shown in the plot below

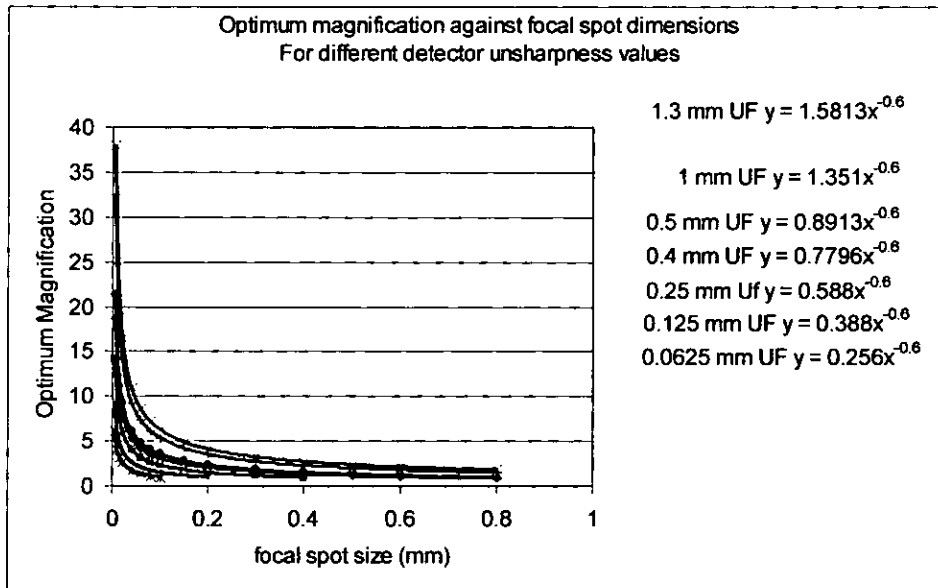


Figure 4-16 Plots of optimum magnification against focal spot size for detector unsharpness values of 0.0625 mm to 1.3 mm.

The graph above has been calculated using detector unsharpness values of 1.3, 0.4, 0.25, and 0.125 mm. The 1.3 mm value was used to compare with the Halmshaw experiments. All other values are considered typical for modern detection systems. Optimum magnifications of less than 1

result from the situation where the focal spot size is the major contributor to the overall unsharpness. In these cases the optimum magnification would be 1, as it is not geometrically possible to have magnification factors less than 1.

Earlier works to derive optimum magnification were limited by the available generators with small focal spot sizes. Below shows a comparison of equation 4-16 and the results above for focal spot sizes of 0.1 mm and greater.

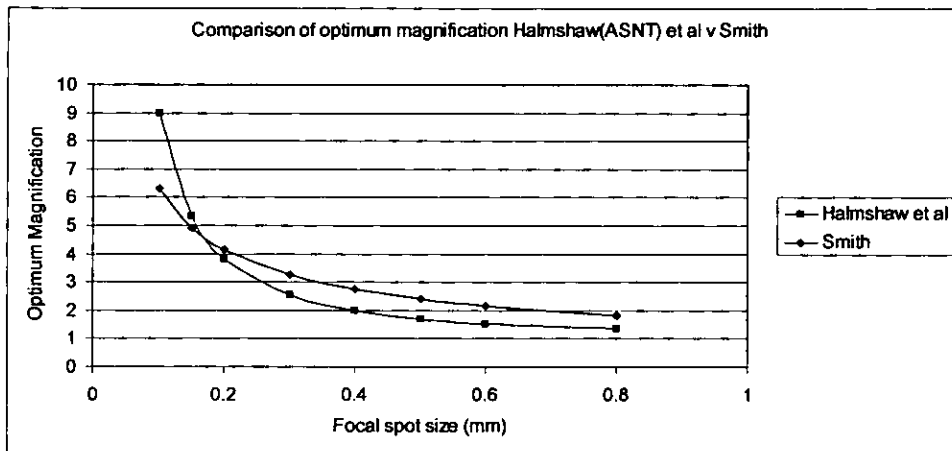


Figure 4-17 Graph showing the difference between the early Halmshaw/ASTM calculations for optimum magnification and the formula derived in this thesis.

It can be seen from the above graph that the two curves deviate considerably for focal spot sizes of 0.1 mm and less. The difference in magnitude above 0.3 mm may be due to the potential error of the human observer used in the early experiments.

Obtaining the point for each focal spot calculation where the optimum magnified object detail to unsharpness value is reached, a plot can be constructed for a number of detector unsharpness and focal spot values and used to obtain the formula for optimum magnification.

$$M_{opt} = (1.351 \times U_f^{0.6}) \times f_s^{-0.6}$$

(4-23)

Equation 4-23 is valid when the detector unsharpness is greater than the geometrical unsharpness and therefore total unsharpness can be improved by geometric magnification. In cases where the focal spot size is the significant contributor to the total unsharpness the optimum magnification will always be 1 which differs from the derivations of Halmshaw and that given in the ASTM standard [ASTM 2003].

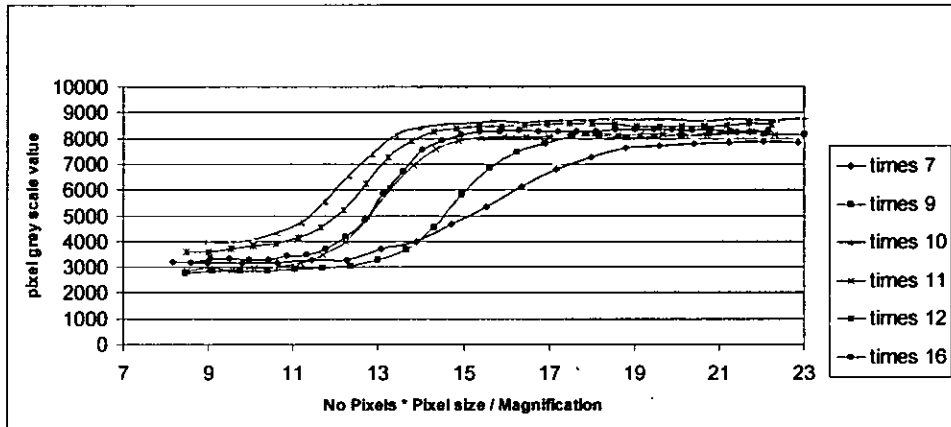


Figure 4-18 Measured unsharpness from an imaged 1mm hole at various magnifications.

The plot above was calculated from an experiment where thin optical disks with holes ranging from 100 μm to 1 mm were imaged at 7, 9, 11, and 16 times magnification. The profile of the edge of the 1 mm holed disk was evaluated for each magnification and plotted as above. From the results shown it is clear that there is a definite improvement in unsharpness at magnifications above 7. It is difficult to determine the optimum magnification as there seems to be little difference above 11 times magnification. The images were captured using a detector with a 0.127 pixel size and the focal spot was estimated at being less than 0.01 mm. Comparing the graph above with the calculated results in fig 4-15 (page 144) there is good agreement between the calculated result for a 0.005 mm focal spot and the results above. Calculated optimums for 0.005 mm and 0.01 mm focal spot sizes are 12.5 and 8.5 respectively and the optimum magnification from the above data is estimated at a magnification of 11. The slight difference in calculated and experimental results is due to variations in spot size and the resolution of the calculation.

4.6.5. Blur

Blur can be described as a smoothing effect that reduces the contrast of image details. Small image features that possess a reasonable linear attenuation difference from that of the parent material i.e. exhibit good contrast parameters can still be difficult to detect because of the blurring effect of the image collection device and/ or blurring caused by noise. Whilst noise effects have been discussed previously blur can also occur in the image conversion device. Blur due to the image conversion device is usually related to the thickness of the conversion material used. The thicker the material the better the conversion efficiency but this also brings with it a longer path length for the light to travel and spread through the conversion material and therefore photon interactions over a small area on the screen surface are enlarged by the time the light exits the opposite side.

4.6.5.1. Motion Blur

Most radioscopic systems used for industrial applications have motion control systems to manipulate the part, the X-ray generator, the detection device or any combination of the three. The ability to move the X-ray devices and or the part does mean that images could be collected whilst either the source ,detector or component or any combination of these three are in motion. In the extreme this will be obvious as the resulting image would be very blurred and not interpretable. Small amount of movement whilst the image is being captured may however go unnoticed. The automated systems studied in this work were programmed to follow a pre-determined scan path but stop movement as each image acquisition site was reached. One manipulator system is fitted with DC servo motors whilst the other is fitted with stepper motors. The stepper motor system is controlled by sending clock and direction pulses to the amplifiers which in turn increment the motor for each pulse transmitted. Once the pulse train stops, the stepper motor rotation stops irrespective of the position achieved. DC servo motors however are normally fitted with encoders that provide positional feedback to the control circuits. On command a DC servo will accelerate towards its target position and come to rest when the position is

found by the encoder. The encoders are extremely accurate and the resolution is in the region of 100 to 200 counts per millimetre. The problem here is that a DC servo motor will never completely achieve its position but will be very close, within a pre-set error band. Having reached its final position within the error band the motor will servo to maintain its position until it receives another command. If the error band is too wide the manipulation system will lose accuracy but if the error band is too narrow then due to mechanical tolerances it will be impossible for the motor to achieve the position. In this case the motor will overshoot the position, change direction in an attempt to correct the error and overshoot in the opposite direction. Eventually the motor will go into oscillation as it continues to drive in successive positive and negative directions searching for the correct encoder position. When the error band is set so that oscillation does not occur and positional accuracy is within tolerance the servo motor still attempts to maintain position having initially reached its target. This servoing in position can be the cause of motion blur in a radiosopic system and it is important that motion is kept to less than pixel size whilst images are being captured.

Motion control and error analysis due to motion control parameters is discussed in detail in chapter 6.

4.6.6. Total Unsharpness or blur

The total blur or unsharpness in an image has three contributing factors, namely motion blur, geometric unsharpness caused by the focal spot and inherent unsharpness of the detection system all of which have been discussed previously. Sprawls [Sprawls 1995] defines total blur by the following formula but states that if one of the contributing factors dominates then the value of the dominant is generally regarded as the total blur value.

$$B_t = \sqrt{B_r^2 + B_f^2 + B_m^2} \tag{4-24}$$

where B_r , B_f and B_m are blur caused by the receptor, focal spot and motion respectively.

For small focal spot sizes geometric magnification can be used to overcome receptor blur. Equation 4-20 and 4-26 states that as the focal spot gets smaller the optimum magnification increases. There is however a point where the size of the focal spot becomes significant and therefore the major source of unsharpness. In the medical field nomograms are used to determine the radiographic blur at different object locations these graphs are constructed to plot the three types of blur and their effect with respect to object location and also plot the total blur for object location. The figures below show a typical nomogram for a mini and micro focus system using the same receptor. It can be clearly seen that using a micro focus source practically eliminates the blur caused by the focal spot and total unsharpness can then be minimised by use of geometric magnification. The minimum total unsharpness for a mini focus system however is restricted to a point where the focal spot size becomes a significant addition to the total blur. At this point the total unsharpness has been reduced from 0.25 mm to 0.16 mm and this is the minimum image blur possible.

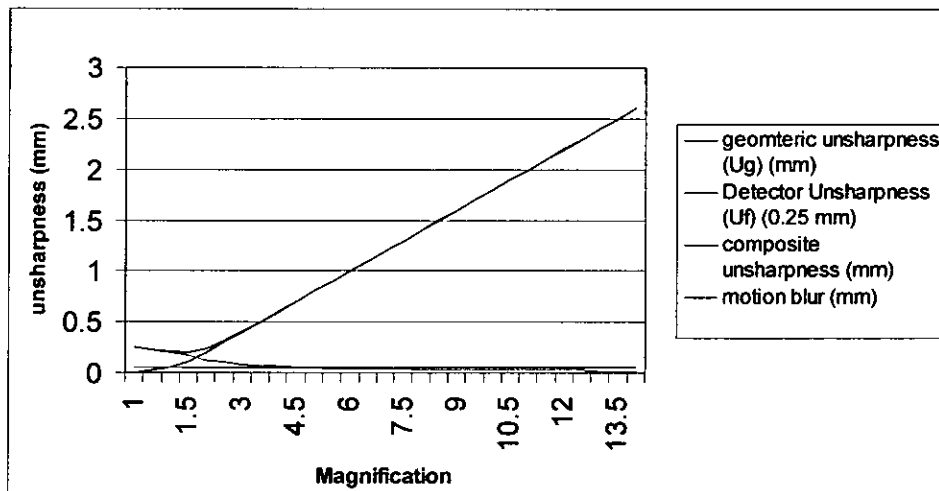


Figure 4-19 Results from the calculations proposed by Sprawls for a mini focus system with an inherent detector unsharpness of 0.25 mm

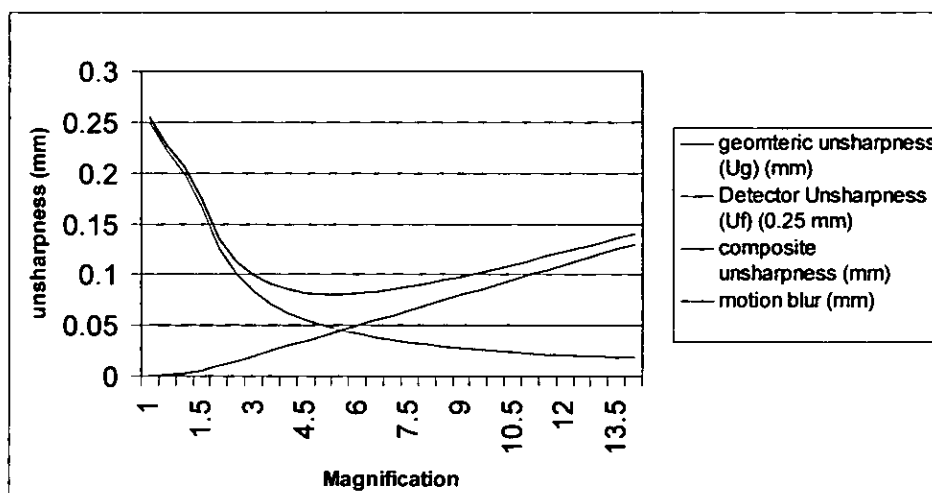


Figure 4-20 Results from the calculations proposed by Sprawls for a micro focus system with an inherent detector unsharpness of 0.25 mm.

Maintaining a micro focus spot in the order of μm is difficult and specially adapted focussing coils have to be used. These coils have to be constantly adjusted as the kV is increased to a point where the total power being focussed on such a small area of the tungsten target will damage the surface. At this point the photons released from the target decrease as the hole or pit that has resulted from too much power causes a heel effect where photons are absorbed within the tungsten hole boundaries. High power micro focus radiography is therefore a compromise between achievable focal spot size and energy.

4.6.6.1. Distortion

Image distortion is a measure of an objects dimension within an image compared to the physical dimensions of the actual object. Distortion can be caused by geometric effects particularly when placing the object very close to the source and hence acquiring an image of high geometric magnification or by the detection system itself. Geometric distortion effects usually correspond to variations in the magnification factor from features that do not lie on the same plane. The diagram below demonstrates this principle.

Distortion by dissimilar magnification is to be expected and is easily corrected for. Distortion caused by the detection system is discussed later in the description of the image intensifier but does require careful

assessment and calibration before image processing methods can be used for correction.

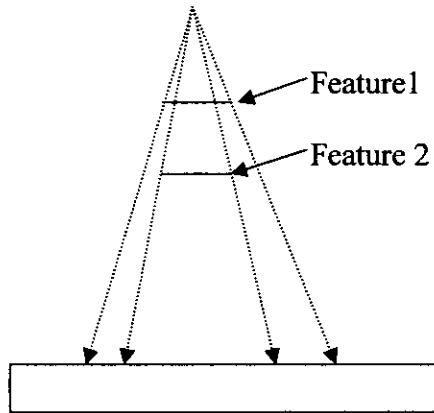


Figure 4-21 Simple diagram to explain distortion by magnification.

4.7. Image Formation systems

4.7.1. Film

Radiographic film is a layered structure in which a polyester base material supports an emulsion. The emulsion is the active component and can either be layered on one or both sides of the base material. The emulsion is made from silver halide crystals suspended in gelatine. The purpose of the gelatine is to separate the crystals and protect them from damage during handling. Typical emulsions are around 10 μm thick.

The silver halide in general use for radiographic purposes is silver bromide. Silver bromide comes in the form of crystals or grains and each grain contains around 10^9 atoms [Sprawls1995].

Each film grain contains a large number of silver and bromide ions. The silver ions have one electron missing and the bromide contain an extra electron. The silver is therefore positively charge and the bromide negatively charged. Each grain has a structural defect known as a sensitive speck. When photons interact with the emulsion the absorption of photons by the bromide generates a free electron. The free electron is attracted to

the sensitive speck and as it moves towards the speck it becomes negatively charged. The speck therefore attracts a positively charged silver ion which is neutralised as it reaches the speck. This action converts a silver ion into an atom of black metallic silver. The agent that actually exposes a photographic grain, that is, a silver bromide crystal in the emulsion, is not the X-ray photon itself, but rather the electrons--photoelectric and Compton, resulting from the absorption event. The Black metallic silver atoms are still transparent and further chemical processing has to be carried out in order to render the affected atoms visible. After exposure but prior to development the film is said to contain a latent image.

As the conversion of the film emulsion to the latent image is directly related to the photoelectric and Compton scattering processes the amount of energy entering the emulsion is proportional to the number of crystal grains that will be converted and hence the final density of the film after processing.

Film grain size can be varied depending on the task. Grain size can be made larger which effectively reduces the required exposure time but increases the unsharpness or inversely grain can be made smaller with a resulting longer exposure time but increased resolution. Due to the nature of the emulsion and its small grain size radiographic film exhibits a very high special resolution and is also capable of re-producing images of objects that have small density differences. The exposure time used for film radiography allows the photoelectric and Compton effects to continue for a period of time which in turn causes more end more interactions with the emulsion grains.

This accumulation of events creates subtle changes in the image due to low absorbing objects to become more visible. In comparison digital radiographic detection systems are usually of lower resolution and cannot distinguish very subtle density changes, one because they have a lower conversion efficiency and two because there is little or no mechanism that allows the accumulation of photon energy or its effects. Digital image processing can be implemented to increase contrast but the limitation of the conversion efficiency still restricts the overall image quality.

4.7.2. Image intensifiers

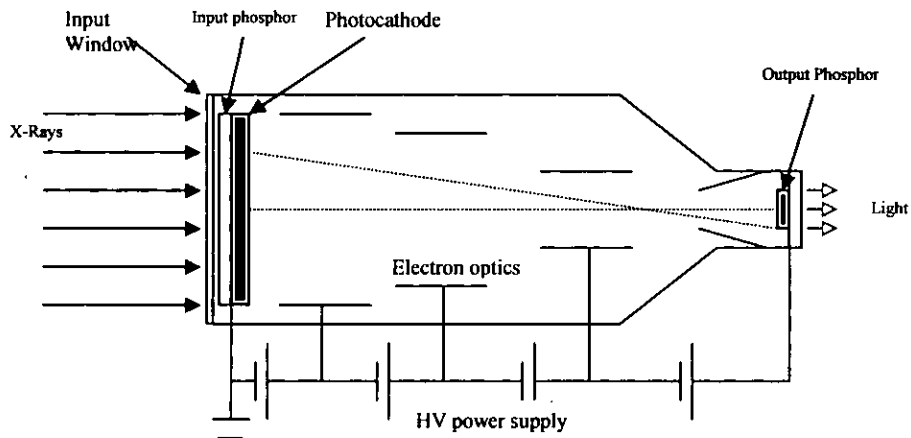


Figure 4-22 Cross section of a typical image intensifier.

The figure above identifies the key modules of an industry standard image intensifier. In short the intensifier is usually cylindrical and evacuated of air. X-rays that have passed through the object reach the input window, pass through it and bombard the input phosphor. The input phosphor which is usually cesium iodide but can be gadolinium oxysulfide scintillates and the resulting photons pass through to the photocathode. Here the emitted photons are converted to electrons and are accelerated towards the output phosphor.

The electrons are focussed towards the output phosphor via the electron optics and on reaching the output phosphor the electrons are converted back to light. The emerging light has a substantially greater intensity due to the acceleration process and therefore is at a suitable level to be imaged using a CCD camera.

The diagram above shows the input phosphor and photocathode as being flat. If this was the case then severe image distortion would occur due to the irregular path lengths of the accelerated electrons. In practice the input screens are spherical which attempts to overcome distortion but results show that there is still significant image distortion with these recording systems.

Parameters that are significant to these devices are the conversion factor, the contrast ratio, the detective quantum efficiency and the modulation transfer function. The conversion factor is the ratio of light output to the input radiation. i.e.

$$\text{conversionfactor} = \frac{\text{Luminance - of - output - phosphor.....(CdM}^{-2}\text{)}}{\text{Input - Air - Kerma - rate.....}(\mu\text{Cys}^{-1})}$$

(4-25)

The output luminance is measured with a photometer and the input radiation with an ionisation chamber. For safety reasons this measurement requires specialised interfacing and therefore the following comparisons have been made using the manufacturers data.

Considering that an average light bulb emits around 10^6 Cd m^{-2} , the output from an image intensifier is relatively weak even after significant amplification.

The contrast ratio is usually measure by placing a lead disk in the centre of the screen and an image collected. The lead disk is then removed and another image is acquired. The contrast ratio is then described as :-

$$\text{Contrastratio} = \frac{\text{Luminance - of - centre - open - field}}{\text{Luminance - with - 10\% - blocked - by - lead - disk}}$$

(4-26)

As mentioned previously scattered radiation at the input will reduce this factor as will scattered light at the input and output phosphor stages.

4.7.3. Flat Panel X-ray image receptors

Flat panel detectors make use of technology similar to that of the active matrix liquid crystal displays where a large area integrated circuit i.e. an active matrix of many semiconductor elements deposited on a substrate material are used to acquire the signal corresponding to amount of X-rays impinging on the surface. Two types of flat panel detector are used the most common being the indirect Amorphous silicon type the other being a relatively recent development in amorphous selenium. Amorphous silicon

is termed an indirect detector whereas selenium is termed as being a direct conversion system.

4.7.3.1. Amorphous silicon

An amorphous silicon radiographic detector consists of an amorphous silicon layer deposited on a glass substrate which is then etched into a pixel array. This technology evolved from the developments of flat panel liquid crystal displays which make use of the ability of amorphous silicon to convert light to electrical charge. The amorphous silicon is coated with a scintillating layer such as cesium iodide or terbium doped Gadolinium dioxide sulphide which converts the X-ray photons to light. This essentially is the same conversion principle as the image intensifier above but the light emitted from the phosphor screen is not subject to an intensifying stage. Instead the light is directly converted into an electrical charge by the amorphous silicon and then passed through a pre-amplification stage followed by conversion from analogue to digital signals. As with the image intensifier the thicker the phosphor screen the more efficient the conversion to light. However thicker scintillating layers do suffer from photoelectric and Compton interactions (see figure 4-23 over page) which essentially spread the response to incoming X-rays over a number of pixels and hence have a blurring effect on the resulting image.

4.7.3.2. Amorphous selenium

Amorphous selenium is an X-ray photoconductive material and as such is capable of directly converting X-ray photons into electrical charge. In flat panel detectors of this type therefore the amorphous selenium is directly placed on the active matrix and the signal is read directly from the array. The advantage of this technology is that an X-ray photon generates electric charge that flows directly towards the contact. The charge flow is perpendicular to the array and does not spread out or affect neighbouring pixels (see figure 4-23 over page). The conversion is therefore without blur and the image represents the object more clearly. Selenium detectors that are commercially available have an active element size around 139 μm which is similar to the amorphous silicon detection systems. It seems that

this limiting factor in terms of resolution is due to the active matrix technology and improvements will therefore be dependant on the developers of liquid crystal displays. The comparison between selenium and silicon is therefore one of evaluating the blurring effects due to the phosphor coating in the silicon display and evaluating how close to the actual object is the reconstructed image for both detector types.

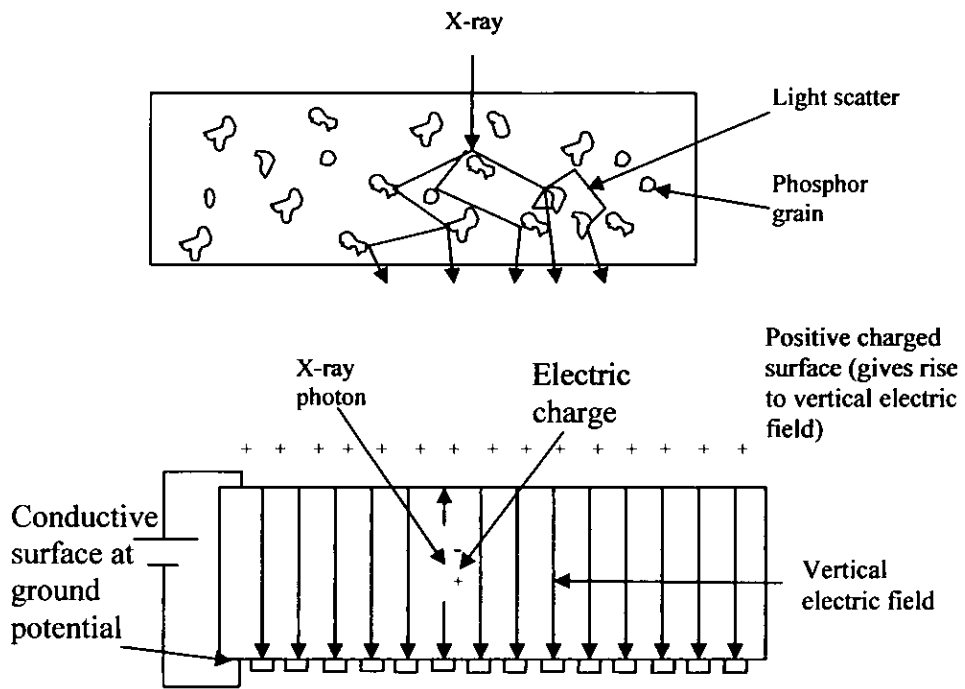


Figure 4-23 Schematic showing the scattering effects that occur in scintillating layers and the charge flow in an Amorphous silicon conversion screen

4.8. Characteristic curves

The relationship between the radiographic exposure and the resulting image density is often plotted graphically. By doing this, it is relatively easy to identify the optimum exposure where small exposure differences result in the optimum change in image density. A typical film characteristic curve taken from Sprawls [Sprawls 1995] is shown below. Here optical density is plotted against relative exposure. From figure 4-24 it can be seen that a change in exposure at the low end of the graph say from 1/16 to 1/8

would result in a density change of approximately 0.1. A similar exposure change from 1 to 2 however would result in a density change of 0.75 i.e. over 7 times the contrast change from that of the lower portion of the curve. Similarly high exposures at the top of the curve resulting lower contrast changes than those made at the steepest gradient on the curve. It is therefore good practice to attempt to optimise the exposure parameters to ensure that the inspection is carried out in the correct portion of the characteristic curve for the particular imaging device.

The gradient of the useful portion of the curve can also be used in Halmshaws formula (4-11 page 138) to determine the expected contrast value of a particular object.

One other feature worthy of note here is that the characteristic curve for a particular device also gives an indication of the devices dynamic range or “latitude”.

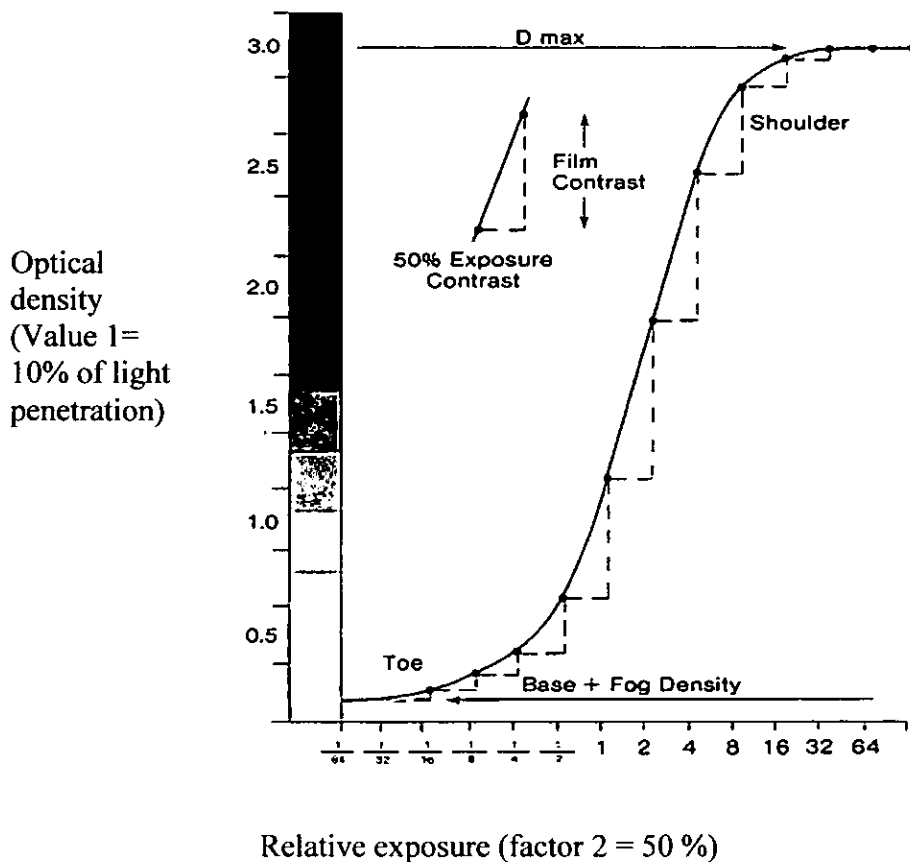


Figure 4-24 Typical characteristic curve (Taken from Kodak radiography in modern industry)

4.9. Assessment of Image quality.

Various methods and standard practices are used to assess image quality. Most practical implementations use image quality indicators (IQI) placed in strategic places over the test object in order to gain quantitative information regarding the sensitivity of the image. European IQI's are generally constructed from various diameters of thin wire of similar material to the test object contained in a plastic transparent wallet. The radiographer can then determine the smallest wire visible in the image and calculate the radiographic sensitivity by calculating the ratio of the wire thickness to the overall material thickness and presenting the result as a percentage. Variations on this are stepped blocks of similar material and shims that contain holes of known sizes.

In the aerospace industry current practices and standards [BAE SYSTEMS 2002] require that the images obtained for weld inspection can be obtained with 1% sensitivity and images for the inspection of super plastically formed diffusion bonded structures are better than or equal to 2% sensitivity. Carbon Fibre Composite material inspection is not currently controlled by British or European standards and therefore sensitivity is usually assessed by the manufacture of control specimens that contain the foreign materials and defects associated with this type of component manufacture.

Problems associated with this practice are

1. The addition of material i.e. the IQI results in a further absorption of the radiation and therefore does not fully represent the effects of a defect where in many cases a defect would be a loss of material and be less absorbing.
2. The detection of an IQI is subjective and there is little definition on how well an IQI has to be imaged before it can be deemed as acceptable.
3. An IQI's geometry does not represent the defect geometry. In fact the detection of a straight line indication from an IQI is most favourable to the viewer whereas a defect indication is less likely to have favourable geometric features.

When assessing digital radiographic image quality both the sensitivity and the resolving power of the system need to be known. To this end a further IQI is used known as a duplex IQI. Again this is constructed from a series of wires but in this instance the wires are manufactured from a dense material (Tungsten) resulting in high radiographic contrast when imaged. Two wires of the same diameter are placed close together with a spacing equal to the wire diameter. Along the IQI are a series of wire pairs that have decreasing diameters and therefore spacing. The operator can then analyse the image of the duplex IQI and determine the smallest resolvable wire pair. British standard EN 462-5 [British standard 1996] states that the resolving power or inherent unsharpness of the detection system is given by $2d$ where d is the width of the wire or spacing.

The method described above is a simple practical way of evaluating the detection capabilities of a digital radiographic system. The intention here is to practically evaluate the defect detection capabilities of a particular system configuration. The limitations of this method are that it is strongly dependant on the interpreters opinion and skill and image does not truly represent the geometries or the contrast ratios likely to be encountered from a real defect.

A further complication is that there are now many different types of detection system and limitless optical configurations being integrated into radiosopic detectors that make comparison of each configuration using the above method difficult and unreliable.

Radiographic systems reproduce object images that are clearly not an exact replication. The transfer function is dependant on three main factors i.e. resolution, contrast and signal to noise ratio. The physical and mechanical restrictions incurred when manufacturing digital detectors results in a complex conversion system where these three parameters are interdependent.

For example decreasing the pixel size and/or increasing the number of pixels increases resolution but has a negative effect on subject contrast and may decrease the signal to noise ratio. The practical image analysis methods above would suggest that the higher the resolution the clearer the defect detection would be. But increasing resolution invariably smears

small indications and makes them less prominent in the image. Furthermore image systems that have poor signal to noise ratios will mask significant contrast changes in the object particularly if the noise level is equal in intensity to the less absorbing features.

Two more precise methods exist that allow a more comprehensive analysis of a radioscopic system. The first being the Modulation transfer function. The simplest way to test a radiographic imaging system would be to stimulate the detector with a point source of radiation. The ideal response from a perfect detection system to this point source stimulation would be a single point in the image. In practice this is never the case and usually a number of pixels in an image display some effect from the stimulation. Typically the centre pixel would show the greatest response with neighbouring pixels having a response but to a lesser degree. This is called the point spread function. Similarly the detector response to stimulation from a very narrow line source would ideally result in a stepped response but in practice delivers a sloped response. Delivery of infinitely narrow point sources or line sources are impractical and therefore the modulation transfer function is used to mathematically derive the transfer function from an image taken from stepped object or in some instances a slit that is considerably smaller than the smallest detail of interest.

4.9.1. Limiting Resolution

As explained previously the limiting resolution of a radiographic systems can be found experimentally by imaging the duplex wire image quality indicator and assessing the smallest pair of wires that can be resolved. This practical method is widely used in industrial applications and the practitioner makes the assumption that objects that contain spatial frequencies less than the limiting resolution will be visible in the image. The drawback with this method is that the relationship between object spatial frequency and the extent of visibility in the image cannot be determined and as the limiting resolution is approached object visibility will be reduced. A practical method is therefore required that can assess

the imaging systems performance in terms of spatial resolution for all frequencies.

4.9.2. Point spread function

The point spread function of an imaging system can be expressed by the following formula [Boreman 2001]

$$g(x,y) = f(x,y)*h(x,y) \tag{4-27}$$

where

$h(x,y)$ = the impulse response

$f(x,y)$ = the ideal image

Boreman [Boreman 2001] states that the ideal image $f(x,y)$ is the distribution that would exist in the image (taking into account magnification) if the system exhibited a perfect response i.e. a delta function impulse response. By convolving $f(x,y)$ with the impulse response $h(x,y)$ the final image representation can be derived. Therefore if $h(x,y)$ is equal to the actual change in the object $\partial(x,y)$ the imaging system has a perfect representation of the object. However due to blurring effects of the image conversion system and blurring caused by scattered radiation $h(x,y)$ will not equal $\partial(x,y)$ and $h(x,y)$ represents the point spread function.

The amount that a point in the object spreads when imaged by the system is dependant on a number of factors, mainly unsharpness parameters discussed previously but an analysis of the point spread function results in a quantitative measurement of the spatial frequency response of the overall system. The point spread function is a two dimensional function that is difficult to measure but can be derived by Fourier transformation of the line spread function. The line spread function [Boreman 2001] is defined as a distribution of absorbed energy per unit area in the image plane when the imaging system is irradiated by an infinitely long narrow slit. It can be thought of as a series of overlapping point spread functions. Providing the imaging system is symmetric the line

spread function is independent of direction and can be used to derive the point spread function. In radiography an accurate image of the line spread function can be difficult to achieve as the slit has to be significantly smaller than the pixel dimension and the image has to be within the dynamic range. Because of this the experimental method used to derive the spatial response of a radiosopic system is to image an edge (Edge spread function, ESF) of a totally absorbing plate and mathematically derive the transfer function. This approach is called the modulation transfer function.

4.9.3. Modulation transfer function

Practical determination of the modulation transfer function is performed by first obtaining an image of sharp edge where the material totally absorbs the radiation and the image plane where there is no material is just within the dynamic range of the detection system. The result is an image which contains the edge spread function. The definition of the edge spread function is similar to the line spread function in that it is the distribution of energy per unit area when a long sharp edge of totally absorbing material is imaged and therefore the edge spread function is composed of many overlapping point spread functions.

The modulation transfer function is derived from the Fourier transform of the line spread function which in turn is derived from differentiating the edge spread function. The European standard for radiosopic testing [EN13068-1 2000] states that :-

$$[LSF](x) = \frac{\partial(ESF)}{\partial x} \tag{4-28}$$

and that

$$[MTF](fx) = \int_{-\infty}^{+\infty} [LSF](x) e^{j2\pi fx} \partial x \tag{4-29}$$

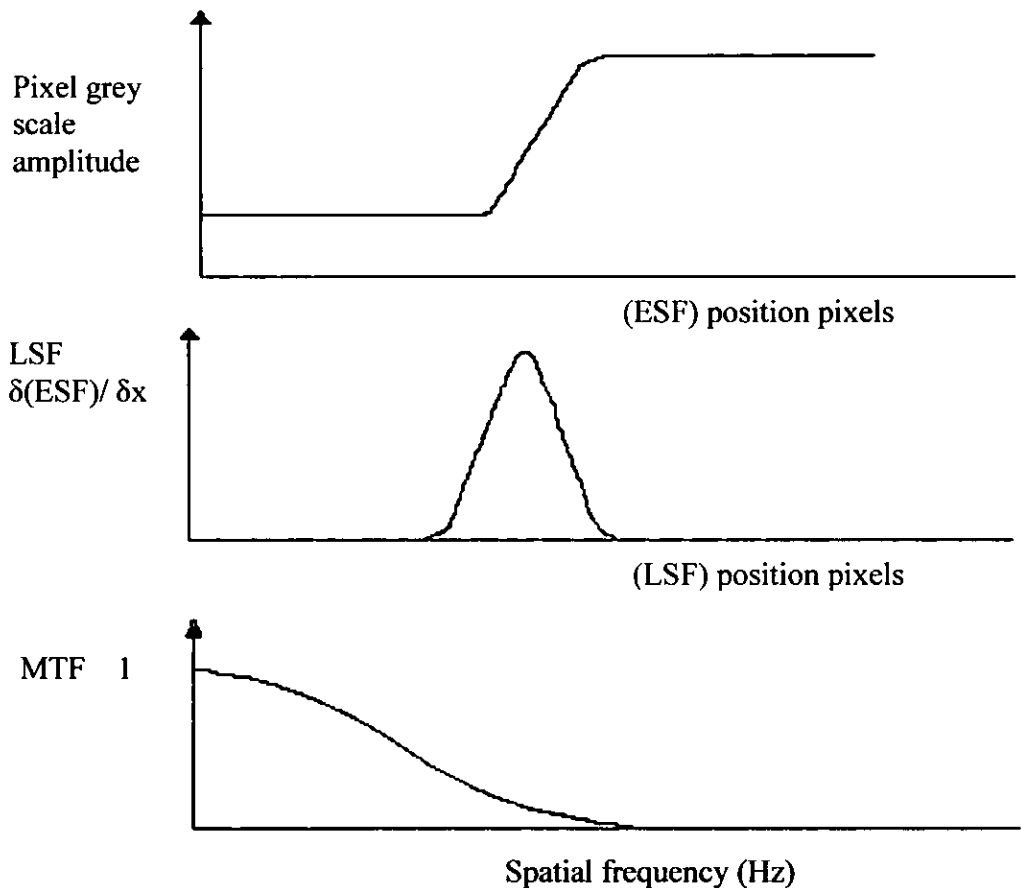


Figure 4-25 Plot showing the edge spread, line spread and the modulation transfer

4.9.4. Detective quantum Efficiency

Whilst spatial resolution is a prominent factor in determining a systems defect detection capability the contrast also plays an important role. Contrast i.e. the ability to display small differences in object density in an image, deteriorates when noise is present in the image. As mentioned previously noise sources can be from scattered radiation or inherent electronic noise from the modules within the system. Having established that the image resolution and contrast form the basis of good defect detection, the assessment criteria appertaining to specific system detection limits can be established. Many practical radiographers estimate defect detection capabilities by imaging wire or step hole type image quality indicators and whilst this may give an approximation to the detection capabilities a more quantitative method is to derive the detective quantum efficiency.

The detective quantum efficiency can be stated as

$$DQE(v) = \frac{(S/N)_{out}^2(v)}{(S/N)_{in}^2(v)} \quad (4-30)$$

where S is the signal amplitude and N is the noise power spectrum (NPS) in the input and output signals. Spatial frequency is represented by v .

Cunningham [Cunningham 2001] has expanded the equation above to give:-

$$DQE(u, v) = \frac{\bar{d}^2 MTF^2(u, v)}{q NPS(u, v)} \quad (4-31)$$

where \bar{d} is the average pixel value in a flat dark subtracted image, $MTF(u, v)$ is the two dimensional system modulation transfer function, q is the average density of X-ray quanta incident on the detector and $NPS(u, v)$ is the two dimensional noise power spectrum measured from image data.

The equation above confirms that noise power spectrum and modulation transfer function are key to defect detection and as such should be measured and used for the evaluation of any radiographic system, as they provide a quantitative measure of a systems capability.

4.9.5. Noise Power Spectrum

The image noise power spectrum can be interpreted as the noise frequency components distributed in an image. The *NPS* is defined as the Fourier transform of the image noise autocorrelation function [Lim 1990]:

$$NPS = F(R_{nn}(x, y)) \quad \text{and} \quad R_{nn}(x, y) = E(n(0,0)n(x, y)) \quad (4-32)$$

where:

\mathcal{F} – the Fourier transform operator

$R_{nn}(x, y)$ – the image noise autocorrelation function

E – the probabilistic expectation operator

In the most cases there is very limited information about the noise characteristics. The noise autocorrelation function is unknown and therefore the *NPS* can not be directly calculated from its definition. Assuming that image noise is a second order stationary random processes the probabilistic expectation operator can be replaced with the spatial expectation operator and the image noise autocorrelation function can be calculated from:

$$R_m(x, y) = R_m(-x, -y) = \lim_{N \rightarrow \infty} \frac{1}{(2N+1)^2} \sum_{k_1=-N}^N \sum_{k_2=-N_2}^N n(k_1, k_2) \cdot n(k_1-x, k_2-y) \quad (4-33)$$

In practice N can not go to infinity, as it is limited by the size of the available data, and therefore the noise autocorrelation function can only be estimated from:

$$\hat{R}_m(x, y) = \frac{1}{(2N+1)^2} \sum_{k_1=-N}^N \sum_{k_2=-N_2}^N n(k_1, k_2) \cdot n(k_1-x, k_2-y) \quad (4-34)$$

Having an estimate of the noise autocorrelation function $\hat{R}_m(x, y)$ the noise power spectrum can be estimated from:

$$\hat{NPS} = F(\hat{R}_m) \quad (4-35)$$

The last two equations describe the so called periodogram method for the estimation of the power spectrum. One of the drawbacks of this method is high variance of the estimator. To reduce the variance, at the cost of reducing the resolution of the estimator, two modifications of the periodogram method are often used. One is periodogram averaging and other is periodogram smoothing. All these methods belong to the conventional power spectrum estimators. Their properties are well researched [Oppenheim 1975] and their computer implementations are

widely available. In this work the matlab periodogram implementation has been used.

4.9.6. Estimation of the modulated transfer function.

The modulation transfer function has been calculated from (4-29) using the images below. Both images were acquired using the same relationship between object detector and radiographic source but the kV was altered to produce images with differing contrast. Figures 4-27 and 4-28 show the edge spread function and the resulting MTF curves. The curves have the same gradient at the lower frequency end of the scale but there is a definite increase in the transfer function in figure 4-28 when compared to 4-27. The limiting resolution (i.e. when the noise in the transfer function is equal to or greater than the MTF value) occurs at a higher spatial frequency in 4-28 than 4-27. This is to be expected as the object used in this experiment did not totally block the radiation from the detector and low energy radiation would produce more scattered radiation at the edge than the high energy radiograph where due to the increased energy the radiation would be more direct.

The limiting spatial frequency is however considerably lower than that calculated using the duplex IQI method. In figure 4-30 below a profile of an IQI image is shown which clearly indicates that the limiting resolution is wire pair 8 which is 0.16 mm in diameter and therefore equates to an unsharpness value of 0.32 mm and a spatial resolution of 3.125 lp/mm. In the MTF plots below the low kV plot (figure 4-28) returns a limiting resolution of 2.0 to 2.3 lp/mm whilst the high kV plot (figure 4-27) yields possibly 2.5 to 2.8 lp/mm. The duplex IQI evaluation method is therefore optimistic in its estimation of limiting resolution. In this case the duplex IQI was evaluated using the MATLAB profile algorithm however in practice the evaluation of the IQI would be subjective judgement and the error would therefore increase.

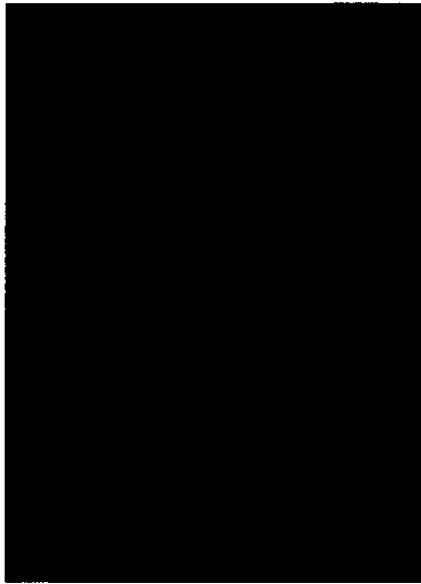
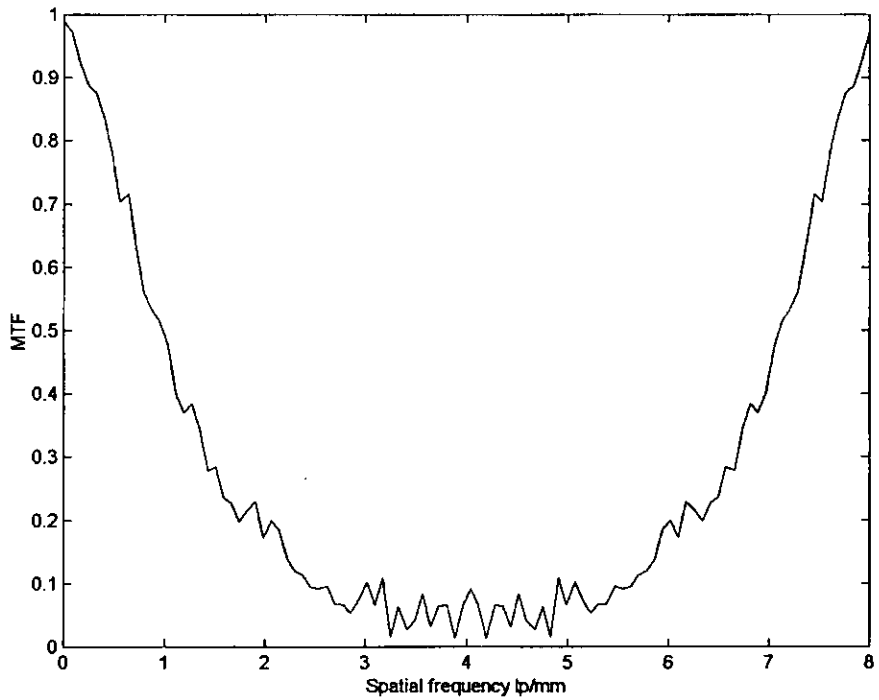
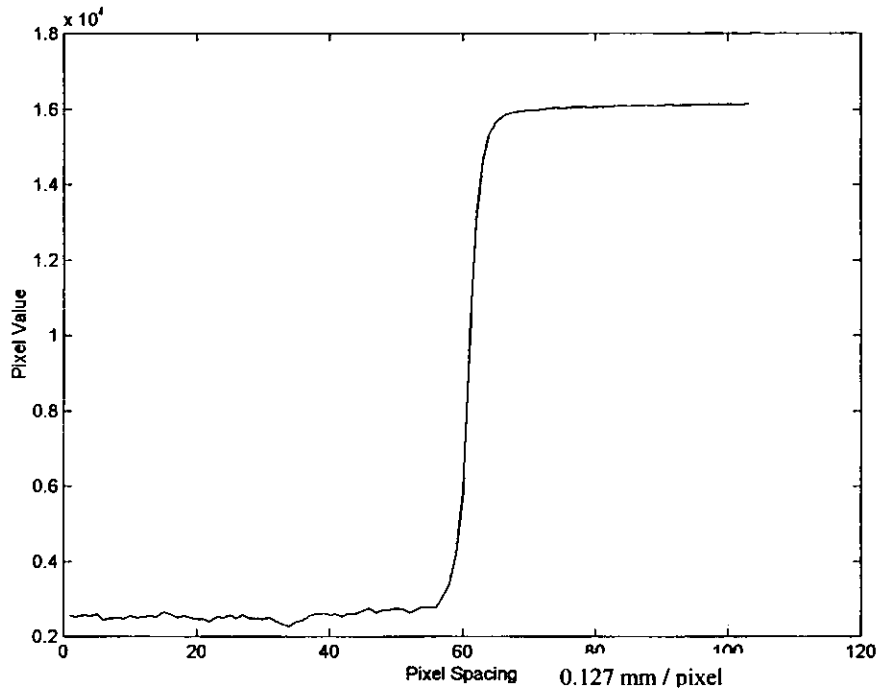
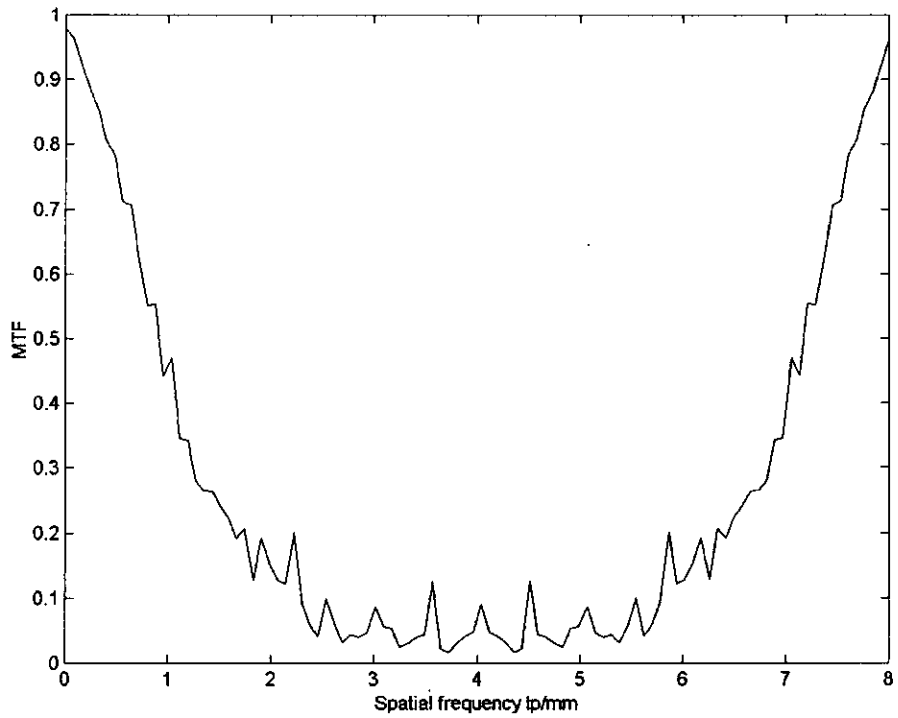
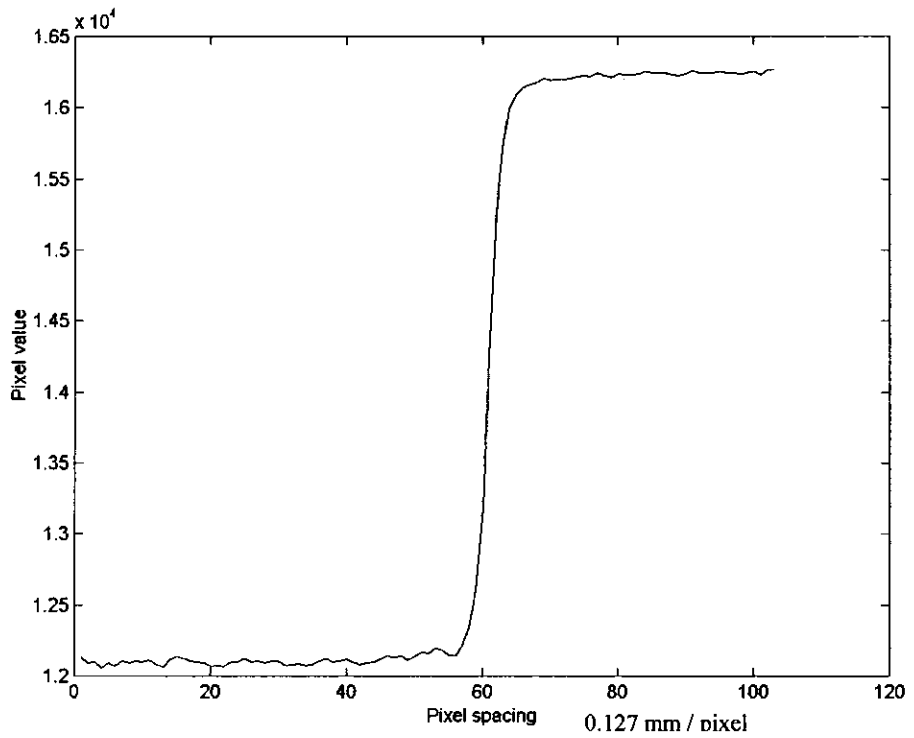


Figure 4-26 low (45kV) and high (70kV) Images used for MTF calculation



(a)

Figure 4-27 Edge spread and modulation transfer function derived from a radiograph of the same object taken at (a) 70 kV



(b)

Figure 4-28 Edge spread and modulation transfer function derived from a radiograph of the same object taken at (b) 45 kV

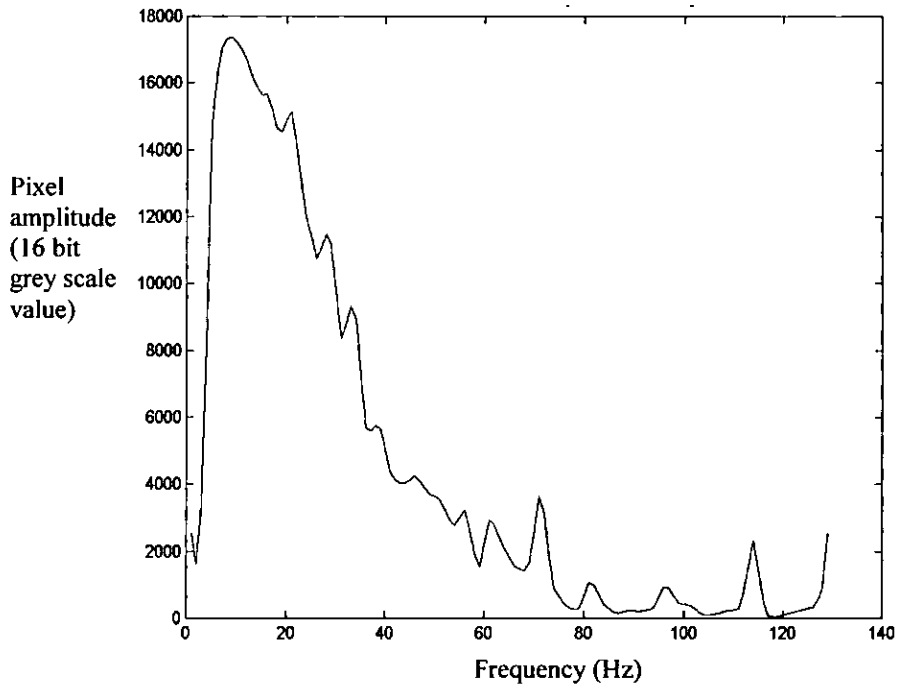
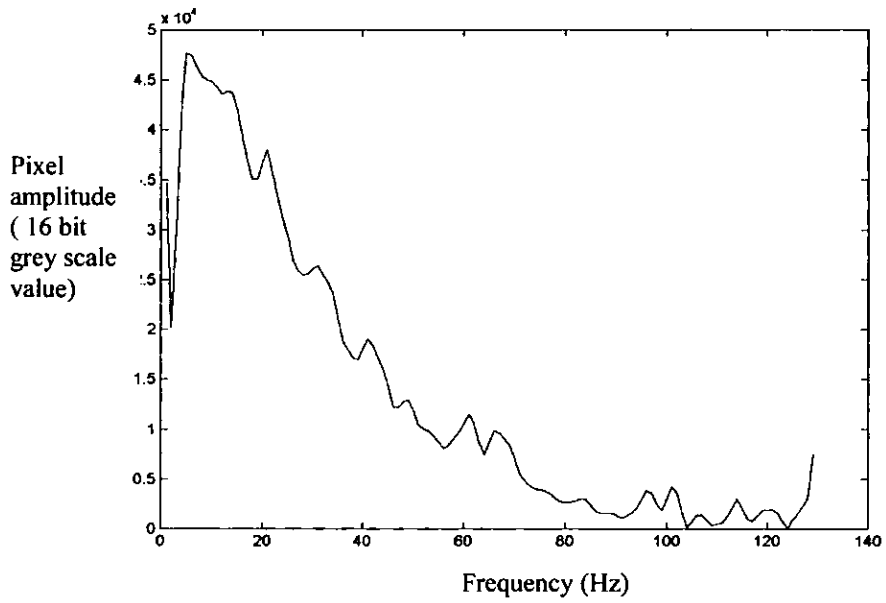


Figure 4-29 Detective quantum efficiency plot for the high kV image and the low kV image

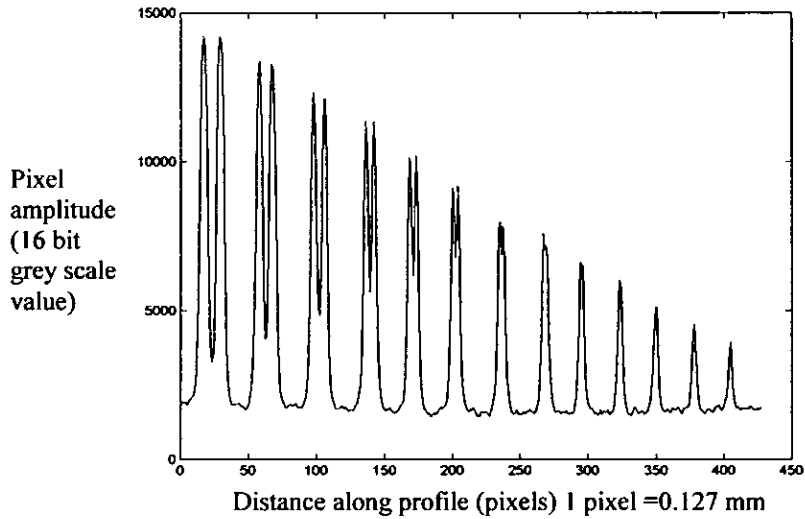


Figure 4-30 Histogram plot across an image of a duplex IQI showing the limit of resolution.

4.10. Defect Detection capabilities

Optimum defect detection is achieved by accounting for the radiographic parameters that affect image quality. As the radiographic process is complex there is no single solution for an inspection problem. However, by making a detailed assessment of the complete inspection process the most influential parameters can be categorised and a judgement can be made on how to set up the inspection. Equation (4-11 page 138) refers to

the radiation component i.e. $\left(1 + \frac{I_s}{I_D}\right)$ the film component i.e. $\frac{1}{G_D}$

the specimen $1/x$ and the viewing conditions D . Whereas in equation 4-12 the distance of the object to the detector is considered when evaluating the contrast effect caused by scattered radiation i.e.

$$L \left(L + R - \sqrt{L^2 + R^2} \right) \left[1 - \frac{s}{\sqrt{R^2 + s^2}} \right]$$

Taking into account that when an object is moved closer to the source and away from close proximity of the detection system image magnification occurs and therefore the overall unsharpness has to be

accounted for a combination of equations 4-11, 4-12 and 4-20 will produce a value that can be used to compare defect detection capabilities of one inspection set up to another.

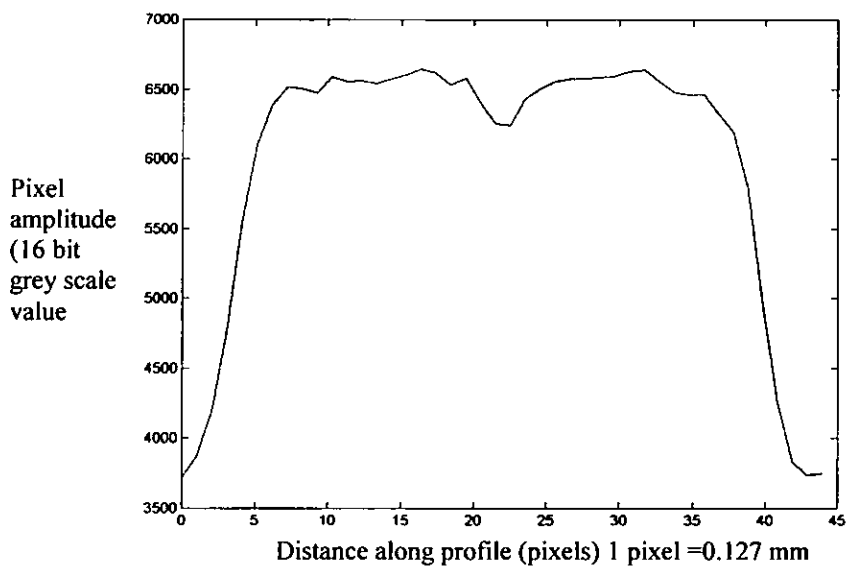
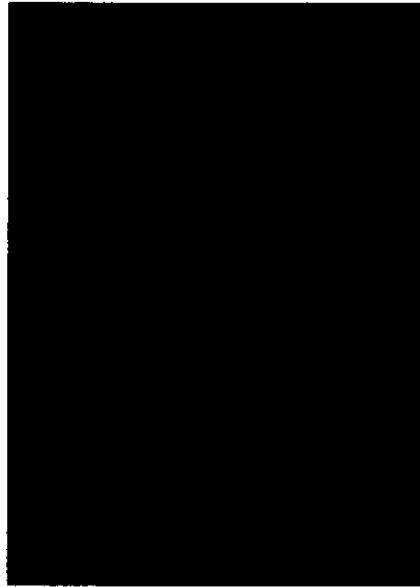


Figure 4-31 Radiographic image of a 100 μm hole in an optical disk and a density profile across the hole.

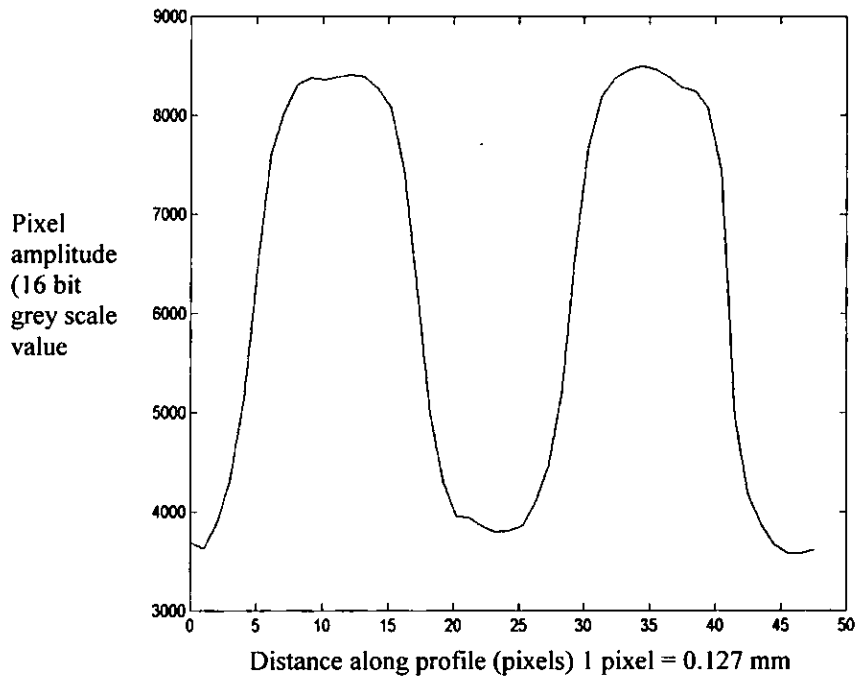


Figure 4-32 Radiographic image of a 1 mm hole in an optical disk and a density profile across the hole.

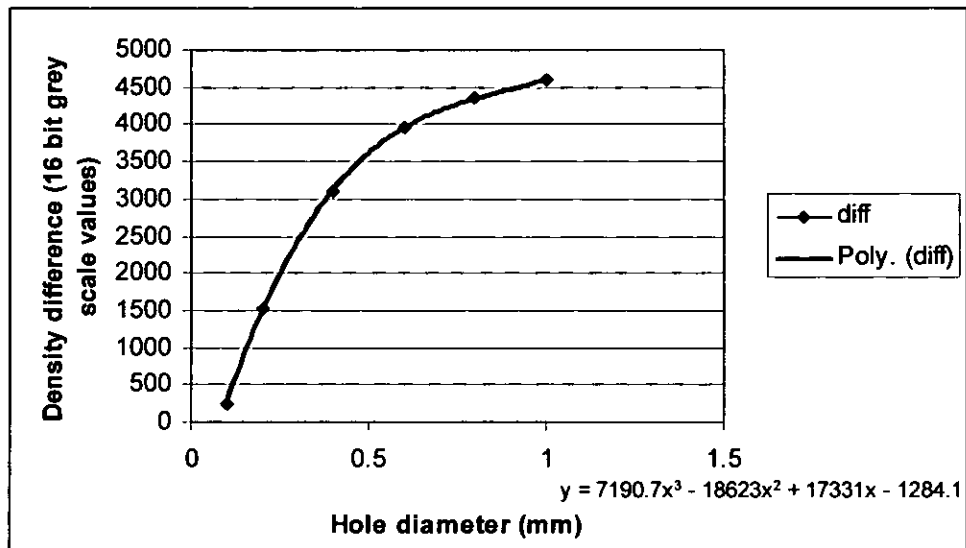


Figure 4-33 Graph that plots the ratio of hole pixel value to the surrounding disk value against the hole diameter.

4.11. Radiographic inspection of SPFDB

Inspection of super plastically formed diffusion bonded (SPFDB) structure can be divided into two distinct parts. One is the inspection of bondline integrity and the second is the geometric conformation of the internal structure. Diffusion bond lines are usually orientated parallel to the surface and as such are not orientated in a manner that allows sensitive radiographic inspection. In these cases ultrasound would be more suitable. The internal structure however also makes a significant contribution to the components properties and as such deviations in the internal geometry are detrimental to the components function or life. A description of typical internal structures for SPFDB components has been given in chapter 2 and are generally large cavities with thin webs connecting the two outer surfaces. The webs are designed to transfer applied loads and maintain the outer profile. The location and conformance of the internal structure to the design requirements has therefore to be verified. The detection capabilities of radiography are ideally suited to this type of application as X-rays are able to penetrate through the material and form an image based on the attenuative characteristics of the various material thickness' the rays pass through. Geometric deviations, tears and cracks are readily imaged providing the imaging system capability and parameters in terms of

resolution and signal to noise ratio are optimised for the particular defect detection requirement.

4.12. Radiographic inspection of Composite

Radiographic inspection on composite structures when performed correctly is able to detect the majority of defects normally encountered in this type of structure. Like diffusion bonding however radiography is not able to detect disbonds and delaminations that lie normal to the surface. Typical defects detected by radiography are porosity and voids in both bond lines and solid carbon, inclusions in terms of foreign objects and foreign materials entrapped during the lay-up process and distortion of honeycomb cells which include cell wall splitting etc. Composite materials are inherently opaque to X-rays and as such very low kV values are used. X-ray generators therefore have to be stable at these low potentials otherwise fluctuations will degrade the final image. In the case of film radiography the film cassette can have a significant effect on the low kV X-rays. To overcome this paper film cassettes are used in preference to the more robust plastic wallets. When inspecting a honeycomb section it is important to ensure that the angle created by the useful beam is sufficiently shallow that it does not overlay the honeycomb cell walls on top of each other in the area of interest as this will mask defects like slight cell wall distortion or split cells. Large film to focus distances will reduce this effect.

Composite radiographic inspection is a very useful tool for the assistance in defect characterisation and as such is regularly used to confirm indications detected by ultrasonic means. Radiographic inspection is a high resolution imaging technique and is therefore able to identify subtle characteristics of defects such as individual pores and voids, precise re-construction of the edges of inclusions and small geometric deviations in honeycomb walls.

Ultrasonic indications of the defects described above would be represented by attenuation in the signal and due to the coarse image reconstruction would be blurred. Characterisation by ultrasonic methods is therefore difficult.

4.13. Application of real time radiography

Real time radiography has the advantage of removing the film and processing costs, and the time associated with processing. It is a fast and efficient process particularly when digital control is implemented. The positional manipulation of the X-ray source, detector and component all contribute to removing operator error thus increasing repeatability. Furthermore, fully integrating control of all system components i.e. control of generator and detector parameters and image capture, make real time radiography suitable for automation. By implementing a reliable and repeatable process, work can then be instigated using modern image and signal processing methods that go some way to automating the data analysis.

In order to ensure that a reliable and repeatable process has been achieved an analysis of all the pertinent variables must be performed and techniques implemented that maintain the system parameters within tolerance.

In contrast to film radiography, real time radiography is limited by its sensitivity and resolution and the engineer must evaluate the effect of these limitations when the method is applied to a particular application. Resolution limitations can be overcome to some extent if the system comprises of a micro focus source as large magnification factors can then be achieved and the limiting resolution can be overcome. Sensitivity is more difficult in that overall noise power will always limit the detection capabilities. Good housekeeping by shielding radiation scatter and applying image filtering will enhance the sensitivity but the engineer should rigorously evaluate the system sensitivity before implementing an inspection technique.

In the paragraphs above it has been demonstrated that the optimum magnification can be calculated by the new formula 4-23 and the plots using the technique that derived the formula show that optimum magnifications of around 11 are typical using current technology. Sensitivity is more difficult to determine but if an accurate representation of an indication is required then the MTF and DQE techniques can be used

to evaluate system limits. MTF and DQE show the Nyquist limiting frequency but as with all methods, fail to show the limits of detection as smaller image features are possible but will be imaged at spatial frequencies that coincide with a harmonic. When this occurs, reliable and accurate measurement of such features is impossible. The detection of features with a spatial frequency less than double the sampling frequency can be confusing and the image interpreter must realise the image capture limitations and detection standards must accommodate this limitation.

4.13.1. Results using an Amorphous silicon detector

The panel below was manufactured from two 1mm sheets that have been bonded together and have had a series of inclusions placed at the bond line prior to bonding. Figure 4-34 (a) shows the radiographic result of a single layer glass cloth inclusion without image processing of any kind. Not surprisingly the 14 bit image lacks contrast when compressed to fit an 8 bit display but when contrast stretching is applied as in figure 4-34(b) the inclusion becomes apparent. This result gives a good indication of the systems sensitivity i.e. 1 ply of glass cloth (approximately 0.125 mm) in 2 mm of carbon fibre composite which is 6.25%. However glass cloth is a relatively dense material when compared to carbon fibre composites and as such there is a large difference in the amount of attenuation between the inclusion and the background material. Backing materials such as the one shown in figure 4-35 however are a similar density to carbon and therefore difficult to distinguish in a digital radiographic image. In figure 4-35 the defect is only slightly visible at the edges and can barely be identified. There is a loss in contrast due to the conversion process used for importing into this document but the defect is difficult to image.

Defect detection by digital radiography is difficult because of the poor conversion factors of imaging technology at X-ray energy values. However by reducing the scatter radiation and using an amorphous detector that does not suffer the inherent filtration caused by the aluminium plate at the entrance of the image intensifier, inclusions that are similar in density to the parent material can be detected.

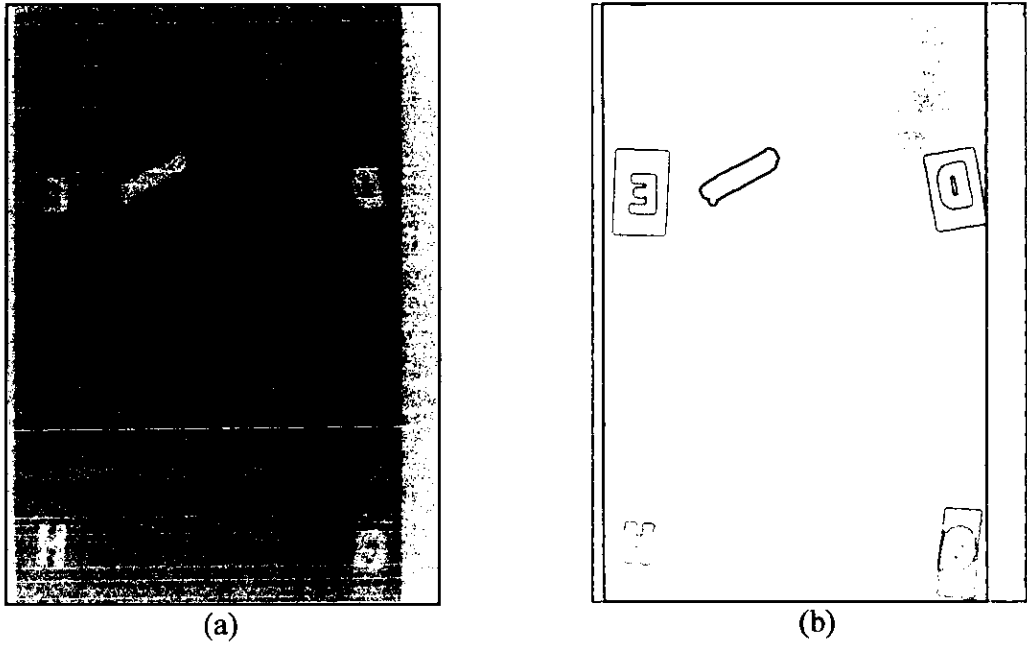


Figure 4-34 Digital radiographic image of 2, 1mm carbon panels that have been joined by an adhesive layer in which a glass cloth inclusion has been placed. (a) unprocessed raw image(b) processed image

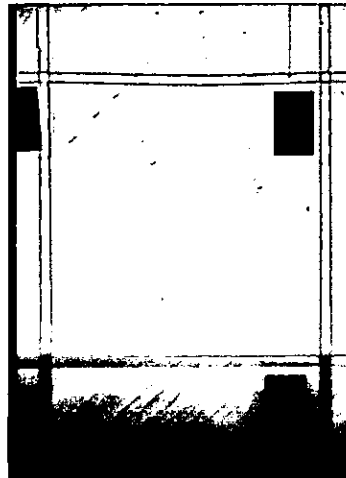


Figure 4-35 A digital radiographic image of a backing material bonded between two 1mm carbon fibre panels.

Figure 4-36(a) is the image resulting from a digital radiograph of the thick skinned honeycomb panel described in chapter 2. Compressing 14 bit fidelity into 8 bits results in poor contrast but with histogram processing applied (figure 4-36(b)) the defects become apparent.

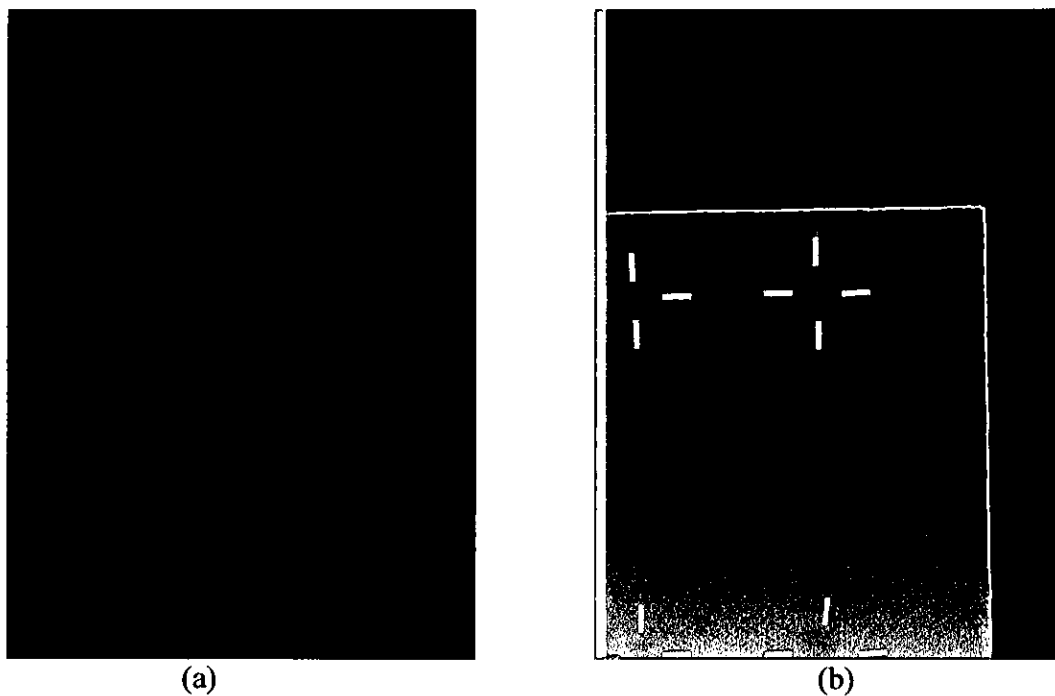


Figure 4-36 Digital image taken using an amorphous silicon detector of the thick skinned honeycomb panel that contained inclusions. (a) unprocessed image (b) processed image.

The Images below are taken using the amorphous silicon detection system and show a poor super plastically formed diffusion bonded panel that has a series of large defects. Before and after processing are shown for clarity but it should be noted that a series of small intentional defects created by placing small circles of stop off material at the edge of the bond line are indicated in right hand side of the centre vane in figure 4-37(b).

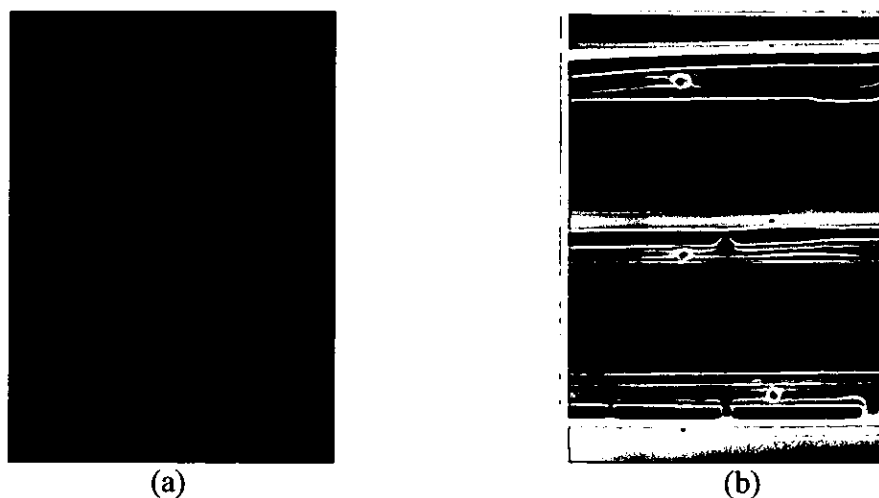


Figure 4-37 Digital radiographic image of a significantly distorted SPFDB structure. (a) before processing (b) after processing.

4.14. Summary

In this chapter the basic principles of X-ray generation have been explained in detail with a view to the implications on suitable defect detection when applied to SPFD and composite inspection. In particular X-ray principles have been studied and applied to digital systems in particular amorphous silicon detectors and micro focus generation systems. By performing this study and evaluating the current standards a new formula for the calculation of optimum magnification has been developed. This formula contrasts significantly with that found in the American Society for materials testing documentation, the American society for non destructive testing handbook and the European standard for real time radiography [En 13068 2001].

However it has been shown by experimental and calculated methods that the optimum magnification for a digital radiographic imaging system can be calculated by equation 4-23. The interesting conclusion made by this finding is that optimum magnification occurs at a significantly less value than that predicted by the former equations derived by Halmshaw et al.

Further to this the proposed use of the MTF and DQE calculations to evaluate the detection capabilities of a system extend the current experimental practices where the limiting resolution is determined by duplex wire imaging and provide a method to quantify the system capabilities which can be used to evaluate system performance over time.

Earlier works of Halmshaw and Mascovski emphasise the effect scattered radiation has on contrast sensitivity and hence defect detection and some plots based on their results are presented. Contrast sensitivity of digital radiography is impaired when compared to the film equivalent and therefore every step must be taken to optimise sensitivity in digital radiographic systems. The proposals within this chapter are to reduce scattered radiation by adequate shielding, where possible use kV values that produce characteristic radiation as this reduces scatter within the material and ensure that the detection system is at the optimum distance

away from the component surface so that scattered Bremsstrahlung radiation has less of an effect.

The application of digital radiography to inspect the internal structure of super plastically formed diffusion bonded components is possible providing the minimum detectable defect is greater than or equal to twice the resolution of the detection system. The system resolution has to be determined by a DQE investigation and subsequent calculation as scattering effects do reduce the specified detector resolution. In terms of contrast sensitivity the amorphous silicon detector achieves the required contrast quantification mainly due to its 14 bit analogue to digital conversion capability. Tests to date have shown that the detection of core distortion tears and geometric deviations are all possible with this type of unit. The system used for this evaluation is therefore adequate for the inspection of SPFDB primary aircraft structures.

In the case of carbon fibre composite inspection resolution is not the prime issue as expected defects are normally much larger than the limits of resolution found from the DQE calculations. The challenge with composite inspection is that composite have a low atomic number and as such do not readily absorb X-rays. Contrast sensitivity is therefore the limiting factor when applying digital radiography. To this end the improvement from 8 bit analogue to digital conversion system to 14 bit has improved matters.

Amorphous silicon detection plates also have less inherent filtration properties than some of the older image intensifier system resulting in more X-ray photons reaching the detecting phosphor and therefore a more realistic representation of the components X-ray attenuation. Image contrast stretching with 14 bit data is capable of imaging many material inclusion type defects that are to be detected in carbon fibre composite materials.

Chapter 5

5. Shearography

Shearography is an optical inspection method that offers many potential advantages over the two well established aircraft inspection methods namely ultrasound and radiography. Shearography benefits, like radiography, from being a full field inspection method which reduces inspection time and requires no contact with the part thus significantly reducing the need for complex manipulation or immersion coupling. Unlike radiography, shearography is not dependant on a transmission of energy through the part and hence can detect planar defects normal to the radiation. Also, as shearography is an optical method it requires access to one side only. As with all non destructive test methods, shearography is unable to detect every type of defect. In general shearography relies on a surface displacement usually caused by an uneven defective material response to a stressing force and therefore is limited to non rigid materials and defects that are close to the surface. Shearography therefore has to be applied where, either the significant defect type or location can be predicted and is therefore detectable using shearography, or in conjunction with other methods to inspect for combinations of defect type and possible locations.

5.1. Principles of shearography.

A shearography system comprises of four key modules. These are the stress application, laser illumination, optical detection, and data acquisition modules. There are now many shearography systems available commercially with each manufacturer optimising the basic modules to meet the customer's application requirement. The result is that there are now many different configurations of shearography system but the basic underlying principles and system modules that fulfil those principles remain unchanged.

Shearography involves illuminating a component under test with an expanded laser beam. The reflected laser light is then detected by an

optical arrangement called an interferometer and then captured by a CCD camera.

Defect detection is possible because images are captured before and after a stressing force is applied to the component under test. Then by image subtraction a defect that causes an undulation in the surface can be identified.

Shearography images are inherently noisy and each part of the system has to be optimised to reduce noise. The following paragraphs detail the fundamentals of a shearography system and also describe the developments undertaken at BAE SYSTEMS where a state of the art shearography system has been developed.

5.1.1. Laser speckle

Shearography is a technique that utilises the information carried in the speckled light reflected from a surface. Speckle patterns are created by local interference on an optically rough surface, the properties of which can be used to obtain information about the state or topography of the surface. The noisy granular pattern shown above was created by imaging a laser illuminated diffusively reflecting surface with a CCD camera. The speckle only appears if the surface discontinuities are greater than the wavelength of the illuminating light hence for shearographic inspection short wavelength laser light is used.

Because the surface of aircraft components is considered optically rough each pixel in the image has light contributions from a small volume of the reflector. The light intensity per pixel is dependant on the coherence of the reflected light which in turn is dependant on the surface topology. The total speckle pattern for a particular surface can therefore be considered unique, as imaging a surface with a laser wavelength of 532 nm identifies each and every crevice on the surface with each part having a different speckle pattern. If the surface is displaced the speckle pattern will move accordingly.

If the surface is deformed then the speckle pattern will change because the geometry of each volume that contributes to the pixel intensity will have changed and therefore affect the coherence length and

result in a change in light intensity collected by the camera. These two types of movement are called rigid body motion and deformation. In shearography only the deformation motion is of interest however if rigid body motion occurs during a shearographic examination the effect will significantly reduce the sensitivity of the test as rigid body movement moves the speckles in the image and therefore reduces the correlation between the speckles prior to and after stressing.

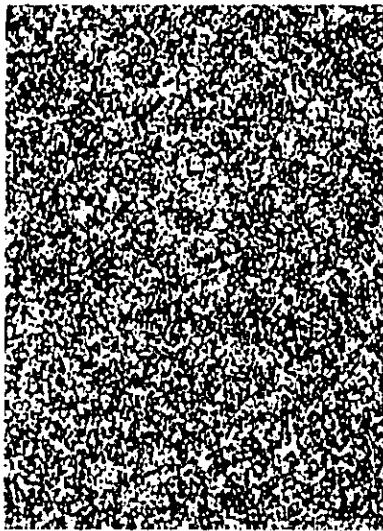


Figure 5-1 Typical laser speckle image.

5.1.2. Speckle Size

Speckle size is an important factor in shearography as it is linked to the amount of de-correlation that can be tolerated and therefore the sensitivity of the inspection. Goodman [Goodman 1975] derived the autocorrelation function for an imaging geometry assuming a uniformly illuminated and scattering object area that is larger than the spatial resolution of the lens used and from this the speckle dimensions can be determined by:-

$$d_s = 1.22 \frac{\lambda z}{D_1} \quad \text{or} \quad d_s = 1.22 \lambda f'$$

(5-1)

where λ is the wavelength of the laser light, z is the distance of the image plane from the lens, D_1 is the aperture diameter and $f^\#$ is the f-number of the lens.

The speckle size can be related to the numerical aperture (NA) by :-

$$NA = \frac{D_1}{2f} \text{ and since the distance } z \text{ is equal to the focal length the speckle}$$

size is given by:-

$$d_s = 0.61 \frac{\lambda}{NA} \tag{5-2}$$

Hence the smaller the numerical aperture the greater the speckle size and vice versa. Haasteren [Haasteren 1994] uses a similar method to calculate the speckle length and gives the formula :-

$$l_s = 2 \frac{\lambda}{(NA)^2} \text{ which suggests that the speckle is a tubular shape.} \tag{5-3}$$

Speckle size is important as the amount of rigid body movement that can be tolerated is directly related to this parameter. A small in-plane translation of the object will cause speckle de-correlation because the CCD elements record part of the original contribution from the speckles before the movement and partly a new contribution from the field generated after the movement. The ratio of new to old contributions depends on the amount of movement relative to the element size and can be written as:-

$$1 - u = \frac{\Delta p_a}{P_a} \tag{5-4}$$

Where u represents the amplitude correlation recorded before and after loading and Δp_a is the area of the CCD element that records the new speckle contribution and p_a is the total are of the CCD element.

Out of plane motion differs in that each object point is imaged as before but now a different part of the field is collected by the CCD camera. Here the amount of de-correlation is given by the portion of the camera aperture that changes :-

$$1 - u = \frac{\Delta A}{A} \tag{5-5}$$

Where ΔA represents the area of the aperture that records a new part of the speckle pattern and A is the total area of the aperture.

This type of de-correlation not only changes the intensity of the speckle image but also the phase as in this case the speckles are not shifted slightly but each speckle point recorded is now different.

In conclusion for shearography small speckle patterns are generally used as this gives rise to large apertures which in turn allows more light to be captured and also reduces the de-correlation effects.

5.1.3. Fringe Patterns

Rigid body motion is the major cause of speckle de-correlation which can reduce sensitivity or destroy phase information. To eliminate these problems shearography systems split a reflected coherent laser beam along two paths which, when imaged by a CCD camera, creates an interference pattern. This method significantly reduces the object stability requirement as both laser beams undergo the same object displacement. If subsequent interference patterns are captured whilst a stressing force is being applied and are subtracted from the first image captured in the unstressed state then fringe patterns will appear that represent the movement of the surface. A typical fringe pattern is shown in figure 5-2. The black lines connected together are contour lines of the gradient of the surface distortion much like contour lines of hills on an ordinance survey map.

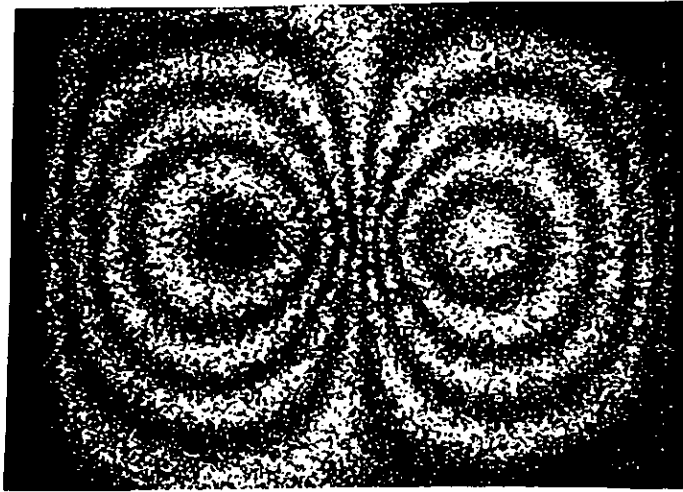


Figure 5-2 Fringe pattern from a large displacement.

The interference pattern or fringe pattern created this way can be described mathematically by the general equation:-

$$I(x, y) = I_b(x, y) + I_m(x, y) \cos(\phi(x, y)). \quad (5-6)$$

Here the intensity $I(x, y)$ consists of three parts. The background $I_b(x, y)$, The modulation $I_m(x, y)$ and the phase between the two interfering beams $\phi(x, y)$.

As mentioned previously the intensity of a speckle image cannot be relied upon for defect detection as a change in the surface caused by stressing may increase or decrease intensity depending on the contribution of coherent light reflected from each surface point. The fringe pattern does however carry phase information and a change in phase has been shown to be proportional to the first partial derivatives of a deformed objects surface displacement [Hung 1982].

Extracting the phase from an image can be conducted from a single intensity interferogram by implementing image processing algorithms such as spatial filtering, fringe tracking or Fourier techniques and approximating the phase distribution by interpolation. These techniques however while simple to implement are not robust and suffer from reduced fringe resolution due to the interpolation method. Often the filter parameters have to be optimised for each interferogram therefore reducing the likelihood of automation.

5.1.4. Phase stepping

A more robust method for phase extraction is to acquire interferograms whilst altering the phase of the interfering image. With this method the phase distribution can be calculated accurately as the phase change for each interferogram is known and can be used to extract the phase in the final image.

Phase stepping methods are implemented by changing the path length of one of the two laser beams between image acquisitions. This is performed by attaching a calibrated piezo electric crystal to one of the two mirrors in the Michelson interferometer which, when stimulated by a precise voltage will expand and move the mirror and hence change the path length. Depending on how many steps are taken and the distance between steps relative to the laser wavelength mathematical solutions for extracting the phase have been derived. Creath [Creath 1998] concludes that a five phase stepped algorithm is robust to noise and insensitive to piezo calibration errors that would result in errors in the value used for φ in the equation below. Calculation of the phase map from five phased stepped images is performed by:-

$$\phi(x, y) = \tan^{-1} \left(\frac{2[i_2(x, y) - i_4(x, y)] \sin \varphi}{2i_3(x, y) - i_1(x, y) - i_5(x, y)} \right) \quad (5-7)$$

Where $\Phi(x,y)$ = Phase of the surface before or after stressing.

$I_n(x,y)$ = intensity distribution of the n th phase stepped image.

φ is chosen to be $\pi/2$.

5.1.5. Image Un-wrapping.

The tangent function above leads to an image where the phase argument is retrieved in a wrapped format(i.e. φ has the same value as $(\varphi+2n) \pi$ or any integer multiple of π). Phase wrapping is undesirable as the fringe patterns tend to jump from white to black at a high spatial frequency and therefore mask potential defect indications. High

frequency fringe patterns are difficult to interpret by the untrained operator which again leads to undetected indications.

Unwrapping the phase information is therefore necessary for optimum defect detection. A phase unwrapping algorithm has to accurately detect where in the image each phase jump has occurred. It must also keep a record of all phase jump and sequentially add 2π to each subsequent phase jump. In practice with real interferograms this is very difficult as the images are noisy and all fringes are never fully complete.

5.1.5.1. Spatial unwrapping

A number of phase unwrapping methods exist, the simplest being an intensity analysis method where the phase map pixel intensity is analysed. In this method a sharp change in pixel intensity i.e. a transition from black to white, is treated to be a wrapping of the phase or to be more precise a further period of the sine term in the formula above, and therefore the unwrapping algorithm adds a value of 2π to the pixel value in an attempt to smooth the image and unwrap the phase. The problem with this method is the inherent noise of the interferogram, as if too low a threshold is used the noise will trigger the 2π addition whereas if too high a threshold is set, wrapped phase information will be neglected. False triggers are also carried on through the image. One way to overcome this is to analyse the image in terms of noise and fringe completeness prior to the unwrapping and then implement the unwrapping algorithm based on the results of the analysis. For instance the noisy areas could be determined and only processed after all other phase unwrapping was complete or alternatively perform the unwrapping process in a number of directions so that incomplete fringes were unable to interrupt the 2π additions. Many researchers and industrial integrators have successfully implemented algorithms that are able to unwrap real phase images. However the problems associated with noise and incomplete fringes does mean that the system has to be precise in terms of phase step, illumination, shear angle, data acquisition and stress application. Errors at any stage will result in incomplete fringes and or

excessive noise which in turn will deteriorate the unwrapping mechanism.

5.1.5.2. Temporal Unwrapping

When implemented correctly temporal unwrapping methods offer a more robust solution to the correct extraction and correction of the phase wrapping problem than the spatial method. The principle of the temporal unwrapping method is to capture a number of phase stepped sequences as the stress is being applied. In this way the timing of image capture can be synchronised with the deformation, and images captured before the deformation in the interval between two images being captured exceeds π . It can then be assumed that two sequential sets of images are unwrapped and the image subtraction that highlights the deformation changes can be performed. The problem with temporal unwrapping is that care has to be taken in ensuring that the image capture frequency is high enough otherwise it is not possible to determine whether a pixel is wrapped or not. The capture interval is dependant on the rate that the stress is applied and the nature of the defect and whilst the stressing rate can in some cases be controlled the defect response to such stress can be unpredictable. For instance large defects can deform very rapidly in thin skin honeycomb structures whereas inclusion materials in sold carbon will only deform slightly.

Colonna [Colonna 1997] and then Parker, Salter [Parker 1999] have also highlighted two other major limitations to the temporal unwrapping process namely data cancellation and the introduction of noise.

5.1.5.2.1. Data cancellation

Data cancellation is better understood by examining the formula below which describes the calculation of phase differences from a sequence of temporally collected speckle images:-

$$\phi = \sum_{i=1}^n \phi_i - \phi_i - 1$$

(5-8)

If this is expanded for n images i.e.

$$\phi = (\phi_2 - \phi_1) + (\phi_3 - \phi_2) + (\phi_4 - \phi_3) + (\phi_5 - \phi_4) \dots etc \quad (5-9)$$

it can be seen that the intermediate terms will cancel and leaving

$$\phi = \phi_n - \phi_1 \quad (5-10)$$

Which can be problematic in that the speckle correlation over a long data acquisition interval may be destroyed leaving just noise in the final subtracted image.

Colonna's modulation filter overcomes the cancellation by decoupling the phase images from each other before they are integrated. The filter works by calculating the sum of neighbouring phase differences (3X3 mask) that are weighted by the square of their respective modulations M^2_i . The centre of the 3x3 mask is therefore assigned a new value calculated in accordance with:-

$$\phi' = \frac{\sum \phi M^2_i}{M^2_i} \quad (5-11)$$

Parker and Salter have implemented this strategy and report that the modulation filter is highly effective as it maximises the use of the available information whilst rejecting inactive speckles. Experimental results gained using the same experimental set up as Parker and Salter shown further on this chapter strengthen this argument but also indicate that the mathematical implementation is capable of enhancing defect detection by modulation whilst maintaining unwrapped defect indications of gross defects.

5.1.5.2.2. Noise

As mentioned earlier differencing temporally collected phase maps when de-correlation has occurred during the acquisition will result in a noisy image.

It can also be shown that partial de-correlation can also increase noise. Coupled to this increased sampling will also increase the inherent noise associated with the frame grabbing electronics. Therefore for temporal unwrapping techniques to be successful it is imperative that object stability is reasonable and that the applied modulation filter successfully de-correlates the phase images from each other.

5.1.6. Stressing methods

The method adopted for stress application has to be tailored to the inspection criteria so that optimum defect detection can be achieved. Ideally uniform large area stressing is preferred and this is best applied by means of reducing pressure around the component. For production inspection a large chamber that is vented via large suction pump is used, whereas for in-situ inspections vacuum hoods can be implemented. Pressure differential methods are particularly useful for the shearographic inspection of honeycomb components with metallic or carbon fibre composite skins. The large volume of air within the honeycomb expands as the pressure difference between the inside of the component and the external surface is ramped down which causes disbond features between skin and honeycomb to blister. These blisters are readily identifiable by the shearographic fringe patterns.

In pressure drop stressing, defect detection can be enhanced by synchronising the pressure drop with the data acquisition and ensuring that surface deformations from disbonds are suitably resolved. When using the pressure drop method in conjunction with temporal unwrapping algorithms, the effective load will follow the curve depicted by the ideal gas law i.e.

$$PV = \frac{m}{M} RT$$

(5-12)

Where

m = mass of the gas in the volume V .

M = molecular weight of the gas molecules.

T = temperature

R = gas constant given as 8314 J.Kmol.K.

In the case of shearography using pressure drop loading methods and assuming that temperature stays constant the change in volume is directly related to a change in pressure as all other parameters in equation 5-12 are constants the volume change can therefore be derived by:-

$$V = \text{constan} * (1/P)$$

(5-13)

A plot of which is given below.

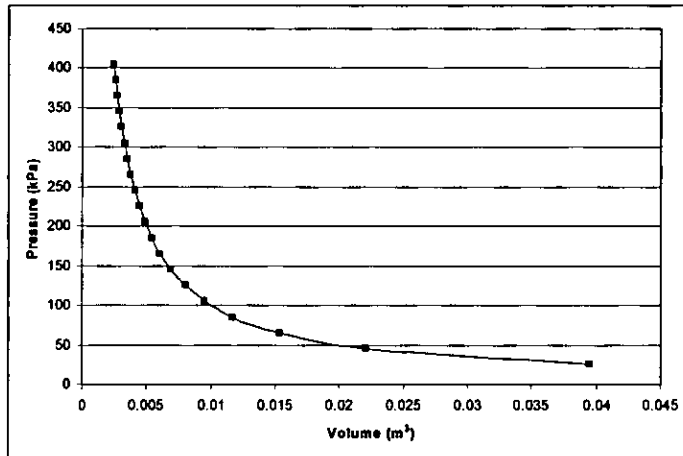


Figure 5-3 Plot showing relationship between pressure and volume.

As can be seen from the plot above the volume increases inversely to the pressure drop. Therefore if a linear pressure drop is programmed the data acquisition must be timed to match this change in volume effect, as it is the change in volume at the defect site that causes the surface deformation. From experimental results however it has been found that optimum defect detection is achieved by implementing a non linear pressure drop. A simple non linear pressure drop is achieved by :-

$$\Delta p = Atmospheric - (TotalP - (TotalP * \frac{1}{T}))$$

(5-14)

where TotalP represents the total pressure drop required and T is the time interval. When the above is implemented the pressure profile follows the same line as shown for volume change shown above. However for such a pressure profile the volume change would be linear and hence match an equal increment for the data acquisition rate. The above pressure profile would be advantageous as it produces an even change in volume and allows time for the capture of the five phase stepped images and calculation of the resulting phase map. Practical implementation problems do exist however with producing such a large initial pressure differential, in that it is very difficult to extract a great volume of air from a large chamber in such a short time without creating disturbances within the chamber. One solution would be to extend the time interval but this increases the chance of image de-correlation through the acquisition cycle. Practical experiments have shown that with the set up at BAE SYSTEMS it is possible to create a pressure differential of around 200 millibars in 20 seconds and that image de-correlation can be avoided within this time span. However when attempting to implement such a pressure profile some rigid body motion is experienced due to the air disturbances within the chamber. Therefore a less aggressive profile was adopted for the majority of experiments.

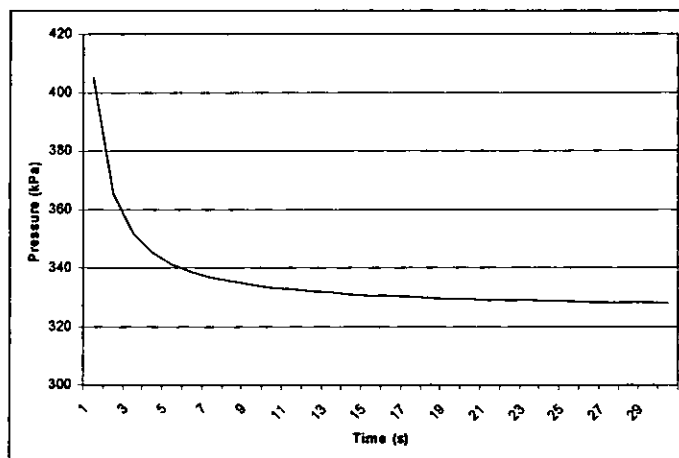


Figure 5-4 Pressure profile over time that would produce a linear change in volume.

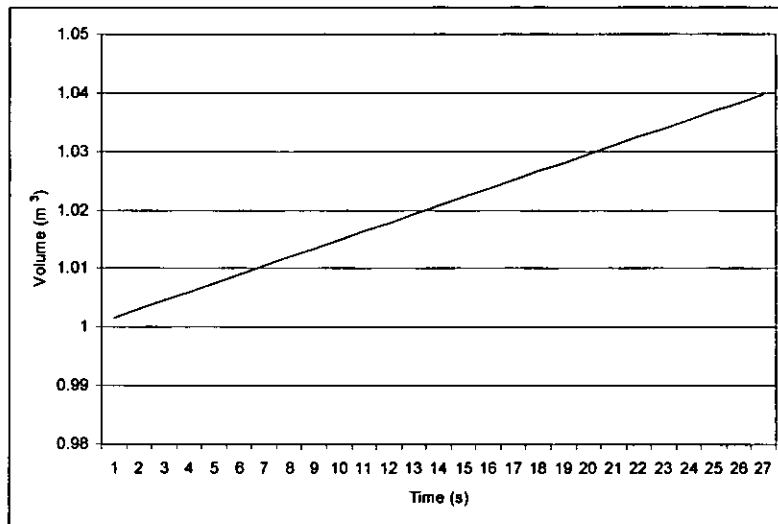


Figure 5-5 Change in volume for the pressure profile shown in Figure 5-4

Thermal loading methods have some distinct advantages over vacuum stressing methods in that a linear change in temperature will result in a linear change in volume assuming that pressure remains constant. Over small temperature changes the assumption that the pressure within a defect remains constant can be justified by examining the effects of thermal stressing when applied to carbon fibre composite materials. Most Carbon fibre materials exhibit very small or even negative amounts of thermal expansion. Therefore when a defective area is heated the air or gas held within the defective area has either to expand or the pressure has to increase. Experimental evidence shows that deep lying defects, typically defects that are difficult to image using pressure drop stressing are more readily detected using thermal methods (figures 5-14, 5-15, 5-16, 5-17). It can be concluded therefore that within composite materials the change in temperature at the defective site creates an increase in the gas volume which is evident by a surface deformation. Application of an even temperature gradient can be problematic however and researchers [Parker 1999] have reported that this is best applied with infra red lamps. In the experiments carried out for this work white light halogen lamps were used which were capable of producing a reasonable temperature gradient but caused the imaging system to saturate during heating therefore data acquisition could only be attempted during the cooling period. Under these conditions the thermal properties of the

material under test make a significant contribution to the test results as the test is reliant on the thermal conductivity of the parent and defective material during cooling whereas during heating the heat input can be such that thermal dissipation is negligible.

Pezzoni and Ettemeyer [Pezzoni 2000] have reported that thermal loading is particularly useful for detecting impact damage in carbon fibre composites. The results presented later in this chapter confirm that thermal stressing does indeed identify impact damage where pressure stressing is unable to detect this material flaw. Other potential benefits in terms of defect detection are flaws that break out to an edge of a component or indeed have a leak path to the surface. In these cases thermal stressing is advantageous. The explanation for this can be ascertained from the analysis of the loading cycle above. In the pressure cycle case it has been stated that practically it is very difficult to decrease the pressure quickly enough in order to create a linear change in volume. As this is the case then it can be assumed that the volumetric change of the defective area is slow. Therefore, if a leak path is present the expansion of air within the defect site has time to escape and the pressure differential is equalised resulting in little or no deformation at the surface. In the case of thermal stressing however the material temperature change can be quite rapid and the volumetric change within the defective will also be rapid. Therefore the surface will deform sufficiently for the detection system to measure.

5.1.7. Application of thermal stressing methods

Early experiments with thermal stressing were conducted by capturing and calculating an initial phase map, applying heat by heating the component with a hot air gun, then capturing a second set of images and producing a resulting image by subtracting the two phase maps. This was only partially successful and at the time it was decided that vacuum stressing was the better method as it was easier to apply evenly over the area of inspection, could be accurately controlled and was more suitable for production inspection. However, it has been found that the temporal unwrapping process which was originally developed for the vacuum

stressing also has significant benefits when thermal stressing is applied and initial trials have indicated that this form of stressing not only improves defect detection in certain circumstances but in the case of barely visible impact damage it can detect defects that are undetectable by the vacuum stressing method. However, like vacuum stressing the optimum defect detection is achieved by controlling the timing of the data capture so that each set of phase images are captured before the surface deformation deforms more than 2π . Whilst it is practically more difficult to subject a component to an even heat distribution, it is possible to rapidly raise the surface temperature of the component albeit slightly more unevenly. As stated previously the change in volume of a void type defect containing air is proportional to the increase in temperature at a constant pressure. Therefore under ideal conditions the displacement at the surface will increase linearly for a linear increase in temperature. Matching the image capture and ensuring the timing interval is sufficient to overcome wrapping of the phase information can be readily controlled by a steady rise in temperature. Thermal stressing methods are therefore beneficial when searching for defects that have a leak path to the surface as the heat input can be tailored to create a rapid rise in temperature thus creating a surface deformation before the expanded air is able to leak to the outside surface. Typical defects that exhibit leak paths to the outer surface are impact damages in carbon fibre composite materials and disbanded structures where the disband breaks an edge. In these cases it is difficult to capture the phase maps in such a short period as the leak paths are relatively large in comparison with the overall defect size and hence rapid heating is required. Temporal unwrapping techniques for this kind of stressing therefore have to be fast and short term. The short term aspect is due to the rapid expansion of the volume which initially deforms the surface but is then equalised as the defect opens and the change in volume is lost due to an exhaust of air to the open surface. Long term integration of numerous phased stepped images have no effect on defect enhancement and only serve to add noise and increase the risk of rigid body movement de-correlation.

5.1.8. Laser illumination.

Lasers illumination in shearography causes a speckle pattern to be generated on the surface of the component under test. Speckles are the bright and dark spots that appear on a diffuse scattering surface when illuminated by laser light. This phenomenon occurs when an object is illuminated by a coherent light source as all illuminated object points emit waves that can interfere. The speckles form a random pattern in space which is stationary in time but fluctuates in intensity from point to point. Speckle patterns are considered a source of noise in most laser applications however the speckles do carry information about the wavefront phase which is of interest in shearography inspection.

Lasers used for shearography are normally continuous wave and operate in the transverse mode (TEM_{00}). Most shearography systems modify the laser beam using an optical beam profile arrangement to diverge the laser into a large circular illumination pattern. This method produces a beam with a Gaussian intensity profile. Therefore when a surface scatters light in all directions i.e. a perfect reflector, the resulting image will appear brightest at the centre. Salter et al report that around the periphery of the image, the image will be darker and the noise level will have increased. Many researchers have attempted to overcome this problem by using more powerful lasers so that at the periphery even though there is a decrease in intensity the signal to noise ratio is still high. The main problem with this approach is that larger lasers require more rigorous safety precautions, are more expensive and not easily integrated into a shearography system.

Parker and Salter [Parker 1999] have analysed the illumination methods used for shearography and concluded that the mean speckle modulation can be approximated by:-

$$\overline{M} \approx 0.24i_1 + 3.6$$

(5-15)

and from their experiments have demonstrated that even illumination raises the average grey level (i_1) from 64 to 170 thus increasing the modulation depth and signal to noise ratio by a factor of 2.32.

Having demonstrated that even illumination is beneficial in that it increases the signal to noise ratio Parker and Salter then went on to implement an even illumination method on the BAE SYSTEMS shearography system. This was accomplished by scanning a laser line which was projected on to an oscillating mirror.

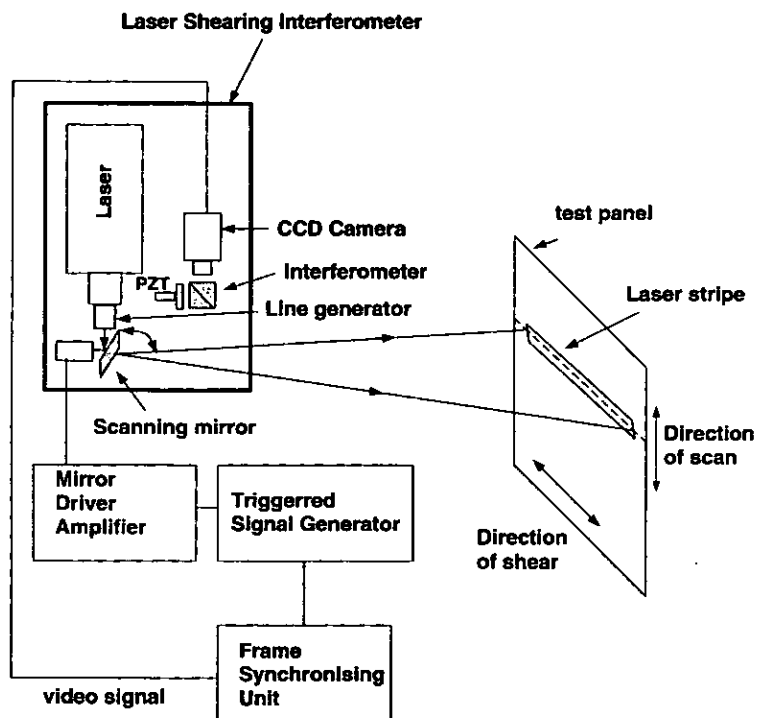


Figure 5-6 Schematic showing the modules required for illumination by a scanning laser.

Care has to be taken to ensure that the coherent speckle is present simultaneously and the line width has therefore to be sufficiently wide and parallel to the direction of shear. A practical way to ensure speckle coherence and parallelism is to expand the line by a line generator, see figure 5-6 above. Figure 5-8 below shows the even illumination produced by the laser scanning method. The width of the illuminated field is governed by the length of the projected laser stripe hence the amount of

illumination in this plane is governed by the distance from the scanning mirror to the component surface. The height of the laser illumination is controlled by the amount of sweep that the scanning mirror takes. In the case of this experimental set-up the sweep was controlled by the amplification of the sine wave output from the function generator. The larger the peak voltage applied to the motor the greater the rotation of the scanning mirror and therefore the greater the extent of the sweep of the scanning laser beam.

5.2. System Implementation

Theoretical problems associated with shearography have been examined in previous paragraphs and suggestions on how these problems can be overcome have been put forward. Implementation of the practical enhancements however requires a series of electronic modules and bespoke software to control each module so that the correct parameters can be applied. Phase stepping increments, vacuum control, laser swept illumination, positioning of the imaging system and data acquisition all have to be performed at precise times within the inspection period. Synchronisation of each module to perform its particular function at the correct stage is therefore achieved via software communication to bespoke electronic instruments whose analogue outputs are connected to each device. The experimental set up can be logically divided into the optical imaging system, manipulator, illumination and vacuum devices which are all controlled by an external personal computer. The optical set up, laser illumination device, manipulator and image capture CCD camera are all housed in a large chamber.

The chamber (figure5-7) serves two purposes, it provides a safe environment for the laser illumination and also a method for producing a suitable pressure drop. Whilst control of the pressure drop and positioning of the imaging device are important, the optical device that facilitates image shearing, phase stepping, and component illumination are primarily the key to reliable and robust defect detection.

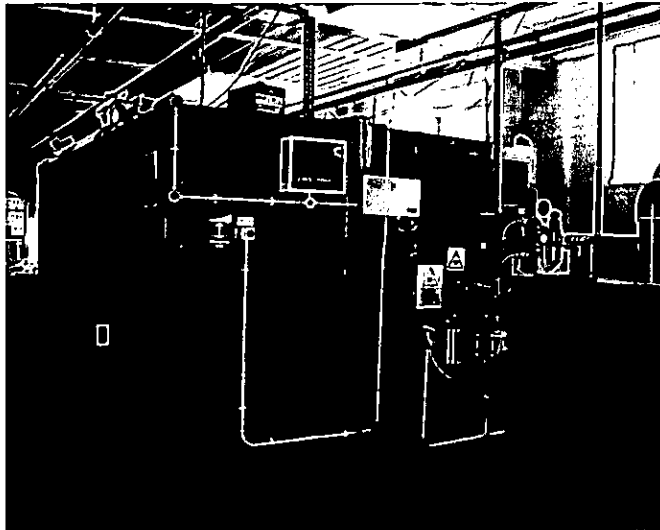


Figure 5-7 Shearography vacuum chamber, vacuum pump and voltage controllable valve

5.2.1. Illumination stage

The component under test is illuminated from a Nd Yag Atlas laser working at a wavelength of 532 nm. The point emitting from the laser is immediately diverged into a line of approximately 1mm width. This line is then projected onto a scanning mirror, which sweeps the laser line across the component under test. The advantages in this method of illumination are that even intensity illumination is achieved over the whole area. This approach differs from all other shearography systems where the laser is diverged into a cone thus producing a Gaussian beam profile, i.e. uneven illumination from the centre to outer edges of the beam. For the scanning mirror to work the scanning frequency has to be synchronised with the camera used for image capture. This is achieved by stripping the synchronisation signal from the camera video signal and using this signal to initiate a sine wave output from a function generator. The sine wave is then amplified sufficiently to drive the motor on the scanning mirror. The data capture camera and scanning mirror are therefore synchronised and the captured image does not exhibit the beat pattern that is common when two imaging systems are used serially, for instance, a video

image of a computer screen. Figure 5-8 below demonstrates the even illumination achieved by the scanning laser line method.

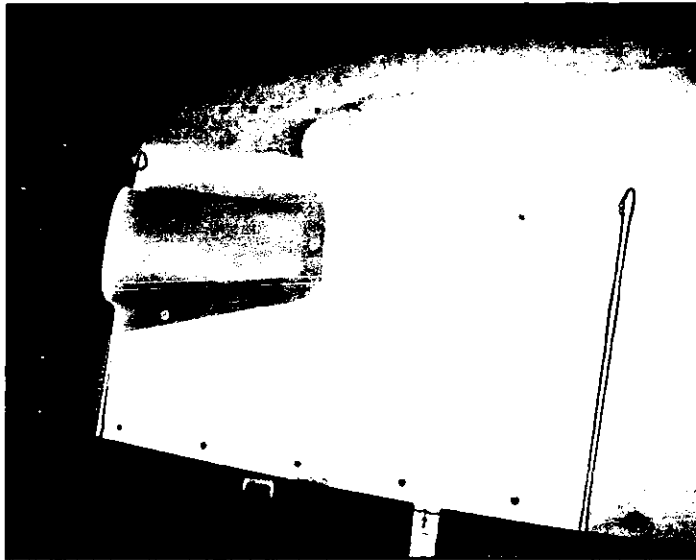


Figure 5-8 Even illumination achieved with a scanning laser

5.2.2. Shearing optics

Shearography images are produced by capturing an image that is formed by the reflection of laser light from a components surface but has passed through an interferometric optical system where the incoming light is equally split along two paths. Each of the optical paths are a different length and therefore the captured image has the same image duplicated and spatially shifted by the path difference amount. The apparatus used to create a sheared image in the experimental system is shown below (Figure 5-9). The optical prism with two reflecting mirrors is generally described as a Michelson interferometer set up.

The Michelson interferometer comprises of a split cube where one face of the cube is coated with a mirror finish. The camera is placed at the face opposite this surface. On the face at a right angle to this, a further mirror is situated, but this is connected to a piezo shifter, which moves the mirror very small amounts when a small voltage is applied. The angle of the mirror attached to the piezo shifter is adjustable (not shown in the diagram above) which creates an optical path difference between the split beams. The net result of this optical set up is a single

image containing data from an optical source with different path lengths
i.e. a sheared image

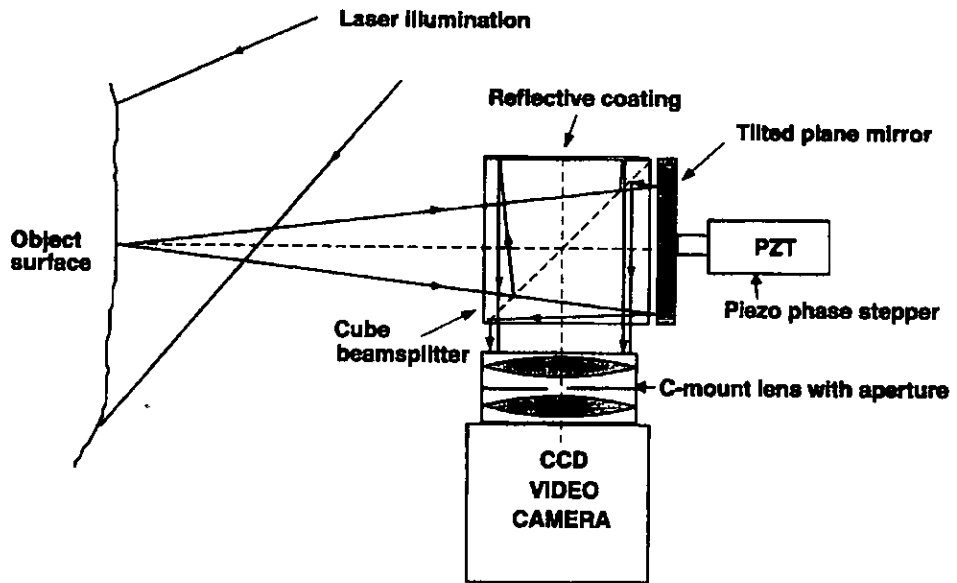


Figure 5-9 Michelson interferometer with phase stepping mirror

The mirror connected to the piezo shifter is used for phase stepping. This is the method of calculating the phase image (described previously) from several intensity images by incrementing the shearing distance, capturing several intensity images and using the speckle patterns and the step value to produce a phase map. Phase stepping requires sub micron increments ($\lambda/4$) of the piezo shifter and hence the angled mirror. The amount of phase shift generated is controlled from the data acquisition PC via a serial to IEEE 488 converter which communicates with an accurate millivolt DC source. The PC and software provide the synchronisation of the image capture with the phase stepping sequence.

5.2.3. Optical Detection system.

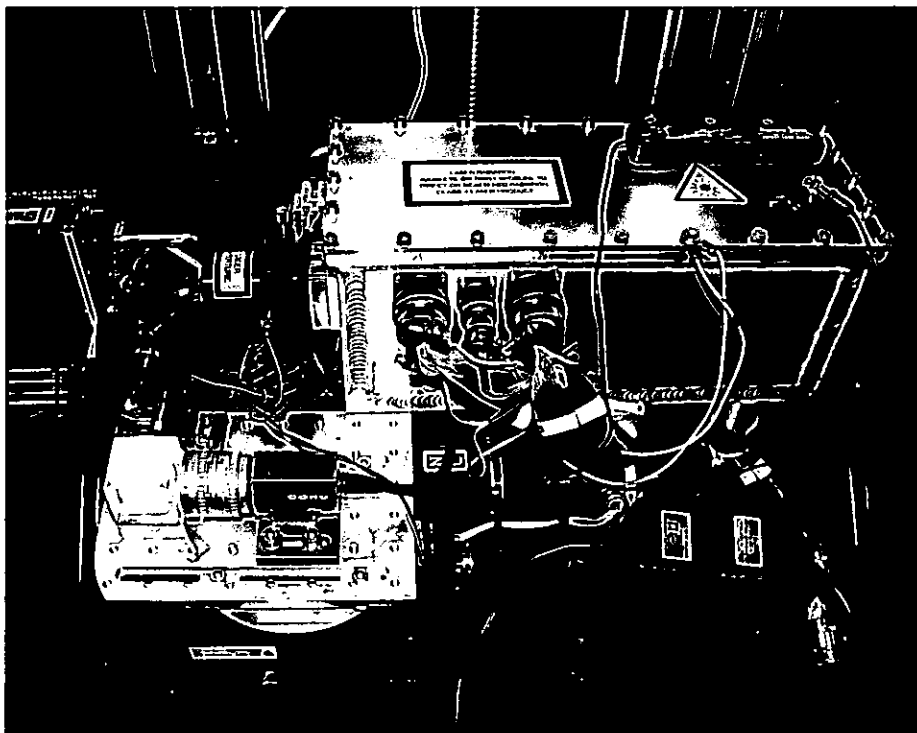


Figure 5-10 Experimental set up mounted on a gantry manipulator.

The interferometer set-up has been described previously and is shown in the picture above. However the optical detection system would not be complete without a suitable CCD camera and lens. In the experimental set up a COHU 4992 CCD camera was used that was connected to a Imaging technology MVC40 framestore. This camera framestore combination captured 512 X 512 X 8 bit images. Camera aperture was set manually and was adjusted to avoid camera saturation which was dependant on the reflectivity of the components surface being inspected.

5.2.4. Graphical User Interface

A major part of the development was the computer control of all the system modules described above. Communication between PC and the manipulator and image frame grabber is performed by cards fitted internally in the expansion slots of the PC, whereas the piezo controller and the vacuum pump have to be controlled by communicating across the RS232 serial line. The developed software therefore takes two

approaches to controlling the external modules. Firstly the image frame grabber and manipulator are supplied with source code library files that can be called from the program and compiled into executable software. The piezo controller and vacuum pump valve however, do not have PC expansion cards or library source code for control and therefore specific communication software had to be developed. Both the programmable power supply for the vacuum valve and the piezo controller are fitted with IEEE 488 interfaces, therefore the developed interface software sends serial data to a converter where the data is translated from RS232 to IEEE 488 format. The benefit of IEEE488 communication is that various instruments can be daisy chained and addressed by a specific device number. Therefore, when the data is translated to IEEE488 format and passed on to the instruments in the chain, only the instrument with the corresponding device number will react to the data that follows. There are various methods for communicating across serial links from a PC system, the method chosen here was probably not the most elegant solution but was quick to implement and therefore served the purpose for a demonstration system.

The majority of the system software was developed using the Microsoft C language and compiler, however the graphical user interface that interfaces between the operator and the system modules was developed using visual Basic. This allows the operator to change the various inspection parameters, manipulate the shearography head and view the resulting images in a windows NT4 environment. The end result is a windows NT4 based software package that controls all the data capture, processing, manipulation, parameter setting and presents the inspection results on a second monitor. Image phase maps that are being derived temporally as the stressing force is being applied are sequentially displayed on the monitor thus providing a progressive realisation of defective areas.

5.2.5. Vacuum Pump

A large vacuum pump (figure 5-7 page 204) has been installed beside the chamber that is capable of reducing the pressure inside by 250 mbar

in approximately 30 seconds. This is sufficient to provide suitable stresses for most defect detection. A computer-controlled valve is connected between the pump and the chamber so that complete control of the pressure drop profile can be achieved. The valve operates according to the voltage applied to its control circuitry. A programmable power supply applies a voltage to the valve, the value of which is controlled from the PC via a further RS232 communication port. The chamber itself is constructed from 6mm sheet steel supported by a box section frame. The frame work is designed to withstand the external force produced by the pressure differential during the inspection stage but in order to eliminate the possibility of speckle de-correlation during the vacuum process no part of the shearographic system is connected or touches the outside walls of the chamber.

5.2.6. Manipulation stage

Within the vacuum chamber there is a Naples Coombe three axis manipulator that carries the laser and interferometer. This is constructed from aluminium box section that can be bolted together to form a rigid structure. As shearography detects very small deformations of the surface it is essential that the manipulation stage does not suffer from inherent vibrations during the inspection, the construction and design chosen achieves this. The table that houses the optics is fastened to the manipulator and can be moved in the horizontal and vertical directions around the chamber. This is performed via ball screws and sliders on each axis, which are connected to DC servomotors.

The third axis is a rotary stage that has not been fully implemented but was intended to give the ability to angle the optical head to be normal to the surface being inspected. Work to date has shown this to be unnecessary. The accuracy and repeatability of the manipulation stage is better than 0.5mm in both cases. Control of the manipulator is performed from the control PC that communicates with a Gallil motion controller via a PC expansion card.

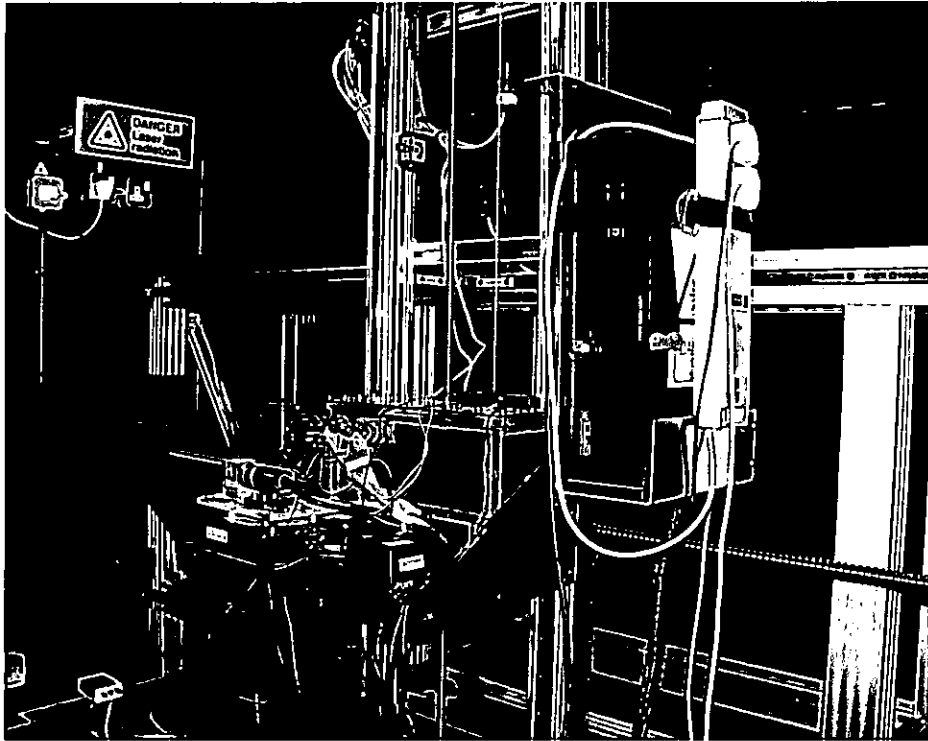


Figure 5-11 Manipulator carrying the laser and optical set up

5.3. Application to composite aerospace components

Bare carbon composite materials have a relatively rough, dark black surface. Thus when attempting to illuminate an aircraft component made of carbon fibre composite the amount of light reflected is low due to the non reflecting matt black surface and the speckle pattern is noisy due to surface roughness. Low light levels reduce the dynamic range of the optical system and as such reduce the defect detection because intensity changes caused by surface deformations will be small. Composite materials are also relatively stiff which means that surface deformations are small relative to the size of defect. Also in comparison to metallic components of similar design the type of defects that can be expected in composite materials is extended as they are prone to impact damage and foreign material inclusions. Impact damage usually causes a cracking of the polymer matrix and as such there is an air leak path to the surface which as mentioned previously complicates the detection method. Inclusions can, and usually do, become bonded in the fibre resin matrix, when this happens there is little or no air gap and therefore no differential in pressure in a vacuum stressing situation. Defects of this type are

therefore very difficult to image. Fortunately many composite designs are thin skinned nomex honeycomb configurations where the prime structural requirement is the bond between the skin and the honeycomb. In this instance shearography can readily identify failures at the bondline and has the advantage of being able to give a definite indication as to whether a skin is bonded or otherwise. Compared to ultrasound and radiographic testing this is unique as ultrasound will indicate areas of suspected disbond but does confuse areas of thick adhesive with disbond indications. Radiography cannot readily detect unbonded areas as the defect is planar. Shearography combined with a vacuum stressing method is therefore ideally suited to thin skin honeycomb bonded applications as it can be readily applied either by a vacuum hood or pressure drop chamber but more importantly is unambiguous in its detection of this type of defect.

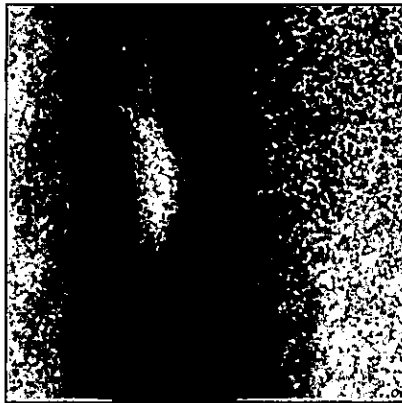


Figure 5-12 Disbond on a thin skinned honeycomb panel

5.3.1. Impact damage detection

Figure 5-14(a)(page 214) below shows the results of a 20 second five phase stepped temporal unwrapping shearographic inspection. This image was captured using vacuum stressing on a solid carbon fibre laminate that had been subject to impact (ref figure 2-14). Figure 5-14(b) shows the same portion of the panel after heating. The same data acquisition method was used to produce this image in terms of timing and phase calculation but the raw laser speckle images were captured as

the panel was cooling. Figure 5-14(c) shows a further portion of the panel which was imaged in the cooling stage with the same timing and phase map calculation. From the results below it is quite clear that vacuum stressing did not succeed in detecting any of the impact damage sites. The fringe patterns in the images acquired during thermal stressing are wrapped because the surface displacement is rapid and short term. The data acquisition could not be performed before the defect had displaced the surface by more than 2π and therefore the result is a wrapped defect. The background however is unwrapped which helps to highlight the defect indication. It should also be noted that there is a significant difference between the backgrounds Figure 5-14(a) and (c). Both images were captured in the cooling process however Figure 5-14(c) was captured earlier in the cooling process and as such has been affected by thermal currents and a general bending of the panel (rigid body motion) which has added to the noise (thermal currents) and created an amount of speckle de-correlation. The wrapped fringes at the impact sites are not well defined. There is only one fringe per impact site. This is due to the 10 mm shear used during the inspection being greater than half the diameter of the surface displacement (reference figure 5-13). The surface displacement shown in the upper part of figure 5-13 shows large shearing that is less than half the diameter of the defect. In this case large shearing gives greater sensitivity as small displacements would still result in a difference in the sheared image. In the lower part of the diagram it can be seen that a large amount of shear i.e. greater than half the defect diameter, would result in only a partial fringe and the deformation measured is not optimised. This is the case for the thermal images of the impact specimen.

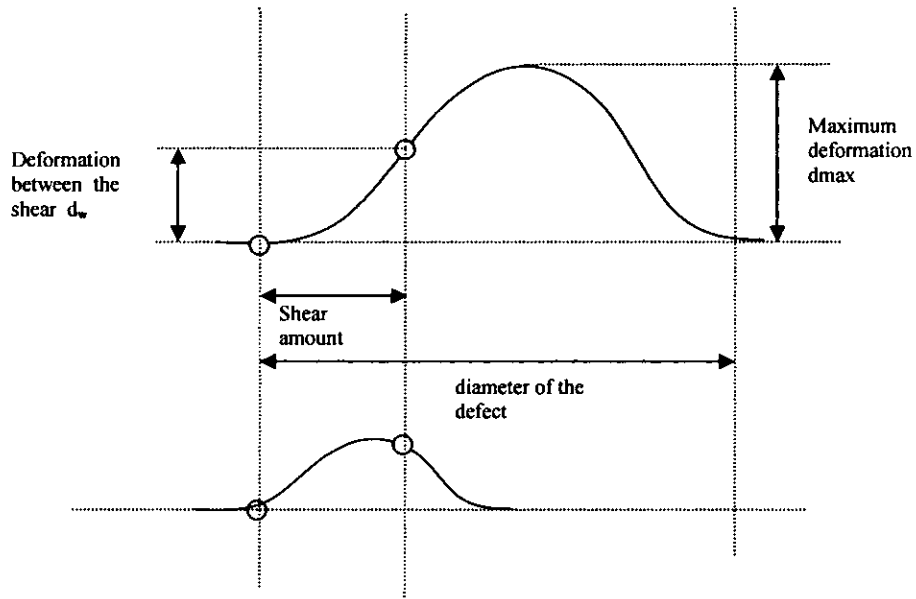


Figure 5-13 Schematic detailing the relationship between the amount of shear and the defect diameter

The defects present in the impact specimen are however, far greater diameter than the deformation recorded in the thermal shearographic images. Impact damage in carbon fibre composites normally takes on a Christmas tree effect where the delamination at the surface is small in diameter and further delaminations increase in diameter as the impact travels through the thickness of the material. Barely visible impact damage (BVID) as represented by this panel is therefore not detectable by vacuum stressing shearographic methods and under thermal stressing shearography only detects the surface damage. The full extent of the damage cannot be distinguished and both large and small area impact sites are represented in a similar manner.

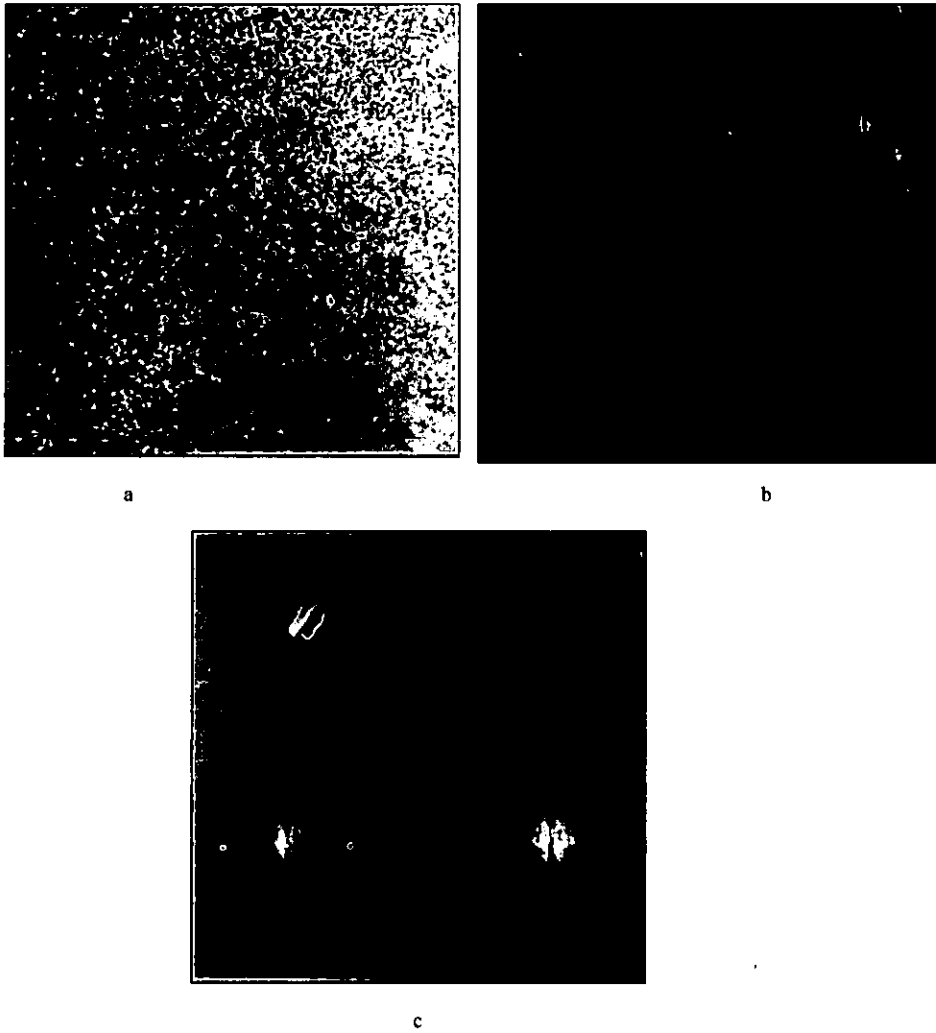


Figure 5-14 Impact damaged specimen

Figure 5-15 (page 217) below shows the results obtained by the same data acquisition method described above when applied to the material inclusion specimen. Thermal stressing was applied in this case of image “a” and a combination of thermal and vacuum was applied for image “b”. The mixture of thermal and vacuum stressing has raised the defect detection capability and five out of six inclusions present in the material can now be detected. It should be noted however that the smaller square inclusions are wrapped and more noticeable in the thermal only image and the difference in the large oval inclusion which is unwrapped in the thermal image but wrapped in the combination of vacuum and thermal image. These results can be explained by examining how the stressing

was applied and the limitations of the experimental system. Thermal loads were created using two halogen lamps which when switched on saturated the imaging system. Shearography could only take place during the cooling process. If a vacuum was drawn while the component was cooling the two stressing methods would counteract each other as a drop in external pressure would cause the defect areas to expand whereas the cooling effect would contribute to the defect areas contracting. Defect detection would be dependant on which stressing force was the dominant. For these experiments the thermal load was applied and a vacuum drawn prior to the data acquisition. The application of heat was removed and after a few seconds the vacuum was released and the chamber began to return to atmospheric pressure. Defect detection was therefore reliant on the additive effects of thermal and vacuum relaxation. As mentioned previously the rate of expansion of a void differs under a change of pressure to that of a change in temperature. Optimum defect detection is achieved when the sampling and calculation of phase maps are synchronised to be shorter than a 2π period. In the results below the optimum data acquisition rate has not been achieved and due to the fact that the smaller defects were originally wrapped in the thermal image but are not in the combination image it can be assumed that the application of a vacuum to a thermally loaded specimen has retarded the relaxation of the surface displacement. The wrapping of the large oval defect in the combination image however contradicts the above theory but can be explained by assessing the contribution from the vacuum. The defect immediately above the large oval defect is only visible when the vacuum and thermal loads are applied hence the vacuum part of the cycle must make an important contribution to the identification of this defect. The change in pressure was not controlled as the valve was opened to vent and there was a sudden increase in external pressure. It can be assumed therefore that the initial change in pressure within the chamber was very rapid which resulted in a non-linear change in volume of the defect. This rapid change made a significant contribution to the initial behaviour of the largest oval defect and the one immediately above which resulted in them being detected. Once the initial change in pressure had subsided the

thermal cooling became the dominant factor which results in a linear change which is slow in relation to the data acquisition and hence all subsequent defects are detected unwrapped.

The conclusion to be drawn here is that defect detection can be enhanced for certain applications if a very rapid change in pressure can be achieved. Rapidly creating a vacuum in such a large chamber is very difficult and would require a very large capacity pump. However, releasing a vacuum by opening a large bore valve does result in a rapid change in pressure which in this case increased defect detection. The contribution of the thermal load during this rapid change in pressure is unknown.

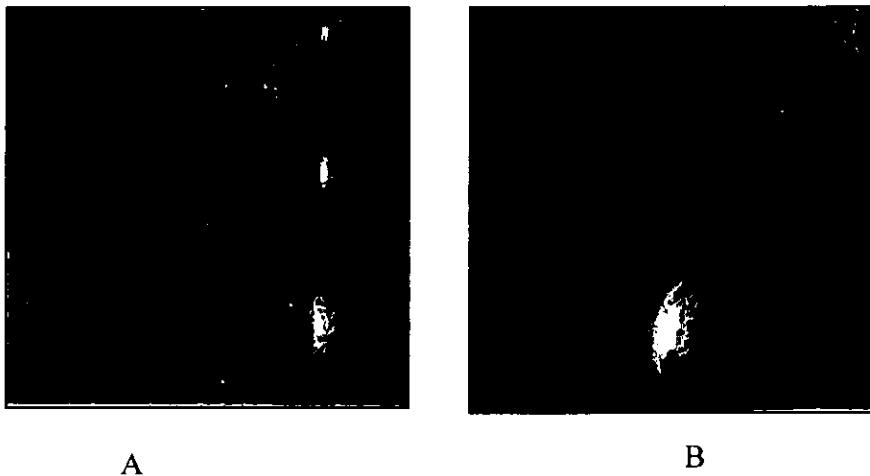


Figure 5-15 Shearographic results for the Ancillary material specimen A) Thermal stressing B) Combined thermal and Vacuum stressing.

Figure 5-16 shows four shearographic images of a thin composite skinned honeycomb panel with two areas containing simulated defects. The simulation is achieved by including PTFE patches in the lay-up(see chapter 2 for a description). The upper two images were captured during pressure drop stressing whilst the lower two images were captured using thermal stressing. The two leftmost images are the pressure drop and thermal results for the same area of the panel. It can be seen that both methods identify all the simulated defects. There is however a slight masking of the defects in the thermal image which is caused by rigid body movement. Thermal stressing is however able to detect all the

defects in the area shown to the right of figure 5-16 whereas two of the smaller defects are missing in the pressure drop image. The difference between this part of the test sample and the area depicted by the leftmost images is the presence of a peel ply and copper mesh on the surface. In this case it is likely that the additional layers are sufficient to render the deeper defects undetectable for pressure drop stressing. For thermal stressing however, the conduction of the copper mesh acts as a barrier to the thermal wavefront and therefore more heat is required before the defects become visible. The increase in heat input does however cause a greater rigid body movement and one defect is just barely visible because of this effect.

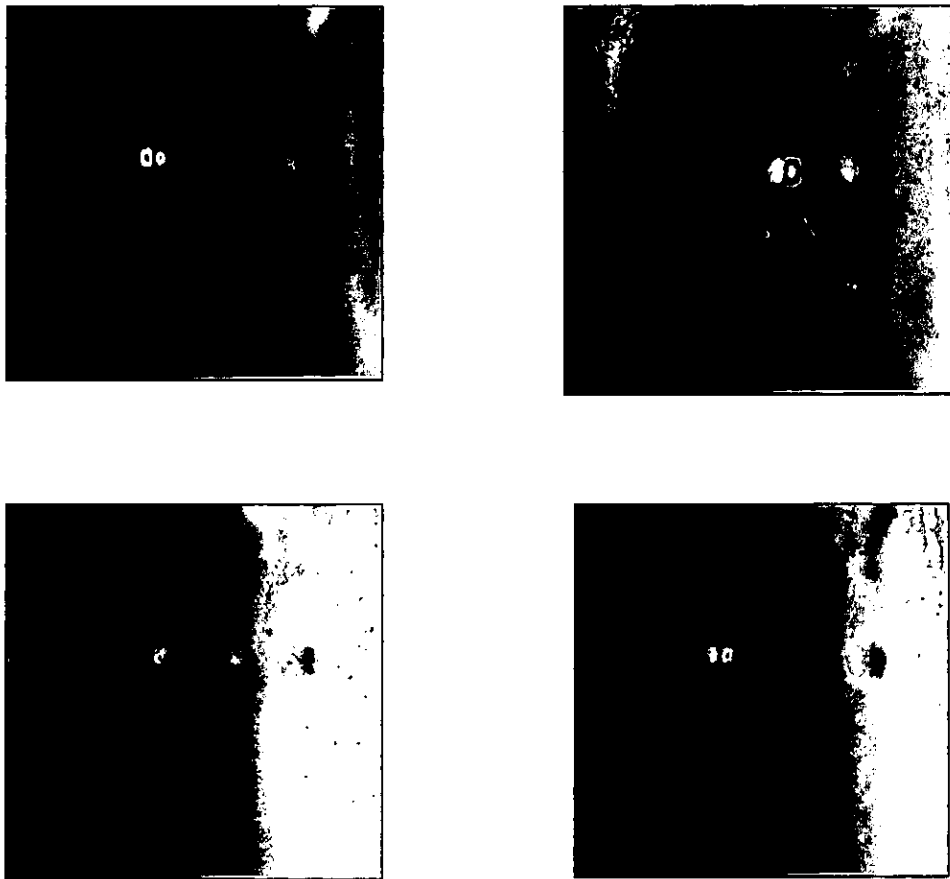


Figure 5-16 Shearographic images resulting from vacuum stressing (upper images) and thermal stressing(lower images).

Figure 5-17 shows images captured from vacuum and thermal stressing for a scarfed repair of thin skinned honeycomb structure. The

repair appears to be successful in terms of bond quality and as such there are no indications of disbond in either image. In the vacuum image there is a small area that is different from the background but this is due to the substructure at this site being more rigid than the surrounding area. In the thermal image there are numerous indications of changes in the rigidity of the sub-structure. All the circular ply layers and the underlying honeycomb can be distinguished in the outer parts of the image and there are two indications where the repair patch has been joined. This result demonstrates that whilst thermal stressing is useful for enhancing defect detection the increase in sensitivity to defects also increases the sensitivity to underlying structure and the operator must therefore understand how the underlying structure is represented in the results.

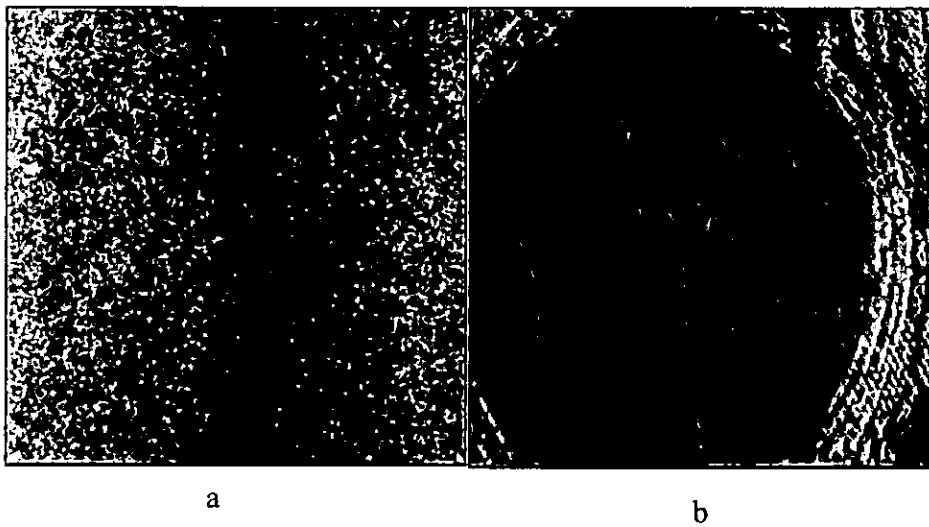


Figure 5-17 Shearographic results of a spliced repair to a thin skin honeycomb structure. a) Vacuum stressing, b) Thermal stressing

5.4. Application to metallic honeycomb structures bonded to thin metallic skins.

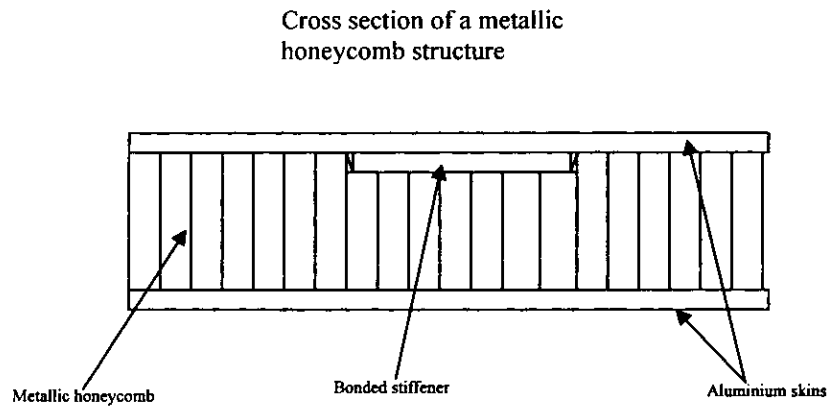


Figure 5-18 Cross sectional diagram of a typical metallic honeycomb structure

Metallic honeycomb bonded structures are typically configured as described in the figure above. Aluminium honeycomb is machined to the shape of the inner structure which can be tapered aerofoil section with machined pockets to allow for increases in skin thickness. The aluminium outer skins are thin and they have thicker section aluminium plates bonded to the inner surface in places where extra strength is required. In the section above therefore there would be an adhesive bond between the outer skins and the honeycomb, an adhesive bond between the outer skin and the stiffener and a foaming adhesive bond in the gap formed between the honeycomb and the edges of the stiffener plate. Foaming adhesive is used to fill in any gaps that may be present between the honeycomb and the inner surface interface.

When shearography is applied to this type of structure a rapid inspection method that is capable of detecting all incidences of unbond is achievable. In the experimental work for this thesis vacuum stressing was applied and the results are shown below.

Figure 5-19 below shows the surface of a metallic honeycomb section when imaged through the shearing lens but illuminated by white light.

From this, the amount of shear being applied can be determined and focusing of the camera optics can be ensured. The hatched area in the middle of Figure 5-19 is the area of a disbond between the outer skin and the metallic honeycomb that was detected using a mechanical impedance analyser. There is another smaller disbond area to the upper left and right of the image. The camera aperture is set so that under ambient white light conditions the image is just verging on saturation. Under these conditions when laser illumination is used and the ambient white light turned off, the laser light entering the camera does not saturate and therefore makes best use of the 8 bit dynamic range.

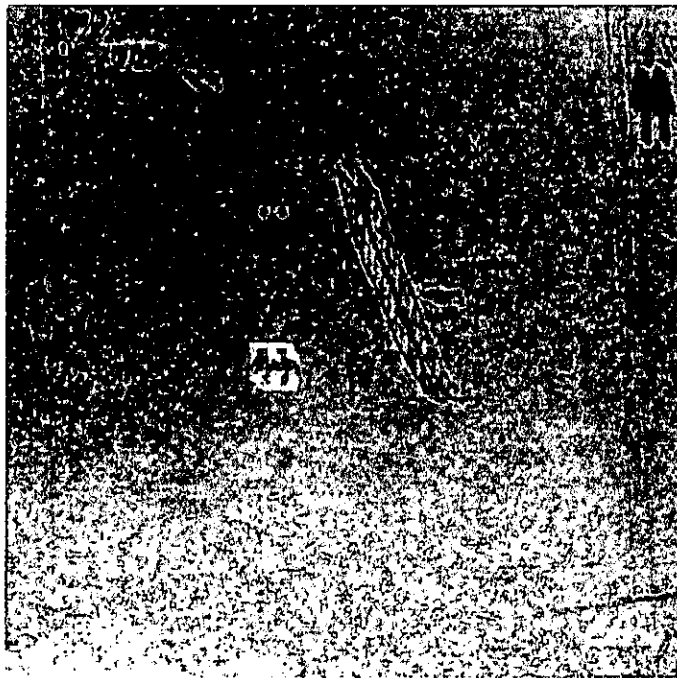


Figure 5-19 Raw image captured through the shearing optics

The image below shows the shearographic result after a 20 second temporal data acquisition sequence. The underlying structure is so badly disbonded that when subjected to a pressure differential it immediately displaces the surface. The area around the stiffener plate contains numerous areas of disbond and as such produces wrapped fringe patterns of all different shapes and sizes. So much so that it is difficult to determine if any part of this area is bonded. What should also be noted

here is that there are fringes in the stiffener area with distinct pairs of white and black fringes indicating that there are areas of disbond at either the skin to plate bondline or the honeycomb to plate interface. One further point is that there are areas that indicate deformation but do not appear as wrapped fringe patterns. These areas whilst not significant in appearance in such an image are indications of a defective bond and as such should be included in the analysis. The unwrapped areas are indications obtained from isolated disbond sites which are relatively small in comparison to the main disbond around the stiffener. Because of their size the change in pressure acts over a smaller surface area and therefore the rate of expansion is slower than the phase map calculation process. The temporal un-wrapping algorithm is therefore able to process the phase maps and present a smoothed image of these disbond sites. Figure 5-20 (B) is an image of a well bonded structure of similar construction. In this image the extra rigidity of the stiffener can be detected and the honey comb cell pattern in the underlying structure is evident. This image is useful in that it clearly shows what a temporally captured shearographic image should appear like when the structure is bonded correctly and therefore confirms the poor bond quality of the structure shown in figure 5-20(A). Sectioning the structure to confirm results is therefore not necessary and the sample can be retained for future use.

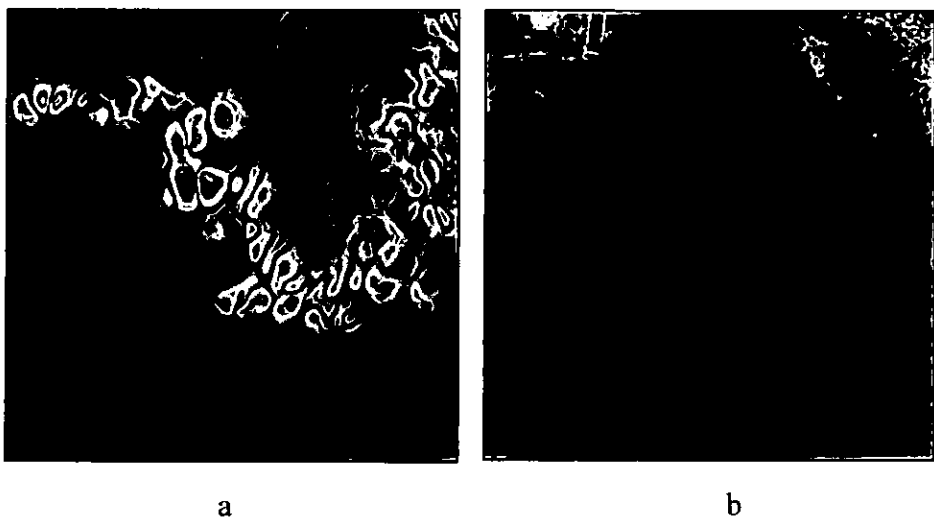


Figure 5-20 Shearographic results of a) Poorly bonded structure b) well bonded structure

5.5. Defect detection capabilities.

Defect detection capabilities of shearography systems can be determined from the laser wavelength, amount of shear and the noise power spectrum of the captured images. The laser wavelength will determine the minimum surface displacement that is measurable which can be calculated by :-

$$S = \frac{2\pi}{\text{imaging} - \text{depth}} \quad (5-16)$$

where S is the theoretical sensitivity and the *imaging-depth* = 256 for 8bit hardware resolution.

Hung [Hung 1982] derived that if the angle between the illumination and the CCD image acquisition camera was very small then the relative phase change Δ is related to the relative deformation δw between two points in the out of plane direction and can be calculated by :-

$$\Delta = \frac{4\pi}{\lambda} \delta w \quad (5-17)$$

Combining equations 5-16 and 5-17 the theoretical minimum relative deformation (δw) can be expressed as:-

$$\delta w = \frac{\lambda}{4\pi} \frac{2\pi}{256} = \frac{\lambda}{512} \quad (5-18)$$

Therefore for a laser wavelength of 532 nm the theoretical measuring sensitivity for deformation is 1 nanometre. Of course the relative deformation is the deformation difference between two points and therefore the theoretical deformation is dependant on the amount of applied shear. If small amounts of shear are used then the ratio of deformation to shear will be low and the sensitivity will be low. Larger amount of shear should therefore be adopted. However, as explained earlier (reference figure 5-13 page 214) if the shear amount is too large the maximum deformation will be lost. Shearographic detection capabilities are therefore very much dependant on the relationship

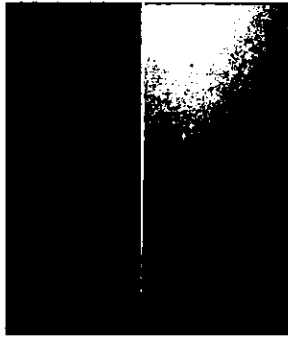
between applied shear and the expected deformation from a potential defect. Deformation of defect sites is dependant on the size of the defect, the materials elastic properties and the applied load. Therefore an estimate of the defect detection capabilities by using the minimum detectable defect size and depth and applying elastic theory to obtain the expected deformation can be performed.

A theoretical approach to the determining the deformation per applied load has been suggested by Yang et al [Yang 2005] who use elastic theory to calculate the maximum deformation at the centre of a defect by:-

$$w_{\max} = \frac{3(1-\nu^2)\Delta p}{16Et^3} X \left(\frac{D}{2} \right)^2 \quad (5-19)$$

Where Δp represents the applied load, E = the modulus of elasticity, ν = Poisson's ratio, t = the depth of the defect and D = the defect diameter.

Whilst w_{\max} can be theoretically calculated and the amount of shear should be set to a maximum of half the expected minimum defect size the theoretical minimum deformation that can be measured should be treated with caution as speckle noise etc. will significantly reduce this figure. Figure 5-21 shows two images of a laser illuminated transition from a black to white surface. It is noticeable that the larger aperture has a larger illumination range and the subsequent profiles (figure 5-22) show that the speckle noise is less for the larger aperture. As expected the power spectral density has a much greater dynamic range for the larger aperture image.



(a)



(b)

Figure 5-21 Laser illuminated image of a transition from a black to white surface (a) f28 aperture, (b) f4 aperture

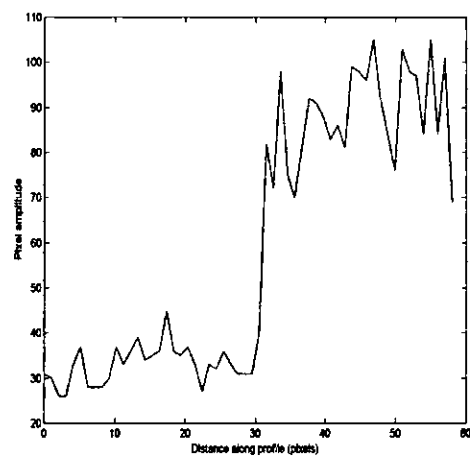
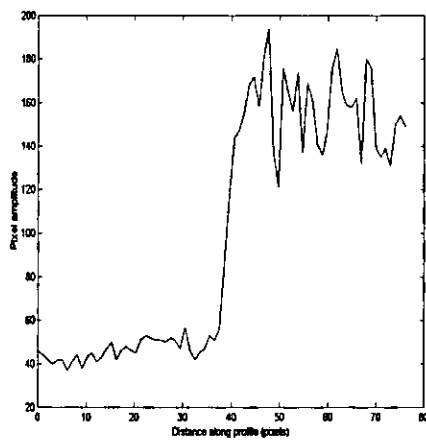


Figure 5-22 Profile of the transition in figure 5-21 a and b, note the noise levels for the white background (high reflectivity).



Figure 5-23 Raw image extracted from the high reflective white backgrounds at apertures f28 and f4 which is used for the power spectral density calculation

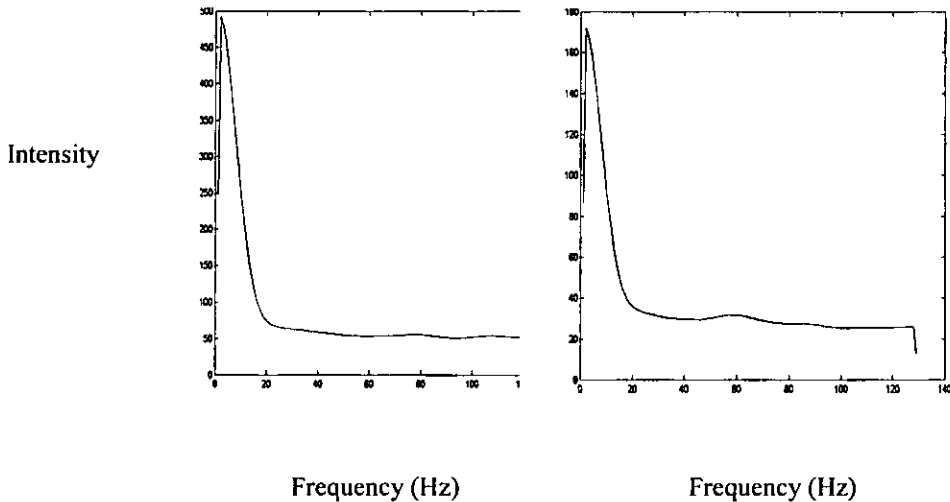


Figure 5-24 Plot of the power spectral density calculated from figure 5-23

5.6. Summary

It has been demonstrated that shearography is an ideal inspection tool for thin skin bonded honeycomb structures when the defect of interest is disbonds between the skin and the honeycomb core. Real aircraft components have been tested by shearography and mechanical impedance, and the results from shearography show the disbond sites to be far greater than that detected by mechanical impedance. Results

presented within this chapter also show the capabilities of the present shearography system on solid composite laminates.

The implementation of the temporal unwrapping method devised by Parker and Salter has enhanced the shearographic inspection capability beyond that of most commercial systems. The synchronisation of the stressing method with the data acquisition and implementing full control of the stressing, phase shifting and data capture [Smith. Patent, 2003] leads to a robust and reliable inspection procedure. However the overall inspection procedure could be further improved by eliminating rigid body motion. If this was achieved larger pressure drops or greater thermal differences could be used which would result in smaller defects appearing as deformations on the surface.

Practically matching the pressure drop to the image capture is difficult as the defect volume increases inversely to the reduction in pressure. This explains why the results from this system show a mixture of wrapped and un-wrapped defect indications. Whilst this does make interpretation more difficult the large defects usually expand more rapidly and therefore appear wrapped and are easily identified whereas the un-wrapped indications can be mis-interpreted due to the subtle changes in the image. The detection of barely visible impact damage was unsuccessful using pressure drop stressing methods due to the leakage path caused by matrix cracking in the composite. Thermal stressing however was more successful but did suffer from rigid body movements that hindered the detection.

One further result and novel contribution to shearography as a non-destructive testing method is the method used for evaluating the detection capabilities. Employing the calculations suggested by Hung et al for the theoretical minimum relative deformation (δw) gives an over optimistic result. However by using the edge spread function the power spectral density can be calculated and then the ratio of the two extremes of the PSD can be used as the maximum available imaging depth and therefore calculate δw in equation 5-18 9 (page 223).

Chapter 6

6. Calibration and Data processing

6.1. Introduction

Previous chapters have described many of the parameters that affect the quality of the inspection method and have discussed in detail how these parameters can be optimised. Traditionally the inspection parameters are derived by experimentation on a test sample with known or simulated defects with each parameter being optimised for the particular inspection. The mixture of parameters that produce the best defect detection are then recorded and used for subsequent inspections. With many of these inspections there is a degree of latitude that allows for some deviation in the set parameters. Minimum significant defect sizes are usually set to reflect the loss of defect detection when parameters deviate from those determined experimentally. The intention of this thesis is to propose non-destructive inspection improvements by emphasising and demonstrating the effects of changes in individual parameters. By doing this the inspection capability can be improved in terms of minimum detectable defect, but also the process can be more robust as the most pertinent parameters are known and can therefore be monitored and controlled. This then allows automated evaluation tools to be successfully implemented without ambiguity caused by fluctuations at the data acquisition stages.

The term automation in this sense is used to describe automation used for the physical data acquisition and also data processing. For any automation to be implemented successfully it is important that the inspection parameters are monitored and maintained within set limits. If limits are exceeded then there is a danger that incorrect results will be obtained. In practical operational terms, automation is usually linked with a reduction in operator skill level, and therefore a degradation of the inspection, could go unnoticed.

When significant automation of the inspection process occurs, the need for accurate monitoring of the equipment calibration is vital. This chapter therefore describes calibration requirements, proposes methods of

automating the task, and goes on to show enhanced data processing methods that then become possible when a robust, well controlled inspection method is implemented.

6.2. Calibration

Calibration can take on different meanings depending on which context it is applied. The correct use of the term calibration in non-destructive testing would be the measurement and alteration of an equipments response to a known standard. However the term calibration is often used to describe the method of obtaining a certain signal response from a reference specimen and using this as a base line for all other measurements. This practice is frequently used for the inspection of aircraft components. There is a potential problem associated with this kind of standardisation or calibration in that flaws do not normally present themselves as ideal reflectors and as such do not produce the same signal response as the reference standard. The range of flaws in the reference specimen cannot include all flaws that need to be detected in the component, therefore the calibration process cannot guarantee optimisation for all occurrences of flaws. Whilst this form of standardisation or calibration is important prior to an inspection (even though it has some limitations) it is equally important to ensure that the equipments' response does not deteriorate through time as subtle changes in, for instance, frequency response, may not be detected by standardising on a reference specimen but would result in a deterioration in flaw detection. Non-linear responses from an amplification stage would result in defects being either over or under sized and they could therefore be classified incorrectly. A further complication to this scenario arises when steps to automate the process are invoked. In particular automated data processing as this requires repeatable and stable data to produce the correct results. Fortunately many modern NDT methods are now digitally controlled in all aspects and this functionality can be used to further automate the calibration procedure.

6.2.1. Calibration procedures

Documented calibration procedures exist in many forms. British standards, European normatives, International standards and society documents such as the American society of materials testing all produce documents that give guidance on how NDT instruments should be periodically checked and suggest methods of checking the pertinent system parameters. Periodic calibration is a quality control procedure that is adopted by the majority if not all aerospace manufacturers. This type of calibration should not be confused with the use of a reference standard that is inspected prior to the inspection of a part but is a periodic check that interrogates the behaviour of the measurement system to ensure that the performance of the combined system accurately captures and represents the input signal. As mentioned previously the use of reference specimens alone is limited because real defects do not always behave like the perfect reflectors used in reference standards and the variation in defect size usually encountered in reference standards is not sufficient to check the linearity, spatial resolution or dynamic range of the measuring instrument.

This thesis has concentrated on improved defect detection by identification and optimisation of the inspection parameters and has demonstrated that it is possible to significantly enhance current capabilities by closely analysing and optimising certain parameters. However the claimed capability must be sustainable as aircraft safety is dependant on robust inspection techniques. Therefore enhancing capability must be matched by enhanced calibration and control. The systems described in this thesis are all modern digital data measuring and acquisition systems which by their digital nature can be readily calibrated by electronic means.

6.2.1.1. Ultrasonic calibration

Both the composite and SPFDB ultrasonic inspection cases described previously make use of multiple channels and a series of measuring gates. Normal practices call for amplifier linearity to be checked and recorded but this is inadequate when adopting enhanced defect detection methods. The

frequency response, pulse shape and duration, the gate position, quantisation accuracy, and the linearity all contribute to robust enhanced defect detection and as such a process that ensures that they are functioning as expected has to be in place

Electronic calibration routines are easily automated and are therefore quick to implement and can be controlled by software. The testing of an ultrasonic pulser / receiver has been implemented by switching a function generator to the input of the amplifier. The output of the function generator is then software programmed to sweep the amplitude and frequency of the input signal and the results after amplification and analogue to digital conversion are measured using the data capture hardware. The time periods measuring accuracy can also be checked in a similar way if the period of the waveform is known and can be adjusted then the delay duration and trigger value of each measuring gate can be set to coincide with the gate parameter and a software function could check the expected response. Out of position gates or errors in quantisation would be highlighted by an incorrect measurement.

The pulse shape has also been identified as being critical to defect detection particularly when inspecting SPFDB. Testing the pulse parameters could use a similar method but an attenuation stage would have to be switched before the pulse input to the amplifier. The attenuation stage must not alter pulse shape throughout the pulse shape range.

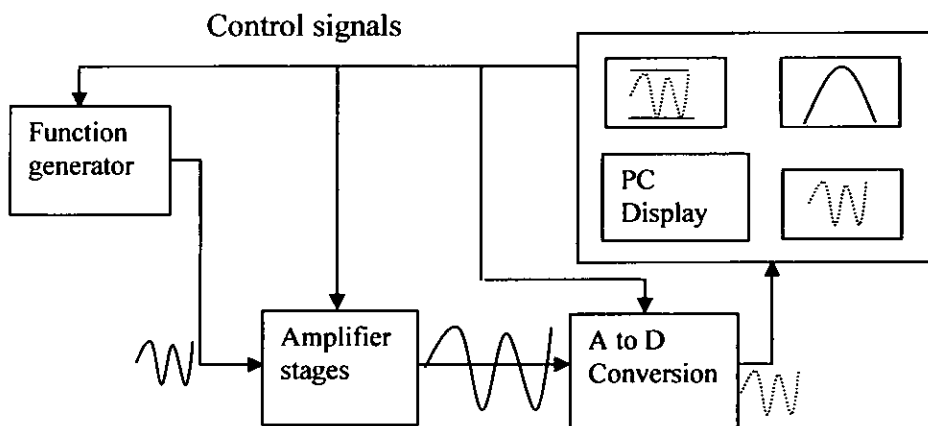


Figure 6-1 Schematic block diagram of an electronic means of testing the performance of an ultrasonic amplifier

Figure 6-1 shows a schematic of an electronic calibration system where the personal computer controls all the system functions and can therefore adjust the input signal and the measuring devices and as such can be programmed to check that the system is functioning correctly.

In ultrasound inspection it is imperative that the amplifier and transducer function perform as per specification and there are various standards that describe performance checks that will identify any failings. ASTM E 317 -02 for instance is a standard practice for evaluating the performance characteristics of ultrasonic pulse echo examination instruments and systems without the use of electronic measurement instruments and ASTM E1324-00 advises on the measuring of some electronic characteristic of ultrasonic examination instruments both of which detail methods for checking ultrasonic instrumentation. Ultrasonic transducers are covered by a further ASTM where the bandwidth frequency and beam profile can be interrogated by various means. The above electronic method does not cater for the system performance once a transducer is connected neither does it check the transducer performance. However, once all other modules have been tested and correct performance has been ensured, the transducer bandwidth and sensitivity can be checked automatically by obtaining signals from a known reflector i.e. scanning a ball bearing to determine the ultrasonic field.

6.2.1.2. Radiographic calibration

Similar documents exist for digital radiography ASTM E 1255-96 is the standard practice for radioscopy and EN 13068 is the European document for controlling digital radiography. Modern digital detectors are yet to have specific regulatory documents applied to them. En13068 does suggest the use of the modulation transfer function as a practical method of ensuring repeatable and reliable imaging and the ASTM suggests measurement to be taken to prove correct operation. However, new detectors such as the amorphous silicon type do exhibit lost pixels and conversion differences across the screen all of which must be measured and corrected for in the inspection image.

The calibration of an amorphous silicon detector requires a method of determining and correcting for bad pixels i.e. pixels that are defective and pixels that are out of tolerance, calculating the value and applying an offset to detector regions that are under responsive and calculating a gain value so that all valid pixels give an equal output for a specific radiation dose.

6.2.1.2.1. Bad Pixels.

The first stage of correction for bad pixels is to determine those that do not respond. This is achieved by acquiring images without an applied radiation dose, a medium dose and a high dose. Pixels can then be thresholded and classified as bad pixels or pixels with poor dynamic response. Correction for bad pixels is performed by evaluating the neighbouring pixels and using an average value. Clusters of bad pixels have to be corrected for by interpolation. Pixels with a poor dynamic response are corrected for by applying a gain factor. The periodic calibration therefore for an amorphous detection system must perform the above measurements and corrections but must also detect when the detector response has deteriorated to such an extent that defect detectability is impaired beyond the minimum requirement.

6.2.1.2.2. Gain correction.

The response of an amorphous silicon detector may not be linear throughout its entire dynamic range and therefore a linear gain adjustment that intends to maximise the output to the analogue to digital conversion module is not appropriate. High radiation doses are readily converted into electrical signals whereas low radiation produces weak electrical signals that cannot be considered proportionate to the high dose signals. The amplification gain applied to low radiation signals is therefore greater than the high dose signals. The best method to calibrate this non linear gain would be to capture images throughout the entire dose range required by the inspection and obtain the dynamic response of the detector. A curve could

then be fitted to the response and used to calculate the gain value. In practice three images are used, a dark, mid, and a high image and a bilinear fit between dark to mid and mid to high is used to calculate the required gain. As with bad pixel compensation the calibration procedure should correct for the non linear response but should also detect when the non linearity has deteriorated and defect detection is likely to be affected.

6.2.1.3. Shearographic calibration

Shearography being a relatively new method does not have the same degree of documentation as ultrasound and radiography to support it. One ASTM (ASTM F 1364-03) exists but this defines a shearographic calibration device for using shearography to inspect tyres and therefore does not interrogate the pertinent parameters that ensure adequate control when inspecting aircraft structures.

In chapter 5 it was demonstrated that when the signal to noise ratio decreases with reduced laser intensity the minimum surface deformation detectable increases as it is directly linked to the illumination. Also the shear amount and the phase step have to be accurately controlled if defect detection is to be maintained. In the case of shearography a simple test sample that produces an identifiable response when the imaging parameters are correct would suffice but this technique is similar to the reference specimen idea already implemented for production ultrasonic and radiographic inspection and as mentioned previously would suffer from being unable to include all pertinent features. A more robust solution is to measure the responses by electronic means and compare the results with the initial set up.

One method of checking the performance of a shearographic system would be to use a test object with a specific optical surface roughness similar to the test component on one portion of the object and a further portion with high reflectivity. The step response can then be measured and an estimate of the dynamic range be calculated. This would then highlight any deterioration in the laser output. The phase stepping accuracy can be determined by measuring the output voltage from piezo controller and the amount of shear can be physically measured on the image. The accuracy and repeatability of

the stressing method is also a very significant factor and as such measurements to obtain the rate of pressure change and the maximum pressure should be carried out. If thermal stressing is employed then rate of temperature change and maximum temperatures achieved should be measured and recorded.

A simple test card image could be used to check the correct operation of the image capture module.

6.2.1.4. Motion Control

Whilst all of the above documents give excellent direction on how to perform calibration measurements for a specific method and advise on what tolerances should be considered permissible, non to date have included the significance of positional accuracy of the sensor. It has been shown that manipulation of the transducer or the component plays a significant part in defect sensitivity and therefore routine checks should be implemented to cover this.

A method to calibrate motion control has been described by the analysis of positional error compensation in chapter 3. Because motion control is a computerised and therefore an automated function, the calibration and periodic check that positional accuracy is being maintained can easily be automated by using the NDT modules. For ultrasonic inspection the use of the through transmission ultrasonic signals identifies any deviations in position of the two water jets. In radiography a target fastened to the detection system whilst the motion for the source and detector are controlled would identify any positional error. Positional accuracy for shearographic inspection is not as important however, as it is more the stability of the sensor during data acquisition that affects defect detection than the sensor alignment. As shearographic inspection is a step and repeat process the motion control can be programmed with delays at the end of each step to allow time for the axis to settle in position. Any oscillation can be determined by image analysis.

The use of electronic signals as stimulus to a NDT measuring system and using the digital controls and data acquisition to evaluate the response is a method that is not well documented either in terms of NDT standards or research papers. However an electronic calibration does have the advantage of eliminating variables such as the mechanical properties of an ultrasonic transducer for ultrasound or variables associated with x-ray generation both of which have a significant effect on the validity of the acquired data from the acquisition system. This ensures that the acquired data is accurate at the time of acquisition. Furthermore data processing may be adjusted based on calibration results thus enhancing capability.

6.3. Data visualisation and analysis

The data captured by the inspection methods detailed previously is, after processing, represented as an image on a computer screen. The operator then assesses the image for artefacts and defects. The successful detection of defects therefore not only relies on the accuracy of the data capture and processing instrumentation but is also dependant on correct visualisation methods.

The human eye has the ability to operate over a very large dynamic range. The eye cannot however distinguish its entire dynamic range at any one time but adjusts to a background brightness level and is limited to the range of intensities about this background intensity. Intensities that are below and above the range will appear as black and white respectively. The Weber ratio states that at any darkness adaptation level, the eye has a dynamic range of approximately 2.2 log units i.e. approximately 155 grey scale levels. NDT data is often quantised at 8 bits or above. Ultrasonic signals are usually captured by an 8 bit analogue to digital converter whereas the amorphous silicon imaging system used in chapter 4 produced a 14 bit image. It is therefore not possible to present the whole NDT data dynamic range in a single image and be able to discern each change in image intensity. Of course the object being inspected and its associated flaws may be captured and represented within the 155 grey levels that the eye can adapt to but in general

this is not the case and the data has to be displayed in a number of images so that the eye and the display screen can accommodate all intensity levels.

Screen resolution and the resolving power of the eye also have to be catered for, and again limits of resolution determine how the data should be displayed. Campbell and Maffei [Campbell 1974] state that the eyes limit of resolution is approximately 50 cycles per degree. This translates into a 15 μm feature viewed at 100 mm. However this is the theoretical resolution limit derived from defined grating patterns and therefore does not account for the irregular shape of the many features found within an NDT image.

Image manipulation algorithms are therefore very important to successful defect identification and simple image processing techniques are readily available to the NDT engineer that assist in the image analysis stages. Contrast stretching is regularly used to ensure that the data has been observed at the optimum sensitivity and zoom functions are used to overcome resolution limitations. In ultrasound contrast stretching is usually performed by displaying the data at different quantisation levels for instance an 8 bit thickness c-scan can be quantised so that it is displayed in 8 colour bands where each colour band represents 0.2 mm. Therefore the total thickness represented in the image is 1.6 mm. The maximum thickness measured however could be 16 mm but significant defect depths are 0.2 mm therefore using 8 colours for display purposes requires a series of 10 quantised images in order to fully all possibilities of defect location. Similarly a radiographic image which is captured at 14 bits may only have significant data ranging in value between 12000 and 13000. Contrast stretching has therefore to be performed over this range only in order to fully asses the results.

Resolution limitations are overcome by zooming and like contrast stretching the operator should use the resolution value of the display device and the resolution of the image to calculate the amount of zoom required that ensures that each data point has been displayed correctly in the image.

Whilst standard contrast and image magnification functions are readily available the following paragraphs describe advanced processing methods that aid the operator in image assessment and have the potential to be developed into automated data analysis procedures.

6.4. Data Processing

6.4.1. Mosaic Construction

Due to the relatively large size of aircraft components, non-destructive test (NDT) systems are usually capable of inspecting a comparatively small part of the component under inspection at a time. It is therefore necessary to perform an image mosaicing operation to merge a large number of sub-images acquired during the inspection process into one complete image of the entire component under inspection [Smith 2000, Shark 1999, Matuszewski 2000,2001,2002,2003]. From the implementation viewpoint, the inspection system is required to produce a certain degree of overlapping between the neighbouring images in order to achieve mosaic construction, and the initial positions of images in the mosaic can be obtained from the data acquisition sequence and hardware settings. During mosaic construction, three key problems have to be addressed: (1) determination of possible class of geometrical image transformation for image alignment; (2) estimation of unknown transformation parameters; (3) method of blending of overlapped images.

The possible class of geometrical transformation needed to align images depends on not only the component geometry, but also sensor position, orientation and movement with respect to the component under inspection. With the component surface perpendicular to the ultrasonic sensor, the necessary geometrical transformations for image alignment are translation and rotation [Smith 2000, Matuszewski 2002]. With the component orientation fixed with respect to the sensor in the radiographic system, the required geometrical transformations reduce to image translation only [Smith 2000, Matuszewski 2000, 2001, 2003]. However, due to the existence of an uncertainty in the component position and orientation with respect to the sensor in the shearographic system, perspective distortion occurs. Consequently, it is not possible to achieve accurate alignment of the neighbouring images using rotation and translation only [Smith 2000, Shark 1999].

With the possible class of geometrical transformation determined, estimation of unknown transformation parameters for the initial alignment of neighbouring images is based on the evaluation of the similarity (cross-correlation) between pixels in the neighbouring images covering the same component area. With a higher correlation value indicates a higher degree of similarity between the two images, the translation vector and rotation angle are estimated iteratively. Following the initial estimation of the translation vector, the rotation angle is then estimated by moving the second image to the position defined by the translation vector found, transforming the images to polar co-ordinates (as rotation in Cartesian co-ordinates becomes translation in polar co-ordinates), and determining the overlapping position of the images' sub-areas. The whole process is repeated until no significant changes in the estimated parameters are detected. To reduce computation cost, the calculations are performed in a hierarchical manner using image pyramid decomposition with the translation vector and the rotation angle found for a lower resolution level used as the initial estimates for a higher resolution level.

However, as the number of images involved in the mosaic construction increases, the problem of mosaic inconsistency becomes apparent, i.e. the local transformation estimated for an overlapping image pair based on their image contents differs from the corresponding transformation computed based on their positions and orientations in the mosaic. Using an example of a mosaic of five images, the problem of mosaic inconsistency is illustrated in Fig. 6-2

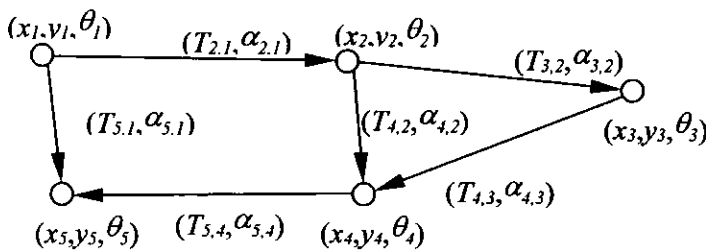


Figure 6-2 Diagram of a mosaic of five images

In Fig. 6-2, the position and orientation of a images with respect to a common co-ordinate system in the mosaic are denoted by (x_i, y_i, θ_i) , the local translation and rotation estimated for images i and j are denoted by $(T_{ij}$ and $\alpha_{ij})$. Mosaic inconsistency implies

$$T_{1,5} \neq T_{1,2} + T_{2,4} + T_{4,5}; \quad T_{2,4} \neq T_{2,3} + T_{3,4} \quad (6-1)$$

$$\alpha_{1,5} \neq \text{mod}_{2\pi}(\alpha_{1,2} + \alpha_{2,4} + \alpha_{4,5}); \quad \alpha_{2,4} \neq \text{mod}_{2\pi}(\alpha_{2,3} + \alpha_{3,4}) \quad (6-2)$$

This inconsistency occurs because the local translation and rotation are obtained based on the similarity existing in an image pair without relating to their positions and orientations in the mosaic, and are also contaminated by some inherent estimation errors. For large mosaics the accumulated errors of the local transformation can cause a serious degradation in the mosaic quality and the estimated local transformations based on image similarity should not be used directly for mosaic construction. Hence, both image similarity and image consistency are used in the determination of the optimal local transformation. This is implemented as a problem of minimising the sum of squared differences between the two local transformations with one estimated using the image similarity and the other computed using the image positions and orientations in the mosaic. The inclusion of image consistency as an additional condition has the effect of distributing the alignment errors evenly across the whole mosaic, thereby enabling high precision mosaic construction [Smith 2000, Matuszewski 2000, 2001, 2003].

After correct alignment, the Voronoi diagram construction method is performed to combine the overlapping areas of the neighbouring images into one image. In this method, the value of each pixel in the mosaic is taken from one image only with the image having the image centre closest to the location of the pixel concerned.

Figure 6-3 shows the mosaic constructed from three ultrasonic sub-images of an aircraft component. The mosaic was constructed without any initial constraints imposed on the images' position or orientation [Smith 2000].



(a)



(b)

Figure 6-3 (a) three ultrasonic sub-images of an aircraft component, and
(b) constructed ultrasonic mosaic

Figure 6-4 shows the mosaic of 217 x-ray images of an aircraft component captured by using a real-time radiographic system [Smith 2000, Matuszewski 2000, 2001, 2003]. In this case, translation only was used to model the image displacement with the parameters estimated using cross-correlation. The initial positions of images were acquired from the real-time radiographic machine.

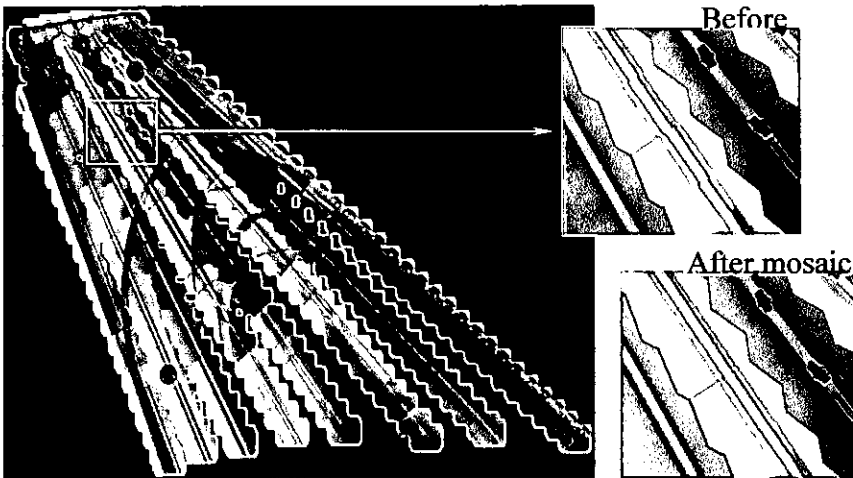


Figure 6-4 Mosaic of 217 x-ray images

Figure 6-5 shows the mosaic of 32 shearographic images of an aircraft component called 'panel 3', where the necessary transformations to align images are computed based on the laser illuminated images, because the shearographic image data of the same component part in the overlapping regions are different. Furthermore, the alignment involves correction of perspective distortion [Smith 2000, Shark 1999].

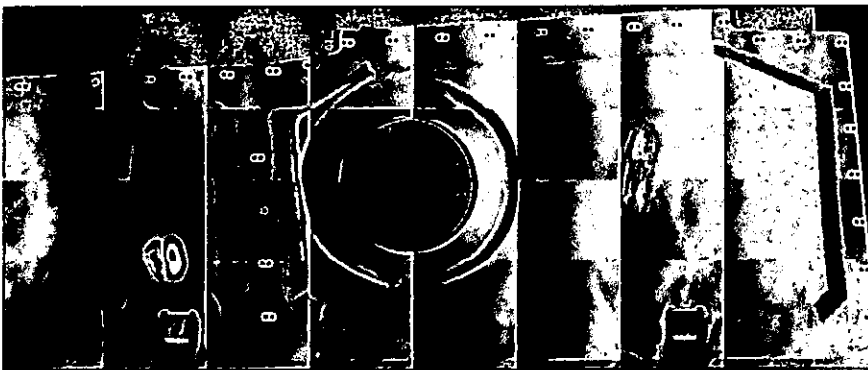


Figure 6-5 Mosaic of shearographic images

6.4.2. Data Registration

Defect analysis, interpretation and characterisation can be a very time consuming process especially in the examination of large and complex aircraft components. This led to the development of data registration to map the NDT image of a component to its corresponding CAD model [Smith 2000, Matuszewski 1999, Shark 2001, Deng 2002, 2003, 2004]. With the CAD model superimposing on NDT images, an accurate geometry reference is provided for rapid identification of defect size, location and distribution by inspectors. Data registration can be manually guided or performed automatically. Whilst it is desirable to have the automatic methods, it has to be recognised that they are currently restricted to components with relatively simple geometrical structures.

6.4.2.1. Computer assisted data registration

Computer assisted data registration consists of displaying the selected 3D wire-frame CAD model onto 2D image plane and aligning the projected 3D wire-frame CAD model with the NDT image [Deng 2002, 2003, 2004]. Users are required to rotate and scale the 3D wire-frame CAD model and to shift the NDT image until a best match is obtained. As an example, Figure 6-6 shows the 3D CAD model and the radiographic image of an aircraft component before and after data registration. With the 3D CAD model projected onto the radiographic image, a geometrical reference is provided thereby facilitating a comparison of the actual NDT images with the desired CAD models as well as characterisation of defects in terms of size, location and distribution. One of the potential errors in radiography is perspective distortion when the component under test is viewed at an angle away from the normal perpendicular position. As a result, there will be a change in the relationship of geometrical features observed, giving rise to the potential of incorrect judgement of defect size and shape as well as the errors in geometrical measurement. This potential error could be detected and corrected based on the geometrical reference provided by the component CAD model and its geometrical relationship with the corresponding NDT image.

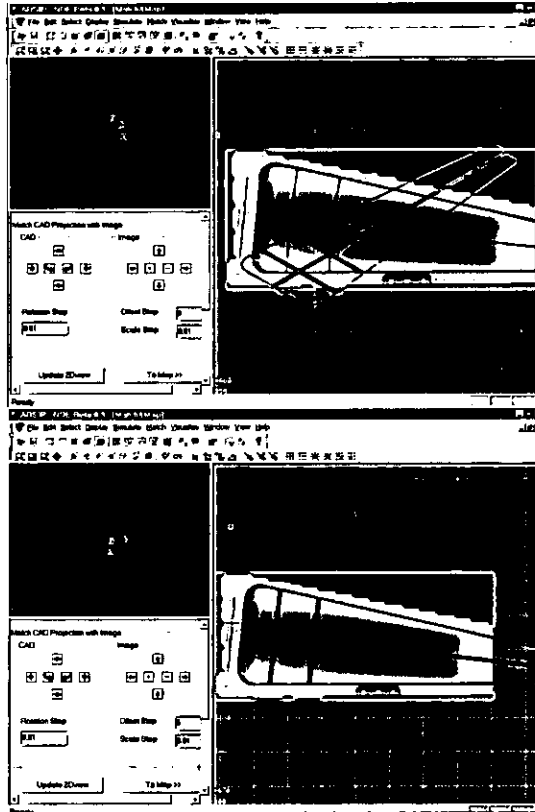
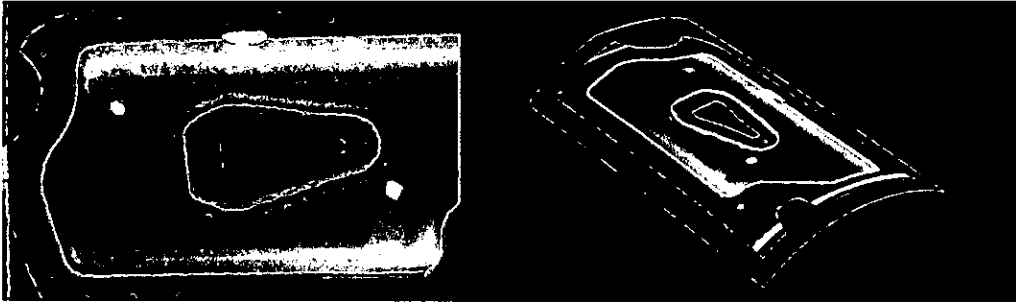


Figure 6-6 3D CAD model and X-ray image before and after data registration

With the projected CAD model aligned with the corresponding NDT image, surface rendering can be performed for curved aircraft components to map the NDT image onto the CAD model surface, thereby enabling defect visualisation and examination in 3D. This is achieved by generation of a triangular mesh to approximate the CAD model surface and establishment of the geometrical correspondence between 3D vertex coordinates on the surface and 2D texture coordinates in the image plane. The associated pixel value in the NDT image is then mapped on the surface point-by-point as texture and the linear interpolation is used if there is no one-to-one correspondence. Figure 6-7(b) shows the result of mapping an ultrasonic image (Figure 6-7(a)) onto the curved CAD model surface as texture, which is also overlaid with the wire frame of selected CAD model parts and can be rotated for viewing from any arbitrary 3D orientation. With each pixel in a NDT image associated with their corresponding 3D surface positions on a

component, an appropriate geometrical relationship is established to facilitate not only defect visualisation in 3D, but also accurate defect measurement and characterisation.



(a)

(b)

Figure 6-7 Texture mapping: (a) original ultrasonic image, and (b) texture mapped ultrasonic image

6.4.2.2. Automatic data registration

If aircraft components have a relatively simple geometrical structure (such as a relatively flat panel) and if the sensor can be maintained at normal to the component surface, then automatic data registration needs to find the necessary geometrical transformations, in terms of translation, rotation and scaling, to align the NDT image with the wire-frame CAD model. The main processing stages for automatic data registration consist of feature selection, feature extraction and feature matching [Smith 2000, Matuszewski 1999, Shark 2001].

In feature selection, a set of features is selected from the wire-frame CAD for alignment, and this operation is only performed once for each component type. Although different types of features, such as points, lines, circles, and polygons, could be used, straight-line segments were found to be most suitable, because line segments were found to be most suitable, because not only they are invariant under perspective projection, but also it is relatively easy to extract them from the wire-frame CAD model, to detect them in NDT images and to measure the potential misalignment. To facilitate feature detection, the straight-line segments in the CAD model corresponding to the

most visible lines in NDT images should be selected. As an example, for aircraft component 'Panel 3' with the CAD model shown in Fig. 6-8, the straight-line segments selected for matching (shown as eight labelled lines in Fig. 6-8) correspond to the most visible lines in the ultrasound image. Different sets of straight-line segments may be selected for different image types and the straight-line segments selected for matching can be conveniently stored in a database associated with the CAD model.

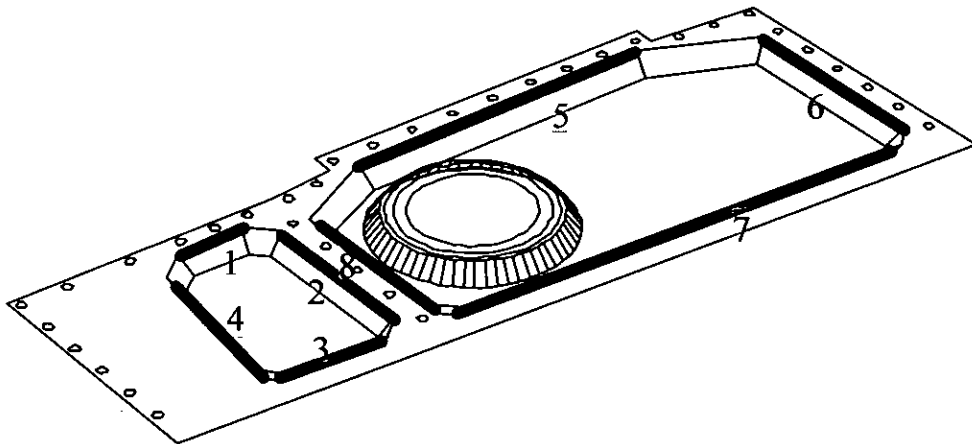


Figure 6-8 CAD model and segments selected for matching

In feature extraction, a set of straight lines is extracted from the NDT images of aircraft components. This is achieved by performing edge detection followed by applying the Radon transform in an iterative mode. As the highest peak in the Radon transform domain indicates the position and orientation of the longest straight-line contained in the binary edge image, its co-ordinates are converted to the longest straight-line in the spatial domain, and the first group of straight-line segments lying on the longest straight-line are estimated. The values of the pixels belonging to the first group of straight-line segments detected are then set to zero in the binary edge image, and the Radon transform is re-applied to the new binary edge image with the first group of straight-line segments removed to detect the next longest straight-line. The whole process repeats until the pre-specified maximum

number of lines is reached. Whilst Fig. 6-9 shows the detected binary edges as white lines overlaid on top of the actual ultrasound image of aircraft component 'Panel 3', Fig. 6-10 shows the final result of straight-line segments extracted.

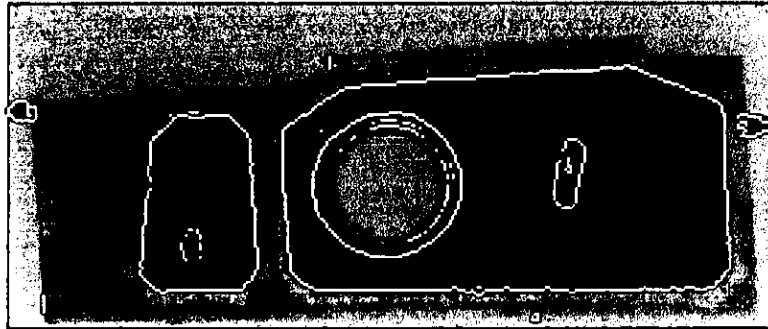


Figure 6-9 Binary edge image (white) on top of ultrasound image

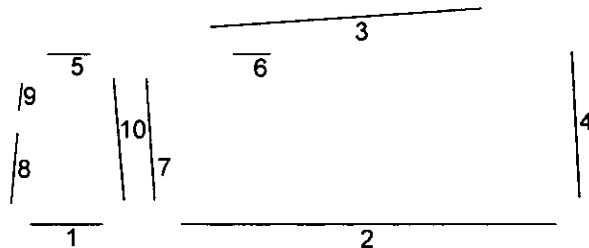


Figure 6-10 Straight-line segments extracted

In feature matching, the set of lines extracted from the NDT image are aligned with the corresponding set of lines selected from the CAD model. This involves generation of a better correspondence between two sets of lines using a numerical combinatorial optimisation method, and minimisation of the matching error by selecting the best transformation to rotate, translate and scale the lines extracted from the radiographic image to reduce their distances to the corresponding lines in the CAD model. Figure 6-11 shows the final result of mapping the ultrasonic image of aircraft component 'Panel 3' to its wire-frame CAD model.

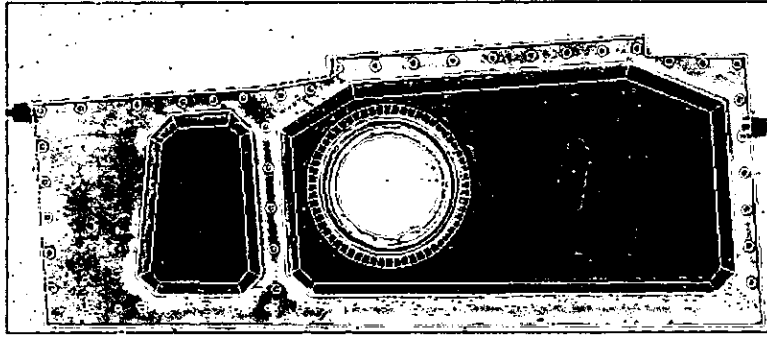


Figure 6-11 Ultrasound image matched to CAD model

6.4.3. Defect Visualisation

With the NDT images mapped to their corresponding CAD models as described in Section 6.4.2, the information contained in the component CAD model can be exploited and utilised to aid defect visualisation and interpretation.

6.4.3.1. Visualisation by structure decomposition

By utilising the structural and material information available in the CAD data, a NDT image can be divided into several viewing layers having the same material structure, thereby enabling defect analysis to be carried out on component sub-structure in a hierarchical manner [Shark Sept.1999]. This can be easily performed for relatively flat aircraft components. As an example, for the matched ultrasound image shown in Fig. 6-11, it can be divided into three layers, namely, a thin carbon fibre composite structure around the edges of the component, a thick nomex honeycomb structure with carbon fibre composite bonded skin, and a transition structure that tapers off from the thick structure to the thin structure. Using the structure decomposition to mask off the thick and taper layers of the aircraft component yields the thin layer ultrasound image shown in Figure 6-12, which can be used to assess the structure uniformity.

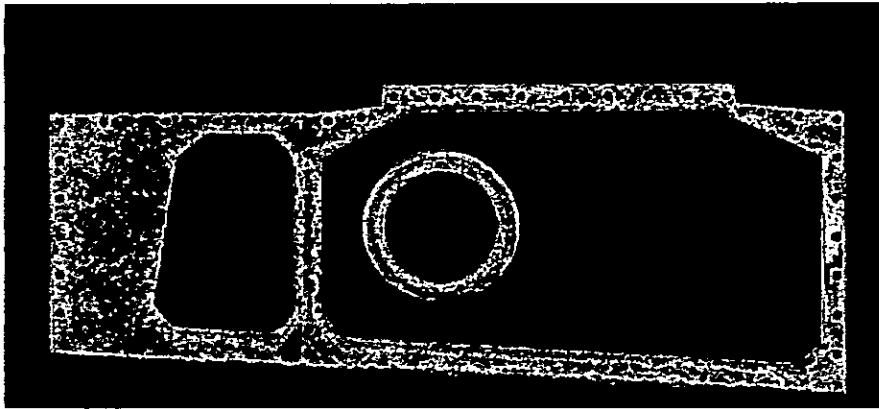
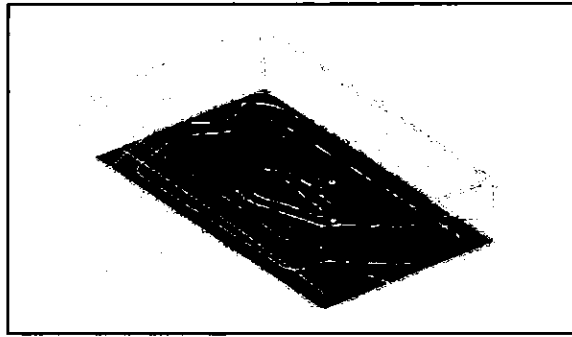


Figure 6-12 Thin layer ultrasonic image

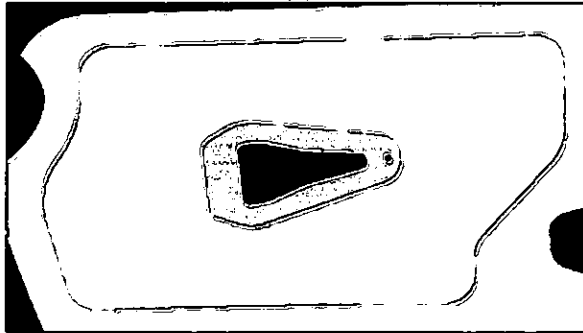
For curved aircraft components, visualization by structure decomposition requires linking between the structural/material information available in the 3D CAD data and the 2D NDT images acquired. This consists of the following steps [Deng BINDT 2004]:

- (i) Select structure boundaries based on wire frame from the 3D CAD model.
- (ii) Generate a clipping plane that is perpendicular to the NDT image plane.
- (iii) Move the clipping plane across the image plane according to the image resolution.
- (iv) Find the intersection points between the clipping plane and the structure boundary and project these intersection points back to the image plane.
- (v) Create structure masks based on the projected intersection points.
- (vi) Map the associated pixel value in the NDT image to the CAD surface according to the decomposition mask.

Using the ultrasonic image shown in Fig. 6-7 as an example, Fig. 6-13(a) shows the 3D structure boundaries selected (shown in red), the clipping plane (shown in green), and the projected 2D boundary contours (shown in white in the image plane). The final result of structure decomposition is shown in Fig. 6-13(b), where the middle thick structure is represented by green, inner edge strip by blue, and outer edge strip by red.



(a)



(b)

Figure 6-13 (a) Projection of 3D boundaries, and (b) 2D structure mask

Using the structure mask shown in Fig. 6-13(b) to mask off the inner and out edge strips of the aircraft component yields the ultrasound image for the curved thick structure as shown in Figure 6-14.

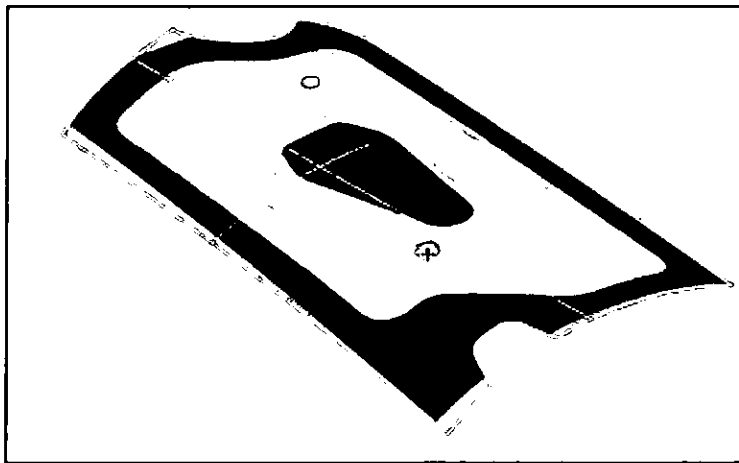


Figure 6-14 Decomposition of curved aircraft component

6.4.3.2. Visualisation by 3D surface construction

As the shearographic image provides the surface information of a component, it can be used to construct a 3D surface of the component. With the shearographic image mapped to the CAD model, the co-ordinates of each image pixel in 3D space are available from the CAD model and are used to construct the 3D surface [Smith 2000, Shark Oct. 1999]. Using the mosaic of shearographic images shown in Fig. 6-5 and the CAD model shown in Fig. 6-8 as an example, Fig. 6-15 shows the 3D shearographic surface image constructed. By rotating the 3D surface for viewing from any arbitrary 3D orientation, a better defect visualisation environment is provided. For example, defects in the taper region can be more accurately measured without the influence of perspective distortion.

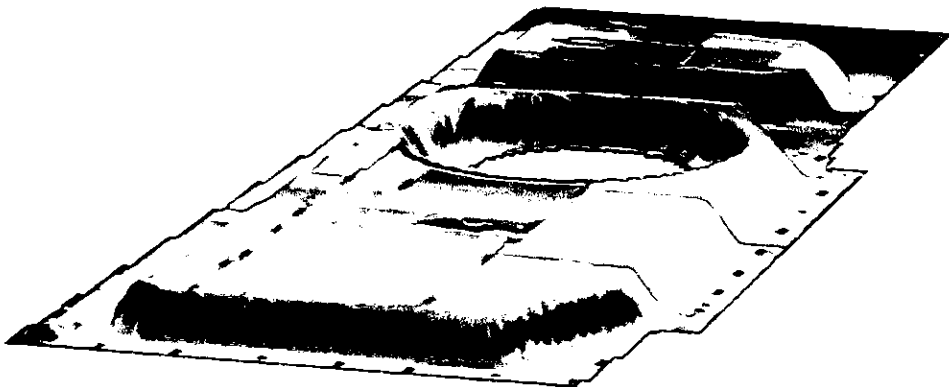


Figure 6-15 3D shearographic surface image

6.4.3.3. Visualisation by data fusion

This report presents three complementary NDT methods for aircraft component sentencing, namely, ultrasonic, radiographic and shearographic inspection techniques. As the image features generated by each type of inspection technique are very different from one another, each inspection method requires its own trained operators to accurately classify the observed

image features as component defects or image artefacts inherent in that particular inspection method. Consequently, the use of these three different NDT techniques, as independent and separate processes for the detection of different types of defects, significantly increases the overall manufacturing cost due to the extra time and manpower required to process and analyse extra data sets. One possible method to achieve cost savings while maintaining a full defect detection capability is to combine the three NDT images by fusion, because this enables defect processing, analysis and classification to be carried out only once on one fused image instead of individually on three separate images [Shark Sept & Oct 1999, Smith 2000, Matuszewski 2000, Deng 2004].

However, it is not possible to fuse the three NDT images into one image directly, because each NDT system has its own resolution resulting in a different image size for the same component. With data registration to map each individual NDT image separately to the CAD model, the geometrical relationships between the three NDT images are established. By performing appropriate interpolation on the registered NDT images to achieve uniform resolution between them, the three NDT images can be fused on a pixel-by-pixel basis using three different colours. With the CAD model shown in white, and the ultrasound, radiographic and shearographic data represented respectively by red, green and blue colours, Fig. 6-16 shows the final fused image for aircraft component 'panel 3'.

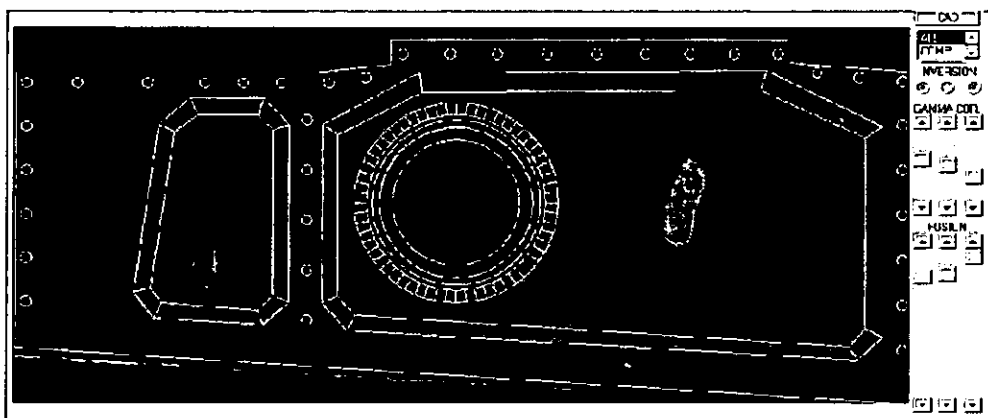


Figure 6-16 Pixel-by-pixel fusion with CAD model

Also shown in Fig. 6-16 is a set of sliding scales provided to allow inspectors to adjust the contribution of, and to apply gamma correction to, a particular NDT data set in the final fused image. By using fusion to integrate and present the complementary defect information provided by different NDT techniques, it is less likely for inspectors to make incorrect subjective judgements based on an individual NDT image, thereby improving the confidence level of component sentencing in terms of reliability and consistency.

6.4.4. Defect Detection

In general, defects can be categorised into material flaw or geometrical deviation. Through data registration with CAD model and structure decomposition to divide NDT image into regions having similar image features, automatic detection of defects becomes possible as shown in the following sections.

6.4.4.1. Automatic extraction of defects

If an aircraft component can be decomposed into different areas according to its material structure, then a regular image pattern should be observed in each region of its NDT image if does not contain a defect [Smith 2000]. Hence automatic defect extraction can be implemented after data registration and structure decomposition to detect any irregularities (usually representing defects) from the NDT images. This can be achieved by analysing the consistency of the pixels of each decomposed region having the same material structure to yield a predefined distribution. By using a threshold, a significant departure from the expected distribution is treated as a representation of a potential defect.

To illustrate the principle, Fig. 6-17 shows the defects extracted from the thick honeycomb regions of the ultrasonic image shown in Fig. 6-11 by an intensity thresholding operation, where the component holders having the

same intensity values as the defects were not identified as defects because they are not in the region of interest.



Figure 6-17 Defects extracted

6.4.4.2. Automatic detection of geometrical deviations

With the CAD model superimposed on the NDT image via data registration, the evaluation of the geometrical structure becomes identification of the geometrical differences between them [Smith 2000]. Firstly, it is required to detect predefined structures which geometrical data have to be examined. This can be achieved by region based detection procedures, with the region of interest selected based on the location of the geometrical structure in question in the CAD model and NDT data registration parameters. An example of this procedure is shown in Fig.6-18, where super-plastic formed diffusion bonded geometry is examined.

The region of interest is selected based on the position and orientation of the inspected bonded geometry in the CAD model and include neighbouring pixels in the registered NDT data. In Fig. 6-18, two such regions are shown using green and yellow lines as the region border lines. Region based feature detection improve detectability and accuracy of the detection process as the procedure can adapt itself to the local image characteristics. Additionally CAD information is used not only for region of interest definition but also for improvement of detection quality by defining expected primary orientation of

the structure. After feature detection the calibrated distance measurement can be performed between selected points and structures. As an example, Fig. 6-18 also shows two histograms of the distances between pixels from the detected structures and corresponding CAD model structures. Whilst the red coloured distance histogram is fairly typical, the yellow coloured distance histogram shows the worst case of misalignment between the examined structure and corresponding CAD model structure.

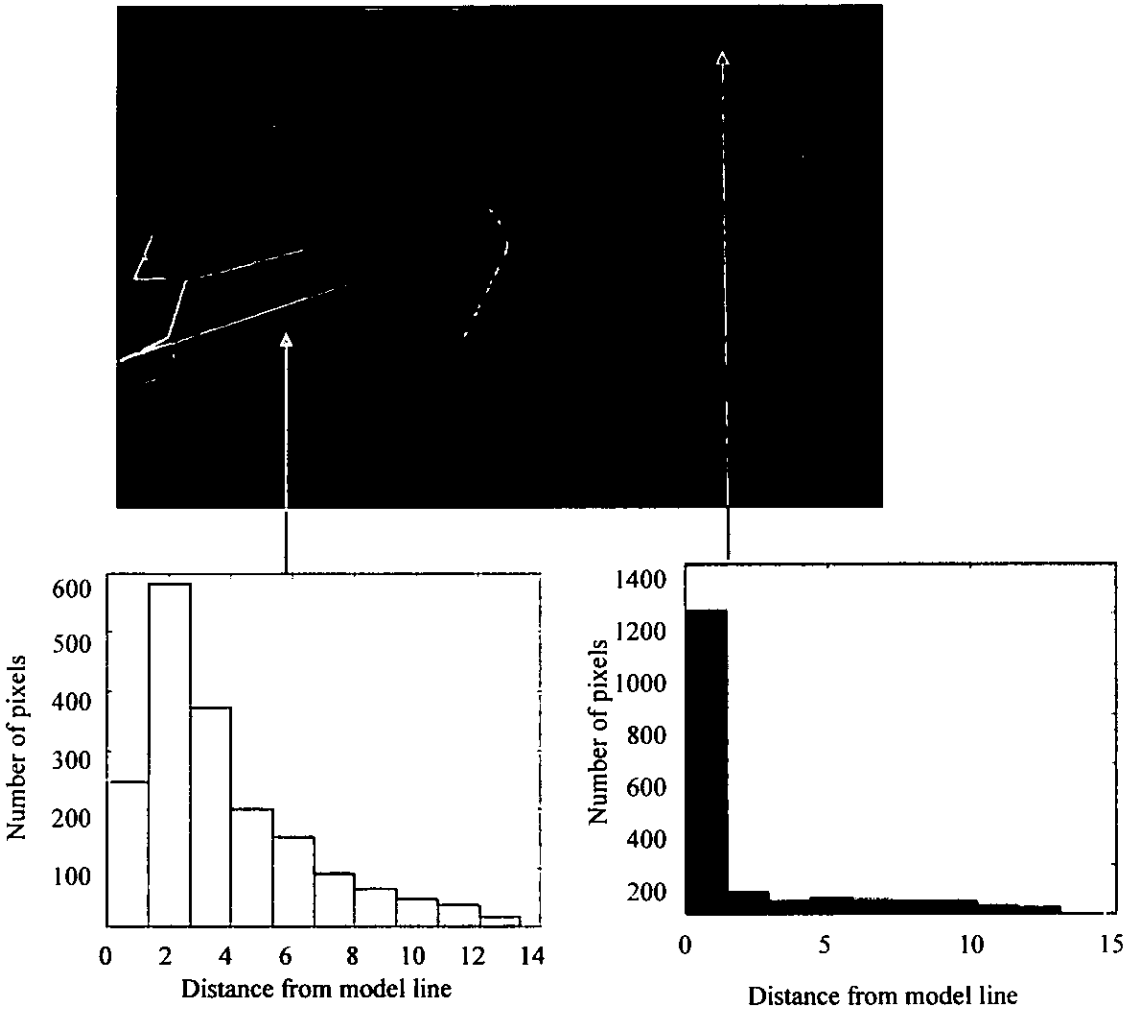


Figure 6-18 Automatic assessment of component geometry

6.5. Summary

This chapter has described a number of current calibration practices and referenced standards that are typically used to control NDT inspection systems. It has also emphasised the need for extended calibration procedures when enhanced defect detection capabilities are used and suggests methods that could be readily implemented that would ensure the correct system operation was achieved during each data acquisition process. The chapter then moves on to data visualisation and highlights the requirement that data is presented and that tools are available that allow the interpreter to view the data within the operating range of the human eye.

Having established the correct calibration and interpretation methods the chapter then proceeds to describe and demonstrate results of enhanced image manipulation and processing methods. These methods were developed in a project funded by the engineering and science research council under the innovative manufacturing initiative in a project entitled “Data integration and processing for NDT on aircraft structures” (DIAPS).

Chapter 7

7. Conclusions and recommendations for further work

This chapter provides an overall summary to the work detailed in the previous chapters and draws conclusions on the result obtained from the research. Section 7.1 also draws attention to the contributions to knowledge in the thesis whilst section 7.2 discusses the implications of the work and therefore makes recommendations for further work.

7.1. Summary and conclusions

7.1.1. Introduction

Chapter 1 serves as an introduction to non-destructive testing and as such does not offer the reader any new material but sets the scene for the work described in other chapters. Similarly chapter 2 is used to describe the application of new materials and processes used in airframe manufacture and therefore demonstrate the need for improvements in NDT defect detection capabilities. The next four chapters in the thesis in turn introduce the topics of ultrasonic, radiographic, shearographic and calibration and data processing and proceed to develop the topical research and enhance the defect detection capabilities of the method. The following paragraphs summarise the findings and highlight the contributions to knowledge achieved through this work.

7.1.2. Ultrasound

Modelling of the piezoelectric properties and experimenting with the model showed that optimum ultrasonic pulse shape and energy was achieved when the timing of the excitation pulse matched the resonant frequency of the transducer. Low voltage practical experiments were conducted to confirm the modelling results. Diffusion bonding inspection requires high axial resolution and high defect sensitivity, therefore focused transducers were

adopted. The effect of focusing was studied and it was discovered that tightly focused transducers still experience around 6 dB loss in signal for a 3 degree inclination. In terms of diffusion bonding inspection this severely impairs the defect detection capability. A thorough analysis of complex contour scanning revealed that compensation for positional error caused by mechanical tolerances was highly dependent on the accuracy of the scanner's kinematic model, correct PID loop tuning and accurately determination of the velocity of sound in water as this was used for zero calculation and water path distance measurement. As maintaining surface normal is critical to defect detection an interface between the computer aided design and the motion control software was developed and tested. The result of the work above is an enhanced defect detection capability that has been implemented in a production testing environment. The in depth analysis both practical and theoretical which was supported by experimental data has resulted in a deeper understanding of complex geometry ultrasonic scanning systems. Analysis of factors affecting positional errors has allowed the motion control to be optimally tuned which has removed the necessity for excessively tight mechanical tolerances that were practically unachievable. Many aerospace companies are now developing their laser ultrasonic capability in preference to multi axis scanning as laser ultrasound does not suffer from loss of sensitivity due to inclination. The work in this thesis has demonstrated that it is possible to scan very large and complex shapes with a high level of defect detection capability providing the significant parameters are measured and corrected for.

The contributions to knowledge for the ultrasonic research described in this thesis are therefore:-

1. The demonstration that positional accuracy has a significant affect on defect detection and a method to measure positional accuracy by evaluating the compensation required in a ten axis scanning system.
2. A method to reliably detect 15 μm voids in a diffusion bonded joint at frequencies of 20 MHz and above by optimising transducer excitation, focussing and normalisation

3. A method of determining the minimum detectable attenuation variation by plotting the measuring error when calibrating the alignment of a ten axis scanning system

7.1.3. Radiography

The radiographic research focused on factors affecting image quality particularly the quality of digital imaging systems coupled to micro focus sources. After assessing the available literature a flaw in the calculation of the optimum magnification was discovered. Mathematical and experimental work showed that optimum magnification for focal spot sizes of less than 0.1 mm the optimum magnification deviated significantly from the Halmshaw et al calculation and for a 5 μm source the optimum magnification was an order of magnitude less than that predicted. A new formula has been derived which is in good agreement with the experimental results.

Further to this the usual method of image quality assessment was found to be unsatisfactory as features with spatial frequencies less than twice the sampling resolution were apparent in the images and could be wrongly used to estimate the limiting resolution. Implementing a method for determining the modulation transfer function and the detective quantum efficiency has overcome this problem but also gives the engineer a quantitative measure of the resolving power of the system. Having determined the limiting resolution by the described method indications in subsequent inspections that are close to the limit can be further evaluated by increasing geometric magnification. However some caution must be practiced as it is now known that higher magnification does not necessarily lead to clearer images. Having performed the assessment above and discovered the critical imaging parameters the defect detection capabilities of a modern amorphous silicon detection system have been reported with respect to carbon fibre composite and super plastically formed diffusion bonded structure.

The contributions to knowledge with respect to the radiographic research described in this thesis are therefore:-

1. A new formula for the calculation of the optimum magnification. Particularly applicable for focal spot sizes less than 0.1 mm.

2. A practical method of measuring the detection capabilities of a digital radiographic system by calculating the modulation transfer function and the noise power spectrum from a reference image.
3. The practical application of digital radiography to the inspection of super plastically formed diffusion bonded and carbon fibre composite structure has been demonstrated but has also been supported by quantitative measurement of the imaging systems capabilities.

7.1.4. Shearography

Shearography is a relatively new method that is now becoming a popular inspection method for honeycomb bonded structures. The contribution to knowledge claimed within this thesis is:-

1. A method adopted of integrating all the modules of the system for which a patent has been granted.
2. The matching of the applied stress to the data capture and processing which contribute significantly to the defect detection capability.
3. The testing and validation of the Parker and Salter [Parker 1999] temporal unwrapping and laser illumination work has led to the realisation that producing a pressure drop that would result in a linear change in surface deformation over time was difficult to achieve.
4. The defect detection capabilities achievable by thermal stressing were discovered by applying the pressure drop algorithms to a thermally stressed part.

In conclusion shearography could benefit by implementing a method to calculate rigid body movement and the need for an algorithm to remove unwanted rigid body indications has come from this analysis. Furthermore a method for the estimation of defect detection capabilities has been proposed

that makes use of the modulation transfer and detective quantum efficiency calculation adopted for radiography has been reported.

7.1.5. Calibration and data processing

During this research there have been a number of discoveries which were identified as the ultrasonic, radiographic, and shearographic system were being developed. Implementing new NDT technology regularly uncovers new information and it is this practical approach to NDT research that has resulted in more reliable and robust inspection methods, all of which have an enhanced defect detection capability.

Implementing reliable and robust processes that have been carefully analysed provides the necessary data required for future calibration and control. In chapter 6 an evaluation of current standards and practices has revealed that many of the pertinent parameters identified in this thesis for ultrasound and radiography could be controlled by adapting methods suggested in the appropriate documents. However motion control accuracy is not addressed. Therefore the method adopted in chapter 3 can be used for positional calibration and can be adapted for different makes of motion control system. A literature search for calibration documents appertaining to shearography revealed one ASTM document that was specific for tyre inspection. Whilst this thesis has not specifically addressed the calibration of a shearography system the use of the modulation transfer function and the detective quantum efficiency calculation could be used for checking that a system has not deteriorated since its defect detection capabilities were last assessed.

The latter part of chapter 6 details advanced data processing techniques that were developed during the EPSRC funded Data integration and processing system for non-destructive testing of aircraft components (DIAPS) project. The work described in this thesis played an active part in providing robust and reliable data for this research and the author contributed by:-

1. Capturing NDT data with optimised technique and communicating the important features in the resulting images.
2. Assessing the data acquisition processes based on the results produced by the data processing methods with a view to enhancing further the data capture methods to overcome problems associated with image registration and mosaic construction.
3. Validated the results in terms of correct data representation and analysis
4. Project managed and steered the work by providing knowledge of the NDT processes.

For the work above and much of the work described in this thesis the author has been awarded two BAE SYSTEMS bronze innovation awards and the British Institute of NDT Nemet award in recognition for his work in automating the NDT process.

		Ultrasound	Radiography	Shearography	Comments
Composite defect detection	Impact damage	Yes	No	Yes (Thermal excitation)	Not detected using vacuum stressing shearography
	Inclusions	Yes but some materials are difficult	Yes but some materials are difficult	Dependant on the depth of the defect	Shearography is limited to the first few mm
	PTFE artificial defects	Yes	Yes	Dependant on the depth of the defect	Shearography is limited to the first few mm
	Honeycomb to skin disbonds	Yes	No	Yes	Shearography shows good detection capabilities
SPFDB defect detection	Large Voids	Yes but internal structure may not be accessible	No	Not proven (unlikely)	No proven detection method for defects in the internal structure
	Micro voids	Yes	No	No	Enhanced Ultrasound
	Intimate contact disbonds	Yes	No	High stressing may break the intimate contact disbond	Enhanced Ultrasound
	Geometrical deviations	No	Yes	No	Access to internal structure prevents ultrasound and shearography

7.2. Recommendations for further work

It has been clearly demonstrated that the practical implementation of NDT methods and a robust and reliable process is reliant on a thorough assessment of the parameters pertinent to the method. Enhancing any particular method does not solely rely on improving the electronic modules or the transducer but can be achieved by improving the stimulation, ensuring that the correct translation of the part under test is achieved and optimising all the relevant parameters. This text has defined the current requirements that dictate the enhancement of current NDT methods but as aircraft designs become more complex the requirement to enhance defect detection will also increase. The recommendation in concluding this work is that all new NDT technologies are properly evaluated to ensure that they are capable of detecting the required minimum detectable defect. Whilst the use of simulated defects in reference specimens is a well known and widely used evaluation method it has been shown that factors such as motion control etc. contribute significantly to the overall performance. Therefore reference specimens containing simulated defects should not be used in isolation.

Having performed this research it is now apparent that strict calibration and process control is of paramount importance when implementing automated data processing techniques. However once these have been established automation of NDT data analysis can progress. Suggested future work should concentrate on automatic data analysis which would reduce subjective judgements and operator intervention and could lead to increased reliability. The challenge is to produce generic algorithms that are readily adapted to specific inspection problems. The use of computer aided design information and matching the NDT data to the design is a step towards automated data analysis as this represents part of the underlying knowledge that a human operator would use in a manual inspection process.

References

- AMP Piezo Film Sensor catalogue, AMP of Great Britain Ltd., Merrion Avenue, Terminal House, Stanmore, Middlesex, England, HA7 4RF.
- ASNT Non Destructive Testing Handbook Vol. 7, 1991 pp245
- American society for the testing of materials (ASTM) standard E 1000-98 "Standard guide for Radioscopy" reapproved 2003
- American society for the testing of materials (ASTM) "Standard practice for evaluating performance characteristics of ultrasonic pulse echo examination instruments and systems without the use of electronic measurement instruments". ASTM standard E317-01(2001).
- American society for the testing of materials (ASTM) "Standard guide for measuring some electronic characteristics of ultrasonic examination instruments. ASTM E 1324-00 (2000).
- American society for the testing of materials (ASTM) " Standard practice for use of a calibration device to demonstrate the inspection capability of an interferometric laser imaging Nondestructive tire inspection system. ASTM F 1364-03 (2003).
- American society for the testing of materials (ASTM) " Standard guide for radioscopy" ASTM E 1255-96 (2002).
- BAE SYSTEMS "Non destructive testing – Process specification Radiographic methods R05-6113 2002.
- Baker T.S and Partridge P.G. (Proceedings of the 5th international conference on titanium Munich 1984 vol 2 (p861))
- Barrowcliff R.P. "Non-Destructive Evaluation of Carbon Fibre Composite Bonded joints" M.Sc. Thesis University of Salford 1988
- Berlincourt D.A., Corran D.R., Jaffe H., " Piezoelectric and Piezomagnetic Materials and their Function in Transducers". Physical Acoustics, W.P.Mason, Ed. New York: Academic Press,(1964).
- Boone J.M , Seibert J.A " An accurate method for computer generating tungsten anode x-ray spectra from 30 to 140 Kv" Med. Phys 24(11) November 1997 pp1611-1670.

Boreman G.D. "Modulation transfer function in optical and electro optical systems" vol. TT52, Tutorial texts in optical engineering SPIE press. ISBN 0-8194-4143-0, 2001

British standard "Non-Destructive Testing, Image quality of radiographs" BS EN 462-5:1996.

Callister, W.D., "Materials science and engineering An introduction" John Wiley and sons, Inc fifth edition 2000.

Campbell and Maffei "Contrast and spatial frequency", Scientific American, Vol. 231, november 1974, pp106-114

Colonna de Lega, X 2 processing of non-stationary interference patterns: adapted phase shifting algorithms and wavelet analysis. Application to dynamic deformation measurements by holographic and speckle interferometry. Doctoral thesis, Ecole polytechnique Federale de lausanne (EPFL), 1997

Creath, "Phase measurement interferometry techniques" progress in optics, Vol. XXVI (Ed E. Wolf, 1998)

Cunningham 'The detective quantum efficiency of fluoroscopic systems: A case for a spatial temporal approach' medical imaging 2001: Physics of Medical Imaging, Proceedings of SPIE 4320(2001)

Curtis , P.T " An investigation of the mechanical properties of improved carbon fibre composite materials" RAE TR86021. RAE Farnborough 1986.

Davey R."NDT of carbon fibre reinforced composites, BAe Warton, Final report MDR0127, Dec 1977.

Delta Tau data systems, inc. applications notes. www.deltatau.com

Deng, W., Matuszewski, B. J., Shark, L.-K., Smith, J. P., Ciliberto, A., and Cavaccini, G.: "CAD based simulation and visualisation for non-destructive testing", BINDT, NDT 2002 Conference Proceedings, pp119-124, Southport, September 2002.

Deng W., Matuszewski B. J., Shark L.-K., Smith J. P., Cavaccini G., and Agresti M.: "Mapping 2D NDT images to 3D CAD surface for defect visualisation and interpretation of curved aerostructures", BINDT, NDT 2003 Conference Proceedings, pp113-118, Worcester, September 2003.

Deng W., Shark L.-K., Matuszewski B. J., Smith J. P., and Cavaccini G.: "CAD model-based inspection and visualisation for 3D non-destructive testing of complex aerostructures", Insight, Vol.46, No.3, pp157-161, March 2004.

Deng W., Shark L.-K., Smith J. P., and Cavaccini G.: "CAD based structure decomposition and reverse engineering for visualisation and modelling of defects", BINDT, NDT 2004 Conference Proceedings, Vol.2, pp73-78.

Deng W., Matuszewski B. J., Shark L.-K., Smith J. P., and Cavaccini G.: "Multi-modality NDT image fusion and its mapping on curved 3D CAD Surface", 16th World Conference on Nondestructive Testing, Montreal, 2004.

EN 13068-1 Non-Destructive Testing Radioscopic testing part 1 "Quantitative measurement of imaging properties" 2000.

Floyd C.E., Baker J.A., Lo J.Y., Ravin C.E., "Measurement of scatter fractions in clinical bedside radiography", Radiology 183, 857-61, 1992.

Goodman "Statistical properties of laser speckle" Laser speckle and related phenomena, Springer-Verlag , Berlin,1975)

Halmshaw R "Industrial radiology techniques", Wykeham publications 1971,pp166-169

Haasteren "Real time phased stepped speckle interferometry, PhD Thesis Delft University of technology, Delft 1994

Hung Y.Y "Shearography: A new optical method for strain measurement and non-destructive testing" Opt.Eng, pp391-395, May/June 1982.

Hunt J.W, Arditi M. Foster F.S. " Ultrasound transducers for pulse echo medical imaging" IEEE transactions on biomedical engineering, Vol. BME-30, No.8 August 1983.

Hutchins D.A, Mair H.D., Taylor R.G., "Transient pressure fields of PVDF transducers" The journal of the acoustical society of America, Vol82, No 1, July 1987, pp183-192.

Jones R. and Stone W. " Towards an ultrasonic attenuation technique to measure void content in carbon fibre composites" Nondestructive Testing, 1976, 9, 71-79

Klasens H.A "Measurements and calculation of unsharpness combinations in X-ray photography" Phillips research report 1,2 1946 pp 241-249.

Kossoff G. " Design of narrow-beamwidth transducers," Journal of the acoustical society of America, vol. 35, pp905-912, June 1963.

Krautkramer "Ultrasonic testing of materials" second edition, 1977, pp 63,79.

Lee M.H.and Park S.B. "New dynamic focusing techniques in ultrasound imaging" Electronic letter,21(17), pp749-751.

Lim, J.S. "Two-Dimensional Signal and Image Processing", Prentice Hall 1990.

Lockwood J.C., Willette J.G., "High speed method for computing the exact solution for the pressure variation in the nearfield of a baffled piston", The journal of the acoustical society of America, Vol. 53, No 3,1973, pp735-741.

Lowe M.J.S “Plate waves for the NDT of diffusion bonded titanium”, PhD thesis, Mechanical Engineering, Imperial College London, 1992, Chapter 7.

Macovski.A. “Medical Imaging Systems” Prentice Hall(1983)

Maher (Digital Radiography notes web page)

www.bh.rmit.edu.au/mrs/DigitalRadiography/DRPapers/AtStth.html

Mason W.P., “ Electromechanical Transducers and Wave Filters”. New York: D. Van Nostrand, (1942).

Matthews, F.L., Rawlings, R.D. “Composite Materials and Engineering science” Chapman and Hall. 1994.

Matuszewski, B., Shark, L.-K., Smith, J. P., and Varley, M. R.: “Automatic fusion of multiple non-destructive testing images and CAD models for industrial inspection”, IEE 7th International conference on Image Processing and its Applications, IPA’97, Manchester, pp661-665, 1999.

Matuszewski, B., Shark, L-K., Smith, J. P., and Varley, M. R.: “Automatic registration of ultrasound images with wire-frame CAD models for industrial inspection”, Proceedings of the IASTED International Conference on Signal and Image Processing, SIP’99, Nassau-Bahamas, pp134-138, October 1999.

Matuszewski, B. J., Shark, L-K., Smith, J. P., and Varley, M. R.: “Automatic mosaicing with error equalisation of non-destructive testing images for aerospace industry inspection”, 15th World Conference on Non-Destructive Testing, Roma 15-21 October 2000.

Matuszewski, B. J., Shark, L-K., Smith, J. P., and Varley, M. R.: “Region-based wavelet fusion of ultrasonic, radiographic and shearographic non-

destructive testing images”, 15th World Conference on Non-Destructive Testing, Roma 15-21 October 2000.

Matuszewski, B. J., Shark, L.-K., Smith, J. P., and Varley, M. R.: “Sparse image mosaic construction for radiographic inspection of large structures”, BINDT, NDT 2001 Conference Proceedings, pp221-226, Coventry, September 2001.

Matuszewski, B. J., Shark, L.-K., Ciliberto, A., and Cavaccini, G.: “Large size image mosaic construction for ultrasonic inspection of primary aircraft structures”, BINDT, NDT 2002 Conference Proceedings, pp99-104, Southport, September 2002.

Matuszewski, B. J., Shark, L.-K., Varley, M. R., and Smith, J. P.: “Error equalisation for sparse image construction”, Proc. BMVC, pp508-518, 2003.

Morris S.A., Hutchens C.G., “Implementation of Mason’s Model on Circuit Analysis Programs”. IEEE Transactions on Ultrasonics, Ferroelectrics, and Frequency Control. Vol.UFFC-33. No 3,(May 1986).

Nikoonahad and Iravani, “Focusing ultrasound in biological media” IEEE transactions on Ultrasonics, Ferroelectrics, and Frequency Control. Vol 36 No 2 march 1989 pp209-215

O’Neill. H.T “Theory of focusing radiators”, Journal of Acoustics, 1949,Vol 21, pp516-526

Oppenheim, A. V. R.W. Schafer “Digital Signal Processing” Prentice Hall , 1975

Parker and Salter “ A Novel Shearography System for Aerospace Non-destructive Testing” Proc Instn Mech Engrs Vol 213 Part G, 1999 pp23-33

Robinson D.E., Lees Bess S.L., "Near field transient radiation patterns for circular pistons", IEEE Transactions on Acoustics, Speech, and Signal Processing, Vol. ASSP-22, No 6, Dec. 1974, pp395-403.

Partridge P.G. "Diffusion bonding of metals" Advisory group for Aerospace Research and Development (AGARD) AGARD lecture series No 168 October 1989 pp5-1 to 5-23.

Pezzoni R., Ettemeyer "Laser – shearography for non-destructive testing of large area composite helicopter structures" 15th World NDT Conference, WCNDT, Rome 2000

Silk M.G., "Ultrasonic Transducers for Nondestructive Testing". Adam Hilger Ltd., Bristol, (1984).

Shark, L-K., Matuszewski, B., Smith, J. P., and Varley, M. R.: "Automatic mosaicing and construction of three-dimensional shearographic surface images for inspection of aircraft components", Proceedings of the IASTED International Conference on Signal and Image Processing, SIP'99, Nassau-Bahamas, pp183-187, October 1999.

Shark, L.-K., Matuszewski, B., Smith, J. P., and Varley, M. R.: "Defect visualisation using CAD model in multi-technique inspection environment", Conference Proceedings of NDT'99 and UK Corrosion'99 at Poole, Dorset, pp25-30, September 1999

Shark, L-K., Matuszewski, B. J., Smith, J. P., and Varley, M. R.: "Automatic feature-based fusion of ultrasonic, radiographic and shearographic images for aerospace non-destructive testing", INSIGHT Vol.43, No.9, pp607-615, 2001.

Shark, L-K., Matuszewski, B. J., Smith, J. P., and Varley, M. R.: "Automatic feature-based fusion of ultrasonic, radiographic and shearographic images for

aerospace non-destructive testing”, INSIGHT Vol.43, No.9, pp607-615, 2001.

Silk M.G “Ultrasonic transducers for non destructive testing” Bristol : Adam Hilger Ltd. 1984.

Smith G.C. British National Physics Laboratory News No 365

Smith J.P., Shark L.-K., Terrell T.J., “Detection of aircraft component defects using low voltage excitation of ultrasonic transducers”. Review of progress in quantitative non-destructive Evaluation, Vol. 16a, 1996, pp935-942.

Smith, J. P., Shark, L.-K., Varley, M. R. and Matuszewski, B.: “Data integration and processing system for non-destructive testing of aircraft components”, Final Project Report submitted to EPSRC for the DIAPS project (Grant Ref: GR/L34464), December, 2000.

Smith, Salter and Parker “Apparatus and method for the non-destructive testing of articles using optical metrology” Patent EP 1 200 797 B1, 2003

Sprawls.P. “Physical Principles of Medical Imaging”, 2nd edition, Medical physics publishing(1995) 1-15,252-281&303-316

Stephen D. Swadling S.J “Advanced joining of metallic materials AGARD CP 398 1986 p7.7-1.

Steinberg, B.D. “ Principles of aperture and array system design”, New York, NY: John Wiley and Sons (1976)

Tober G. Elze. S AGARD conference proceedings no398 Advanced joining of Aerospace Metallic Materials p 11-1

Von Ramm, O.T. and S.W. Smith "Beam steering with linear arrays" ,
Transactions on biomedical engineering, Vol. BME-30, No. 8, New York,
NY: Institute of electrical and electronics engineers, August 1983,pp438-452.

Wells P.N.T. Biomedical Ultrasonics Academic press, London 1977

Yang, Chen, Steinchen and Hung, "Digital shearography for non-destructive
testing: Potential, Limitations and applications"
www.personalwebs.oakland.edu/~yang/linkfile/paper01.pdf

Yerima Y., "A high frequency phased ultrasound array" Ph.D. thesis,
UMIST, 1991.

Appendix A

Patent



(12) EUROPEAN PATENT SPECIFICATION

(45) Date of publication and mention
of the grant of the patent:
09.04.2003 Bulletin 2003/15

(51) Int. Cl.: G01B 9/02, G01B 11/16,
G01J 9/02

(21) Application number: 99936870.7

(86) International application number:
PCT/GB99/02553

(22) Date of filing: 03.08.1999

(87) International publication number:
WO 00/011430 (02.03.2000 Gazette 2000/09)

(54) APPARATUS AND METHOD FOR THE NON-DESTRUCTIVE TESTING OF ARTICLES USING OPTICAL METROLOGY

VORRICHTUNG UND VERFAHREN ZUR ZERSTÖRUNGSFREIEN PRÜFUNG VON GEGENSTÄNDEN UNTER ANWENDUNG OPTISCHER MESSTECHNIK

APPAREIL ET PROCÉDE POUR TESTER DES ARTICLES DE FACON NON DESTRUCTIVE PAR METROLOGIE OPTIQUE

(84) Designated Contracting States:
DE ES FR GB IT SE

• PARKER, Steve Carl Jamieson
Bristol Avon BS16 7AT (GB)

(43) Date of publication of application:
02.05.2002 Bulletin 2002/18

(74) Representative: MacLean, Martin David
BAE Systems plc,
Group IP Dept.,
Lancaster House
PO Box 87
Farnborough Aerospace Centre
Farnborough, Hampshire GU14 6YU (GB)

(73) Proprietor: BAE SYSTEMS plc
Farnborough, Hampshire GU14 6YU (GB)

(72) Inventors:
• SMITH, John Patrick W25A
Br. Aerosp. Milit. Aircraft
Preston, Lancashire PR4 1AX (GB)
• SALTER, Phillip Langley FPC 267
British Aerospace
Bristol Avon BS12 7QW (GB)

(56) References cited:
EP-A- 0 875 744 WO-A-84/01998
DE-A- 4 231 578 GB-A- 2 307 550
US-A- 5 094 528 US-A- 5 481 356

EP 1 200 797 B1

Note: Within nine months from the publication of the mention of the grant of the European patent, any person may give notice to the European Patent Office of opposition to the European patent granted. Notice of opposition shall be filed in a written reasoned statement. It shall not be deemed to have been filed until the opposition fee has been paid. (Art. 99(1) European Patent Convention).

[0001] This invention relates to an apparatus and method for inspecting and testing a sample, such as an aircraft skin panel, by optical metrology and is particularly, but not exclusively, concerned with such method and apparatus applicable to optical non-destructive testing by shearography for aerospace components.

[0002] Coherent optical techniques such as holography, interferometry, electronic speckle pattern interferometry (ESPI), speckle interferometry, particle image velocimetry (PIV) and shearography are currently being utilised for applications such as non-destructive testing (NDT), vibration analysis, object contouring, stress and strain measurement, fatigue testing, deformation analysis and fluid flow diagnosis. All these techniques have associated drawbacks with performance being to some extent a trade-off against specific disadvantages inherent in the individual techniques.

[0003] For example shearography has high sensitivity and tolerance to environmental noise but known NDT techniques involving shearography are of limited application because of difficulties in inspecting large areas due to inefficiencies in the laser power available and optical beam expansion and delivery systems. Additional problems are encountered with a relatively low signal to noise ratio.

[0004] A shearography system works by generating two laterally displaced images of a test sample. In practice this is achieved using a shearing element of which there are many variants, and imaging optics. When the sample is illuminated using coherent radiation such as visible radiation from a laser, these twin images are modulated by a speckled pattern due to the high coherence of the light. These two images interfere to form a macroscopic speckle pattern, which may be recorded electronically using a charge couple device (CCD) and a frame store. Interferometric images or fringe patterns may be generated by subtracting two speckle patterns of the sheared twin image where the second speckle pattern is recorded after the test specimen has been subjected to a stressing force, such as thermal, pressure or vibration. If an appropriate stressing force is applied defects in the structure of the sample are revealed by highly characteristic "figure of eight" fringes. Such an arrangement is described in US5481356.

[0005] In practice the resulting fringe patterns are noisy due to spurious intensity variations and consequently the sensitivity of the shearography technique is reduced. Many techniques have been proposed for suppressing such noise by extracting the phase difference between the sheared images from the interferogrammes. One proposed technique, described in our UK patent application number GB2324859, involves the phase stepping of the two laterally displaced images of the sample, by stepping the phase of one of the two images by $\frac{2\pi}{3}$ during each of the line scans of a camera so that successive lines are incremented in phase to en-

may be decoded by running a vertical convolution mask over the image. This technique has the advantages of suppressing a substantial proportion of noise whilst providing single frame analysis. A laser shearing interferometer suitable for providing such interferogramme images is disclosed in our UK patent application no GB2324859 and is further described below in the context of the present invention. Another relevant scanning technique is described in GB2307550.

[0006] In known applications of shearography for non-destructive testing, a coherent light source is usually a split beam laser. Splitting of the beam allows a larger area of the sample to be tested, but in expanding the beam intensity of the light varies with radius of the circular beam. This variation in intensity of light incident on the sample being tested results in poor quality of the reflected images and hence poor quality interferogrammes.

[0007] Furthermore when the sample is to be tested under stress induced by temperature or pressure variations, the known methods generally require that the laser beam is delivered via a fibre optic cable into a sealed chamber containing the sample, and in which the pressure or temperature can be varied. The laser is generally situated outside of the sealed chamber as known lasers used in NDT are susceptible to variations in pressure and temperature changes and may not perform to the required standard when exposed to the temperature or pressure variations required for stressing the sample. An example of this is described in WO-A-8401998.

[0008] It is generally less desirable to use temperature variations to induce stress changes as it is usually difficult to keep the entire sample at the same required temperature and yet to be able to quickly and accurately alter the temperature in the chamber to a new value.

[0009] A known pressure variation stressing technique allows the pressure in a chamber to cycle between two pressure levels. Speckle pattern images are recorded at ambient pressure then again at a lower, pre-determined pressure level. An interferometric image is then generated by subtracting the speckle pattern images recorded at the two different pressures. This technique however can produce poor images if the sample undergoes vibration whilst either speckle pattern image is being recorded.

[0010] The present invention seeks to provide improved apparatus and methods for the NDT of articles using shearography, in which the articles are subject to pressure stressing to provide interferometric images.

[0011] According to a first aspect of the present invention, there is provided apparatus for inspecting or testing a sample using shearography techniques including:

a laser shearing interferometer including:

a source of coherent radiation.

line generating means for producing a line of coherent radiation from said source.

line scanning means for scanning said line of coherent radiation over said sample.

shearing element means for generating two laterally displaced images of the sample, and

phase stepping or ramping means for stepping or ramping the phase of one of the two images, and

a video camera for viewing images of the sample and for providing corresponding video output signals.

an image processor operable to receive the video output signals and to extract therefrom the frame rate of the camera in substantially realtime,

signal generating means for providing to said stepping or ramping means and said line scanning means a signal substantially in phase with the frame rate of said camera.

decoding means for phase unwrapping or extraction.

a vacuum chamber for containing at least the laser shearing interferometer and sample.

pressure control means capable of varying the pressure within the vacuum chamber between several pre-determined pressure values, and

control unit means for interfacing and synchronising said processor, said signal generating means, said decoding means and said pressure control means.

[0012] Preferably said laser shearing interferometer is mounted on a movable gantry. Advantageously the movement of the movable gantry is controlled by the control unit.

[0013] The gantry may be adapted to operate in synchronisation with the pressure control means and the line scanning means.

[0014] According to a second aspect of the present invention, there is provided a method for inspecting or testing a sample using shearography techniques comprising the steps of:

providing a vacuum chamber,

locating the sample and a laser shearing interferometer within the vacuum chamber, the laser shearing interferometer comprising at least a source of coherent radiation, line scanning means, shearing

element means, and phase stepping or ramping means.

illuminating said sample by using the line scanning means to scan a line of coherent radiation across the surface of the sample to generate, via the shearing element means, two laterally displaced images of the sample.

phase stepping or ramping the phase of one of the two images during each of the line scans using the stepping or ramping means.

observing and recording said phase stepped images by means of the video camera, whilst maintaining the scanning of a line and phase stepping of the images in synchronisation with the frame scan rate of the camera.

pre-programming a control unit with a pressure versus time profile and indicating point of said profile when images should be recorded and processed, and

using the control unit for controlling and synchronising the pressure in the vacuum chamber, the scan rate of the line scanning means, the phase stepping means and the image processor, to provide a substantially real time dynamic image of the object under test on a monitor.

[0015] For a better understanding of the present invention, and to show how the same may be carried into effect reference will now be made, by way of example, to the accompanying drawings in which:

Figure 1 shows a diagrammatic representation of apparatus according to one aspect of the present invention for inspecting or testing a sample by optical metrology utilising the method of the present invention.

Figure 2 shows a diagrammatic view to an enlarged scale of an interferometer for use in the method and apparatus of the present invention.

Figure 3 shows a diagrammatic representation of interfaces of apparatus according to the present invention, and

Figure 4 shows a graph of pressure versus time for providing test profiles.

[0016] Figure 1 shows a vacuum chamber 1, in which is a laser shearing interferometer system 3 and an article to be inspected 17. The laser shearing interferometer system 3 comprises a laser 5 which is adapted to be capable of operating in a vacuum, a movable mirror

15. a charge coupled device (CCD) imaging camera 11 which may be used for shearography and for electronic speckle interferometry and which is capable of providing an output signal 21, and an interferometer 9. A line generator 7 is located adjacent the laser 5, for generating a line of coherent radiation 19. The line generator 7 can conveniently be a lasiris line scanner which is commercially available.

[0017] The interferometer 9 comprises a movable mirror 33 which is attached to a PZT piezo electric transducer 31 for providing phase stepping. The interferometer 9 further comprises a tilted mirror 41 for enabling shearing, and a shearing element 29. Situated outside of the vacuum chamber 1 are a frame synchronising unit 23 for processing the output signal 21 from the CCD camera 11, and a triggered signal generator 25 and an amplifier 27, for providing and amplifying a signal to drive the movable mirror 15 and the transducer 31 in synchronism with the CCD camera 11.

[0018] Figure 2 shows the interferometer 9 in more detail. The shearing element 29 comprises two prisms 35 and 37 for receiving light reflected from the surface of the article 17 and for generating two laterally displaced images in the direction of the arrow E.

[0019] In operation, the article 17 is illuminated by scanning a line 19 of coherent radiation across the surface of the article 17. The coherent radiation is provided by the laser 5 operating via the line generator to generate the line 19. The beam from the line generator is directed along path A to fall on the movable mirror 15. The mirror 15 rotates backwards and forwards, as shown by the arrow B, to scan the line 19 up and down the article 17 in the direction of the arrow D. Light reflected from the surface of the article 17 falls on the shearing element 29. The CCD camera 11 is operable to view the article 17 via the shearing element 29, and provides an output signal 21. This is received by the frame synchronisation unit 23 which extracts the frame rate of the camera 11 which it uses to synchronise the rate at which the line of coherent radiation 19 is scanned across article 17 by the movable mirror 15. Thus the frame synchronisation unit 23 yields frame synchronising pulses which can be filtered to drive the movable mirror 15 directly so that the mirror 15 is synchronised to the camera output signal 21 to yield a stable image on a monitor. The filtered synchronising pulses trigger the signal generator 25 which provides signals which are amplified by amplifier 27 and which drives the mirror 15 and the transducer 31 in synchronism with the camera 11. As the transducer 31 receives the output signal from the amplifier 27 it expands or contracts accordingly, and causes the attached mirror 33 to move, thereby providing the required phase stepping. The resulting interferograms are decoded by processor using a vertical convolution mask technique, as described in our UK patent application number GB2324859 and produce high quality images of the article 17 for identifying defects for viewing on a monitor.

[0020] Figure 3 shows a laser shearing interferometer

3 located on a gantry 39, within a vacuum chamber 1. The laser shearing interferometer 3 produces and scans a line 19 over the surface of article 17, as described with reference to Figures 1 and 2. A vacuum pump 45 is connected to the vacuum chamber 1 via an electronic valve 43, arrow E showing direction of exhaust. A control unit 47, situated outside of the vacuum chamber 1 controls the movement of the gantry 39. Control unit 47 also comprises the frame synchronising unit 23, the signal generator 25 and the amplifier 27. The control unit 47 therefore takes the output signal 21 from the camera 11 and controls the synchronisation of the mirror 15 and the transducer 31. The number of phase steps is controlled by the number of different signals the signal generator 25 is programmed to send to the transducer 31. In this embodiment 5 phase steps are used to provide a satisfactory signal to noise ratio. The control unit also controls the electronic valve 43, thereby controlling the amount of air introduced to or removed from the vacuum chamber 1, and when this airflow takes place. Thus the control unit 47 is able to synchronise the complete operation of the NDT facility.

[0021] The control unit 47 is capable of being programmed to allow phase stepped images to be taken at various times, at various pressures during the test. The images are processed by the control unit and displayed on a monitor.

[0022] Figure 4 shows a graph of pressure versus time, with two profiles F and G. These represent different profiles programmed into the control unit, for testing different articles or for varying the conditions under which articles are tested. For example, profile F shows a linear correlation between pressure and time, with the pressure being increased steadily and the points being marked at those times and corresponding pressures at which interferometric images are recorded. Profile G shows a rapid increase in pressure initially, during which time images are recorded with a very short time interval between them, followed by slower increase in pressure, with longer intervals between recorded images.

[0023] For any profile the pressure may be lowered and/or raised depending on testing requirements. In this example when the control unit is programmed with profile F it controls the flow of air to or from the vacuum chamber during the time period of the profile. At each pre-determined point shown on the profile F the control unit 47 ensures that the camera 11 records 5 phase stepped sheared images, and that the phase stepping means (the transducer 31) and the line scanning means (the movable mirror 15) are operating in phase with the scan rate of the camera 11 to provide stable images to the monitor. Every set of 5 phase stepped sheared images are combined by the control unit into a single interferometric image which is decoded and displayed on the monitor, in real time. The second decoded interferometric image, recorded at the second point on the profile F, is combined in real time with the first interferometric image, to provide a dynamic image of the article being test-

ed. The third interferometric image is combined with the result of a combination of the first and second images, and so on. This allows the user to see on the monitor a real time dynamic image of the state of the article being tested as the pressure is varied.

[0024] Recording images at various points upon a pressure curve allows the user to see when the object starts to react to the change in pressure, and by how much. Having several images recorded also means that if one is inaccurate, due to vibration of the laser or article for example, then the test will still provide accurate data from the other points and will not have to be repeated.

[0025] For large articles, the control unit controls the movement of the gantry on which the laser shearing interferometer is mounted, in synchronism with the pressure control valve and the rate of scan of the camera, so that images of the entire article may be scanned at the same pressure. This provides very quick and accurate means for testing large articles.

Claims

1. Apparatus for inspecting or testing a sample (17) using shearography techniques including:

a laser shearing interferometer (3) including:

a source (5) of coherent radiation,

line generating means (7) for producing a line of coherent radiation (19) from said source (5),

line scanning means (15) for scanning said line of coherent radiation (19) over said sample (17),

shearing element means (29, 41) for generating two laterally displaced images of the sample (17), and

phase stepping or ramping means (31) for stepping or ramping the phase of one of the two images, and

a video camera (11) for viewing images of the sample (17) and for providing corresponding video output signals (21),

an image processor (23) operable to receive the video output signals (21) and to extract therefrom the frame rate of the camera (11) in substantially realtime, signal generating means (25) for providing to said stepping or ramping means (31) and said line scanning means (15) a signal substantially in phase with the frame rate of said camera (11).

decoding means for phase unwrapping or extraction.

a vacuum chamber (1) for containing at least the laser shearing interferometer (3) and sample (17).

pressure control means (43, 45) capable of varying the pressure within the vacuum chamber (1) between several pre-determined pressure values, and

control unit means (47) for interfacing and synchronising said processor (23), said signal generating means (25), said decoding means and said pressure control means (43, 45).

2. Apparatus for inspecting or testing a sample as claimed in claim 1 and wherein the laser shearing interferometer (3) is mounted on a movable gantry (39).

3. Apparatus for inspecting or testing a sample as claimed in claim 2 and wherein the movement of the movable gantry (39) is controlled by the control unit (47).

4. Apparatus for inspecting or testing a sample as claimed in claim 2 or claim 3 and wherein the gantry (39) is adapted to operate in synchronisation with the pressure control means (43, 45) and the line scanning means (15).

5. A method for inspecting or testing a sample using shearography techniques comprising the steps of:

providing a vacuum chamber,

locating the sample and a laser shearing interferometer within the vacuum chamber, the laser shearing interferometer comprising at least a source of coherent radiation, line scanning means, shearing element means, and phase stepping or ramping means,

illuminating said sample by using the line scanning means to scan a line of coherent radiation across the surface of the sample to generate, via the shearing element means, two laterally displaced images of the sample,

phase stepping or ramping the phase of one of the two images during each of the line scans using the stepping or ramping means,

observing and recording said phase stepped images by means of the video camera, whilst maintaining the scanning of a line and phase

stepping of the images in synchronisation with the frame scan rate of the camera.

pre-programming a control unit with a pressure versus time profile and indicating point of said profile when images should be recorded and processed, and

using the control unit for controlling and synchronising the pressure in the vacuum chamber, the scan rate of the line scanning means, the phase stepping means and the image processor, to provide a substantially real time dynamic image of the object under test on a monitor.

Patentansprüche

1. Vorrichtung zur Inspektion oder Prüfung eines Gegenstandes (17) unter Benutzung einer scherographischen Technik mit den folgenden Merkmalen:

ein Laser-Scher-Interferometer (3) mit den folgenden Teilen:

eine Quelle (5) kohärenter Strahlung.

ein Zeilengenerator (7) zur Erzeugung einer Zeile kohärenter Strahlung (19) aus dieser Quelle (5),

Zeilen-Abtastmittel (15) zum Abtasten der Zeile kohärenter Strahlung (19) über dem Gegenstand (17).

eine Scher-Element-Vorrichtung (29, 41) zur Erzeugung von zwei seitlich versetzten Bildern des Gegenstandes (17), und

Phasenabstufungs- oder Rampenmittel (31) zur Abstufung oder Abschrägung der Phasen eines der beiden Bilder, und

eine Videokamera (11) zur Betrachtung von Bildern des Gegenstandes (17) und zur Lieferung entsprechender Video-Ausgangssignale (21).

ein Bildprozessor (23), der die Video-Ausgangssignale (21) empfängt und daraus die Bildrate der Kamera (11) im Wesentlichen in Echtzeit extrahiert.

Signalerzeugungsmittel (25), die den abgestuften oder abgeschrägten Mitteln (31) und den Zeilen-Abtastmitteln (15) ein Signal liefert, das im Wesentlichen in Phase

ist mit der Bildrate der Kamera (11).

Dekodiermittel zum Phasen-Auspacken oder zur Extraktion.

eine Vakuumkammer (1), die wenigstens das Laser-Scher-Interferometer (3) und den Gegenstand (17) aufnimmt.

Drucksteuermittel (43, 45), die in der Lage sind, den Druck innerhalb der Vakuumkammer (1) zwischen verschiedenen vorbestimmten Druckwerten zu ändern, und

Steuermittel (47) zum Interface-Anschluss und zur Synchronisation des Prozessors (23) der Signal-Erzeugungsmittel (25) des Dekoders und der Drucksteuermittel (43, 45).

2. Vorrichtung zur Inspektion oder Prüfung eines Gegenstandes nach Anspruch 1, bei der das Laser-Scher-Interferometer (3) auf einem beweglichen Gestell (39) montiert ist.

3. Vorrichtung zur Inspektion oder Prüfung eines Gegenstandes nach Anspruch 2, bei der die Bewegung des beweglichen Gestells (39) durch die Steuereinheit (47) gesteuert wird.

4. Vorrichtung zur Inspektion oder Prüfung eines Gegenstandes nach den Ansprüchen 2 oder 3, bei der das Gestell (39) synchron mit den Drucksteuermitteln (43, 45) und den Zeilen-Abtastmitteln (15) arbeitet.

5. Verfahren zur Inspektion oder Prüfung eines Gegenstandes unter Benutzung einer scherographischen Technik mit den folgenden Schritten:

es wird eine Vakuumkammer hergestellt,

es wird der Gegenstand und ein Laser-Scher-Interferometer in die Vakuumkammer eingebracht, wobei das Laser-Scher-Interferometer wenigstens eine Quelle kohärenter Strahlung, Zeilen-Abtastmittel, Scher-Element-Mittel und Phasen-Abstufungs- oder Abschrägungsmittel enthält.

es wird der Gegenstand durch Benutzung der Abtastmittel beleuchtet, um eine Zeile kohärenter Strahlung über der Oberfläche des Gegenstandes abzutasten und um über die Scher-Element-Mittel zwei seitlich versetzte Bilder des Gegenstandes zu erzeugen.

es wird die Phase eines der zwei Bilder wäh-

Fig.1.

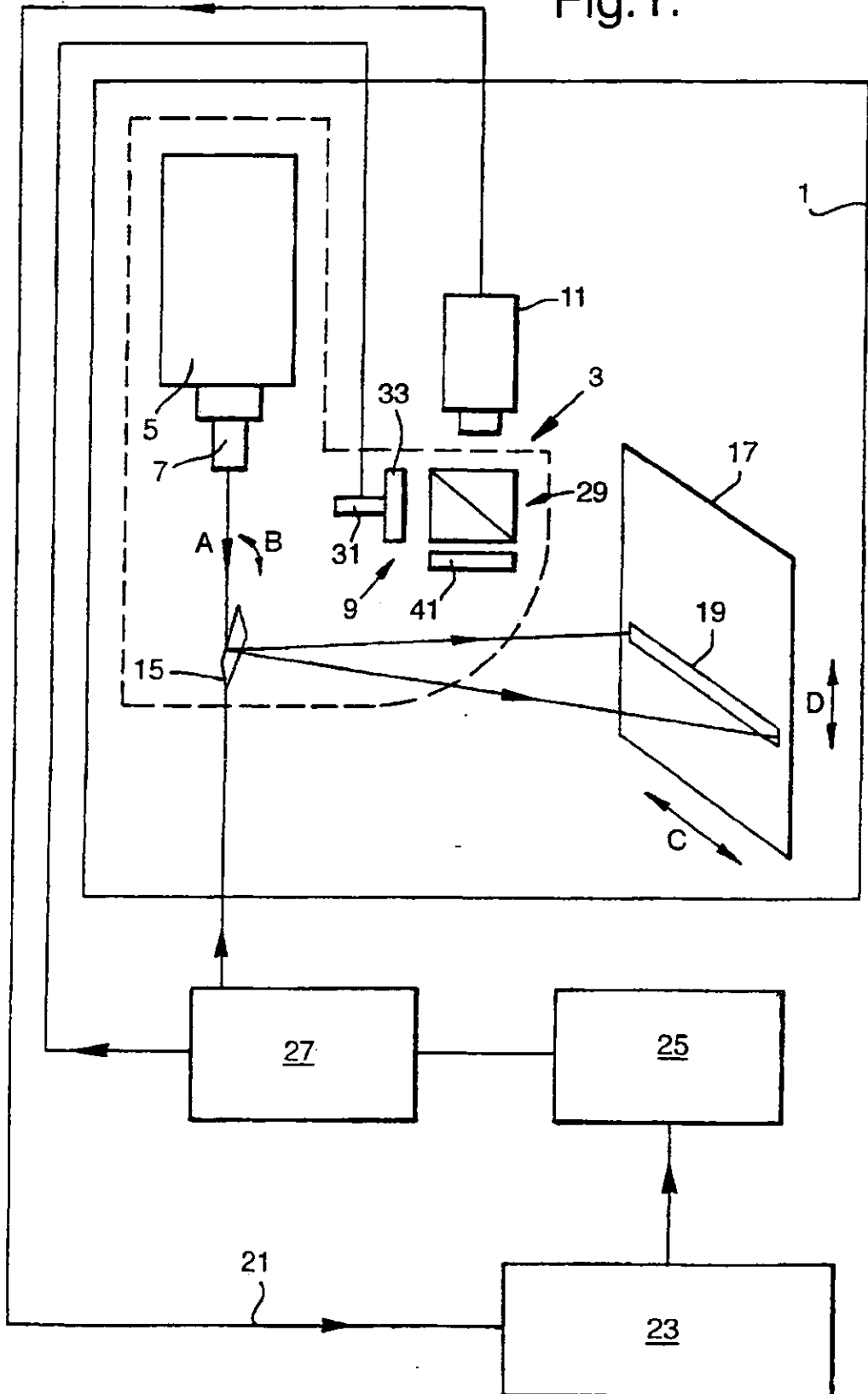


Fig.2.

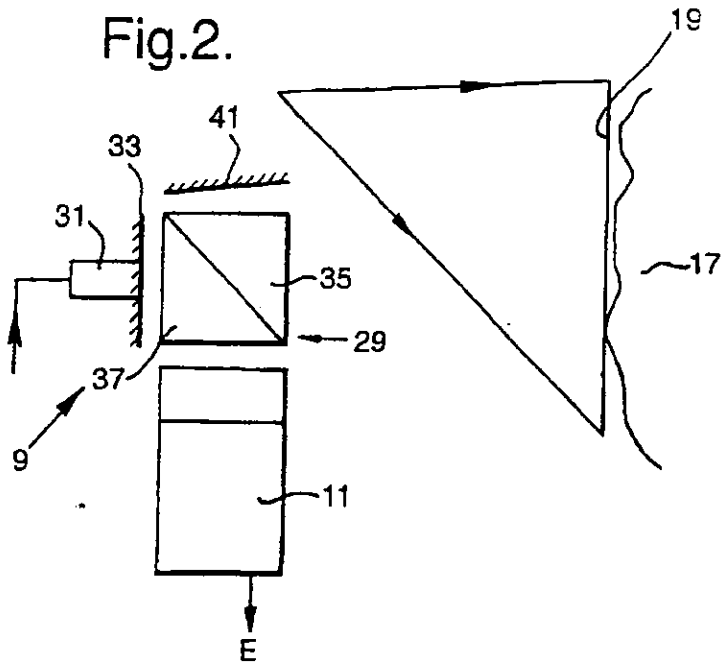
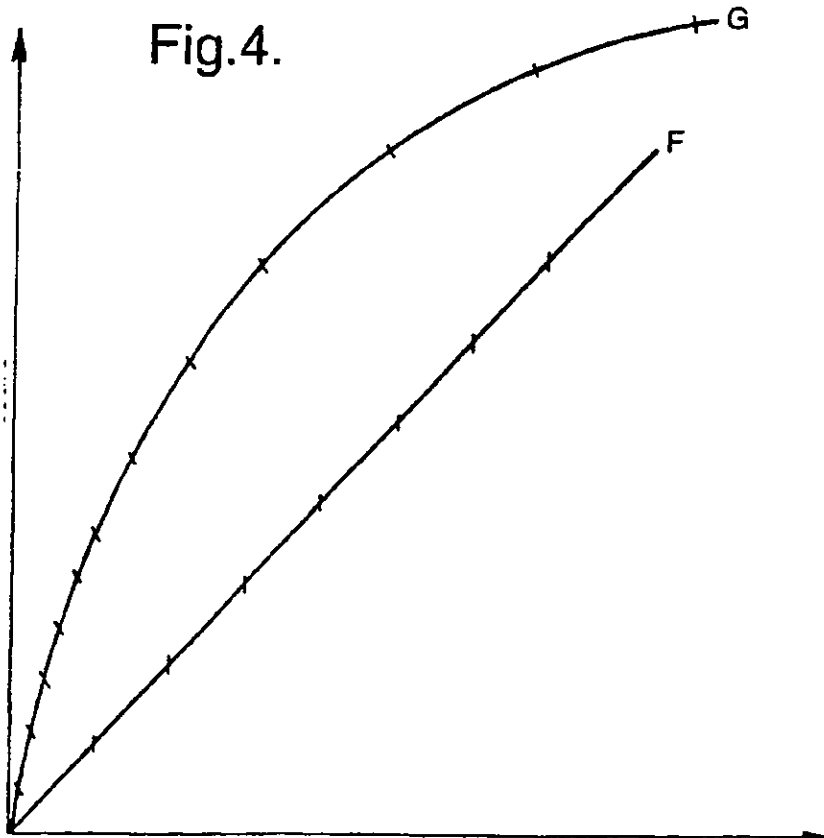
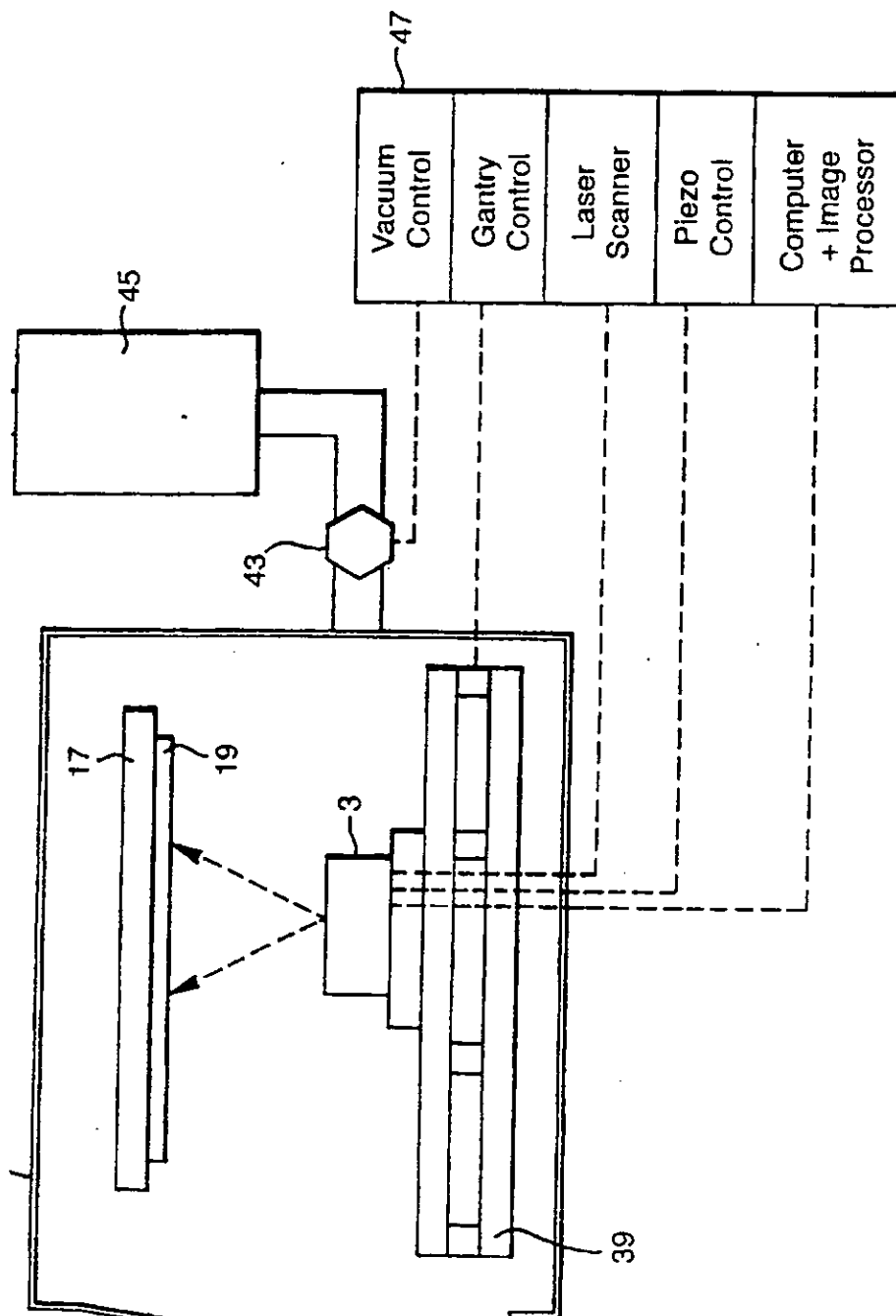


Fig.4.





Appendix B

Awards

**THE
BRITISH
INSTITUTE of
NON-DESTRUCTIVE
TESTING**



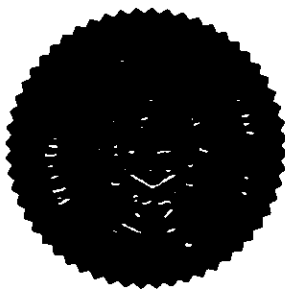
THE NEMET AWARD

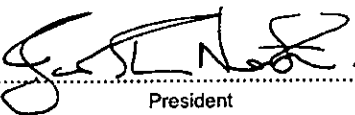
in recognition of the outstanding example of effective use of NDT

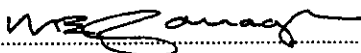
2003

John P Smith

in recognition of his work automating the NDT process




.....
President


.....
Secretary



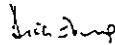
Chairman's Bronze Award
for Innovation

1998

INNOVATION AND TECHNOLOGY - OUR COMPETITIVE EDGE

WE WILL ENCOURAGE A HUNGER FOR NEW IDEAS
NEW TECHNOLOGIES AND NEW WAYS OF WORKING TO SECURE
SUSTAINED COMPETITIVE ADVANTAGE FOR OUR COMPANY

*The Innovation Team
Military Aircraft and Structures
Warton*



R H Evans
Chairman

BRITISH AEROSPACE 



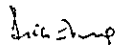
Chairman's Bronze Award
for Innovation

1998

INNOVATION AND TECHNOLOGY - OUR COMPETITIVE EDGE

WE WILL ENCOURAGE A HUNGER FOR NEW IDEAS
NEW TECHNOLOGIES AND NEW WAYS OF WORKING TO SECURE
SUSTAINED COMPETITIVE ADVANTAGE FOR OUR COMPANY

*Peter Dawson and John Smith
Military Aircraft and Structures
Farnborough*



R H Evans
Chairman

BRITISH AEROSPACE 

Appendix C

Publications

Smith J.P., Shark L.-K., Terrell T.J., "Detection of aircraft component defects using low voltage excitation of ultrasonic transducers". Review of progress in quantitative non-destructive Evaluation, Vol. 16a, 1996, pp935-942.

Smith, J. P., Shark, L.-K., Varley, M. R. and Matuszewski, B.: "Data integration and processing system for non-destructive testing of aircraft components", Final Project Report submitted to EPSRC for the DIAPS project (Grant Ref: GR/L34464), December, 2000.

Smith, Salter and Parker "Apparatus and method for the non-destructive testing of articles using optical metrology" Patent EP 1 200 797 B1, 2003

Deng, W., Matuszewski, B. J., Shark, L.-K., Smith, J. P., Ciliberto, A., and Cavaccini, G.: "CAD based simulation and visualisation for non-destructive testing", BINDT, NDT 2002 Conference Proceedings, pp119-124, Southport, September 2002.

Deng W., Matuszewski B. J., Shark L.-K., Smith J. P., Cavaccini G., and Agresti M.: "Mapping 2D NDT images to 3D CAD surface for defect visualisation and interpretation of curved aerostructures", BINDT, NDT 2003 Conference Proceedings, pp113-118, Worcester, September 2003.

Deng W., Shark L.-K., Matuszewski B. J., Smith J. P., and Cavaccini G.: "CAD model-based inspection and visualisation for 3D non-destructive testing of complex aerostructures", Insight, Vol.46, No.3, pp157-161, March 2004.

Deng W., Shark L.-K., Smith J. P., and Cavaccini G.: "CAD based structure decomposition and reverse engineering for visualisation and modelling of defects", BINDT, NDT 2004 Conference Proceedings, Vol.2, pp73-78.

Deng W., Matuszewski B. J., Shark L.-K., Smith J. P., and Cavaccini G.: "Multi-modality NDT image fusion and its mapping on curved 3D CAD Surface", 16th World Conference on Nondestructive Testing, Montreal, 2004.

Matuszewski, B., Shark, L.-K., Smith, J. P., and Varley, M. R.: "Automatic fusion of multiple non-destructive testing images and CAD models for industrial inspection", IEE 7th International conference on Image Processing and its Applications, IPA '97, Manchester, pp661-665, 1999.

Matuszewski, B., Shark, L.-K., Smith, J. P., and Varley, M. R.: "Automatic registration of ultrasound images with wire-frame CAD models for industrial inspection", Proceedings of the IASTED International Conference on Signal and Image Processing, SIP'99, Nassau-Bahamas, pp134-138, October 1999.

Matuszewski, B. J., Shark, L.-K., Smith, J. P., and Varley, M. R.: "Automatic mosaicing with error equalisation of non-destructive testing images for aerospace industry inspection", 15th World Conference on Non-Destructive Testing, Roma 15-21 October 2000.

Matuszewski, B. J., Shark, L.-K., Smith, J. P., and Varley, M. R.: "Region-based wavelet fusion of ultrasonic, radiographic and shearographic non-destructive testing images", 15th World Conference on Non-Destructive Testing, Roma 15-21 October 2000.

Matuszewski, B. J., Shark, L.-K., Smith, J. P., and Varley, M. R.: "Sparse image mosaic construction for radiographic inspection of large structures", BINDT, NDT 2001 Conference Proceedings, pp221-226, Coventry, September 2001.

Matuszewski, B. J., Shark, L.-K., Varley, M. R., and Smith, J. P.: "Error equalisation for sparse image construction", Proc. BMVC, pp508-518, 2003.

Shark, L.-K., Matuszewski, B., Smith, J. P., and Varley, M. R.: "Automatic mosaicing and construction of three-dimensional shearographic surface

images for inspection of aircraft components”, Proceedings of the IASTED International Conference on Signal and Image Processing, SIP'99, Nassau-Bahamas, pp183-187, October 1999.

Shark, L.-K., Matuszewski, B., Smith, J. P., and Varley, M. R.: “Defect visualisation using CAD model in multi-technique inspection environment”, Conference Proceedings of NDT'99 and UK Corrosion'99 at Poole, Dorset, pp25-30, September 1999

Shark, L-K., Matuszewski, B. J., Smith, J. P., and Varley, M. R.: “Automatic feature-based fusion of ultrasonic, radiographic and shearographic images for aerospace non-destructive testing”, INSIGHT Vol.43, No.9, pp607-615, 2001.

Shark, L-K., Matuszewski, B. J., Smith, J. P., and Varley, M. R.: “Automatic feature-based fusion of ultrasonic, radiographic and shearographic images for aerospace non-destructive testing”, INSIGHT Vol.43, No.9, pp607-615, 2001.